# TOWARDS LARGE AREA SINGLE CRYSTALLINE TWO DIMENSIONAL ATOMIC CRYSTALS FOR NANOTECHNOLOGY APPLICATIONS


Yimin A. Wu

St. Anne's College, University of Oxford

Department of Materials, University of Oxford

A THESIS SUBMITTED FOR THE DEGREE OF *DOCTOR OF PHILOSOPHY*

AT THE UNIVERSITY OF OXFORD

Trinity TERM, 2012

To my parents and sister

“Where there is a will, there is a way”

有志者事竟成

# TOWARDS LARGE AREA SINGLE CRYSTALLINE TWO DIMENSIONAL ATOMIC CRYSTALS FOR NANOTECHNOLOGY APPLICATIONS

Yimin A. Wu,
St. Anne's College, University of Oxford
Trinity Term 2012

ABSTRACT OF A THESIS
SUBMITTED FOR THE DEGREE OF DOCTOR OF PHILOSOPHY

Nanomaterials have attracted great interest due to the unique physical properties and great potential in the applications of nanoscale devices. Two dimensional atomic crystals, which are atomic thickness, especially graphene, have triggered the gold rush recently due to the fascinating high mobility at room temperature for future electronics. The crystal structure of nanomaterials will have great influence on their physical properties. Thus, this thesis is focused on developing the methods to control the crystal structure of nanomaterials, namely quantum dots as semiconductor, boron nitride (BN) as insulator, graphene as semimetal, with low cost for their applications in photonics, structural support and electronics.

In this thesis, firstly, Mn doped ZnSe quantum dots have been synthesized using colloidal synthesis. The shape control of Mn doped ZnSe quantum dots has been achieved from branched to spherical by switching the injection temperature from kinetics to thermodynamics region. Injection rates have been found to have effect on controlling the crystal phase from zinc blende to wurtzite. The structural-property relationship has been investigated. It is found that the spherical wurtzite Mn doped ZnSe quantum dots have the highest quantum yield comparing with other shape or crystal phase of the dots.

Then, the Mn doped ZnSe quantum dots were deposited onto the BN sheets, which were micron-sized and fabricated by chemical exfoliation, for high resolution imaging. It is the first demonstration of utilizing ultrathin carbon free 2D atomic crystal as support for high resolution imaging. Phase contrast images reveal moiré interference patterns between nanocrystals and BN substrate that are used to determine the relative orientation of the nanocrystals with respect to the BN sheets and interference lattice planes using a newly developed equation method. Double diffraction is observed and has been analyzed using a vector method.

As only a few microns sized 2D atomic crystal, like BN, can be fabricated by the chemical exfoliation. Chemical vapour deposition (CVD) is as used as an alternative to fabricate large area graphene. The mechanism and growth dynamics of graphene domains have been investigated using Cu catalyzed atmospheric pressure CVD. Rectangular few layer graphene domains were synthesized for the first time. It only grows on the Cu grains with (111) orientation due to the interplay between atomic structure of Cu lattice and graphene domains. Hexagonal graphene domains can form on nearly all non-(111) Cu surfaces. The few layer hexagonal single crystal graphene domains were aligned in their crystallographic orientation over millimetre scale.

In order to improve the alignment and reduce the layer of graphene domains, a novel method is invented to perform the CVD reaction above the melting point of copper (1090 $^{o}$C) and using molybdenum or tungsten to prevent the balling of the copper from dewetting. By controlling the amount of hydrogen during the growth, individual single crystal domains of monolayer over 200 μm are produced determined by electron diffraction mapping. Raman mapping shows the monolayer nature of graphene grown by this method. This graphene exhibits a linear dispersion relationship and no sign of doping. The large scale alignment of monolayer hexagonal graphene domains with epitaxial relationship on Cu is the key to get wafer-sized single crystal monolayer graphene films. This paves the way for industry scale production of 2D single crystal graphene.

# Author’s Declaration

I declare that the work in this thesis was carried out in accordance with the regulations of the University of Oxford. No part of this work has been submitted previously for a degree at this or any other universities. All the work is original and is the result of my own investigation except where special reference is made to the work of others. All the research was carried out under the guidance of Dr. Jamie H. Warner， Professor G. Andrew D. Briggs and Dr. Kyriakos Porfyrakis, at the University of Oxford between October 2008 and August 2012.

# List of Publications

## Publications released within this thesis

1. **Y. A. Wu**[*], J. H. Warner, *Shape and Property Control of Mn doped ZnSe Quantum Dots: from Branched to Spherical.* ***Journal of Materials Chemistry***, **2012**, 22, 417-424 (*Corresponding author)

2. **Y. A. Wu**, A. I. Kirkland, F. Schäffel, K. Porfyrakis, N. P. Young, G. A. D. Briggs, J. H. Warner, *Utilizing Boron Nitride Sheets as Thin Supports for High Resolution Imaging of Nanocrystals*. ***Nanotechnology***, **2011**, 22, 195603-195612

   Selected as *"IOP Highlights of 2011"* by Institute of Physics Publishing group

3. **Y. A. Wu**, A. W. Robertson, F. Schäffel, S. Speller, J. H. Warner, *Aligned Rectangular Few-Layer Graphene Domains on Copper Surfaces.* ***Chemistry of Materials***, **2011**, 23, 4543-4547

4. **Y. A. Wu**, Y. Fan, S. Speller, G. L. Creeth, J. T. Sadowski, K. He, A. W. Robertson, C. S. Allen, J. H. Warner, *Large Single Crystals of Graphene on Melted Copper using Chemical Vapour Deposition*. ***ACS Nano***, **2012**, 6, 5010-5017

## Other publications of the author

1. C. J. Wang, **Y. A. Wu**, R. M. J. Jacobs, J. H. Warner, G. R. Williams, D. O'Hare, *Reverse Micelle Synthesis of Co-Al LDHs: Control of Particle Size and Magnetic Properties.* ***Chemistry of Materials***. **2011**, 23, 171-180

2. G. Liu, **Y. A. Wu**, and K. Porfyrakis, *Synthesis and Chemistry of Endohedral Fullerenes*. ***Current Organic Chemistry***, **2011**, 15, 1197-1207

3. J. Moghal, **Y. A. Wu**, J. H. Warner, Mechanical Response of Few Layer Graphene on Copper Foils. ***Scripta Materialia*, 2012**,67, 273-276

4. A. W. Robertson, A. Bachmatiuk, **Y. A. Wu**, F. Schäffel, B. Rellinghaus, B. Büchner, M. H. Rümmeli, J. H. Warner, Atomic Structure of Interconnected Few Layer Graphene Domains. ***ACS Nano***, **2011**, 5, 6610-6618

5. A. W. Robertson, A. Bachmatiuk, **Y. A. Wu**, F. Schäffel, B. Büchner, M. H. Rümmeli, J. H. Warner, *Structural Distortions in Few Layer Graphene from Creases*. ***ACS Nano***, **2011**, 5, 9984-9991

6. E. J. Lawrence, G. G. Wildgoose, L. Aldous, **Y. A. Wu**, J. H. Warner, R. G. Compton, P. D. McNaughter, *3-Aryl-3-(Trifluoromethyl)diazirines as Versatile Photoactivated Linker Molecules for the Improved Covalent Modification of Graphite and Carbon Nanotube Surfaces*. ***Chemistry of Materials,*** **2011**, 23, 3740-3751

7. B. Li, H. Cao, J. Yin, **Y. A. Wu**, J. H. Warner, *Synthesis and Separation of Dyes via Ni @ Reduced Graphene Oxide Nanostructures.* ***Journal of Materials Chemistry***, **2012**, 22, 1876-1883

8. L. Q. Mai, X. Xu, C. Han, Y. Luo, L. Xu, **Y. A. Wu**, Y. Zhao, *Rational Synthesis of Silver Vanadium Oxides/Polyaniline Traxial Nanowires with Enhanced Electrochemical Property*. ***Nano Letters***, **2011**, 11, 4992-4996

9. M. Zaka, Y. Ito, H. Wang, W. Yan, A. Robertson, **Y. A. Wu**, M. H. Rümmeli, D. Staunton, T. Hashimoto, J. J. L. Morton, A. Ardavan, G. A. D. Briggs, J. H. Warner, *Electron Paramagnetic Resonance Investigations of Purified Catalyst-free Single-walled Carbon Nanotubes.* ***ACS Nano***, **2010**, 4, 7708-7716

10. A. Robertson, C. S. Allen, **Y. A. Wu**, K. He, J. Olivier, J. Neethling, A. I. Kirkland, J. H. Warner, *Spatial Control of Defect Creation in Graphene at the Nanoscale*. ***Nature Communication***. **2012**, 3, 1114

11. A. Robertson, C. S. Allen, **Y. A. Wu**, K. He, J. Kim, J. Olivier, J. Neethling, A. I. Kirkland, J. H. Warner, *Dynamics of Single Fe Atoms in Graphene Vacancies*, **Submitted, 2012**

# Acknowledgement

When I sat down to look back to my D. Phil life, the memory of last four years flashed in my mind. I try to thank all the people who make my graduate studies both fun and fruitful. The list is long but distinguished. I could never make it without anyone on this list but also beyond.

I would like to begin by expressing my profound gratitude to my family, namely my mom, *Mrs Xinghua Zheng*, dad, *Mr. Fengbo Wu* and sister, *Ms Wenhui Zheng*, for their love, encouragement and unwavering supports throughout my whole life and academic study in Wuhan and Oxford.

The completion of D. Phil work would not be possible without the contributions of my supervisors, colleagues, and collaborators. First, I would like to give my sincerely thanks to *Professor Andrew Briggs*. Without the meeting with Andrew at the conference in Wuhan in 2007, my postgraduate study in Oxford would not be possible. Great thanks to him for giving me the opportunity to study in Oxford. This changed my life. His support, inspiration and vision helped me immeasurably.

Truly deepest special gratitude gives to *Dr. Jamie Warner* as a supervisor for his unyielding support of my research. Without his constant support and guidance over the past four years, this thesis would not be possible. I benefit enormously from the weekly one to one meeting with him on Monday morning at 10 am. I greatly appreciate valuable discussions and helpful suggestions in this kind of meetings, which I learned a lot about how to do research, analyze data and solve problems. I appreciate his in depth reviews of my every manuscript and also of this thesis. I appreciate his hand-in-hand demonstration and training on high resolution transmission electron microscopy, fluorescence spectroscopy during my very early stage of D. Phil. Some of the discussion in bars (normally Royal Oak) inspired me a lot. As a role model, he showed me how to be a leader and an excellent scientist. Thanks Jamie!

Great thanks give to *Dr. Kyriakos Porfyrakis* for his great patient as a mentor and collaborating with fullerene work. Also, thanks him for paying me to go to the 5th International meeting on molecular electronics, Grenoble, France in December 2010. Thanks to *Dr. Arzhang Ardavan* for discussions on electron spin resonance.

My D. Phil work would not be possible without the help and support from my colleagues and collaborators, who have generously given me the opportunity to learn from their experience and collaborate with various projects. At University of Oxford, in department of materials, thanks to *Professor Angus Kirkland* for sharing his insight into TEM theory, *Dr. Susannah Speller* for helping with EBSD work, *Dr. Franziska Schäffel* for proof reading of manuscripts, *Dr. Christopher S. Allen* for helping with Matlab programming and measurement of the sheet resistance of graphene, *Mr. Alexander Robertson* for helping with CVD instrumentation and collaborating with some TEM projects on the structure of graphene, *Mr. Kuang He* and *Mr Ye Fan* for assisting with some CVD synthesis, *Dr. Guoquan Liu* and *Dr. Yasuhiro Ito* for collaborating with fullerene work, *Dr. Jonathan Moghal* for collaborating with the project on mechanical response of graphene, *Dr. Mujtaba Zaka* for collaborating on EPR investigation on carbon nanotube. In department of chemistry, thanks to *Dr. Chengle Wang* and *Professor Dermot O'Hare* for collaborating work on layer double hydroxides. Thanks to *Dr. John Hutchinson, Dr. Mike Jenkins, Dr. Crispin Hetherington, Dr. Neil Young, Mrs Gabriella Chapman, Mr Ron Doole* who trained me on electron microscopy, and *Dr. Colin Johnston* who trained my on Raman spectroscopy at Oxford materials electron microscopy and microanalysis group, at department of materials. Thanks to *Mr Paul Pattinson* for giving me access to the clean room at department of physics.

Away from Oxford, thanks give to *Dr. Graham Creeth* at University of Leeds, and *Dr. Jerzy Sadowski* at Brookhaven National Laboratory for measuring the angle resolved photoemission spectroscopy of graphene for me. Thanks to *Dr. Gregory Wildgoose* at University of East Anglia for collaboration work on functionalized carbon Nanotube. Thanks to *Associate Professor Huaqiang Cao* for collaboration work on Ni/Fe on graphene oxide and *Associate Professor Jun Luo* for collaboration work on atomic structure and electrical properties of carbon nanotube at Tsinghua University. Thanks to *Professor Liqiang Mai*, who is my bachelor thesis advisor at

Wuhan University of Technology, for collaboration work on silver/vanadium oxide/Polyaniline triaxial nanowire.

I also would like to give thanks to my past and present officemates, *Dr. Ling Ge, Dr. Li Xiao, Dr. Simon Plant, Dr. Marcus Schaffry, Dr. Volker Lang, Dr. Stephanie Simmons, Mr. Alexander Robertson, Mr. Benjamin Farrington, Mr Roberto Nardo, Mr Gary Wolfowicz and Mr Hanns Maier-Flaig* for making my office time enjoyable. Also, I would like to thank all the people from 12/13 parks road, who made this ancient historical building fun and memorable. Furthermore, great thanks to all the friends who I have met from St. Anne's college, Wellington square graduate accommodation, Oxford Chinese Students and Scholars Association, Chinese Students and Scholars Association at United Kingdom, China Oxford Scholarship Fund community and the Chinese Society of Chemical Science and Technology in UK. Because of you, the social life for me in U.K. became colourful and fun.

Last but not least, I would like to take this opportunity to give my sincerely thanks to my funding agencies. Great thanks to China Oxford Scholarship Fund (COSF) and Wolfson Foundation for not only giving me this prestigious Wolfson China Scholarship but also providing an interesting social platform within the community. Special thanks to the *Mr. Timothy Beardson*, the chairman of COSF, *Mr. Paul Ramsbottom*, the chief executive of Wolfson Foundation, *Mrs. Araceli Keelan*, the benefactor of COSF, *Mrs Susan Yu*, the administrator of COSF. Financial support from EPSRC International Doctoral Scholarship, Overseas research scholarship, Wolfson China Scholarship, Chinese Government Award for Outstanding Students Abroad, Graduate travel grant from St. Anne's College, Conference funding from Department of Materials, is gratefully acknowledged. I appreciate EPSRC offered me an EPSRC Doctoral Prize for doing a postdoctoral research at Oxford after D.Phil.

Thanks all. 谢谢。

# Contents

# Chapter 1:

# Introduction

## 1.1. Overview

The current electronic industry is based on the determinism of classical theory implementation in CMOS (complementary-metal-oxide-semiconductor) technology. As each individual component reaches the nanoscale, they enter a regime where quantum effects are apparent. Driven by these new physics and potential applications, it is important to learn to fabricate structures and materials with nanoscale dimensions, to enable the further development of nanotechnology. It is an exciting and challenging area of research crossing the border of a wide ranges of disciplines, like physics, materials science, chemistry, biology and engineering.[1]

In order to develop nanotechnology, it is necessary to study nanomaterials. Nanomaterials, by definition, are materials with at least one dimension sized less than 100 nm.[2] Based on their dimensions, nanomaterials can be divided into zero-dimensional (0D), quantum dots, one-

dimensional (1D), nanowires, and two-dimensional (2D), like graphene and boron nitride (BN), systems. Among them, 2D atomic crystals are relatively new to the nanomaterials family.[3] The discovery of 2D atomic crystals, which are layered materials with atomic scale thickness, is often given credit to Professor Andre Geim and Professor Konstantin Novoselov for isolating monolayer graphene using micromechanical cleavage method (also called "Scotch tape" method).[3-4] Their ground breaking experiments, winning them Nobel Prize in physics in 2010,[5] showed the fascinating high mobility and Dirac fermion nature of charge carriers in graphene. This opened a golden rush of research for graphene or other two dimensional atomic crystals. The next section will give a review on the nanomaterials studied in this thesis which are graphene, boron nitride 2D atomic crystals and 0D quantum dots.

## 1.2. Research Background

### 1.2.1. Two Dimensional Atomic Crystals: Graphene

Graphene, an example of a two dimensional atomic crystal, is a one atom thick planar sheets of $sp^2$ bonded carbon atoms that are densely packed in a honeycomb crystal lattice, which other carbon nanomaterials can be derived from, shown in figure 1.1.[6] Although the crucial publication of graphene in 2004 catalyzed the rapid development of the field,[4] it is not the first time in the history

that graphene was described. Hanns-Peter-Boehm investigated a single layer carbon foil by TEM.[7] The thickness of it was measured by the relative absorbance. The preparation of this sample is done by oxidizing graphite, which increased the interlayer spacing and allowed the solvent molecules to intercalate into the layers. This leads to the exfoliation of graphene oxide films into possible single layers. Then the graphene oxide could be reduced to graphene. This is similar in principle to recently developed chemical exfoliation routes to produce graphene. However, it is not clear by the TEM contrast how thin this graphite material was and also the unusual properties of graphene were not revealed. But the term graphene appears in IUPAC definition.[8]

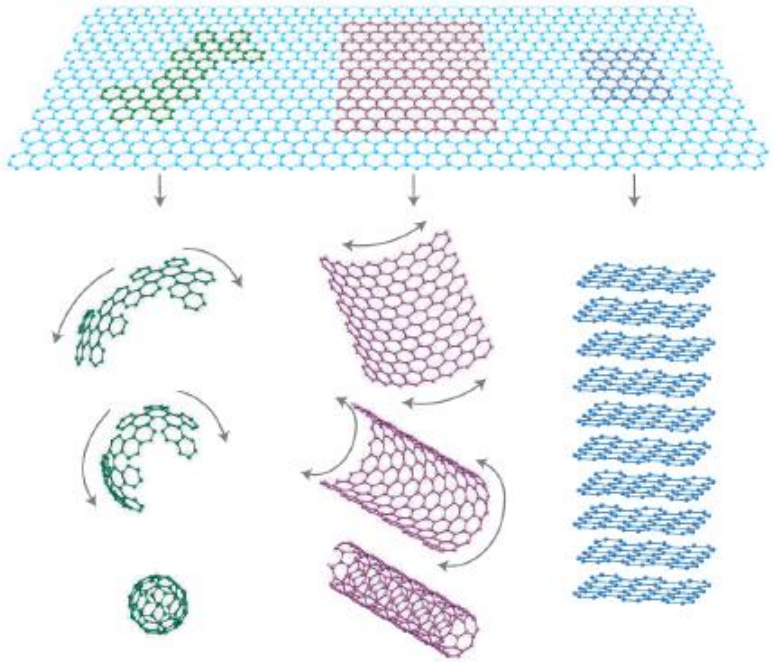

**Figure 1.1.** Graphene has the hexagonal honeycomb crystal lattice which can wrap into nanotube or fullerenes or stack into graphite. [[6]] (Reprinted with permission from ref 6. Copyright 2007 Nature Publishing Group)

Some old literature claimed that free standing 2D crystals should not exist.[9] Thermal fluctuations in crystal lattice would lead to atomic displacements comparable to the inter-atomic distance at any finite temperature, resulting in substantial crystal defects and thermodynamic instability.[10] The theory was expanded[11] and reinforced by the direct observation of film decomposition into islands.[12-13] This single layer crystal was considered to exist only epitaxially, only to be lattice matched on top of a larger structures.[12-13] 2D crystals were merely building blocks, only known within context of their 3D counterparts. This is the reason that it has long been speculated whether graphite layers could split into individual atomic layers and if they would subsequently thermodynamically stable.[14]

This debate was on-going until "atomically thin carbon films" [4] were discovered at University of Manchester in 2004, followed by other 2D atomic crystals (like BN, $MoS_2$, $NbSe_2$, $Bi_2Sr_2CaCu_2O_x$).[3] Importantly, these 2D atomic crystals are isolated from their surroundings and can be considered as free standing when they are transferred to the holy TEM grids. They can all be fabricated by the mechanical exfoliation method from their 3D counterparts. For example, graphene flakes were peeled off from highly oriented pyrolytic graphite (HOPG) by using scotch tape. Then these graphene flakes can be transferred to a silicon wafer by simply pressing this scotch tape onto the silicon wafer. This single layer of graphene can be observed under the optical

microscope.[4] It was found to be up to 10 microns in lateral size and stable under ambient condition.[4] More importantly, graphene is found to exhibit a strong ambipolar electric field effect induced by applying a gate voltage to get electron or hole concentrations up to $10^{13}$ $cm^{-2}$ and exceptional high intrinsic mobility of 10,000 $cm^2V^{-1}S^{-1}$ at room temperature.[4] This exceptional high mobility at room temperature is due to the virtually massless Dirac fermion nature of the carriers in graphene.[15] This fascinating behaviour of graphene allowed experimentally observation of quantum phenomenon, such as quantum hall effects.[15-16] From then on, this novel 2D atomic crystal with unusual new physics has attracted scientists from many disciplines: materials science, physics, chemistry, biology； and has triggered the rapid growth of the field.

Although 2D atomic crystals have been discovered experimentally since 2004, the contradiction between experiments and predicted theory required a revaluation. In 2007, arguing with the statement from Mermin's paper[11] that 2D crystals are quenched and exist in a metastable state, Geim *et. al.* argued that the small size (<<1mm) and strong interatomic bonds with respect to their 3D counterparts ensure the thermal fluctuation cannot lead to the generation of crystal defects.[6] Meyer *et. al.* gave a possible experimental explanation of this issue by investigation of the structure of free standing graphene in HRTEM. The gentle undulation in third dimension of graphene, shown in figure 1.2, may be enable the 2D atomic crystal to become intrinsically stable.[17] Although this undulation results in a strain in elastic energy, anomalously large thermal

vibrations in the 2D crystals was suppressed, minimising the total free energy above certain temperatures.[6,18] To date, there is still no resolution of the theory regarding this contradiction.

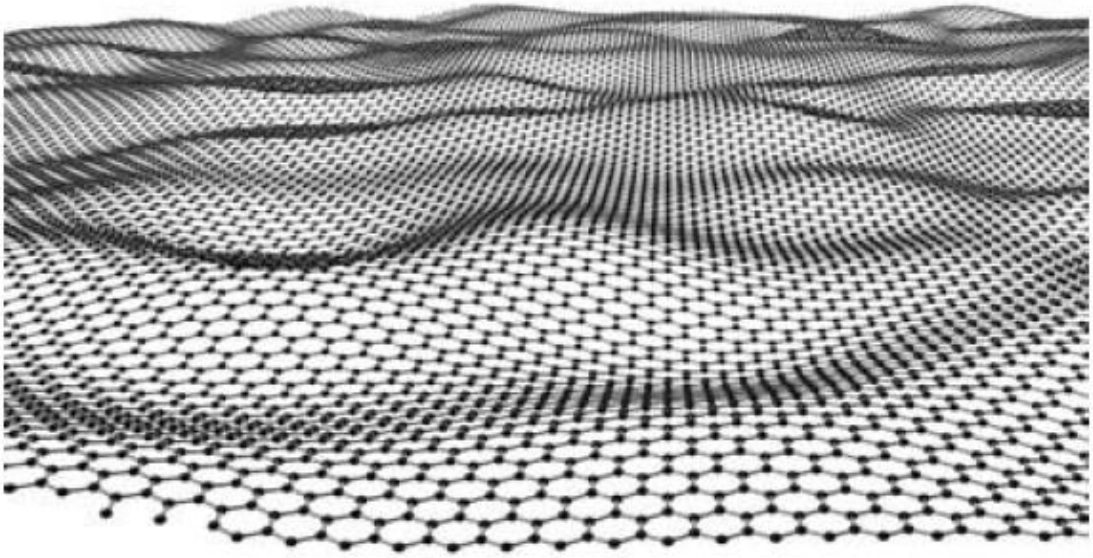

**Figure 1.2.** A visualisation of the crumpling of graphene observed on a freely suspended graphene sheet. [17] (Reprinted with permission from ref 17. Copyright 2007 Nature Publishing Group)

No matter what the reason is for graphene turning from a "theoretic material" into a reality, this novel nanomaterial indeed exhibits excellent unique properties, which makes it important and interesting. Graphene is the thinnest material known but is also the strongest. Prior to the discovery of graphene, it had been predicted that graphene has an intrinsic strength greater than any with an atomic force microscope.[19] The breaking strength was measured to be 42 $N \bullet m^{-1}$, about 200 times that of steel, and the Young's modulus is about 1.0 TPa, comparable to nanotubes.[19] Monolayer graphene has an unusually high opacity, which is defined as $\pi a$ to be precise, where a is the fine structure constant; about 2.3% of white light absorbed.[20-21] This is because of the unusual low energy electronic structure where the electron and hole conical bands meeting each

other at Dirac point, which is shown in figure 1.3.[22] The thermal conductivity of graphene is excellent, measured to be between (4.84±0.44) x$10^3$ to (5.30±0.48)x$10^3$ W•$m^{-1}$•$K^{-1}$ around four times larger than that of graphite, diamond, and nanotube.[23]

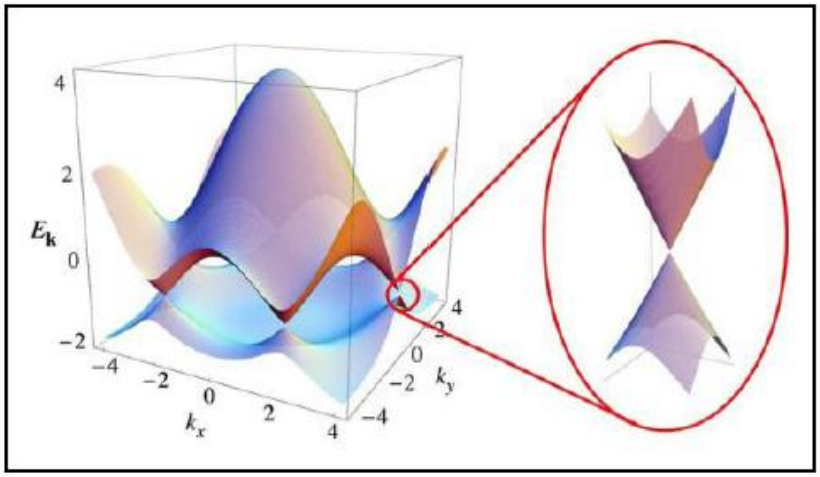


**Figure 1.3.** Energy momentum dispersion for graphene, showing six Dirac points. [22]. (Reprinted with permission from ref 22. Copy right: 2009 American physical society.)

Besides these excellent mechanical, optical and thermal conductivity properties, the extraordinary electronic properties are where the majority of interest lies. The unique band structure of graphene is one of the reasons for these exciting electronic properties. Monolayer graphene has a linear relationship around the Dirac point, shown in figure 1.4, and this linear relationship becomes parabolic in bilayer graphene with slightly semimetal band overlap.[24] The band overlap increases with the number of layers approaching to ten layers, when the band structure becomes graphite structure.[6,24] This means that few layer graphene is the term given when the number of layers is less than ten. Due to this unique band structure, graphene is a semimetal or zero-gap semiconductor, where the valance and conductive bands meet at the Dirac point and both electrons

and holes contribute to the electrical conduction. As the carriers encounter these Dirac points periodically through the crystal lattice, new quasi-particles are formed, named Dirac fermions, which is similar to a charged neutrino with no rest mass, shown in figure 1.5.[25] These massless particles seldom interact with matter and behave like relativistic particles, with speeds approaching that of light. This leads to the extremely high carrier mobility of graphene even at room temperature.[4] The initial mobility was measured to be between 3,000 to 10,000 $cm^2 v^{-1} s^{-1}$ at 5 x $10^{12}$ $cm^{-2}$ carrier concentration for both electrons and holes and was nearly independent of temperature. With comparison, pure silicon's electron mobility is about 1400 $cm^2 v^{-1} s^{-1}$, [26] which is the major material in current electronic industry. What is even more fascinating is that this mobility remains high even at large carrier density.[6] As a result of this, the ballistic transport is seen to occur on a submicrometre scale.[4]

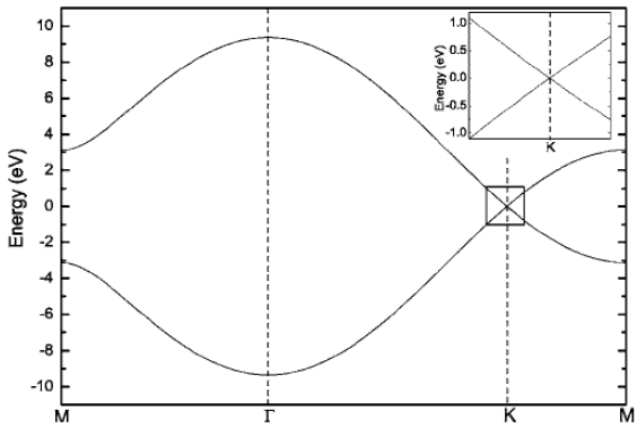


**Figure 1.4.** Band structure of monolayer graphene. The inset shows the linear dispersion relation about the k point, often referred as Dirac point. [24] (Reprinted with permission from ref 24. Copy right: 2006 American physical society. )

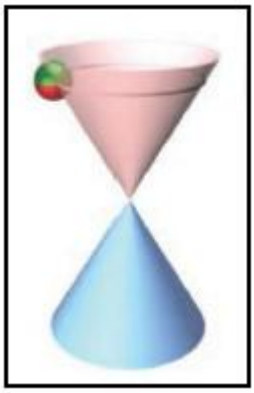

**Figure 1.5.** Massless Dirac fermion represented on graphene zero band gap structure. [25] ((Reprinted with permission from ref 25. Copy right: 2009 American Association for the Advancement of Science. )

Besides the effect on high electron mobility, the Dirac fermion presents several other novel effects indentified by the Manchester and Columbia groups.[15-16] Firstly, graphene's conductivity never drops below a minimum value of a quantum unit of conductance ($4e^2/h$). Secondly, an anomalous Quantum Hall Effect (QHE) is presented in graphene. The QHE is a quantized hall effect. In the Hall Effect, when a current is applied through a conductor in a perpendicular magnetic field, a Lorentz force is applied on the charge carriers resulting in potential difference across the conductor. In the QHE, the hall conductivity $\sigma$ becomes quantized at low temperatures with following equation.[27-28]

$$\sigma = \nu \frac{e^2}{h} \qquad (1.1)$$

Where $\sigma$ is the hall conductivity, $\nu$ is the filling factor, $e$ is the elementary charge and $h$ is Plank's constant. The QHE in graphene was observed experimentally with anomalies, which is shown in figure 1.6.[15] It occurs at half integer filling factors $\nu$ rather than integer and is observed

at room temperature comparing to the sub 30 K required by others.[28] This effect allows a quantum phenomenon to be observed at the macroscopic scale at room temperature.

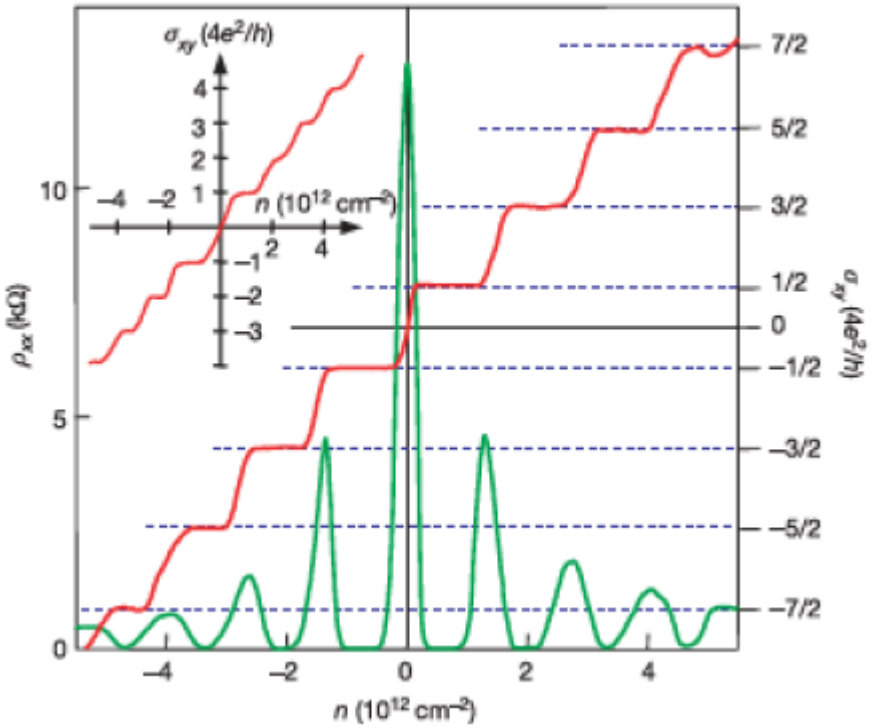


**Figure 1.6.** Anomalous QHE for massless Dirac fermions in monolayer graphene and longitude resistivity. The inset shows the integer behaviour QHE for bilayer graphene, as opposed to the anomalous integer plus a half behaviour QHE for monolayer graphene. [15] (Reprinted with permission from ref 15. Copyright 2005 Nature Publishing Group)

The extraordinary properties of graphene listed above boosts the application potentials for graphene. Graphene may be the solution for a room temperature ballistic transistor for the semiconductor industry due to its high carrier mobility and bipolar electrical field effect at room temperature. The electrons and holes can be continuously tuned with extraordinary switching speed by the gate electrical field. This provides outstanding processing power in the field effect transistors (FET). Large scale graphene transistor arrays have been fabricated with uniform

electrical properties.[29] This uniform graphene FET arrays have the potential to overcome the bottle neck in Moore's law from Si semiconductor industry as the performance of the graphene FET arrays can be linearly increased with number of the graphene devices. Another limitation in current Si microprocessor advancement is heat dissipation. Graphene has the potential to counter this with its excellent thermal conductivity.[23] The only problem for FETs is the low on-off ratio of intrinsic graphene devices due to its zero band gap structure. However, this can be solved by opening the band gap of graphene. Currently, two approaches have been made to introduce a band gap in graphene. A band can be split up to 0.26 eV when graphene is grown epitaxially on a SiC substrate due to the interaction between graphene and substrate.[30] An alternative way to open the band gap in graphene is to generate a quasi one dimensional graphene nanoribbons (GNR). This GNR could be fabricated by electron beam lithography (EBL) patterning coupled with oxygen plasma etching. A GNR FET with a width of 15 nm was fabricated with a band gap of 0.2 ev.[31] GNR could also be fabricated from 'unzipped' carbon nanotubes, which is shown in figure 1.7, using plasma etching[32] or chemical oxidation[33]. Direct electron beam lithography using EBL or scanning tunnelling microscopy (STM) is a possible method to fabricate GNR device by cutting graphene into ribbons.

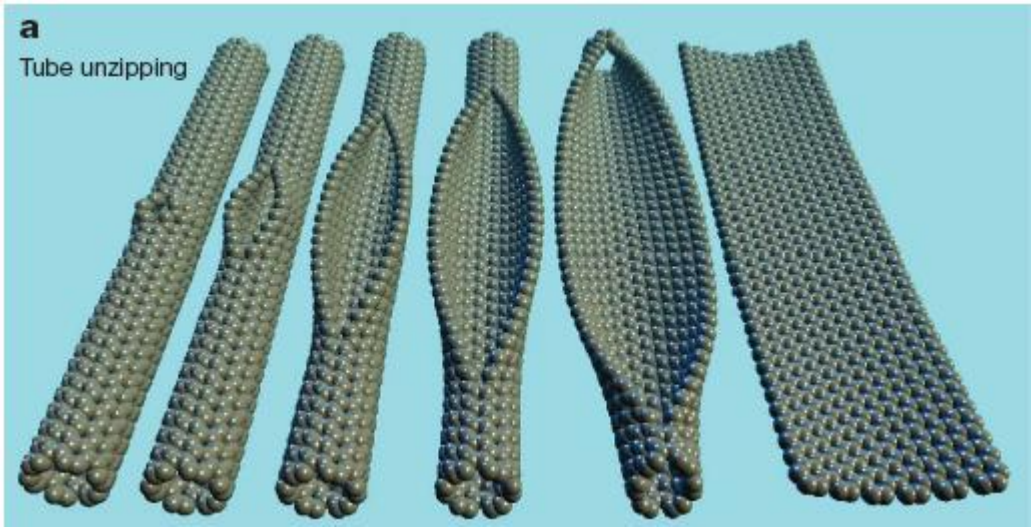


**Figure 1.7.** Unzip carbon nanotube to fabricate graphene nanoribbons. [33] (Reprinted with permission from ref 33. Copyright 2009 Nature Publishing Group)

Graphene, with high electrical conductivity, high carrier mobility, and relatively high optical transparency in the visible range of the spectrum, has great potential for the usage for transparent conductive films (TCF). As indium is a rare and expensive metal compared with the most common element carbon, graphene has great promising to replace Indium Tin Oxide (ITO), which is now the key material for TCF in industry. It will greatly reduce the cost in TCF industry if graphene is used instead. This idea has been realized on the industrial scale and it is worth in production.[34-35] The best result for graphene as a TCF is 125 $\Omega\square^{-1}$ sheet resistance with 97.4% optical transmittance.[35] These graphene TCFs have been used as touch screen[35], electrodes for dye-sensitized solar cells,[36] liquid crystal devices,[37] and organic light-emitting diodes.[38] The intrinsic sheet resistance of graphene is argued about 30 $\Omega\square^{-1}$.[39] Thus, it still has potential for improving the quality of graphene for TCF devices.

Graphene is also an excellent candidate as a sensor due to its large surface area and low Johnson noise[6,15-16] (electronic noise generated by thermal agitation of charge carriers inside an electrical conductor at equilibrium). When a molecule adsorbs to the surface of graphene, charge transfer between the molecule and graphene can occur. Graphene acting as a donor or acceptor will change the Fermi level, carrier density and electrical resistance as the chemical response to the absorbed molecules. This graphene sensor device has been realized to detect variety of gases,[40-43] and biomolecules.[44-45]

In energy research, graphene can act as the electrode material due to its high surface area and excellent 2D channel for electrons or holes. A graphene based electrode has been used in rechargeable lithium ion batteries[46] and electrochemical double layer capacitors.[47] The reversible capacity can be enhanced by a graphene-nanoparticles composite, for example, graphene-Si nanoparticles,[48] graphene-$SnO_2$ nanoparticles, [49-50] graphene-Sn nanocomposites.[51] Graphene has also been used in hydrogen storage,[52] fuel cells,[53-57] and solar cells.[58-59]

Other new application for graphene is the usage as the supporting membrane for atomic resolution transmission electron microscopy (TEM).[60-63]Also, graphene has potential as spintronics device due to its long spin relaxation time.[64] A novel pseudospin field effect transistor (BiSFET) could be designed as the next generation FET using graphene.[65]

Lots of application potential of graphene has been demonstrated. Now, the question comes as how to scale it up to make high quality large area graphene films in industry for commercial applications. In order to answer this question, it is necessary to review the recent synthetic methods to make graphene. The methods of producing graphene can be divided into six categories by physical principles. The first category is attributed to liquid phase exfoliation from colloidal suspensions. The principle of this method is to choose the right organic solvent whose cohesive energy matches the surface energy of graphene.[66] These organic molecules, which are normally polar solvents like DMF or NMP,[66] intercalate within a graphite precursor and then high intensity ultrasound sonication is applied. This ultrasound provides energy to the organic molecules to help overcome the van der Waals force between layers and will increase the layer to layer distance in the graphite precursor. This will eventually exfoliate graphite into monolayer graphene derivatives, which can be turned into graphene chemically. The similar method can be applied to different precursors such as graphite,[66] graphite oxide,[67-69] reduced graphite oxide,[70-78] or graphite intercalation compound.[79-82] The advantage of liquid phase exfoliation from colloidal suspension is scalability. Also, this method is versatile as it is suitable to chemical functionalization.[83] However, it also has obvious drawbacks, as it is easy to introduce heteroatomic contamination and topological defects.[84]

The second method is mechanical exfoliation which is the most widely used and easily available way to fabricate high quality graphene. It is possible to find graphene species among the debris of pencils. This method is first introduced by Ruoff and co-authors[85-86] in 1999 and improved to be a standard scientific method named "Scotch tape method" by Andrei Geim and co-authors.[4] The basic principle of this method is just to peel repeatedly in order to separate graphene layers from graphite. To locate graphene flakes from the graphite debris is quite time consuming. It is really a top down approach. The advantage of this method is producing high quality graphene which is excellent for fundamental physics study. This technique has produced the best quality of graphene fabricated to date, considering the carrier mobility due to the exceptionally low level of defects that is possible to achieve. That is why this method is widely used to study graphene properties. However, this method is not scalable to large area graphene in industry and it is only a lab scale method.

The third method is to unzip carbon nanotube to make graphene nanoribbons. Multiwall carbon nanotubes can be cut open chemically in solution in the presence of sulfuric acid and potassium permanganate.[33] Plasma etching of nanotubes partly embedded in polymer films can lead to production of graphene nanoribbons.[32] This method is scalable and can produce graphene nanoribbons with high yield. However, it requires the starting material of carbon nanotube with a controlled shell number and diameter to achieve narrow width distribution and monolayer

graphene ribbon. Thus, to fabricate a controlled carbon nanotube as starting material will cost a fortune and this method is not promising to be used in industry.

The fourth method is a bottom up approach of polymerization of small molecular aromatic hydrocarbons into larger polycyclic aromatic hydrocarbons and eventually into small area graphene.[87] It has the advantage to design and control the atomic structure to produce atomically pristine, rather than macroscopically pristine graphene.[88] However, due to the diminished solubility of large, polycyclic aromatic hydrocarbons, graphene produced with this method is significantly smaller size than that of graphene prepared by other methods.[84] Thus, it is not promising in industry to produce large area graphene.

The fifth method is epitaxial growth of graphene by thermal decomposition of silicon carbide. The growth of graphene could be on either silicon terminated (0001) plane or carbon terminated $(000\bar{1})$ plane by desorption of silicon from either 6H-SiC or 4H-SiC polymorph using high vacuum annealing with high temperature.[89-93] Recently, this growth could be done at atmospheric pressure.[94] The rate of silicon desorption can be manipulated by temperature to control the thickness of graphene films. SiC acts as an insulating substrate and wafer-sized graphene was grown on top of it with carrier mobility about 200,000 $cm^2 V^{-1}S^{-1}$.[94] This method has the advantage to produce high quality graphene. However, the drawback for this method is obviously, namely

size and cost. The graphene prepared by this method is polycrystalline with domain diameter from 30 nm to 200 nm. But no millimetre graphene flakes have been produced by this method. The process in the method involves several expensive steps. It is not promising to scale it up in industry.

The sixth method involves chemical vapour deposition (CVD) of hydrocarbons onto transition metals to grow graphene. It is a widely used method in the microelectronic industry to deposit thin films, such as silicon and high k dielectric, synthetic diamond,[95] and carbon nanotube.[96] The general principle of this method involves volatile carbon precursors either breaking under the high temperature (thermal decomposition) or decomposing over the catalytic substrate (catalytic decomposition) to initial the reaction on the substrate upon which the product is deposited. Graphene has been produced with this method on various catalytic transition metals, such as copper,[97] nickel,[34,98-99] ruthenium,[100-102] iridium,[103-104] cobalt,[105] platinum.[106] Copper and nickel are the most promising candidates, considering the cost and quality of graphene. This CVD synthesized graphene could be transferred to various substrates for applications.[99] This CVD approach can be carried out at atmospheric pressure[34, 107-110] or under low vacuum.[35, 97,111] This method has obvious advantages to produce high quality graphene scalable in industry with relatively low cost. After transferring graphene to the desired substrate, it could be compatible with state of the art electron beam lithography in the current microelectronics industry. Although

most of the graphene film produced by this method is polycrystalline, the mobility of devices fabricated with this graphene film could be 800 to 16000 $cm^2V^{-1}s^{-1}$, comparing to 2500 to over 40000 $cm^2V^{-1}s^{-1}$ for exfoliated graphene.[112] The polycrystalline nature of graphene[113] fabricated by this method needs to be investigated in detail regarding the growth mechanism, which will discuss more in chapter 2, in order to improve the quality of graphene by this promising method.

As discussed above, different methods have different advantages and disadvantages. To choose the right method depends heavily on the intended use. Now, if coming back to the question being raised above, how could high quality large area graphene film be fabricated in industry with relatively low cost for commercial applications? Mechanical exfoliation method is only lab scale. Unzip carbon nanotube method will cost a fortune as requirement of controlled shell and diameter carbon nanotube as starting materials. Polymerization method could not produce large area graphene. Epitaxial growth on SiC method is too expensive to use in industry. What about liquid phase exfoliation method and chemical deposition method? Although liquid phase exfoliation method has drawbacks as introducing contaminations and defects and the polycrystalline nature of CVD graphene, these two methods hold the promise of producing graphene in large quantity for real commercial applications. Can we improve these two methods to make large area single crystalline graphene? Trying to answer this open question is one of the aims of this thesis.

### 1.2.2. Two Dimensional Atomic Crystals: Boron Nitride

In the last section, graphene, as one of the two dimensional (2D) atomic crystals, has been reviewed. Boron nitride (BN) is a synthetic material with both hexagonal and cubic structure.[114-116] Hexagonal BN (*h*-BN) is another example of 2D atomic crystals, consisting of $sp^2$ bond between boron and nitrogen atoms in a honeycomb 2D structure. These layers are stacked to be AA stacking few layer boron nitride sheets via Van der Waals force, which is shown in figure 1.8, unlike the AB stacking in few layer graphene. Overall, BN 2D atomic crystals are isoelectronic to the carbon based graphene. However, the slightly ionic bonds in h-BN make this material unique in the 2D atomic crystal family. It is an intrinsic insulator with a direct band gap about 5.9 eV,[114-115,117] unlike graphene which is a semimetal with high levels of conductivity. This unique structure makes atomically thin *h*-BN an ideal model to study atomic configurations, including defects, edges, and vacancies of 2D ionic crystals.[118] The structure of free standing *h*-BN atomic sheets has been studied using high resolution transmission electron microscopy regarding its thickness, defects, edges, and identification of individual atoms.[118-121]

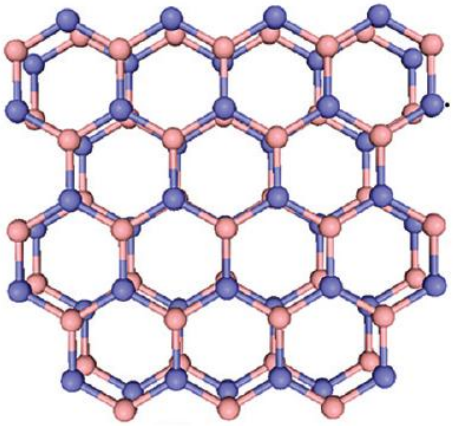

**Figure 1.8.** AA stacking few layer boron nitride sheet.

Boron nitride 2D atomic crystal is an insulator, which acts as an excellent complementary material to graphene, offering some unique properties to enrich the applications of the whole 2D atomic crystal family. Its outstanding thermal and chemical stability has been used in parts of high temperature equipment.[122] Its mechanical strength is inferior only to diamond and graphene.[123] But h-BN is also an excellent lubricant, even in vacuum. Thus, it could be particular useful to replace graphite as lubricant due to the electrical conductivity and chemical stability problem of graphite.[124] Its lubricity does not require water or gas molecules intercalate between layers, which is the advantage over graphite. Thus, it could be used in space applications.[124] The non-cytotoxicity[125] and its lubricity are widely used in the cosmetic products, such as foundations, eye shadows, lipsticks and so on.[122] The thermal conductivity of *h*-BN nanoribbons was estimated to approach 1700-2000 $Wm^{-1}k^{-1}$.[126-128] More importantly, the thermal transport in boron nitride nanoribbons is anisotropic, which means the thermal conductivity along the zigzag-edge is about 20% larger than that of armchair edge at room temperature.[129] The deep ultraviolet band gap

emission in the range of 215-250 nm offers great potential in ultraviolet laser devices used in applications, such as optical storage, photocatalysis, sterilization, ophthalmic surgery and nanosurgery.[114] Due to its outstanding dielectric and thermal properties, BN has been used in electronics as a substrate for semiconductors, microwave-transparent windows and as a structural material for seals.[129] Thus, *h*-BN 2D atomic crystal, which is perfectly flat and insulating, offers a unique candidate to serve as the excellent dielectric substrate for graphene electronics.[130-132] It has been found *h*-BN 2D substrate dramatically improved the I-V characteristic of graphene transistors.[133]

Although *h*-BN could have potential application in photonics, most of the applications of BN 2D films are structural supporting materials due to its excellent high thermal and chemical stability. Also, considering *h*-BN is an ideal model to study the atomic configuration of 2D crystals without carbon and its non-cytotoxicity nature, a natural question is raised. Can we use BN 2D atomic crystal as a carbon-free TEM ultrathin supporting film to study atomic configuration of other nanomaterials and then in future for biological materials, most of which are carbon based?

As a supporting material for structure analysis of other nanomaterials, it should have minimum contrast signal and a well understood structure. As for *h*-BN, it is better to fabricate single crystalline 2D film because its structure information is periodic and can be eliminated during the

signal processing procedure. Then, the following question is arising. How can single crystalline BN 2D sheets be obtained? In order to answer this question, a brief review of the synthetic BN 2D atomic crystal should be taken. Similar to graphene, a BN 2D crystal was first isolated by mechanical exfoliation, with size of to several microns.[119] This method was further improved by a so called *ex situ* isolation of suspended single layer *h*-BN sheet using a combination of mechanical exfoliation and reactive ion etching.[118] At the same time, an *in situ* method to fabricate single layer BN sheet was developed using electron beam sputtering directly inside TEM,[121] or a combination of mechanical exfoliation and electron beam sputtering.[120] These methods produce BN films with non-uniform thickness even within one sheet, with part of the region being monolayer. Also, these methods are not scalable to produce BN in large quantity. Uniform large area *h*-BN films have been synthesized using thermal catalytic chemical vapour deposition on Cu[130] or Ni[134]. The Ni catalyzed BN film is much thicker, more than 10 layers,[134] than the Cu catalyzed ones, about 2-5 layers.[130] However, the Cu catalyzed one is polycrystalline[130] while the Ni catalyzed one is single crystalline.[134] Thus, it is hard to produce both thin but single crystal BN 2D films using CVD. In comparison, liquid phase exfoliation seems to be able to produce uniform single crystal thin BN sheets in large quantity.[135-136] It seems to be a good method to fabricate BN sheets as a supporting material for structural analysis with TEM.

After this brief review, coming back to the open question raised above, can we use liquid phase exfoliation to fabricate uniform single crystalline BN sheets as a carbon-free TEM ultrathin supporting film to study atomic configuration of other nanomaterials? One of the aims of this thesis is trying to answer this open question.

### 1.2.3. Semiconductor Quantum Dots

In the previous section, an open question has been proposed to use uniform single crystalline BN sheets as a carbon-free TEM ultrathin supporting film to study atomic configuration of other nanomaterials. Semiconductor quantum dots (QDs), a highly crystalline zero dimensional (0D) nanomaterial, has been chosen to demonstrate this open question. It is a different nanomaterial from 2D atomic crystals but with some links. Unlike graphene as a semimetal with no band gap, and BN as an insulator with wide band gap, QDs are semiconducting. As quantum dots exhibit discrete and tunable energy levels in optical and electronic characterisation, it is also called an artificial atom.[137] In principle, 0D artificial atoms are the basic building blocks to be assembled into other dimensional nanostructures, such as artificial molecules.[137] Quantum dots have been fabricated from 2D nanomaterials, like graphene,[64] or 1D nanomaterials, like carbon nanotubes.[138]. Because of these differences and links between 0D quantum dots and 2D atomic crystals, QD has been chosen to study in this thesis.

Most of the applications of quantum dots have been related to their significant optical properties. Because of the high extinction coefficient quantum dots can absorb more light than organic dyes.[139] Because of its extraordinary quantum yield, it emits more brightly than organic dyes. Also, the stability of quantum dots is outstanding compared with organic dyes in various conditions. Hence, QDs have much less photo bleaching than organic dyes.[140] More importantly, QDs have the wave function of excitons, which are electron hole pairs, confined in all three spatial dimensions. This gives the discrete energy quantization levels similar to atoms due to quantum confinement effect. This quantum confinement effect is related to the size and shape of the quantum dots. Thus, it gives us the opportunity to tune the band structure, optical and electronic properties by changing the size, shape and composition of the quantum dots. This offers the application of quantum dots in photonic devices like solar cells,[141-142] or biology imaging,[140] or even spintronics.[143-144]

In order to broaden the application of quantum dots, it is vital to control exciton properties. Doping is an important strategy to enrich dynamics of excitons as it adds other energy levels to quantum dots. However, it is still an experimental challenge for doping quantum dots.[145] A few strategies have been tried for doping quantum dots. One of them is remote doping, which donates electrons to the quantum dots by external molecules or electrodes. By using the binding ligands on the nanoparticles surface to donate carriers, or using the electrochemical carrier injections, n-type

doping semiconductor quantum dots have been produced.[146-149] Another doping strategy is called substitution doping, which means the dopants substitute atoms in the quantum dots lattice and incorporated into the quantum dots. Colour centre impurities, like Cu atoms, and magnetic impurities, like Mn atoms, have been doped into the quantum dots.[145, 150-152] The location of dopants in the substitution strategy could be controlled by different methods, so called nucleation doping or growth doping.[150-153] Both n-type and p-type doped InP quantum dots have been synthesized using this substitution strategy to produce the first p-n junction devices using quantum dots.[154]

Among these doped quantum dots systems, Mn doped ZnSe quantum dot is a promising candidate to have broad applications. Why it is interesting to study Mn doped ZnSe quantum dots? As an excellent example of cadmium free quantum dot, it is non toxic and will not cause the leakage of toxic cadmium to the environment. Also, because of its non-cytotoxicity, it could be broadly used in biological labelling. Besides retaining the advantages of undoped quantum dots, such as narrow and symmetric emission with tunable band gap, broad and strong absorption, reasonable stability, and solution processibility, doping quantum dots overcomes self quenching problems of undoped quantum dots by their substantial ensemble Stoke's shift (energy difference between absorption spectrum and emission spectrum).[155-156] This large Stokes shift in doped quantum dots is due to their relatively small emission energy gap, in comparison to the absorption band gap of the host

nanocrystals, in their atomic-like emission states. These atomic-like states lie in the inner core of the dopant centres and do not couple to the shell lattice phonon strongly. Consequently, the emission of doped dots can be thermally stable.[157] Also, because of the Mn dopants in ZnSe quantum dots, it provides extra spin and magnetic properties, which makes it more promising for spintronics.[158]

As discussed above, Mn doped ZnSe quantum dot is interesting to study. Then the question coming is how to synthesis Mn doped ZnSe quantum dot. In order to answer this question, it needs to give an overview on the synthetic method of nanoparticles in the literature. The synthetic methods of nanoparticles can be divided into five categories. The first category is a so called micelle method. If the surfactant concentration exceeds the critical micelle concentration in water, micelles are created as the aggregation of surfactant molecules. In normal micelles, the hydrophobic hydrocarbon chains of the surfactants are oriented toward the interior of the micelle, with the hydrophilic groups of the surfactants towards the surrounding aqueous medium.[159] As the concentration of surfactants increases, micelles can deform into different shapes. The structures of micelles are determined by the geometric factors of the surfactant at the interface, such as the head group area, alkyl chain volume, the maximum length of the alkyl chain.[160] This method has been used to synthesize metal or metal oxide nanoparticles.

The second method is hydrothermal method. At elevated temperature, water plays an essential role in the precursor material transformation as the solubility of almost all inorganic substances in water is different at elevated temperature and results in the crystallization of dissolved material from fluid. During the reaction, parameters such as water pressure, temperature, reaction time, and precursors can be tuned to maintain high simultaneous nucleation rate and but poor size distribution.[160]

The third method is called pyrolysis, a chemical process, in which precursors decompose into one solid compound and unwanted waste evaporates away under suitable thermal treatment. However, the pyrolytic synthesis of compounds normally generates powders with a wide size distribution in the micrometer regime. [160]

The fourth method is vapour deposition, including chemical vapour deposition (CVD) and physical vapour deposition (PVD). The principle of CVD to synthesize semiconductor nanocrystals is similar to CVD synthesizing 2D atomic crystals. The vaporized precursors are introduced into CVD furnace and absorbed molecules will either thermally or catalytic decompose and react with other gases to form nanocrystals. Three stages could be considered during the CVD process. First, it is the mass transport of reactants to the growth surface via a boundary layer by diffusion. Second stage is chemical reactions on the growth surface. Thirdly, it is the removal of

gas-phase reaction by-products from the growth surface. The principle of PVD is based on the condensation from the vapour phase. This PVD process also involves three stages. The first stage is to generate a vapour phase of the materials by evaporation or sublimation using the physical methods, such as electron beam, thermal energy, sputtering, plasma, or pulsed laser. The second stage is the transportation of the material from the source to the substrate. The third stage is the formation of the particles or film by nucleation and growth.[160] This method has been widely used to produce high quality semiconductor nanocrystals.

The fifth method is colloidal synthesis. The principle of colloidal synthesis relies on the interplay within a three component system, containing precursors, organic ligands and solvents. When a sufficiently high temperature is applied to the reaction medium, the precursors are decomposed into monomers. Once the monomer concentration reaches a critical point, the monomers in the solvent become supersaturated. The nucleation and growth of nanocrystals then starts up. The monomer concentration is an important factor to affect the nanocrystal growth. The nanocrystal growth can occur in two different regimes, focusing and defocusing. After the initial nucleation from the supersaturated solution, the nanocrystals grow by adding additional precursors. If the consumption rate of the reactants by the growth of nanocrystals is less than the rate of the precursor adding to the solution, the monomer concentration remains above the critical concentration for nucleation. Then the solution remains at supersaturation level. The critical size of

nanocrystals (the size where nanocrystals neither grow nor shrink) is relatively small and nearly all nanocrystals continue to grow from this supersaturation solution. In this regime, small nanocrystals grow faster than the larger ones, since the larger nanocrystals need more atoms to grow. This leads to the "focusing" of the size distribution of nearly monodisperse nanocrystals. The uniform size distribution of nanocrystals could be achieved by controlling the monomer concentration such that the average nanocrystal size is slightly above the critical size. Thus, most of the nanocrystals will grow close to the average size and leads to the sharp size distribution function. When the consumption rate of the reactants depleted during growth is larger than the injection of additional precursors, the monomer concentration is below the critical level. The solution becomes unsaturated and the nucleation stops. The critical size becomes larger than the average size and the distribution become defocus. The nanocrystals continue to grow until the equilibrium concentration of the precipitated species reached. In this regime, Ostwald ripening occurs, which means the larger nanocrystals feel hungry and continue to grow, while the smaller nanocrystals are dissolved to feed into the larger nanocrystals growth.[160] The temperature plays another important role in nanocrystal nucleation and growth. It needs to be high enough for atomic rearrangement and annealing, while it should be low enough for not decomposing the prospective nanocrystals. Ligands also play an important role in shape control of the nanocrystals. They would adhere to different energy facets, which would either activate or passivate the facets. This would lead to the different growth rate in different energy facets.[161]

The colloidal synthetic method is most widely used to fabricate semiconductor quantum dots. Comparing with other synthetic approaches, colloidal synthesis method has some advantages, such as simple accessibility, large quantity produced, flexible tunability on elements, over other synthetic schemes. It is a promising method to fabricate semiconductor quantum dots in large scale for commercial applications. After this brief review, coming back to the open question raised above, how Mn doped ZnSe quantum dots can be synthesized with crystal structure controlled? What is the relationship between crystal structure and optical properties of semiconductor quantum dots? Trying to answer these questions is one of the aims of this thesis.

## 1.3. Aim and Outline of This Thesis

The crystal structure of nanomaterials will greatly affect their properties. For example, the crystal structure will affect the electronic mobility in graphene since the polycrystalline graphene film will contain abundant grain boundaries as the barriers for electronic transport. The potential of using BN as a carbon-free ultrathin TEM supporting film to study atomic configuration of other nanomaterials will be affected by the crystal structure of BN film, since the polycrystalline film will create complicate background signals which is hard to remove during the data processing stage. The crystal structure will also affect the optical properties of semiconductor quantum dots

since the crystal phase will change the band structure of the quantum dots and then the energy dynamics of the excitons. Thus, it is an important scientific issue to study the crystal structure of nanomaterials. In this thesis, three types of nanomaterials are chosen to approach this scientific issue, namely, graphene as a semimetal for electronics, h-BN sheet as an insulator for structural support, and QD as semiconductor for photonics. It is easy to realize that controlled synthesis of single crystalline nanomaterials with low cost will be enormously valuable and highly appreciated to the broad scientific and industry community. The aim of this thesis is to find the methods to control the crystal structure of these three nanomaterials with low cost for their applications in electronics, structural support and photonics. The emphasis will be towards large area single crystalline 2D atomic crystals.

In order to achieve the aim of this thesis, the task is broken down into several open questions, which have been proposed in previous sections. The specific open questions which this thesis will answer are listed below.

(1) How can we synthesize Mn doped ZnSe quantum dots with controlled crystal structure? What is the relationship between crystal structure and optical properties of Mn doped ZnSe quantum dots?

(2) Is it possible to fabricate uniform single crystalline BN sheets as a carbon-free TEM ultrathin supporting film to study atomic configuration of other nanomaterials, for

example Mn doped ZnSe quantum dots? Is it liquid phase exfoliation method good enough to fabricate large area single crystalline 2D atomic crystals?

(3) What is the growth mechanism of graphene using chemical vapour deposition (CVD)? Why polycrystalline graphene is normally produced using CVD?

(4) Based on the understanding of the mechanism of CVD, can we invent a novel method to fabricate single crystalline 2D atomic crystals with low cost using CVD?

Following this logical way to answer these open questions to achieve the aim of the thesis, the whole thesis consists of seven chapters.

(i) Chapter 1 gives an introduction to background of the research, proposed open questions to find the niche, and outline of the structure of the thesis.

(ii) Chapter 2 introduces the working principles and instrumental setups of the characterization techniques used in this thesis, including high resolution transmission electron microscopy, selective area electron diffraction, scanning electron microscopy, electron backscatter diffraction, Raman spectroscopy, Photoluminescence spectroscopy, Photoluminescence excitation spectroscopy, UV-vis-absorption spectroscopy, probe station. Also, the principle and mechanism research progress of the synthetic methods, which have been used in this thesis, including colloidal

synthesis, liquid phase exfoliation, and chemical vapour deposition, have been reviewed.

(iii) Chapter 3 presents the experimental results on the shape, crystal phase, and optical properties control of Mn doped ZnSe quantum dots. A simple method is reported to achieve shape control of Mn doped ZnSe quantum dots from branched to spherical though the control of the zinc precursor and the temperature of injection. High resolution transmission electron microscopy (HRTEM) is used to investigate the crystal structure of the quantum dots. Photoluminescence (PL) spectroscopy, Photoluminescence excitation (PLE) and UV-vis-absorption have been used to correlate PL properties and quantum yield of the quantum dots with their structure. The crystal phase of Mn doped ZnSe quantum dots can be controlled from zinc blende to wurtzite by simply changing the injection rate of the zinc precursor. It is shown that the photoluminescence properties are influenced by the structure of quantum dots. Spherical wurtzite type Mn doped ZnSe quantum dots have the highest quantum yield compared with other shapes or crystal phases of dots grown in similar reactions.

(iv) Chapter 4 presents the experimental results on utilizing BN sheets as thin supports for high resolution imaging of nanocrystals. It is the first demonstration of the use of ultrathin BN sheets as supports for imaging nanocrystals using low-voltage (80 kV) aberration corrected high-resolution transmission electron microscopy. This provides a

carbon-free alternative to the previously utilized 2D crystal supports of graphene and graphene oxide. A simple chemical exfoliation method is applied to get few layer boron nitride (BN) sheets with micrometer-sized dimensions. This generic approach of using BN sheets as supports is shown by depositing Mn doped ZnSe nanocrystals directly onto the BN sheets and resolving the atomic structure from both the ZnSe nanocrystals and the BN support. Phase contrast images reveal moiré interference patterns between the nanocrystals and the BN substrate that are used to determine the relative orientation of the nanocrystals with respect to the BN sheets and interference lattice planes. Double diffraction is observed and has been analyzed.

(v) Chapter 5 focus on the study of growth dynamics and mechanism of graphene domains on copper by atmospheric pressure chemical vapour deposition (APCVD). The nucleation of few layer graphene (FLG) domains, synthesized by copper (Cu) foil catalysts in APCVD, has been investigated. Under the conditions explored it is found that the temperature has to be at least 960 °C in order to form micron sized hexagonal FLG domains. By increasing the quality of Cu foil catalyst and also controlling the growth temperature, hexagonal single crystal domains of few layer graphene are produced that are highly aligned in their crystallographic orientation over a 5 mm distance scale. The analysis of nucleation density of FLG suggests the best condition for the activity of active sites. The fast cooling rate is required to fabricate

homogenous graphene film. It is shown that aligned rectangular few layer graphene (FLG) domains can be produced on Cu surfaces using APCVD. For the growth temperatures of 990 °C and 1000 °C the FLG domains are primarily hexagonal in shape, but at 980 °C, morphology transition of FLG domains is observed associated with different Cu grains. Rectangular FLG domains are synthesized for the first time and it is shown using electron backscattered diffraction that they only grow on Cu grains with (111) orientation due to the interplay between the atomic structure of the Cu lattice and the graphene domains. It is shown that hexagonal FLG domains can form on nearly all other non-(111) Cu surfaces. These results indicate that even at atmospheric pressure, the interplay between the Cu atomic structure and graphene formation can be strong and lead to aligned rectangular domains. Mechanism for the formation and alignment of graphene domains in solid state Cu has been discussed.

(vi) Chapter 6 presents the experimental results on achieving the aim of the thesis, which is obtaining the large area single crystal of monolayer graphene by a novel method. A simple method is presented for synthesizing large single crystal graphene domains on melted copper using atmospheric pressure chemical vapour deposition (CVD). This is achieved by performing the reaction above the melting point of copper (1090 $^{o}$C) and using a molybdenum or tungsten support to prevent balling of the copper from dewetting. By controlling the amount of hydrogen during growth, individual single

crystal domains of monolayer graphene greater than 200 μm are produced within a continuous film. Stopping growth before a complete film is formed reveals individual hexagonal domains of graphene that are epitaxially aligned in their orientation. Angular resolved photoemission spectroscopy is used to show the graphene grown on copper exhibits a linear dispersion relationship and no sign of doping. HRTEM and electron diffraction reveal a uniform high quality crystalline atomic structure of monolayer graphene. Sheet resistance measurements have been performed and discussed using Van der Pauwl method.

(vii) The overall conclusions of the thesis are presented in Chapter 7 and some possible future work is also proposed.

# Chapter 2:

# Background and Theory to Experimental Techniques

## 2.1. Introduction

As proposed in chapter 1, the aim of the thesis is to investigate the methods for controlled synthesis of single crystalline nanomaterials for commercial applications, with the emphasis towards large area single crystalline 2D atomic crystals. As proposed in the open questions in chapter 1, specifically, the relationship between crystal structure and optical properties of Mn doped ZnSe quantum dots, the structural support application of BN sheets, and the growth mechanism of graphene towards large area single crystal monolayer film for electronics, will be investigated. In order to answer these open questions, several techniques have been used in this thesis to get the desired information. These techniques can be divided into two categories, namely, characterization methods and synthetic methods. In the characterization category, High resolution

transmission electron microscopy (HRTEM) has been used to examine the growth dynamics, crystal structure, morphology and thickness of nanomaterials using either imaging mode or diffraction mode. Scanning electron microscopy (SEM) has been used to investigate the growth dynamics, morphology of nanomaterials in larger scale with 3D depth view. Electron backscatter diffraction (EBSD) has been used to examine the crystal structure of metal substrates in order to understand the growth mechanism of 2D atomic crystals. Raman spectroscopy has been used to examine the thickness, defects and structure of 2D atomic crystals. Photoluminescence (PL), photoluminescence excitation (PLE) and UV-vis-absorption spectroscopies have been used to determine the optical properties of nanomaterials, including quantum yield, absorption, transparency, band gap of nanomaterials. Probe station has been used to measure the sheet resistance of 2D atomic crystals. In order to understand why these techniques can provide the desired information, the physical principle of each technique should be understood. Thus, the physical principles and experimental setups of each characterization method will be reviewed and discussed in this chapter. In the synthetic method category in this thesis, colloidal synthesis has been used to synthesize doped semiconductor quantum dots. Liquid phase exfoliation has been utilized to fabricate BN sheets. Chemical vapour deposition (CVD) has been chosen to grow graphene films. The theory and mechanism of these three synthetic methods have been discussed in this chapter. The purpose of chapter 1 was to propose the open questions and set the aim for the

thesis. Here, the discussion in chapter 2 is to build up a methodology foundation before trying to answer the open questions in the following results chapters.

## 2.2. Characterization Methods

### 2.2.1. High Resolution Transmission Electron Microscopy

#### 2.2.1.1. Introduction

High resolution transmission electron microscopy (HRTEM) provides an excellent tool to examine the morphology and crystal structure of nanomaterials. It is a standard technique which is based on a beam of electrons transmitted though an ultrathin specimen, interacting with the specimen as it passes through it. The interaction between the electrons transmitted though the specimen leads to a formation of an image. The image is magnified and focused by an objective lens and projector lens, then captured by an imaging device, for example a fluorescence screen, on a layer of photographic film, or to be detected by a sensor such as charge coupled device (CCD).


**Figure 2.1.** The structure of JEOL 4000 HRTEM used in this thesis, located in department of materials, University of Oxford.

The structure of a TEM can be described as five systems, illumination, specimen stage, imaging, magnification, and data recording. The picture of a JEOL 4000HR HRTEM is shown in figure 2.1 with labels to show the structure of the TEM used in this thesis. In this TEM structure, the electron gun or filament generates a stream of high energy electrons in the illumination system. These electrons are then focused towards the thin specimen by a set of condenser lenses and apertures. The function of the condenser apertures is to restrict the beam and remove high angle electrons to increase the resolution. After passing though the condenser lens and apertures, the focused electrons hit the thin specimen in the specimen stage and parts of it transmitted. Some of the electrons transmit perpendicular to the specimen without changing their direction, called direct beam. Other transmitted electrons deviate from their original moving direction after passing through the specimen, called diffracted beam. The direct and diffracted beams form a diffraction pattern in the back focal plane of the objective lens and form an image on the image plane of objective lens. The optional objective and selective area aperture can restrict the beam. Both lenses belong to imaging system in TEM. High angle diffracted electrons are blocked out by objective aperture to enhance the contrast. The objective aperture is placed on the back focal plane of the objective lens to enhance the diffraction contrast. The plane of selective area aperture lies on the image plane of the objective lens to select an area of the specimen on the image plane. The back focal plane of the objective lens lies between the objective lens and selective area aperture. The diffraction pattern on the back focal plane of the objective lens and image pattern on the selective

area aperture plane is enlarged and passed down the column from intermediate and projector lens, followed by being observed on the image screen or being detected by the CCD. The intermediate lens and projector lens belong to the magnification system in TEM. The fluorescent screen, photographic film or CCD camera belongs to the data recording systems. The schematic principle of the imaging and diffraction mode is shown in figure 2.2.[162-163]

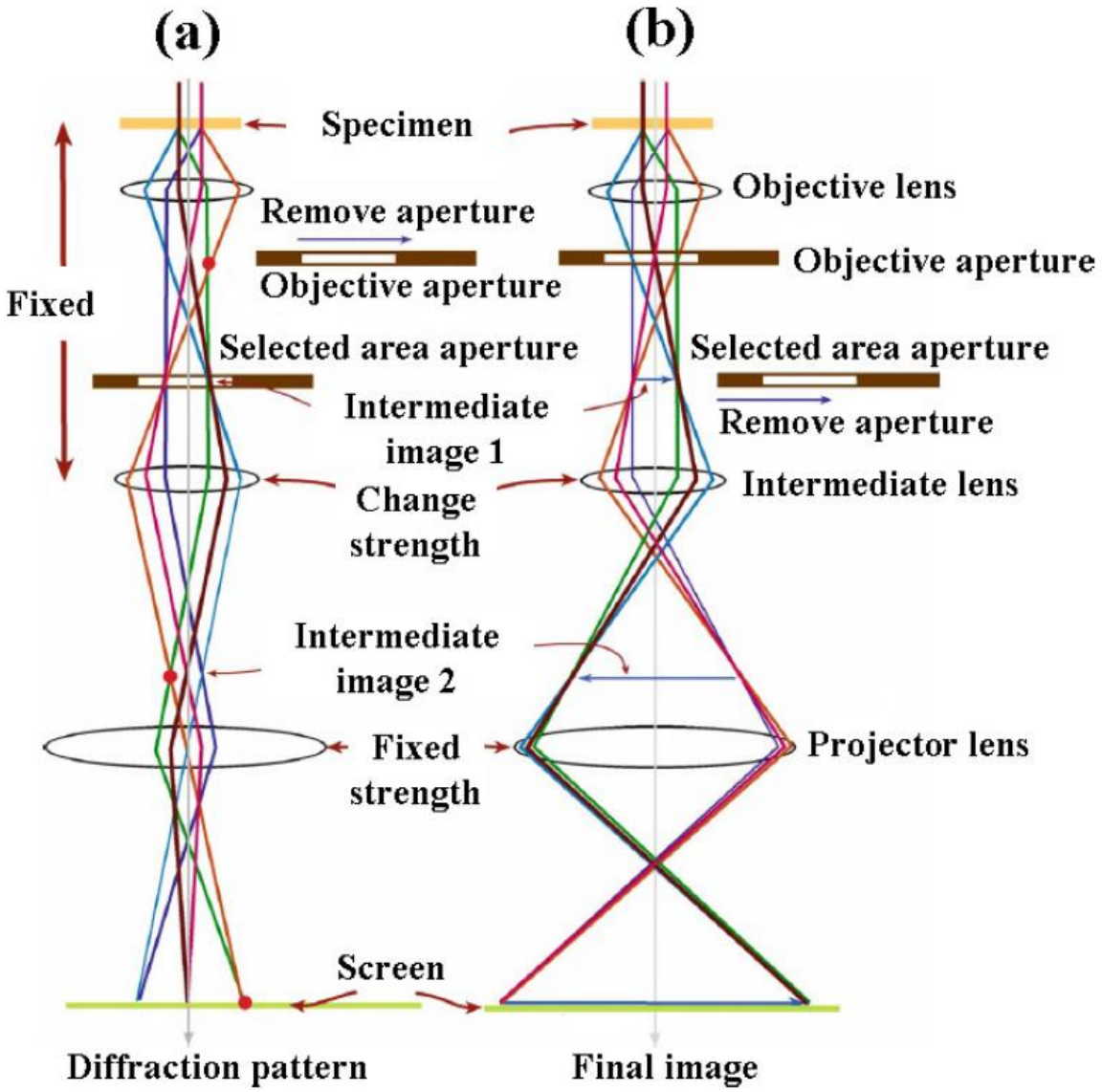


**Figure 2.2.** Schematic principle of the imaging and diffraction mode: (a) diffraction mode (b) imaging mode. Image reprinted from reference [163]. Courtesy of Dr. David B. Williams and Dr. C. Barry Carter.

### 2.2.1.2. Electron Diffraction Mode

Electron diffraction mode in HRTEM is an important technique to examine the crystal structure of nanomaterials. Selective area electron diffraction (SAED) can be used to determine the spacing of the planes in crystals. The interplanar spacing in a crystal is a characteristic property and can be used to determine the crystal phase of crystals. The basic principle of electron diffraction is called Bragg's law. Electron beam will be diffracted strongly by a crystalline specimen at a certain incident angle (the Bragg angle $\theta_B$) with respect to the diffracting planes. The Bragg's law mathematically can be described as the following.[164]

$$2d\sin\theta_B = n\lambda \qquad (2.1)$$

In this equation, $\lambda$ is the electron wavelength, d is the crystal lattice spacing, $\theta_B$ is the Bragg angle and n is the integer representing the number of wavelengths required for constructive interference to occur.

The Ewald sphere can be used to describe and understand diffraction in reciprocal space.[165-166] The reciprocal space is an imaginary space in which planes of atoms are represented by reciprocal lattice points. The correlation between reciprocal space and real space is established by the maths described between reciprocal vector and real space vector. The reciprocal vector $g_{hkl}$ is the inverse in magnitude of the $d_{hkl}$ spacing which is the shortest distance between two planes in $\{hkl\}$ and is geometrically normal to the planes {hkl}.

$$|g_{hkl}| = \frac{1}{d_{hkl}} \tag{2.2}$$

Ewald sphere is normally presented in 2D projection by a circle with a radius of $\frac{1}{\lambda}$, shown in figure 2.3.

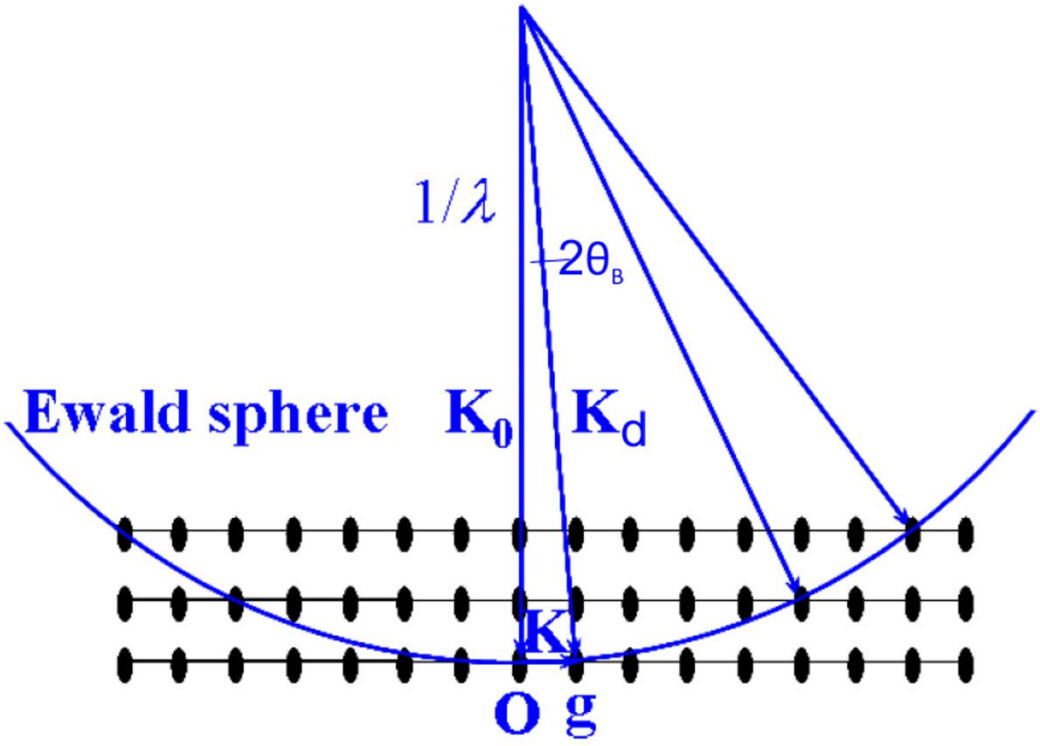


**Figure 2.3.** Ewald sphere in 2D projection.

If any point in reciprocal lattice intersects with the Ewald sphere, the set of planes which corresponds to the point satisfy Bragg's law and hence the beam will diffract strongly by these planes. Therefore strong reflection spots, which is correspond to these sets of planes, will appear in the electron diffraction patterns. As indicated in figure 2.3, point O is the origin of the reciprocal lattice. Vectors $k_o$ and $k_d$ represent the wave vector of the incident and diffracted wave,

respectively. The vector k is the difference between the incident wave and diffracted wave due to the diffraction. The mathematical equations between these vectors are followed.

$$\vec{k} = \overrightarrow{k_d} - \overrightarrow{k_o} \tag{2.3}$$

$$|k_o| = |k_d| = \frac{1}{\lambda} \tag{2.4}$$

As these vectors should satisfy the Bragg's law, the angle difference between incident and diffracted wave is $2\theta_B$. From the simple trigonometry, an expression for $\theta_B$ is described.

$$\sin\theta_B = \frac{\left|k/2\right|}{\left|k_d\right|} = \frac{|k|}{2\lambda} \tag{2.5}$$

If combining the equation (2.1), (2.2) and (2.5) together, we can get the following equation.

$$|k| = \frac{n}{d_{hkl}} = n|g_{hkl}| \tag{2.6}$$

Thus, the distance between electron diffraction reflection spots and origin of the reciprocal space is n order magnitude of the reciprocal vector.

Electron diffraction has unique characteristic when compared to X ray diffraction. Firstly, due to the small wavelength of electrons, comparing to X ray, the radius of Ewald sphere $\frac{1}{\lambda}$ is quite large, and therefore the surface of Ewald sphere is nearly planar to reciprocal lattice. Thus, Ewald sphere intersects with several reciprocal lattices, which leads to many diffraction spots appearing simultaneously even if the Bragg's law is not exactly satisfied. Secondly, the electron diffraction can get higher spatial resolution than X ray diffraction because the direction of moving electrons can be more easier to change comparing with X ray. This is due to the strong interaction between

electrons and matter, leading to electron multiple scattering phenomenons. Thus, electron diffraction can be used as sharper probe for localized information within the nanomaterials. However, electron diffraction does contain intensity information but loses the phase information from the specimen. High resolution imaging mode provides both phase information and intensity information as an excellent tool, which will discuss later.

After discussing the principle of the electron diffraction by Bragg's law and Ewald sphere, a natural question raised is how to index electron diffraction patterns. As single crystal electron diffraction patterns are normally obtained by a parallel beam perpendicularly illuminating a crystal lattice. The direction of the parallel beam is along the zone axis of specific crystal lattice planes. The atomic column is perpendicular to the zone axis. Thus, the single crystal electron diffraction pattern is consisted of sharp reflection spots. For selective area electron diffraction (SAED) patterns of polycrystalline materials, a number of crystals with different orientation will be selected by the selective area aperture and illuminated simultaneously. Thus, the selective area electron diffraction patterns are the mixture of different sets of single crystal electron diffraction patterns. Due to the different rotation orientation of individual crystals, diffraction rings are normally observed in SAED for polycrystalline materials. The zone axis for single crystals can be assigned by comparing with the standard electron diffraction patterns if the crystalline structure is

known. Lattice parameters in the electron diffraction patterns can be indexed if the camera length of the TEM is calibrated with known reference materials.

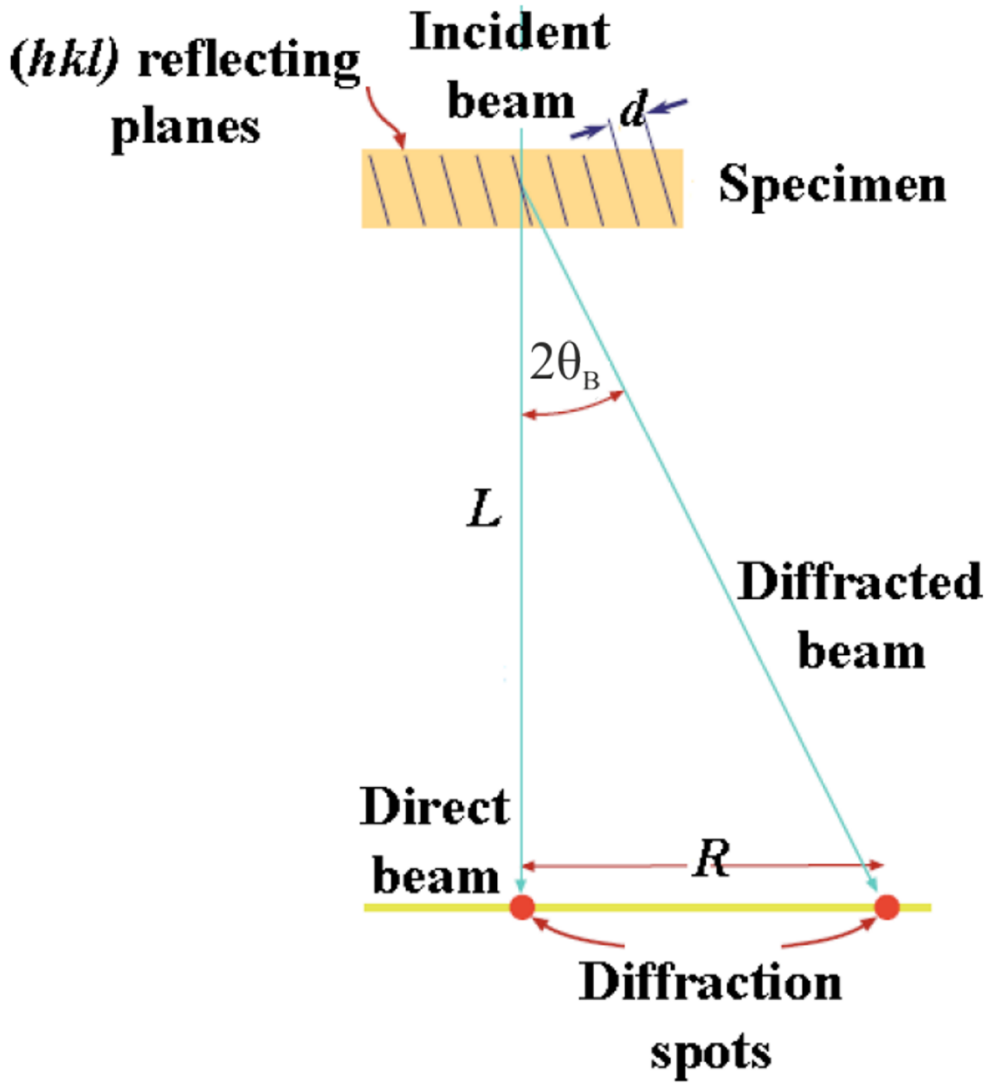


**Figure 2.4.** Geometry relationship between camera length L, d spacing, the spacing R between the directed beam and a scattering maximum (such as a diffracted beam or the radius of a ring of diffracted intensity). Image modified from reference [163]. Courtesy of Dr. David B. Williams and Dr. C. Barry Carter.

As indicated in figure 2.4, when the incident beam hits the specimen, parts of the electrons are scattered by a $2\theta_B$ as diffracted beam while some of the electrons transmitted without changing the direction as the direct beam. The distance between the direct and diffracted beams as measured by

the screen R, is determined by L, the camera length. Supposing the scattering angle is small, the geometry relationship is described as follows.

$$\frac{R}{L} = \tan 2\theta_B \approx 2\theta_B \tag{2.7}$$

Apply the small scattering angle assumption to Bragg's law, the following equation can be obtained.

$$\frac{\lambda}{d} = 2\sin\theta_B \approx 2\theta_B \tag{2.8}$$

Combing the equation (2.7) and (2.8) together, the relationship between camera length and d spacing of crystals can be described as follows.

$$Rd = L\lambda \tag{2.9}$$

As for the same TEM instrument, the camera length L is fixed due to the geometry of the instrument. At the same acceleration voltage, the wavelength of electron λ is the same as well. The diffraction pattern is the projection of the reciprocal lattice. Supposing with a known specimen, the $(h_0k_0l_0)$ plane with d spacing of $d_0$ has a measured distance $R_0$ on the screen in the diffraction pattern. An unknown sample with $(h_1k_1l_1)$ plane with d spacing of $d_1$ has a measured distance $R_1$ on the screen in its diffraction pattern. If the electron diffraction patterns of both samples are measured at the same accelerating voltage, then the following equations can be assigned.

$$R_0d_0 = R_1d_1 \tag{2.10}$$

Then from this equation $d_1$ can be calculated, which is the d spacing of the unknown sample. Nowadays, with CCD to record data, $R_0$ and $R_1$ are recorded as pixels. The image analysis software

can be used to calibrate this using a standard diffraction pattern of a known sample by correlating the pixel information from known diffraction spots. In the diffraction pattern of an unknown sample, the angle between the lines joining spots $h_1k_1l_1$ and $h_2k_2l_2$ to the original spot 000 is the same as the angle between the $(h_1k_1l_1)$ and $(h_2k_2l_2)$ planes since the perpendicular relationship between reciprocal vector and real space vector. By comparing the experimental single crystal electron diffraction pattern with standard electron diffraction patterns, if both the d spacing and angle relationship can match the standard pattern, the electron diffraction patterns are indexed. After indexing the electron diffraction pattern, it needs to compare the d spacing measurement result with the X ray diffraction data of this materials to check whether the measured d spacing exist in the X ray diffraction database. This double check will make sure the index is correct. Another alternative method to confirm the index is to simulate single crystal electron diffraction pattern using software, like *crystal diffract*. If the simulated pattern matches the experimental pattern, it confirms the indexing. These are the methods to index single crystal diffraction pattern. For the index of the diffraction rings rather than spots, the principle is the same. It is needed to carefully measure the radius of each diffraction ring. The ratio between the radii must match the ratio of the corresponding d spacing planes.

#### 2.2.1.3. Imaging Mode

Diffraction contrast is obtained by using an objective aperture on the back focal plane of the objective lens. If placing the objective aperture to select direct beam, a bright field (BF) image is formed, as shown in figure 2.5(a).[163] If the diffracted beam is selected by the objective aperture, a dark field (DF) image is created, as shown in figure 2.5(b).[163]

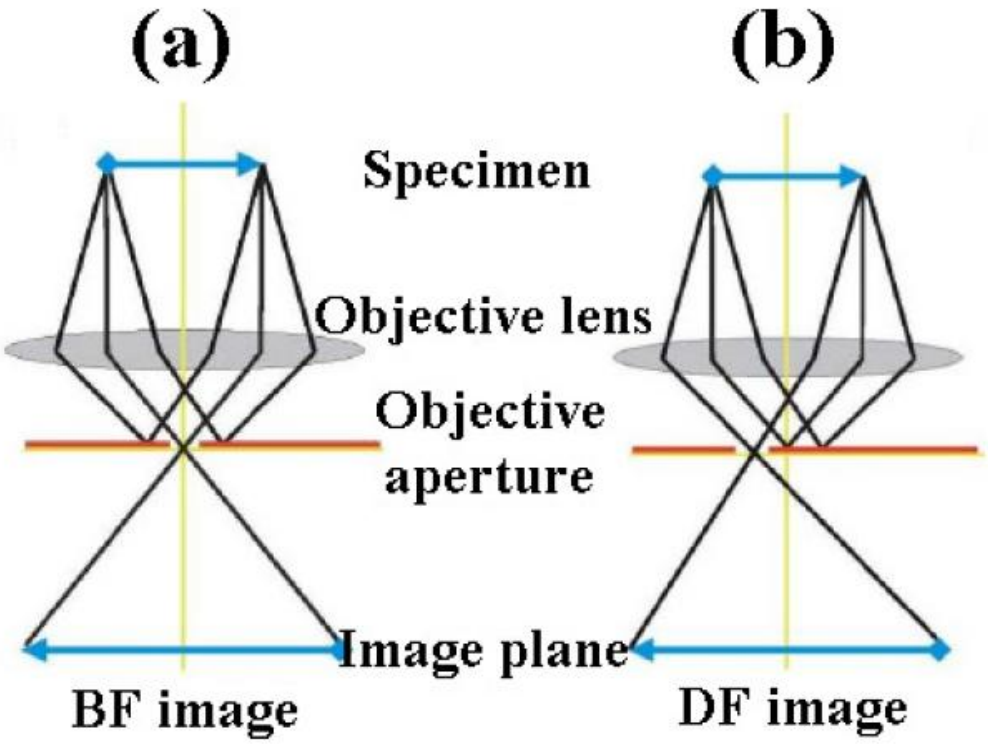


**Figure 2.5.** Comparison of the use of an objective aperture in TEM to select (a) the direct (b) the scattered electron to form (a) BF and (b) DF images respectively. Image reprinted from reference [[163]]. Courtesy of Dr. David B. Williams and Dr. C. Barry Carter.

In this thesis, electron diffraction patterns are taken on JEOL 4000HR or Philip CM20 TEM while HRTEM images are taken on JEOL 4000HR or Oxford's JEOL 2200MCO FEG (field emission gun) aberration corrected HRTEM fitted with both probe and image correctors. The accelerating voltage of HRTEM performing in this thesis is 400 kV for quantum dots and 80 kV for 2D atomic

crystals. The formvar carbon coated copper TEM grids are used for high resolution imaging quantum dots. This is a continuous amorphous carbon film support to hold small size quantum dots. Without holes in the amorphous carbon film, it is easier to form mono-disperse quantum dot films from the solution of quantum dots with appropriate concentration of quantum dots. A lacey carbon coated TEM grid is a good support for imaging layered materials with the edge suspended on the hole against vacuum. Holey silicon nitride support film is used as a support for imaging graphene. This TEM grid can be treated with heat without deteriorating as $Si_3N_4$ is an insulator with high strength within a broad temperature range.

The imaging mode of HRTEM allows direct imaging crystallographic of materials at atomic level. It is an invaluable tool to study the crystallinity, crystal phase, and growth dynamics of nanomaterials, even in-situ imaging of nanomaterials interaction and movement under the electron beam.

Phase contrast is the imaging mechanism of HRTEM. The electron wave interacts with the thin specimen and the amplitude of the wave will be changed slightly due to the inelastic scattering though the specimen lattice. It is thus supposed that the electron wave only suffers a phase change that depends on the projection of the electrical potential along a straight line of the electron wave pathway through the thin specimen. The phase difference $\alpha$ between the electron waves

transmitted via the specimen and the electron wave passing through vacuum is described as following.

$$\alpha \approx \sigma \varphi_p(r) \tag{2.11}$$

In which, $\varphi_p(r)$ is the projection potential of the electron beam incident direction. $\sigma$ is an interaction constant ( $\sigma = \frac{\pi}{\lambda E}$ ). λ is the wavelength of the electron in vacuum. E is the energy of the electrons. The incident electron wave can be treated as plane wave approximately, which is a constant wave with infinite parallel planes of the constant phase and constant peak to peak amplitude normal to the phase velocity vector. The transmission function can be expressed as followed.

$$\psi_e(r) = \exp[-i\sigma\varphi_p(r)] \tag{2.12}$$

If combining formula (2.11) and (2.12) together, the following equation can be got.

$$\psi_e(r) \approx \exp[-i\alpha] \tag{2.13}$$

This equation is called the phase object approximation (POA). It means that the electron wave function after interaction with specimen is dependent on the phase changes. The phase of the electron wave function carries the information from the thin specimen and generates contrast in the image. Thus, it is called phase contrast imaging. The most obvious difference between phase contrast imaging and other forms of TEM imaging (diffraction contrast imaging and mass thickness contrast imaging) is the number of beams collected by the objective aperture or an

electron detector.[167] A phase contrast imaging requires selection of more than one beam, while the BF and DF imaging only requires selection of a single beam using the objective aperture.[167]

The interference between electron wave and specimen generates diffraction contrast in the back focal plane. The mathematical relationship between the diffraction function in the back focal plane and the electron wave function after interaction with thin specimen can be written as followed.

$$\phi(u) = F[\ \psi_e(r)\ ] \tag{2.14}$$

Where $u$ is vector in the diffraction plane in the reciprocal space, the spatial frequency for a particular direction, and F is the Fourier transform operation. Afterwards, the interference of the electron wave from the back focal plane recreates the specimen electron wave function in the image plane. Thus, following this electron beam pathway, the formation of image can be described as two successive Fourier transform of the electron wave function after transmitted via the specimen. Hence, the image wave function in the image plane can be written as followed.

$$\psi(r) = F[\phi(u)] = F\{F[\psi_e(r)]\} \tag{2.15}$$

This equation tells us if in a perfect lens system, all the electron waves leaving the specimen would be recovered with exact phase relationship retained to form image in the image plane. In this sense, in perfect lens system, the image wave function is the exact reproduction of the transmission function (electron wave function after interaction with the thin specimen) of the thin specimen. However, practically no perfect lenses exist. It is possible that the scattered electron wave falls

outside the apertures and this will affect the amplitude of the electron wave in the image plane. Also, the lens aberrations will affect the phase of the electron waves. Spherical and chromatic aberrations of the lens cannot be eliminated completely.[168] Because rays are focused more tightly if they enter the lens far from the optical axis than if they are closer to the optical axis, it does not produce the perfect focus point. This is called spherical aberrations. Chromatic aberration is a kind of distortion in which a lens fails to focus different wavelength rays to a convergence point. This happens because lenses have different refractive index for different wavelength of light (the dispersion of lens). The refractive index decreases with increasing wavelength. Thus, the electron waves of different energy cannot focus to a convergence point in an image plane. Due to this imperfect lens with these aberrations, a point in the specimen is imaged as a disc in the image plane. Thus, a contrast transfer function (CTF), H ($u$), is applied to modify the image function in the image plane. H ($u$) is the Fourier transform of the spread function h(r), which describes how a point spread into a disc. Hence, the modified image function can be written as followed, in which u is the vector in the diffraction plane in the reciprocal space.

$$\psi'(r) = F\{F[\psi_e(r)]H(u)\} \tag{2.16}$$

Figure 2.6 shows the electron beam pathway though an objective lens.[169]

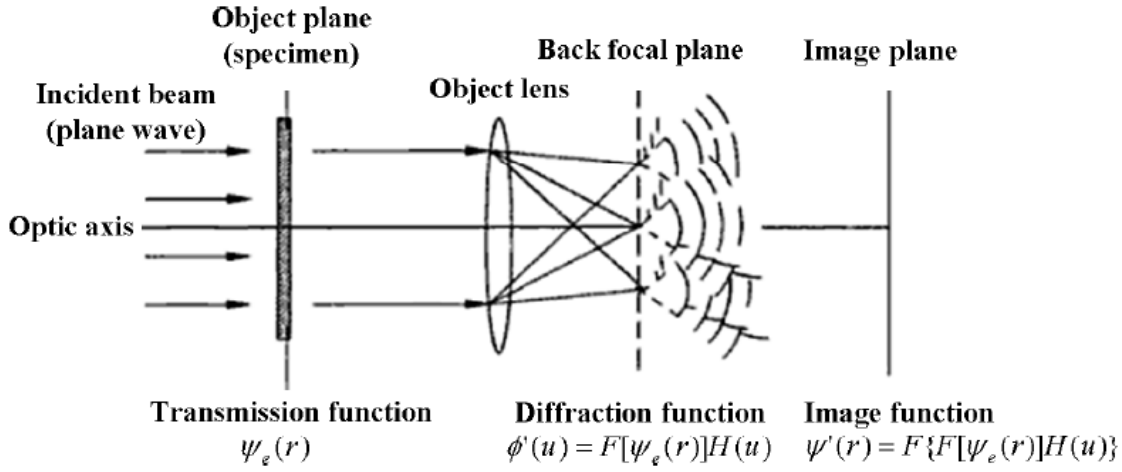


**Figure 2.6.** Schematic diagram of the image formation of HRTEM. Image reprinted from reference [169]. Courtesy of Dr. D. Shi.

Contrast transfer function is affected by three factors, aperture, attenuation of wave, and aberration of lenses. Therefore, the H (*u*) is expressed as the product of these three terms.

$$H(u) = A(u)E(u)\exp[i\chi(u)] \tag{2.17}$$

Where A(*u*) is the aperture function, which can be expressed as a step function and represents the cut off information of the objective aperture. E(u) is the envelop function which describes the attenuation of the wave by the spatial coherence of the source. χ(u) is the function of aberrations in the electron optical system to describe the chromatic effects, which can be written as followed.

$$\chi(u) = \pi\Delta f\lambda u^2 + \frac{\pi}{2}C_s\lambda^3 u^4 \tag{2.18}$$

In which, $C_s$ is the spherical aberration coefficient, λ is the electron wavelength at the accelerating voltage, and Δ*f is* the defocus value chosen to form the image, u is vector in diffraction plane in the reciprocal space. As for a specific specimen, u is the spatial frequency determined by the lattice

spacing. Thus, for a specific sample, $\chi(u)$ depends on $\Delta f$ only. Therefore, choosing the optimum defocus value is important for observing the specific spatial frequency u in high resolution imaging mode. The optimum defocus value is given by Scherzer.[170]

$$\Delta f_{sch} = -\left(\frac{4}{3}C_s\lambda\right)^{\frac{1}{2}} \tag{2.19}$$

### 2.2.1.4. Simulation

The simulation done in this thesis is performed by using a combination of softwares. An atomic model is constructed using *Accelys DS Viewer* and *crystal maker* software. The coordinates of each atom are outputed from an atomic model supercell using *Accelys DS Viewer*. After some formatting of the data, the coordinates are inputed into the specific software for simulation. Electron diffraction simulation is done by software called *crystal diffract* or *single crystal diffraction*. HRTEM simulation is performed by software called JEMS using the principle of the multislice method.

In order to understand the principle of multislice simulation method, it is necessary to describe the weak phase object approximation (WPOA) first. In the multislice method, the thin specimen is divided into many thin slices normal to the incident beam. Each slice obeys the WPOA. The Bloch wave approach is used in JEMS software for calculation. The potential in each slice is projected onto the first projection plane, which is phase grating to modulate the phase. Amplitudes and

phases for all beams generated by interaction with this plane are calculated. All the diffracted beams are propagated though free space to the next projection plane. These processes are repeated. The process is shown in figure 2.7.[171]

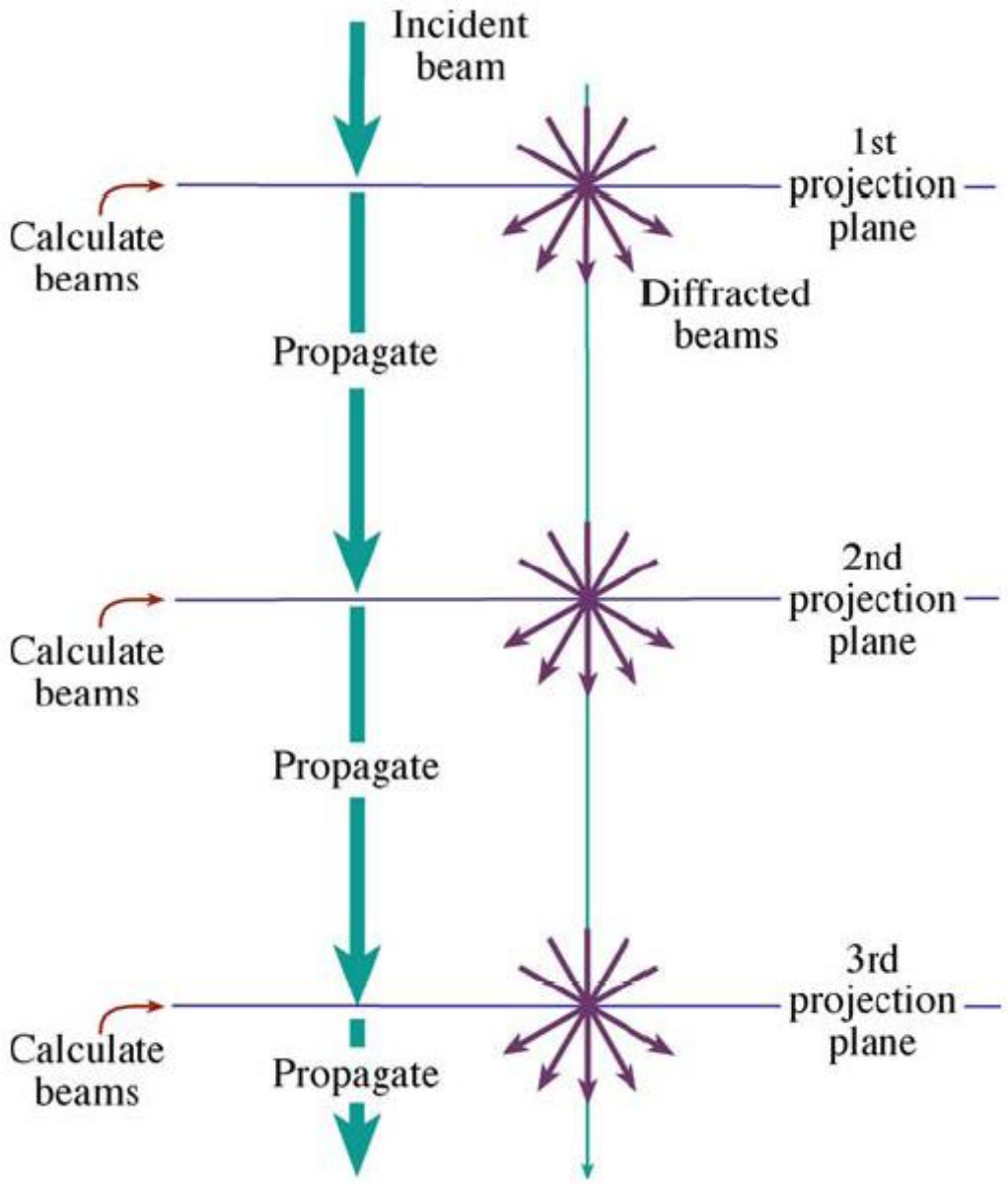


**Figure 2.7.** The principle of multislice method. Image reprinted from reference [[171]]. Courtesy of Dr. David B. Williams and Dr. C. Barry Carter.

The correlation between specimen structure and image contrast cannot be directly found in equation (2.16). Further assumptions should be made to expand equation (2.16) into a simple equation for numerical calculations. It is supposed that the phase changes of an electron wave are also small. That means $\cos[-\sigma\varphi_p(r)]\approx 1$, $\sin[-\sigma\varphi_p(r)]\approx -\sigma\varphi_p(r)$. The equation (2.12) can be explained with the Euler formula and written as followed, which is called WPOA.

$$\psi_e(r) = \exp[-i\sigma\varphi_p(r)] = \cos[-\sigma\varphi_p(r)] + i\sin[-\sigma\varphi_p(r)] \approx 1 - i\sigma\varphi_p(r) \tag{2.20}$$

The directly transmitted wave unaffected by the specimen is represented as constant 1. The scattering function is presented as the second component in the equation and *i* indicates phase changes of $\pi/2$. For this $\pi/2$ phase shift in a small amplitude scattered wave, the resultant wave has only a slight phase modulation but no amplitude modulation. So the image contrast is zero (Figure2.8a). To obtain some information from the image concerning the specimen structure, an additional phase shift is needed to bring the scatter wave either exactly into (Figure 2.8b) or out of the phase (Figure 2.8c) with the primary wave.

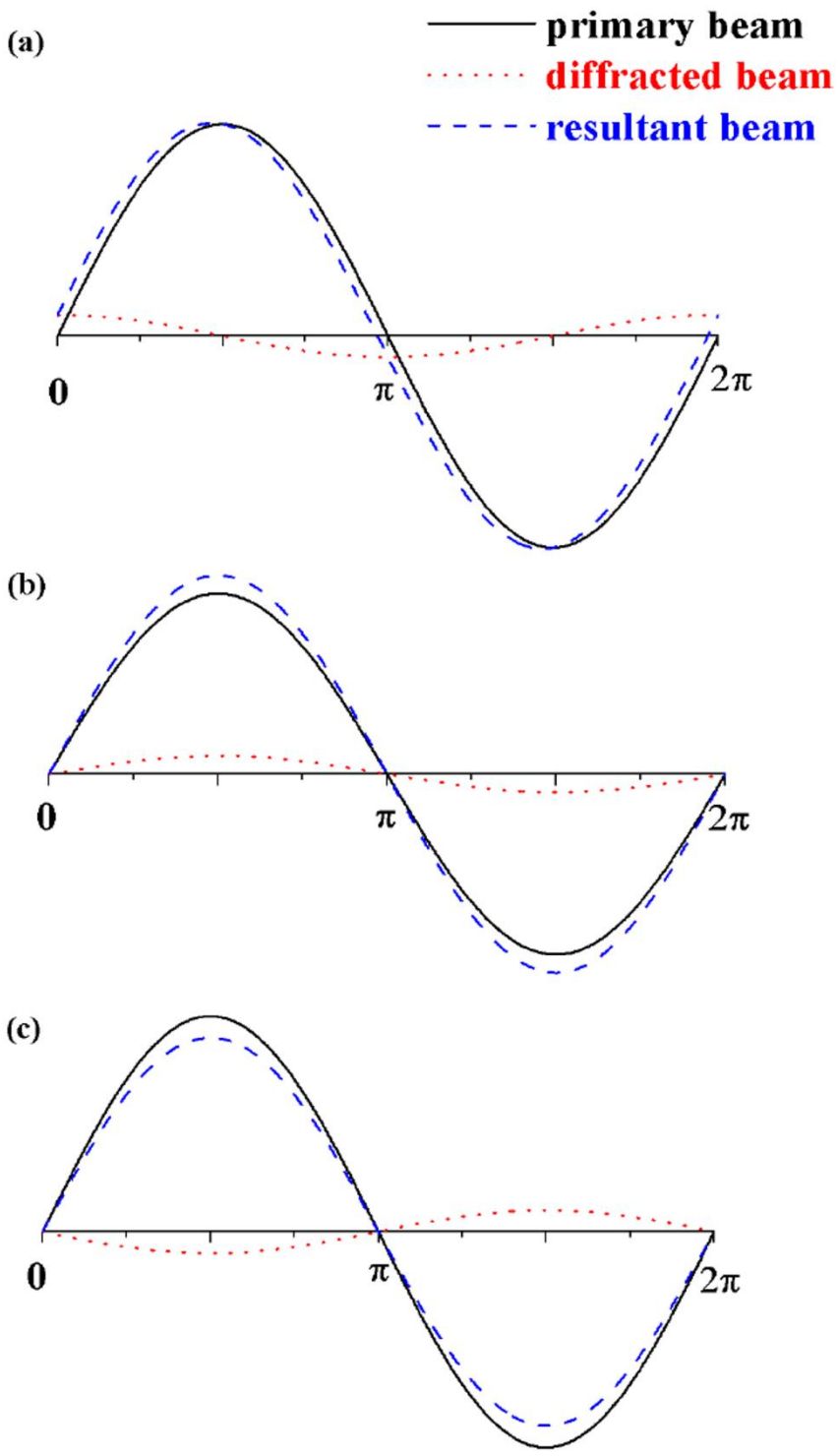


**Figure 2.8.** Schematic showing (a) a π/2 phase shift in small amplitude scattered wave, the reluctant wave has only a slight phase change; an additional phase shift bring the scattered wave either exactly (b) into or (c) out of the phase with the primary wave.

Practically, the imperfect lens gives some image contrast. When the WPOA is applied, the equation (2.16) can be modified as the following.

$$\psi'(r) = [1 - i\sigma\varphi_p(r)] \otimes F[H(u)] \tag{2.21}$$

In which, $\otimes$ sign in equation (2.21) is the convolution operation. The image intensity is found by multiplying the image wave function by its complex conjugate.

$$I = |\psi'(r)|^2 \tag{2.22}$$

Only the imaginary part in exp[iχ(u)] in equation (2.17) contributes to the image intensity in WPOA in equation (2.22) as only this term provides the imaginary part in the Fourier transform of the contrast transfer function $H(u)$.

WPOA is valid for only thin specimen (0.5-2 nm). In addition, unlike X rays, the interaction of electrons is very strong and this strong interaction indicates WPOA theory does not hold for most of the cases. Thus, dynamical effect must be taken into account in the HRTEM imaging simulation to consider these interactions between electrons. Multislice simulation is the practical method using WPOA as the basic and considering dynamical effects.

### 2.2.2. Scanning Electron Microscopy

#### 2.2.2.1. Imaging Mode

Scanning electron microscopy (SEM) is one kind of electron microscopy that images the sample surface by scanning it with a high energy electron beam in a raster scan pattern.[172] The interaction between the electrons and atoms in the specimen produces signals which contain the information about the properties of the sample, such as surface topography, chemical composition and crystallography.

The image formation mechanism of SEM relies mainly on three types of contrast.[173] Atomic number contrast is also called Z contrast, which means the emission coefficient is proportional to the atomic number of the atoms. Normally, heavy atoms will have higher emission coefficient than the lighter atoms. Orientation contrast in SEM has relationship to the crystallography of the crystals or the topography of the sample. This will affect how strongly the electrons can interact with the crystal due to Bragg's law and how much signals can reach the detector. Electron channelling contrast is dependent on the spot size and energy of the primary electron beam. It determines how far the electrons can penetrate into the sample, how much signals can escape from the sample, and the depth of view of the sample. Normally, the more deep electron penetrate, more difficult the signals can get out of the sample, while it gives better depth of view.

In a typical SEM instrument, a source of accelerated electrons is produced by the electron gun, which is the gun fitted with tungsten, $LaB_6$ filament. If the vacuum system is upgraded, the field

emission gun can be used as the electron source, which is the cold cathode type using tungsten single crystal emitter or the thermally assisted Schottky type using $ZnO_2$ emitter.[172] Unlike the optical and transmission electron microscopy, image magnification is not a function of the power of objective lenses. Condenser or objective lenses may exist in the SEM but their function is to reduce the diameter of the electron source and place a small and focus the electron beam to a spot on the specimen. The schematic illustration of the SEM instrument is shown in figure 2.9.[173] The beam is scanned along a line in the deflection system and the line is displaced for the next scan so that a rectangular raster is generated on both the specimen and viewing screen.

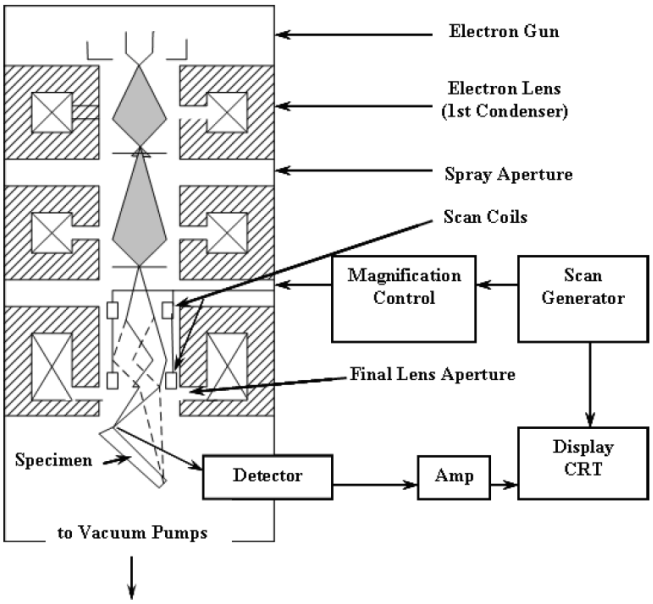


**Figure 2.9.** Schematic drawing of the electron column deflection system and electron detectors in a typical SEM. Image reprinted from reference [173] Courtesy of Dr. J.Goldstein, Dr. D. E. Newbury, Dr. P. Echlin, Dr. D. C. Joy, Dr. Jr., A. D.Romig, Dr. C. E. Lyman, Dr. C. Fiori, and Dr. E. Lifshin.

When the primary electron beam interacts with the specimen, the electron loses energy by repeated random scattering and absorption. The electron beam absorbed by the specimen is within a

teardrop shape volume known as the interaction volume. The size of the interaction volume depends on the electron landing energy, the atomic number of the specimen and specimen density. Several types of signals are generated from the interaction between the electron beams with the atoms in the specimen, including secondary electron, backscattered electron, characteristic X ray, light from cathode luminescence, specimen current and transmitted electrons. Each signal can be detected with specialized detectors to obtain corresponding information or creating images. The most common detection mode is secondary electron imaging. When the non-energetic secondary electron from the inelastic scattering hit scintillator material, the light produced is converted into an amplified electrical signal by the photomultiplier tube, the variation of the signal provides the intensity change and creates contrast in the image.[173]

Signals from the interaction between electrons and specimen atoms contain different information. Secondary electrons which are ejected from the k electron shell (the first electron shell closest to the nucleus) of the specimen atoms by inelastic scattering interactions with electron beam are low energy electrons containing the information from the sample surface within a few nanometres deep. Thus, it contains information about the surface topography. Characteristic X-ray can be detected by energy disperse X ray (EDX) detector for chemical composition analysis or element image mapping. Catholuminescence (CL) is the emission of light when atoms excited by high energy electrons return to their ground state. This process is similar as UV-induced fluorescence. CL

signal can be used to image and map the distribution of the luminescence emitted by the specimen with real colour. The beam current absorbed by the specimen can also be used to create images of the distribution map of specimen current to analyse the electrical conductivity. Backscattered electron from the elastic scattering interaction with specimen atoms can be used to determine the crystallography structure of the specimen, which will be discuss in details in the next section.

#### 2.2.2.2. Electron Backscattered Diffraction Mode

Backscattered electrons consist of high energy electrons originating in the electron beam, which are reflected or backscattered out of the specimen interaction volume by elastic scattering interactions with specimen atoms.[172] Although the energy of backscattered electrons remains the same due to the elastic scattering, the number of electrons being backscattered by the specimen atoms depends on the atomic number of the atoms. Heavy atoms (high atomic number) can backscatter more electrons than light elements (low atomic number). Thus, the total energy of the backscattered electrons from heavy atoms is greater than from light elements. This generates atomic number contrast to distinguish different chemical composition. Backscattered electrons can also be used to generate electron backscattered electron diffraction (EBSD) image.

The major difference between secondary electrons and backscattered electrons are the energy difference and emission direction range. Unlike low energy secondary electrons generated from

the inelastic scattering, backscattered electrons are generated from elastic scattering and thus retain high energy. The deflection angle of backscattered electrons is larger than 90 degrees comparing with the primary beam due to the Coulombic interaction within the electron cloud or Coulombic attraction by the nucleus.[163] The deflection angle of secondary electrons is normally small and random and secondary electrons are ejected from the conduction or valance bands of the atoms.[163]

EBSD, also called backscattered Kikuchi diffraction, is a technique to obtain the crystallographic information.[174] This information can be used for elucidating texture and orientation of any crystalline materials. EBSD can be used to index and indentify crystals, thus has lots of applications, such as crystal orientation mapping, defect studies, phase identification, grain boundary and morphology studies, regional heterogeneity investigation, materials discrimination, microstrain mapping, and chemical identification. EBSD is increasingly common being used as an alternative to electron diffraction in TEM and X-ray diffraction (XRD), with the advantage of fast data acquisition, simple specimen preparation.

How does electron backscattered diffraction pattern (EBDP) form? It forms when many different planes diffract different electrons to form Kikuchi bands which correspond to each of the lattice diffracting planes. The boundaries of a Kikuchi band represent the positive and negative Bragg angles (typically of the order of 1 degree) for a given set of crystallographic planes.[175] Normally,

in order to increase the contrast in the EBDP, the flat/polished crystalline sample needs to be tilted 70° from the horizontal towards the diffraction camera.

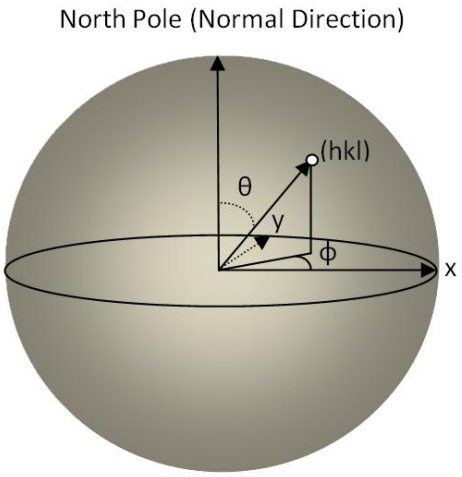


**Figure 2.10.** The generation of pole figures (normal direction, rotation direction, transverse direction) from a 3D space.

How can the electron backscattered diffraction pattern be indexed and interpreted? Once the Kikuchi band location is detected in the EBDP, it is possible to relate these locations to the underlying lattice orientation. The angles between the Kikuchi bands represent the angles between lattice planes. When the position and angles between three Kikuchi bands are known, an orientation solution can be determined. The geometry of the lattice plane, which the Kikuchi bands correspond to, can be determined by pole figures with normal direction as the north pole zone axis and projection to the equator plane as the rotation direction and transverse direction. The geometry relationship to define a crystal plane in 3D space is shown in figure 2.10. The normal direction is the North Pole in figure 2.10 and the crystal plane is indicated as the point in the sphere surface.

The projection of the line, which is the line between the crystal plane point and centre of the sphere, into the equator plane has the angles between x and y axis. The angles between the x axis and projection line indicates the rotation direction, while the angle between the y axis and projection line indicates the transverse direction.

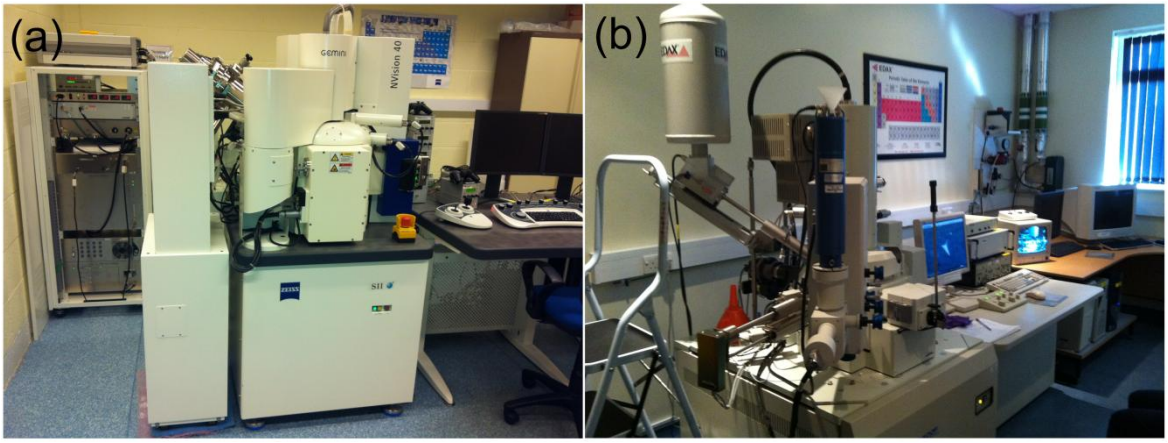


**Figure 2.11.** The SEM and EBSD used in this thesis, located in Department of Materials, University of Oxford. : (a) Zessis NiVision 40 FIB-SEM (b) JEOL 6500F SEM with EBSD detector.

The crystallographic diffraction pattern with specific normal direction can be generated with EBSD software. By comparing the experimental data to this standard crystallographic diffraction patterns, the crystal orientation and lattice plane information can be directly extracted. The grains of different crystal planes can be coated with different colour for analysis of crystal grains and grain boundaries. The instruments of the JEOL 6500F SEM with an EBSD detector and Zessis Nivison 40 FIB-SEM, which are used in this thesis, are shown in figure 2.11.

### 2.2.3. Optical Spectroscopy

#### 2.2.3.1. Introduction

Optical spectroscopy is a means of studying properties of physical objects on measuring how an object emits and interacts with light. Electrons exist in energy levels in materials. In the optical spectroscopy, electrons are driven to another energy level by absorbing photon energy and then transition happens for electrons between energy states in materials. In this section, optical spectroscopies, including Raman spectroscopy, photoluminescence (PL) spectroscopy, photoluminescence excitation (PLE) spectroscopy, UV-vis-Absorption spectroscopy, are discussed on physical principles, instruments and applications.

#### 2.2.3.2. Raman Spectroscopy

Raman spectroscopy is one of the important non-destructive techniques to characterize materials. Useful structural information of the material, such as bonding and defects, can be obtained from the photon frequency and scattering intensity measured by Raman spectroscopy.

Raman scattering was discovered by C.V. Raman in 1928 but the predication could go back to 1922.[176] When a beam of light impinged upon a sample, photons are absorbed or scattered by the materials. The most majority of the scattered photons are via elastic scattering, in which the scattered photons have exact the same wavelength with the incident photons. This process is

known as Rayleigh scattering. In comparison, Raman scattering is the inelastic scattering of light, which means the energy of the scattered photons is not equal to that of incident photons. It occurs when light impinges upon a molecule and interacts with electron clouds and bonds of the molecules. With the light excitation the molecule is raised to the virtual energy states which are imaginary intermediate states in quantum mechanics. For the spontaneous Raman effect, the excited molecules will relax to the vibrational excited states, which generates Raman scattering and Raman shift in the spectrum due to the unequal photon energy via this inelastic scattering process. If the molecule is initially on the ground state before excitation, the Raman shift is called Stokes shift. If the molecule has already been on the elevated vibrational excited states before light excitation, the Raman shift is called anti-Stokes shift.[177] A schematic energy level diagram involving Raman signals is shown in figure 2.12.[178] A molecule polarisability change or amount of deformation of the electron clouds, with respect to the vibrational coordinate, is required to exhibit Raman activity. The amount of polarisability change will determine the Raman intensity while the Raman shift is equal to the difference of the vibration level that involves.

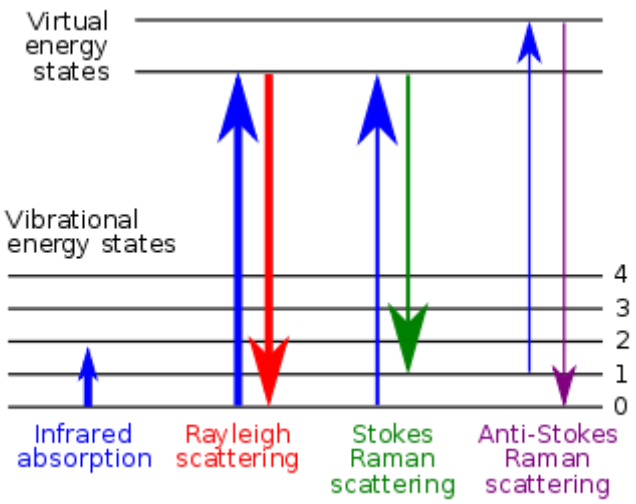


**Figure 2.12.** Energy level diagram and transitions involved in Raman signal. The line thickness is roughly proportional to the signal strength. Image reprinted from reference [178]

The basic principle of the Raman spectroscopy is the interaction between the optical photons and vibration phonons in the lattice. (A phonon is a quantum mechanical description of several type of vibration motion, in which a lattice uniform oscillates at same frequency.) An induced dipole moment $P$ is resulted from the interaction between the electric field E of the photon's electromagnetic wave over with time $t$ and the vibration mode of a diatomic molecule vibration at a frequency $\nu_m$. The mathematical description can be written as followed.[179]

$$p = \alpha_0 E_0 (2\pi \nu_0 t) + \frac{1}{2}\left(\frac{\partial \alpha}{\partial q}\right)_0 q_0 E_0 \{\cos[2\pi(\nu_0 + \nu_m)t] + \cos[2\pi(\nu_0 - \nu_m)t]\} \qquad (2.23)$$

If assuming small vibrations, the polarisability α is approximately to be linear with displacement $q$ from the equilibrium position $q_0$. The first term of equation (2.23) represents Rayleigh scattered photons. The two cosine term represents anti-Stokes scattered (frequency summed) and Stoke

scattered term (difference of the frequency). If the partial derivative component $\left(\frac{\partial \alpha}{\partial q}\right)_0$ is zero, the specimen is Raman silent. Raman instrument normally measures the Stokes Raman scattering term.

A typical Raman spectrometer consists of three parts, the laser, the collection device, and the spectrograph. A coherence beam of monochromatic light is generated by the laser to excite the specimen. Low background emission and good wavelength stability are required for the laser which is used in the Raman spectrometer. A monochromator is normally attached to the laser for this requirement. The function of a collection device is to collect the photons and filter out the Rayleigh scattered photons and background noise. Normally notch or edge filters are applied in the collective device. Raman scattering photons are sent to spectrograph after the collective device. A transmission grating is applied to separate Raman photons by wavelength and these separated photons are passed to the CCD detector separately. The intensity of the Raman signals at each wavelength is recorded by the CCD detector and the data is plotted as the Raman spectrum.


**Figure 2.13.** JY Horiba Labram Aramis imaging confocal Raman microscope used in this thesis, located in the Begbroke science park, Department of Materials, University of Oxford.

In a typical Raman spectrum of graphene, normally three types of characteristic peaks will appear, namely D, G, 2D peak. The origin of D peak comes from vibration mode of the hexagonal carbon ring, providing the information about defect in graphene. The vibration of the $sp^2$ carbon bond is the origin of G peak, The 2D peak is the second overtone of the defect induced D mode, providing the electronic and geometrical structure through double resonance process.[180] This 2D peak is a characteristic peak to distinguish graphene from graphite.[180] The FWHM of 2D peak and the intensity ratio between 2D and G peak can be used to distinguish monolayer graphene from few layer graphene. [181]

Raman spectroscopy is a powerful and non-destructive tool to study the structure of nanomaterials. In this thesis, Raman spectroscopy is used as a supplementary tool to characterize the structure of 2D atomic crystals. The instrument of the JY Horiba Labram Aramis imaging confocal Raman microscope, which is used in this thesis, is presented in figure 2.13. The spot size of the instrument is about 1 μm. Two lasers are equipped with this instrument with 532 nm or 633 nm wavelength. The grating can be switched between 600 grooves/mm and 1800 grooves/mm. It means the 600 grooves/mm grating will generate smaller solid angle on the chip and makes the light more focused than the 1800 grooves/mm grating. Smaller grating will give higher signal to noise ratio but lower resolution.

#### 2.2.3.3. Photoluminescence Spectroscopy

Luminescence is emission of light by a substance not resulting from heat. Thus, it is a form of cold body radiation. Photoluminescence (PL) is a type of luminescence as a result of absorption of photons. There are two type of PL, namely, fluorescence and phosphorescence. Fluorescence is one type of PL, in which the emitted photons are of lower energy than those absorbed. Phosphorescence is another type of PL, in which fluorescence is delayed after initial absorption of radiation on a scale of seconds to hours.

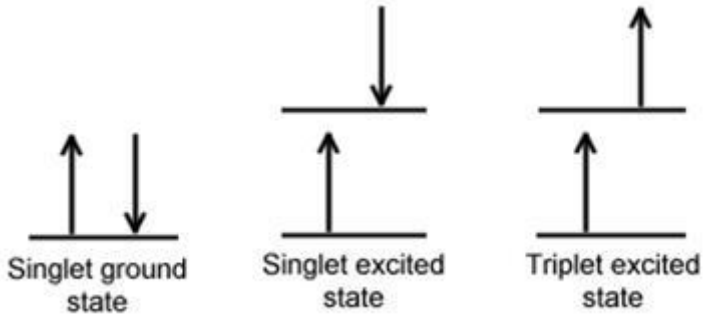


**Figure 2.14.** Singlet and triplet energy levels. Image reprinted from reference [182]

What is the physical principle of these two processes? The electronic states of most molecules can be divided into singlet states and triplet states. Singlet states are the state when all the electrons in the molecule are spin-paired in one orbital due to the Pauli Exclusion Principle. The total spin angular momentum of singlet state is 0.[183] Triplet state is the state when a set of electron spins is unpaired which means the total spin angular momentum is 1.[182-183] Figure 2.14 shows the schematic of ground singlet state ($S_0$), excited singlet state ($S_1$), excited triplet state ($T_1$).[182] In the process of fluorescence, when photons are absorbed, a molecule is excited from a vibration level in the electronic ground state to one of the many vibrational levels in the electronic excited states. This excited state is normally the first excited singlet state. A molecule, which is in the high level of the excited state, will quickly fall into the lowest vibration level of this state (first excited singlet state) by losing energy to other molecules by collision. The molecule will also transfer the excess energy to other possible modes of vibration and rotation. Fluorescence occurs when the molecule returns to the electronic ground state ($S_0$) from the excited singlet state ($S_1$) by emission of photon. If the wavelength of the immediately emitted photon is equivalent to the wavelength of

a particular absorbed photon, it is called resonance radiation. If not equivalent, it is called non-resonance radiation. The fluorescence process can be described as the following two steps, indicated in equation (2.24) and (2.25).

Excitation: $S_0 + h\nu_{ex} \rightarrow S_1$ (2.24)

Fluorescence (emission): $S_1 \rightarrow S_0 + h\nu_{em}$ + heat (2.25)

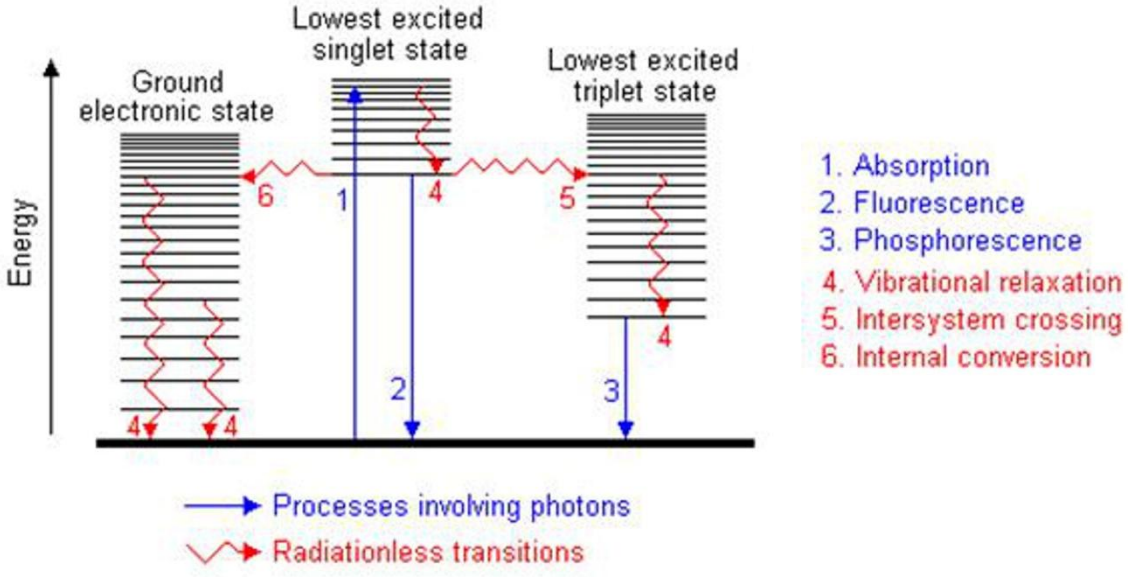


**Figure 2.15.** Possible molecule physical decay pathways following absorption of a photon. Image reprinted from reference [184]

If a molecule, excited by the absorption of photons, does not fluoresce, it must lose its energy in various competing decay pathways. This process is called non-radiative transfer of energy. The possible decay pathways of a molecule excited by a photon are shown in figure 2.15. One of the non-radiative decay is the intra-molecular redistribution of energy between possible electronic and vibrational states. This process is indicated in figure 2.15 via pathway 1, 6, and 4. The excited molecule decays to the electronic ground state via this non-radiative pathway. The excess energy is

converted to vibrational energy via internal conversion process, and thus the molecule is placed in the extremely high level vibrational state of the electronic ground state. This excess vibrational energy is lost by collision with other molecule via vibrational relaxation process, in which heat will be generated. Another non-radiative decay pathway is the combination of the intra and inter-molecule energy redistribution. After the molecule is excited to the excited singlet state, the spin of the excited electrons can be reserved via intersystem crossing, which is the transition between the excited singlet states ($S_1$) to triplet state ($T_1$). The triplet state is of the lower electronic energy than the excited singlet state. Thus, the transition from triplet state ($T_1$) to singlet state ($S_1$) is forbidden. The possibility of this $S_1$ to $T_1$ transition is increasing if the vibrational levels of these two states overlap. For instance, the lowest singlet vibrational level can overlap with one of the higher vibrational levels of the triplet state. The molecule in the high level of the triplet state can lose its energy by the collision with solvent molecules, and then decay to the lowest level of the triplet state. As the transition from the triplet state back to the singlet ground state is classically forbidden but can still occur in quantum mechanics with kinetically unfavoured. The energy is trapped in the triplet state. But the decay pathway can then followed by subsequently relax via phosphorescence or by a secondary non-radiative relaxation step. For the secondary non-radiative step, the molecule undergoes a second intersystem crossing from the lowest triplet state to a high vibrational level of the electronic ground state. Finally, the molecule returns to the lowest vibrational level of the electronic ground state by vibrational relaxation. For the phosphorescence decay, the molecule in

the excited triplet state may not always use the intersystem crossing to return to the ground state. It could lose energy by emission of a photon. This $T_1$ to $S_0$ transition is much less probable than the $S_1$ to $T_1$ transition. The process of phosphorescence can be described with the following equation (2.26).

$$S_0+h\nu \rightarrow S_1 \rightarrow T_1 \rightarrow S_0+h\nu' \quad (2.26)$$

Internal convention, vibrational relaxation, and other radiationless transfer of energy compete so successfully with phosphorescence that phosphorescence is usually seen only at low temperature or in highly viscous media.

In principle, there are some similarities between Raman scattering and photoluminescence process. In both cases, a photon with frequency different from incident photon is produced and the molecule is excited to the higher energy level and then to the lower energy level. The major difference between these two is that Raman scattering can take place for any frequency of the incident light. In contrast to fluorescence, which is associated with specific optical excited state, Raman scattering is not a resonance effect, in which the transition from vibrational states to virtual state and then back can be any pathway and not associated with specific vibrational states. Practically, this means a fluorescence peak is anchored with specific excitation frequency, while a Raman peak is independent of excitation frequency. This can be used to distinguish Raman scattering peak from PL peak. Only thing it needs to do is to vary the excitation energy to see

whether this peak shift or not. If the peak shifts, it is a PL peak, otherwise, it is a Raman scattering peak in the spectrum.

Photoluminescence spectroscopy is an important non-destructive technique to measure the spontaneous emission of light from a material under the optical excitation. The excitation energy and intensity can be chosen to probe different excitation types and also different parts of the sample. The PL spectrum reveals transition energies and the PL intensity gives a measure of the relative rates of radiative and non-radiative recombination. Variation of the PL intensity gives a measure of the relative rates of radiative and non-radiative recombination. Under the pulsed excitation, PL intensity transients yield lifetimes of excited states. This method is called time-resolved photoluminescence. This is useful to measure the carrier lifetime in semiconductors.

What are the applications of PL spectroscopy? It can be used for band gap determination, impurity levels, defect detection, and probing recombination mechanism. The most common radiative transition in semiconductors is between states in the conduction band and valance band. PL can be used to determine the band gap transition. Radiative transitions in semiconductors can also involve localized defect levels. For the detection of defect and impurity levels using PL spectroscopy, the PL energy associated with these levels can be used to identify specific defects, and PL intensity can be used to determine their concentration. PL can also be used to study the recombination

mechanism. The excitons recombination can involve both radiative and non-radiative process. The PL intensity and its dependence on the level of photo-excitation and temperature are directly related to the dominant recombination process. Analysis of PL helps to understand the underlying physics of the recombination mechanism.


**Figure 2.16.** A PL set up used in this thesis, located in 12/13 parks road, department of materials, University of Oxford.

A typical PL setup consists of three parts, the excitation source, the lens system, and the detection system. One of the PL set-ups used in this thesis is presented in figure 2.16. The excitation source could be continuous wave (cw) laser or tunable optical parametric oscillator laser or the

Xe/halogen lamp depending on the required excitation power and whether laser pulse is needed. The monochromator is equipped with the excitation source to select narrow band of the radiation wavelength. After generating from the excitation source and selected by monochromator, the photons get more focused by wavelength and then pass the filter for the further selection of particular range of wavelength and blocking the remainder. Various types of filters can be used in the system, like absorptive filter, dichroic filter, long pass filer, short pass filter, bandpass filter, notch filter, monochromatic filter, polarization filter, infrared filter, ultraviolet filter, neutral density filter. Then the selective wavelength photons then pass to the sample to excite it. The sample could be put in the cryostat to investigate the temperature effect. The emitted photons should be collected along with the perpendicular direction to the excitation beam to avoid re-absorption of the excitation beam. If using a cuvette for the liquid sample, the geometry of the excitation beam and collection of the emission is presented in figure 2.17.

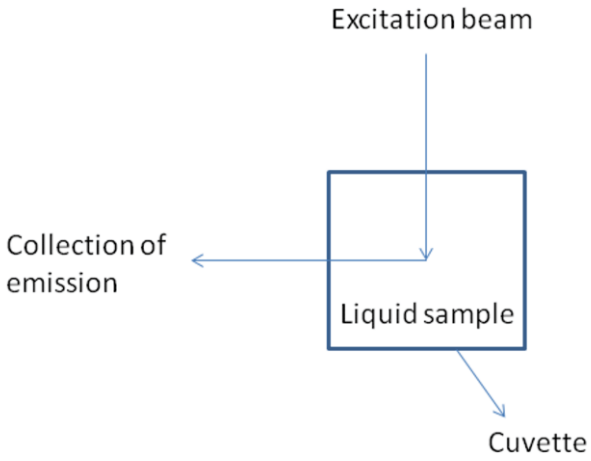


**Figure 2.17.** Schematic diagram of the Geometry used to account for the re-absorption of both the excitation and emission light by the sample in the photoluminescence spectroscopy.

The emission photons will be collected via a designed lenses system and send to the spectrometer equipped with a detector. The detector is a solid state image device capable of performing three essential functions like transducing photons to electrons, integrating and storing, and reading out information via image or spectrum. The coupling between the designed lenses system and detector is important to get PL signals with the best detection efficiency, which is essential for detecting PL signals from the low quantum yield nanomaterials, like carbon nanotubes. The most essential factor to affect the coupling between lenses system and detector is the concept called f number. For a collimated beam entering into a lens, the f number, $f^{\#}$, which is also called "aperture ratio", "focal ratio", "f-ratio", or "relative aperture", relates to the beam waist size and focal length, given by the equation (2.27).

$$f^{\#} = \frac{f}{A} \tag{2.27}$$

Where f is the focal length of the lenses and A is the beam waist size of the collimated beam before entering the lens. For the detector in my setup, the $f^{\#}=4$, which is the technical parameter provided by the Princeton instrument ltd. To give the optimal coupling between the detector and the microscope system (including lenses, filters, in the optical pathway along the emission direction in figure 2.16), it requires satisfying equation (2.28).

$$f^{\#}_{\text{detector}} = f^{\#}_{\text{microscope}} \tag{2.28}$$

Thus, the optimal spectroscopic performance of the InGaAs photodiode array detector requires to attach to a microscope system with an $f^{\#}=4$. The emission beam should be focused on the front slit

on the detector. Considering the larger diameter lens will collect more photons, 2 inch lens is normally used in the system rather than 1 inch lens. This means A=2 inches, which is 50.4 mm. Then the focal length of the lens just before the detector should be $f=A \bullet f^{\#}=200$ mm. Following these rules and considering the geometry of the set up, the design of the lens system could be done.

### 2.2.3.4. Photoluminescence Excitation Spectroscopy

In the previous section, PL spectroscopy has been discussed. As the sister technique of PL, what is the difference between photoluminescence (PL) spectroscopy and Photoluminescence excitation (PLE) spectroscopy? PL spectroscopy is performed at a fixed excitation energy to monitor the luminescence at a wavelength range, while PLE is carried out at a fixed detection energy (emission energy) to monitor the variation of the PL peak intensity at this fixed emission energy. PL provides the information about exciton recombination dynamics, while PLE gives the information about the excited states of optical centres and absorption properties. PLE spectrum is the plot of the changes of PL intensity versus absorbed wavelength. Thus, PLE spectroscopy requires a tunable excitation source, which is normally a lamp and monochromator system. The sample is excited with photons with different wavelengths. These various photons are absorbed by specific optical centres in the sample but decay via a fixed emission decay pathway. The emission wavelength of the PLE spectroscopy, which is used in this thesis shown in figure 2.18, can be fixed at certain wavelength

within the range between 200 nm to 900 nm. The excitation range in this spectrometer is within the range of 200-800 nm.


**Figure 2.18.** JASCO FP-6200 PL/PLE spectrometer used in this thesis, located in 12/13 parks road, department of materials, University of Oxford.

What is the relationship between PLE and UV-vis-absorption spectrum? Although PLE spectrum has similar profile as absorption spectrum, there is some difference between these two. PLE probes optical excited state in the sample while UV-vis-absorption spectrum monitors electronic transitions from ground state to excited state in the molecular orbitals of the sample.

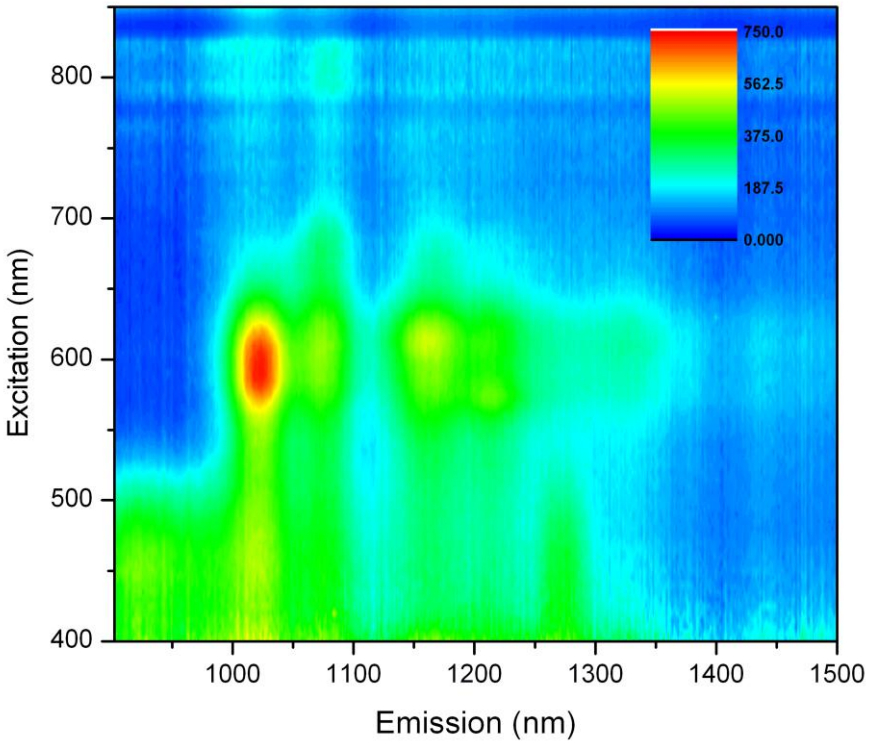


**Figure 2.19.** A PLE measurement of chirality (6, 5) single wall carbon nanotube wrapped with one layer rrP3HT polymer.

The PL spectrometer with linear photodiode array detector can be used to do the PLE mapping, which is the coloured plot of excitation wavelength versus emission wavelength. This provides rich information about the optical properties of the material. Figure 2.19 shows a PLE measurement of chirality (6,5) single wall carbon nanotube wrapped with one layer rrP3HT polymer. The red region is the emission from the nanocomposites material with excitation wavelength $E_{11}$=610 nm and emitted at $E_{22}$=1025 nm wavelength with some emission tails from excess polymer.

### 2.2.3.5. UV-vis-Absorption Spectroscopy

Absorption spectroscopy is one of the important optical spectroscopic techniques that measure the absorption of radiation, as a function of frequency or wavelength due to the light-matter interaction. The absorption in the ultraviolet or visible region directly affects the colour of the molecules due to the electronic transitions. This technique is complementary to PL spectroscopy, in which fluorescence deals with electronic transitions from the optical excited state to the ground state while absorption involves electronic transitions from the ground state to the excited state in the molecule orbital.

Excitation of electrons in chemical bonds ($\pi$ or $\sigma$) or other non-bonding valence electrons (n electrons) is one of the results of the absorption of UV-vis-radiation of a suitable wavelength. Absorption will thus be dependent on the availability of $\pi$ and $\sigma$ bonds or n electrons that can absorb incident radiation. Three types electrons involves in the transitions of UV-vis-absorption. Sigma bond ($\sigma$) is one type of covalent bonds, which are head-on overlapping between atomic orbitals. Sigma bond is a saturated single bond, in which the bonding electrons are called $\sigma$ electrons, for example all the bonding electrons in methane are $\sigma$ electrons. Another type of covalent bond is $\pi$ bond, where two lobes of one atomic orbital overlap with two lobes of the other involved atomic orbital. The two orbitals share a nodal plane which passes through both of the involved nuclei. The electrons involved in the formation of this unsaturated $\pi$ bond, for example double or triple bond, are called $\pi$ electrons. Electrons in the valence shell that are not used up in

the chemical bonds are referred as nonbonding electrons (n electrons), which are unpaired electrons. The possible electronic transitions involve σ, π, n electrons are shown in figure 2.20.[185]

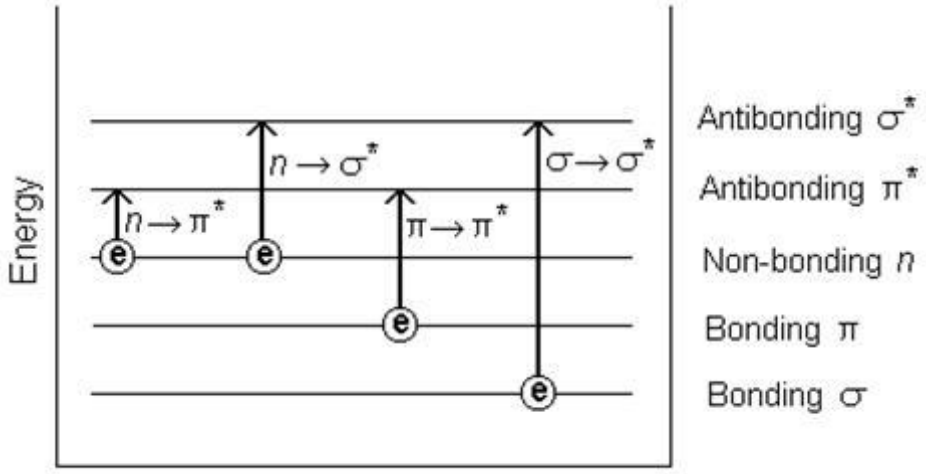


**Figure 2.20.** Electronic transitions of σ, π, n electrons. Image reprinted from reference [185]

During these transitions, $\sigma \rightarrow \sigma^*$ transition requires very high energy which occurs in vacuum UV region (125-185 nm). This high energy could break the σ bond and destroy the molecule. Thus, this transition is not useful. The $n \rightarrow \sigma^*$ transition occurs at about 185 nm and of low energy, however, most solvents strongly absorb in this region, which precludes the use of this transition for the studies in aqueous and other solvents with nonbonding electrons. Therefore, it is impractical to use UV-vis-absorption spectroscopy to determine the analytes based on this $n \rightarrow \sigma^*$ transition. The $n \rightarrow \pi^*$ transition requires very little energy and seem to be potentially useful. Unfortunately, the absorptivity of this transition is very small which precludes its use for sensitive quantitative analysis. The $\pi \rightarrow \pi^*$ transition turns out to be very useful since it requires reasonable energy and has good absorptivity. As discussed above, most of the features in UV-vis-absorption

spectrum is based on the $n \rightarrow \pi^*$ transition or $\pi \rightarrow \pi^*$ transition, which normally happens for organic compound.

The absorption of UV or visible radiation corresponds to the excitation of outer electrons. Besides the transition involving π, σ, and n electrons, another two transition types result from UV-vis-absorption, namely, transition involving charge-transfer electrons, and transitions involving *d* and *f* electrons. In a charge-transfer complex, in which one of its components donates electrons to another component as electron acceptor, the absorption of the UV radiation involves in this electron transfer from the donor to an orbital associated with the acceptor. In the compound containing transitional metal elements, the transitions among *d* and *f* orbitals can be driven by the absorption of UV radiation.

Molar absorptivity ε is the intrinsic property of materials, which describe how strongly a chemical species absorb light at a given wavelength. This ε is a constant in a given solvent at a particular temperature and pressure. It depends on the electronic distribution of the material in the given medium.[186] Electrostatic interaction taking place in the solvent will affect the electronic distribution of the materials, and thus influence the molar absorptivity.[186] When an electromagnetic wave travels through a medium, in which it gets absorbed, it undergoes exponential decay as described by Beer-Lambert law in equation (2.29).

$$A = -\log_{10}(I / I_0) = \varepsilon c L \quad (2.29)$$

Where A is the measured absorbance, $I_0$ is the intensity of the incident light at a given wavelength, I is the transmitted intensity, ε is the molar absorptivity, c is the concentration of the absorbing species, L is the path length though the sample.

The UV-vis-absorption spectrum will show a number of absorption bands corresponding to structural groups within the molecule. It can be used to determine the band structure, indentify chemicals, and measure the quantity of the compound. This is due to the specificity and quantitative nature of the absorption spectrum. The first transition peak along down the wavelength in UV-vis-absorption spectrum normally associate with band edge transition, which can be used to determine the band gap of the material. Unknown chemicals can be identified by comparing a measured spectrum with a library of reference spectra or by modelling the spectrum from first principle to understand the structure of the molecule. The spectrum can be used quantitatively to determine the amount of materials by applying Beer-Lambert law.

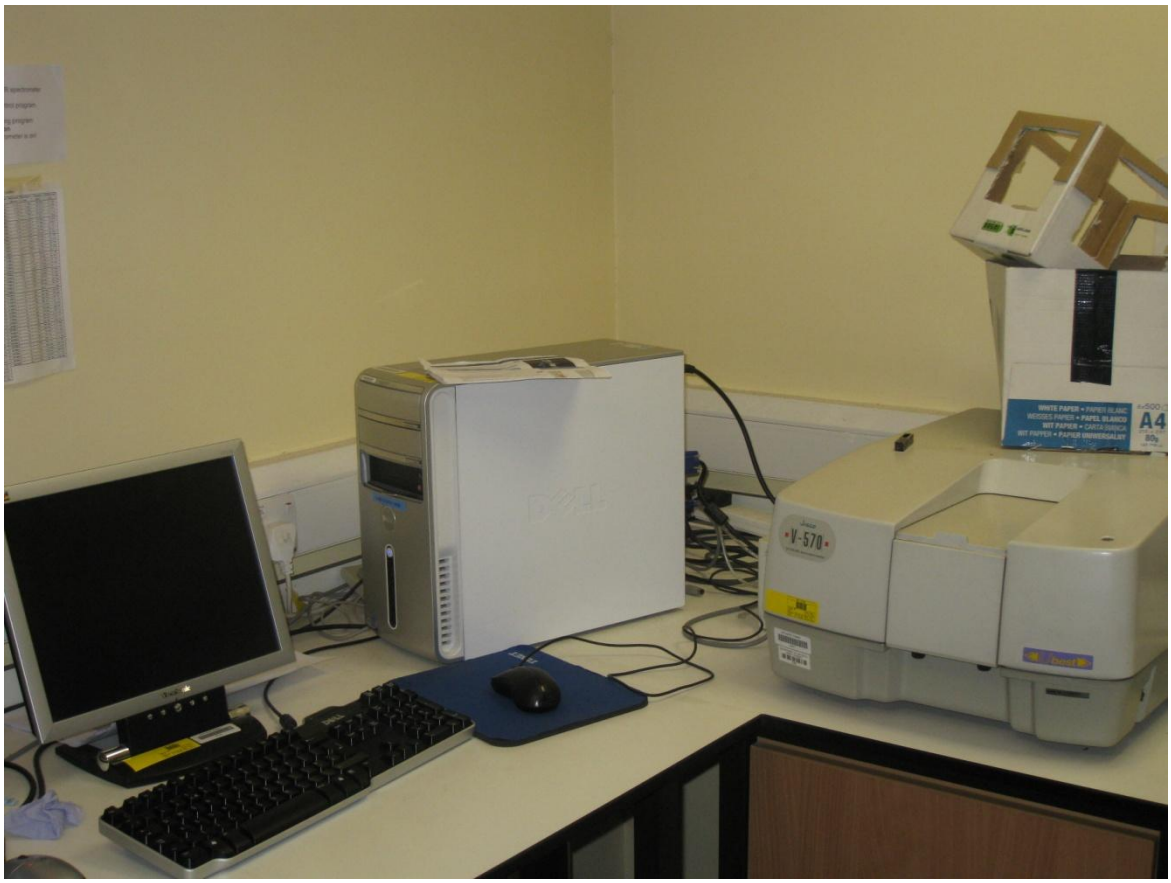


**Figure 2.21.** JASCO V-570 UV/VIS/NIR spectrometer used in this thesis, located in 12/13 parks road, department of materials, University of Oxford.

There are two types of UV-vis-absorption spectrometer. One kind of instrument is to measure the absolute absorbance and plot the absorbance/wavelength spectrum. The spectrometer used in this thesis is JASCO V-570 UV/VIS/NIR spectrometer, which is this type and shown in figure 2.21. It is a double beam system with single monochromator. The light is produced by Deuterium lamp (190~350 nm) and halogen lamp (330 ~900 nm) and then passing through the single monochromator to select the narrow band wavelength of the radiation. Dual gratings are then used to split the beam into two beams to pass through the reference solvent and samples cuvette respectively. Both absolute absorbance values are recorded by the detector. The subtraction of the

reference solvent absorbance from the sample's absorbance as the absolute absorbance of the specimen is recorded and plotted as the absorbance/wavelength spectrum by the single processor. The schematic of this type instrument is shown in figure 2.22(a). Another type of spectrometer is a double beam system with double monochromator. This kind of instrument is to produce the derivative spectrum on time. This online instrumental recording of the derivative spectra involves the use of a dual wavelength instrument with one light source but two monochromator operated at same speed but with a lag of few nm from each other. A chopper will sequentially pass the beams from both monochromator and then pass the sample cuvette. Thus, the difference absorbance $\Delta A$, which is from the sample using two wavelength light $\lambda_1$ and $\lambda_2$, divided by the constant nm lag value $\Delta\lambda$, is recorded versus the average wavelength. The derivative UV-vis-absorption spectrum is then plotted as $\Delta A/\Delta\lambda$ versus $\lambda$. The schematic of this type of instrument is presented in figure 2.22(b). The derivative spectroscopy contains sharper peaks in which better location of peaks and wavelengths maximum could be achieved from the zero crossing of the first derivative. Improved spectral resolution is obtained especially with the second derivative. Spectral features which appear as barely noticeable shoulders in the absolute absorbance spectrum become more prominent. Thus, derivative spectroscopy is excellent for better quantitative analysis and identification of absorbing multi component species in a sample.

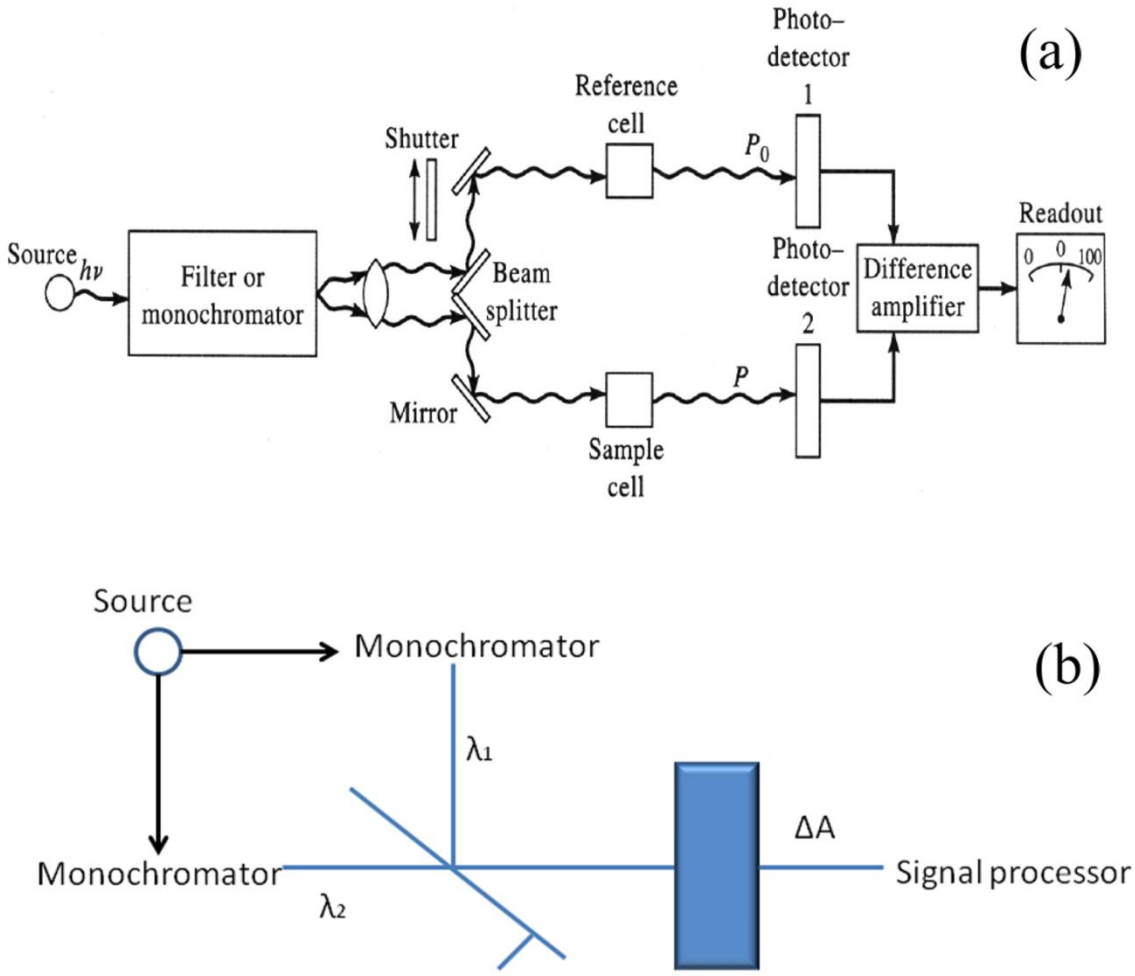


**Figure 2.22.** The schematic of UV-vis-absorption spectrometer instrument (a) absolute absorption spectrometer (b) derivative absorption spectrometer.

## 2.2.4. Electrical Characterization

### 2.2.4.1. Probe Station

Probe station is a flexible tool to measure the electrical properties of semiconductor devices with sharp tips connecting to the contacts in the devices. XYZ transitional stage is utilized to move the positions of probe needles precisely onto the device electrode surface. By sweeping the voltage cross the electrode, current passing through the device is displayed on the oscilloscope as a

function of voltage to produce the IV curve for devices. The gate dependence of the device can also be measured using the probe station by connecting the source, drain and gate of the device with three tips. The various gate voltages should be applied at constant source drain voltage at the same time. The current between source and drain is recorded as a function of gate voltage to present the gate dependence of the device. The probe station could be equipped with magnets to measure the magneto-transport properties. The probe station with laser attachment can be used to measure the electro-optical properties. The temperature of the probe station during the measurements is controlled by cryogenic stage, which is equipped with a sensor and heater to provide fast thermal response and rapid warm up for samples. Active cooling shielding intercepts blackbody radiation before it reaches the sample, ensuring small thermal gradient during the measurements.

The four probe method is also called *Kevin measurement,* after William Thomson, Lord Kelvin. It is an electrical impedance measuring technique that uses separate pairs of current carrying and voltage sensing electrode to make more accurate measurement than the traditional two probe method. The key advantage of Kelvin measurement is to eliminate impedance contributions of wiring and contact resistance. The difference of two probe resistance measurement and four probe resistance measurement is shown in figure 2.23.[187] The current generates a voltage drop across the

wires themselves. To avoid this inaccuracy in the voltage measurement, in the four probe method, voltage is measured immediately adjacent to the target impedance.

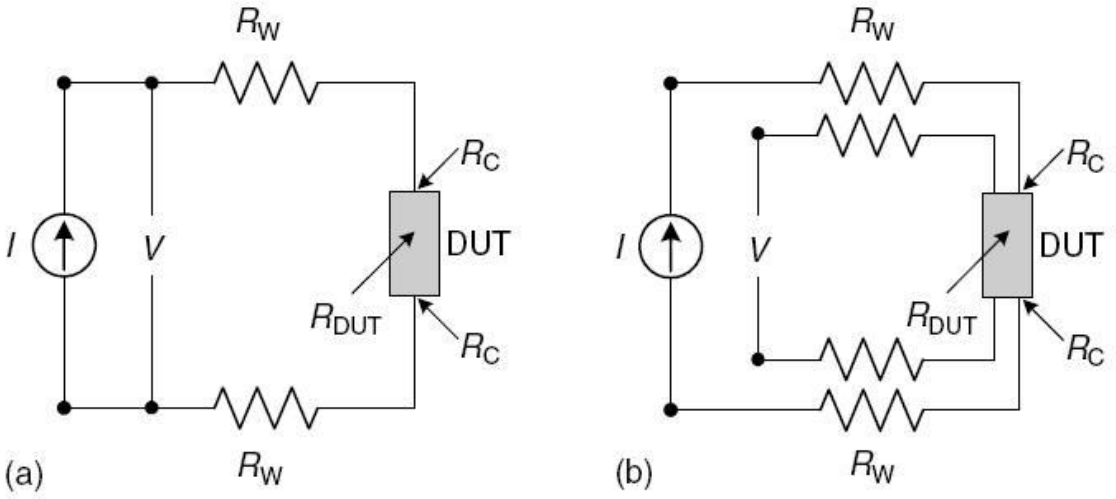


**Figure 2.23.** The schematic of (a) two probe resistance measurement (b) four probe resistance measurement. Image reprinted from reference [187]. Courtesy of Dr. R. Doering, , and Dr. Y. Nishi,

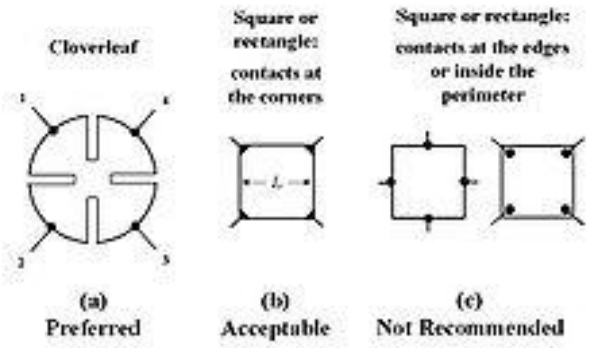


**Figure 2.24.** Some possible contact placements. Image reprinted from reference [188].

The probe station with four probes is normally used to measure the sheet resistance using van der Pauw method. This method is based on the assumption of negligibly small ohmic contacts located on the periphery of the sample. But in reality, contacts have finite dimensions and may not be

exactly on the periphery of the sample. Contacts in the corner introduce less error than placed in the centre of the sample sides. The possible contact placements are shown in figure 2.24.[188]

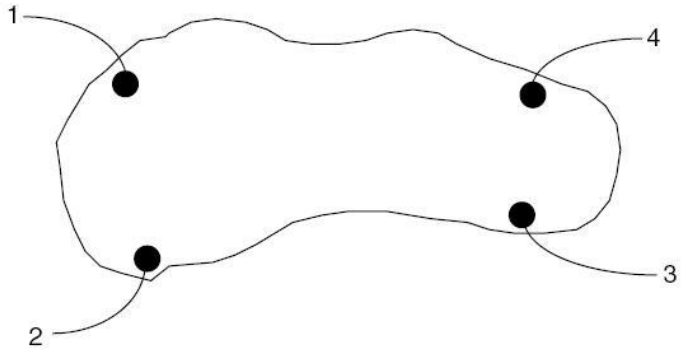


**Figure 2.25.** An arbitrary flat conducting sample with four contacts. Image reprinted from reference [[187]]. Courtesy of Dr. R. Doering and Dr. Y. Nishi.

For the arbitrarily shaped sample, the resistivity $\rho$ is given by the equation (2.30).[189]

$$\rho = 2\pi s F(V/I) \tag{2.30}$$

Where s is the probe spacing and F is a correction factor that depends on the sample geometry. The correction factor F corrects for probe location near sample edges, sample thickness, sample diameter, probe placement, and sample temperature.

For the flat conducting material sample of arbitrary shape, with contacts 1,2,3,4, along the periphery as shown in figure 2.26, the resistance $R_{12,34}$ is defined as equation (2.31).

$$R_{12,34} = \frac{V_{34}}{I_{12}} \tag{2.31}$$

Where the $I_{12}$ is the current flow through contact 1 and contact 2 and $V_{34}=V_3-V_4$ is the voltage difference between the contacts 3 and 4. $R_{23,41}$ is defined similarly. Then the van der Pauw formula can described as equation (2.32).[190]

$$\exp(-\frac{\pi d}{\rho}R_{12,34}) + \exp(-\frac{\pi d}{\rho}R_{23,41}) = 1 \tag{2.32}$$

Where d is the thickness of the sample, $\rho$ is the resistivity. The solution can be written as equation (2.33).[190]

$$\rho = \frac{\pi}{\ln 2} d \frac{\left(R_{12,34} + R_{23,41}\right)}{2} F \tag{2.33}$$

Where F is the correction factor which can be described as the function of the ratio $R_r=R_{12,34}/R_{23,41}$. The relationship between F and $R_r$ satisfies the equation (2.34).[16]

$$\frac{R_r - 1}{R_r + 1} = \frac{F}{\ln 2} ar\cosh\left(\frac{\exp[\ln(2)/F]}{2}\right) \tag{2.34}$$

For the symmetrical samples such as the circle or square shape $R_r=1$, and F=1. Then the sheet resistance $R_s$ can be derived from equation (2.33) and written as equation (2.34) when the sample is symmetrical.

$$R_S = \frac{\rho}{d} = \frac{\pi}{\ln 2} \frac{\left(R_{12,34} + R_{23,41}\right)}{2} \tag{2.35}$$

In order to rule out the thermoelectric potential due to the temperature difference between the two electrodes, the reversed polarity measurement is done by repeating the resistance measurement after switching polarities of both the current source and voltage meter.

$$R_{vertical} = \frac{R_{12,34} + R_{34,12} + R_{21,43} + R_{43,21}}{4} \tag{2.36}$$

$$R_{horizontal} = \frac{R_{23,41} + R_{41,23} + R_{32,14} + R_{14,32}}{4} \tag{2.37}$$

$$R_S = \frac{\pi}{\ln 2} \frac{\left(R_{vertical} + R_{horizontal}\right)}{2} \tag{2.38}$$

Equation (2.38) is normally used in the practical sheet resistance measurement for symmetrical samples. The probe station, which is used in this thesis, is shown in figure 2.26.

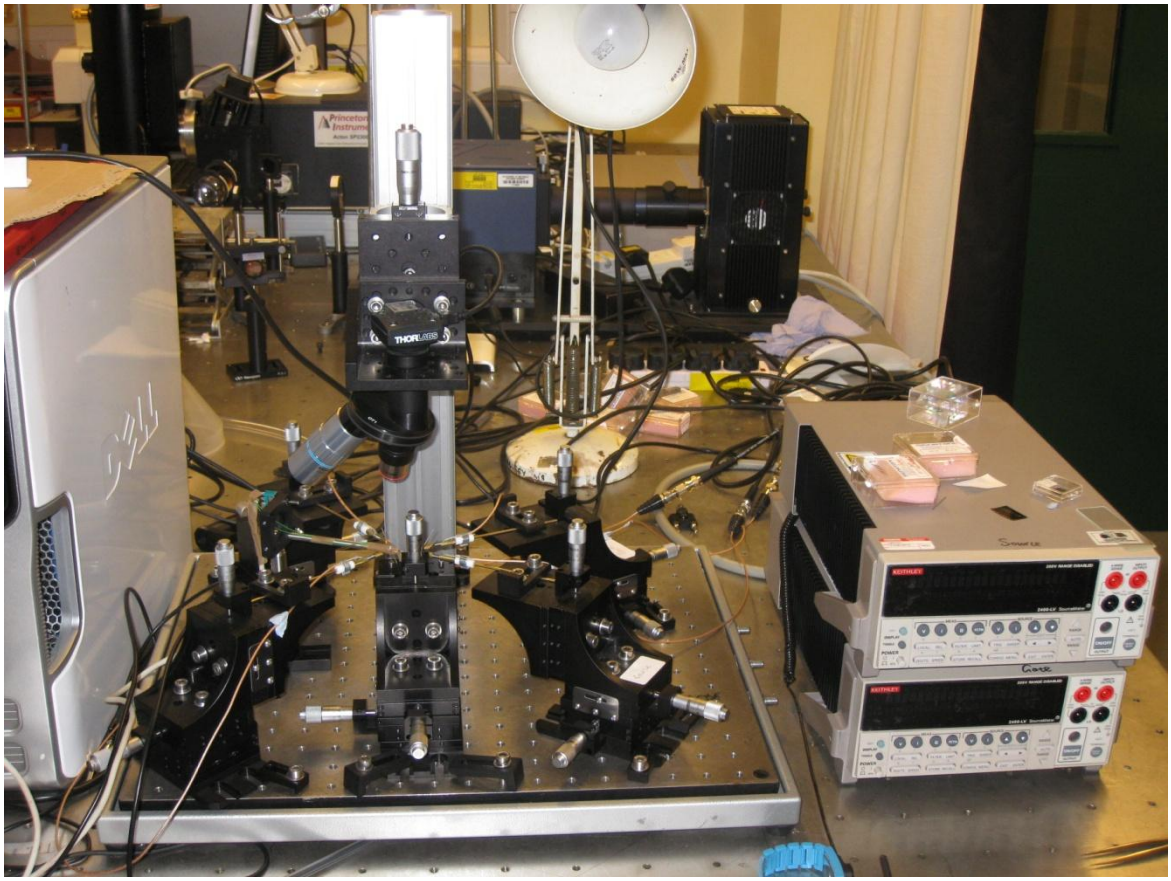

**Figure 2.26.** A custom-built probe station used in this thesis, located in 12/13 parks road, department of materials, University of Oxford.

## 2.3. Theory and Mechanism of Synthetic Methods

### 2.3.1. Colloidal Synthesis of Quantum Dots

#### 2.3.1.1. Introduction

As discussed in the section 1.2.3 of chapter 1, the principle of colloidal synthesis relies on the interplay within a three component system, containing precursors, organic ligands and solvents. The growth dynamics, namely, nucleation and growth stages of colloidal synthesis, as well as the doping strategy of quantum dots, have been discussed in section 1.2.3., chapter 1. In order to lay a foundation to answer open question 1, proposed in section 1.3 of chapter 1, a question about how to control the shape and crystal structure of quantum dots should be answered first. Thus, in this section, the discussion will focus on the mechanism of the shape and crystal structure control of colloidal quantum dots.

#### 2.3.1.2. The Mechanisms of Shape and Crystal Structure Control

Two methods have been applied to control the shape of colloidal quantum dots. One method is to get shape control via the interplays between ligands. The other one is to control the shape by the temperature which can switch the growth region between the thermodynamics and the kinetics driven. These two mechanisms will be discussed in details.

The surface energy of the growing crystal faces is influenced by the surfactant coating. By adjusting the types and ratios of organic ligands, the surface energy of different crystallographic faces can be changed. This will affect the growth velocity of various crystal planes and thus

control the crystal shape.[191-194] In the colloidal synthesis, three types of organic molecules can be chosen for different functions, namely, passivating agent, activating agent, and non-coordinate agent. Passivating agent has the function to alleviate the surface energy of the crystallographic plane, which it binds to, so that the growth velocity of this crystal plane will be slow down. In comparison, the growth velocity of the crystal facet will be speeded up, on which the activating agent attaches to, because the surface energy of the facet will be elevated. Non-coordinate agent is just acting as a solvent to dissolve monomers, precursors, or quantum dots without binding to the quantum dots surface. This non-coordinate agent can act as a stabilizer or adjust the concentration of passivating or activating agent. Different organic molecules are chosen from these three categories to adjust the surface energy of the facet on quantum dots. However, the accurate amount of the surface energy variation should be controlled via choosing appropriate ligands by theoretical calculation first. The number of binding sites on the crystal facet depends on the number of dangling bonds on this crystal plane. However, not all the dangle bonds can act as effective sites for the binding of ligands. Stereochemistry should be considered, such as the steric hindrance effect. For example, if an organic molecule with large configuration groups attaches to one of the binding sites, this large conformation will hinder other ligands bind to the nearby sites. This will affect the growth velocity on this crystal plane due to the decreasing diffusing rate of atoms from the solvent to the plane for the growth. Normally, the longer chain length of the ligand, the slower growth velocity of the plane, which the ligand binds to, due to the steric hinder of the loner

chain.[195] Due to these stereochemical issues, not all the dangling bonds can be satisfied on the crystal planes by the binding of ligands. Thus, the shape control of quantum dots could be done by controlling the concentration of only one type of ligands, either passivating or activating agent, or by controlling the ratios of these two types of ligands. Normally, fatty acid is passivating agent, such as steric acid, phosphonic acid, oleic acid and so on, while fatty amine is activating agent, such as octadecylamine, oleylamine and so on.

Taking as an example, the shape of the CdSe quantum dots has been controlled to form pencil-, arrow-, and tree- like structures by simply changing the concentration of phosphonic acid.[192] On the (001) plane of CdSe quantum dots, there can either be Cd atoms with three dangling bonds or Se atoms with one dangling bond.[192,195] Phosphonic acid can bind strongly to the Cd dangling bonds to passivate it as the cationic character, while acid would passivate Se atoms weakly as the anionic character. Not all the Cd dangling bonds could be passivated by phosphonic acid due to the stereochemical issues.[195] When very low concentration of phosphonic acid is used, there is not enough acid to completely cover any of the crystal facets, hence, the growth of all of the faces takes place at roughly the same rate, resulting in spherical dots with wurtize structure.[192] At medium concentrations of phosphonic acid, the other crystal sides can be passivated by phosphonic acid, but the (001) facet has unsatisfied dangling bonds due to the stereochemistry. Thus, the (001) crystal plane has the fastest growing velocity among all crystallographic planes

due to the existence of unsatisfied dangling bonds which are more reactive, leading to this anisotropic growth of CdSe nanorod.[192,195] At very high molar concentration of phosphonic acid, the differential growth rate between (001) facet and other crystal planes is even larger due to higher area coverage of passivating agent on other crystal planes.[192,195] In this situation, before the deposition of a complete monolayer of atoms, the growth of another monolayer begins. Too many partial monolayers grow on top of one another and then other lower energy crystal faces expose. In order to minimize the surface energy, the crystal then grows on these lower energy crystal faces. The different shapes, such as pencil-, arrow-, and tree-like structures, are formed because the exposure and growth of the low energy faces does not take place at the same time to eliminate the high energy on (001) facet and reduce the overall energy of the crystal.[192,195] The concentration of the phosphonic acid was adjusted by controlling the ratio between phosphonic acid and trioctylphosphine oxide (TOPO), which is acting as an stabilizer.[192]

Also, the shape of quantum dots can be controlled by varying the ratio between passivating agent and activating agent. For example, the shape of Mn doped ZnSe quantum dots has been controlled from branched to spherical by controlling the ratio of stearic acid as passivating ligand and octadecylamine acid as activating ligand. The concentration of this two ligands were varied in order to manipulate the surface passivating and activity coefficients of the monomers.[196] This

discriminating surface energy between different facets leads to the different growth velocity in various crystal planes, resulting in different shapes and crystal phase.

Besides the shape control via the interplay between ligands and crystal facets, the other mechanism for shape control is by manipulating and switching the growth mode between thermodynamics region to kinetics region. Two key factors that influence whether a reaction undergoes kinetic or thermodynamic growth are the temperature and concentration of monomers.[195] If the concentration of the monomer is within the focusing regime, which has been described in section 1.2.3, chapter 1, then the temperature is the key factor for this mechanism.

In order to understand why the temperature is the key to manipulate the growth between thermodynamics driven and kinetics driven, it is necessary to realize that the growth of nanocrystals is based on the diffusion and rearrangement of atoms, which are decomposed from the precursors. Thermal barrier is the decisive factor for these three steps during nanocrystal growth, namely, decomposition, diffusion and rearrangement. The cohesive energy per atom has strong correlation with the decomposition temperature of the solids.[161] However, the temperature for the reaction should be high enough for the diffusion and rearrangement of the atoms for the nanocrystal growth. Obviously, increasing the temperature will increasing the diffusion rate of the atoms. This will favours the nucleation and growth of nanocrystals since the atoms will be more

energetic to mobilize and assemble into crystals. A typical chemical reaction could be described as equation (2.39).

$$nC + mD \xleftrightarrow{k_1, k_2} pE + qF \tag{2.39}$$

Where $k_1$ is the reaction rate coefficient for the forward reaction and $k_2$ is the reaction rate coefficient for the reverse reaction. The reaction rate $r_1$ for the forward reaction can be written as equation (2.40) and for the inverse reaction rate $r_2$ can be expressed as equation (2.41).

$$r_1 = k_1[C]^n[D]^m \tag{2.40}$$

$$r_2 = k_2[E]^p[F]^q \tag{2.41}$$

In which [C] is the molar concentration of reactant C, similar for reactant D, and product E and F. The reaction rate coefficient k can be expressed as Arrhenius equation in equation (2.42).

$$k = Ae^{-E_a / RT} \tag{2.42}$$

Where A is the constant pre-factor, R=8.83144J/mol·k is the universal gas constant, T is the temperature. $E_a$ is the activation energy, which is defined as the energy that must be overcome in order for chemical reaction to occur. The value for A and $E_a$ depends on the reaction. When $r_1=r_2$, chemical equilibrium is reached and the concentrations of the reactants and products no longer change. When $r_1>r_2$, the forward reaction happens.

The kinetics is concerned about the rate of a chemical reaction, while thermodynamics determines to which extend the reaction occurs. The driving force for the chemical reaction in

thermodynamics description is the change of Gibbs free energy ($\Delta G$) of the reaction. When $\Delta G=0$, the thermodynamic equilibrium reaches. When $\Delta G<0$, the forward reaction happens spontaneous. However, even thermodynamically the forward reaction can happen, if the reaction rate is too slow, in practical, the reaction will not happen. Normally, if a reactant can produce two different products, the thermodynamically stable one will be produced as it is more stable than the kinetically controlled product. At this condition the reaction is located in the thermodynamics controlled regime. However, if the rate of the reaction is high enough, the reaction will be controlled by the kinetics and the product which grows faster (kinetically controlled product) will be produced. At this condition, the reaction is located in the kinetics controlled regime. Thus, the key to switch from the thermodynamics controlled regime to kinetics controlled regime is to increase the reaction rate. According to Arrhenius equation (2.42) and reaction rate equation (2.40), if the temperature is increased, the reaction rate coefficient k will increase, leading to the increase of the reaction rate r. In reverse, decreasing the temperature will switch from kinetics controlled regime to thermodynamics controlled regime. Thus, by manipulating the temperature, the reaction can be switched between thermodynamics growth mode and kinetics growth mode. From equation (2.40), the increasing of the monomer concentration will also increase the reaction rate. Thus, manipulating the concentration of the monomer is another way to switch the growth mode between thermodynamics and kinetics controlled regime.

In principle, by using this method, the growth can be controlled to yield more complex structures such as inorganic dendrimers.[195] For example, in the thermodynamic controlled regime, CdSe quantum dots would promote the formation of zinc blende nanocrystals with spherical or tetrahedral structure,[192] which is thermodynamically stable product. On the other hand, in the kinetic controlled regime, the formation of wurtzite phase CdSe nanocrystal would be preferred with rod or arms structure.[192] Thus, if the reaction first is set in the thermodynamic controlled regime, zinc blende spherical nuclei would form. Then the reaction is switched to kinetic controlled regime, wurtzite arms will form out of the (111) faces of the original zinc blende nucleus.[192,195] Hence, the CdSe tetrapod is formed.[192,195] Assuming the reaction is switched back to the thermodynamic controlled regime, the zinc blende tetrahedral will form on the ends of the wurtzite arms.[195] In principle, this cycle would be repeated to produce even more complex dendrimers.

### 2.3.2. Liquid Phase Exfoliation of Boron Nitride

#### 2.3.2.1. Introduction

As discussed in section 1.2.2, chapter 1, liquid phase exfoliation is a promising method to produce uniform single crystalline thin BN sheets in large quantity. It is a cheap and straightforward method for producing 2D atomic crystals.[66, 197] Practically, in order to exfoliate *h*-BN into thin sheet, the right organic solvent, whose cohesive energy matches the surface energy of the *h*-BN

bulk crystal, breaks into the crystal when high intensity ultrasound sonication energy is applied. This sound energy is provided to the organic molecules to overcome the Van der Waals force between layers and will increase the layer to layer distance in BN precursor. This will eventually exfoliate *h*-BN into thin BN sheets. Thus, the key to fabricate thin BN sheets by liquid phase exfoliation is to find the appropriate organic solvent. Before answering the open question 2, proposed in section 1.3, chapter 1, the question about what solvent will lead to the liquid phase exfoliation of BN should be answered first. Thus, the theory of liquid phase exfoliation is discussed here in order to find the appropriate solvent for liquid phase exfoliation of BN.

#### 2.3.2.2. The Theory of Liquid Phase Exfoliation

In theory, this liquid phase exfoliation method can be explained thermodynamically. This exfoliation can only occur if the net energetic cost is minimized.[66] An approximation of this energy cost is expressed as the enthalpy of mixing per unit volume, namely as $\Delta H_{mix}/V_{mix}$.[66] For the effective exfoliation, several factors of the solvent molecule will play an important role, including the size, surface energy, bonding energy, steric hindrance of the molecule. As an approximation, only the surface energy of the solvent molecule will be taken into account. In thermodynamics, the enthalpy of mixture could be written as equation (2.43).

$$\Delta H_{mix} = \Delta G_{mix} + T\Delta S_{mix} \tag{2.43}$$

where $\Delta H_{mix}$ , $\Delta G_{mix}$ , T, $\Delta S_{mix}$ are enthalpy, Gibbs free energy, absolute temperature, entropy of

mixing respectively. As the exfoliation is not a spontaneous forward reaction, $\Delta G_{mix} \geq 0$ is for the exfoliation. The minimum of $\Delta H_{mix}$ would achieve if $\Delta G_{mix}=0$. Thus the liquid exfoliation could occur when $\Delta H_{mix}$ satisfy equation (2.44).

$$\Delta H_{mix} \approx T\Delta S_{mix} \tag{2.44}$$

The enthalpy of mixing could be given by the equation (2.45).[66]

$$\Delta H_{mix} = E_1^{BN} + E_1^{Sol} - (E_2^{BN} + E_2^{Sol} + E_2^{BN-Sol}) \tag{2.45}$$

where $E_1^{BN}$ is the energy required to separate all BN sheets to infinity, $E_1^{Sol}$ is the energy required to remove all the solvent molecules to infinity, $E_2^{BN}$ is the energy retrieved by bringing the BN sheets back from infinity to form N flakes of thickness, $E_2^{Sol}$ is the energy released by bringing the solvent molecules back from infinity to form a liquid but leaving voids to accommodate the reconstituted flakes, $E_2^{BN-Sol}$ is the interfacial energy between BN and solvent molecule associated with placing in the voids.

The enthalpy of mixing per unit volume could be derived from equation (2.45) by making a few approximations and written as equation (2.46).[66]

$$\frac{\Delta H_{mix}}{V_{mix}} \cong \frac{2}{T_{flake}}(\delta_{BN} - \delta_{Sol})^2 \phi \tag{2.46}$$

where $V_{mix}$ is the volume, $\delta_i = \sqrt{E_{sur}^{i}}$ is the square root of the surface energy of phase i. $T_{flake}$ is the thickness of a BN flake and $\phi$ is the BN volume fraction. This equation (2.46) shows the enthalpy of mixing, which is the index of the viability of exfoliation, depends on the balance of the BN and solvent surface energies. For exfoliation of *h*-BN, the surface energy is defined as the

energy per unit area required to overcome the van der Wass forces when peeling two sheets apart. The surface energy of BN, $E_{sur}^{BN}$ is found to be 44~66 mJ/m$^2$.[197, 198] For the solvent, which needs to be chosen, the surface energy $E_{sur}^{Sol}$ is related to the surface tension γ, which can is expressed in equation (2.47).

$$\gamma = E_{Sur}^{Sol} - TS_{Sur}^{Sol} \tag{2.47}$$

Where T is the absolute temperature and $S_{Sur}^{Sol}$ is the solvent surface entropy, which is a generic liquid property that tends to have values in the range 0.07-0.14 mJ/m$^2$k.[66] The surface tension γ can be determined experimentally by the capillary rise method. This method is based on a phenomenon called capillary action, the nature for the liquids to rise in the narrow tube. Experimentally, the surface tension γ can be measured with the equation (2.48).[199]

$$\gamma = \frac{\rho g a h}{2\cos\theta} \tag{2.48}$$

where $\rho$ is the liquid density, $g$ is the acceleration due to the gravity, $a$ is the radius of the tube, $h$ is the height of the liquid column, $\theta$ is the contact angle. Thus, practically, the surface tension can be calculated by measuring the distance of capillary rise and the contact angle between the meniscus and capillary wall.

By combining the equation (2.47) and (2.48) together, the surface energy of the solvent $E_{sur}^{Sol}$ can be measured. From equation (2.47), the surface energy of the appropriate solvent for exfoliation of BN is expected to matches the surface energy of the BN, which is around 44~66 mJ/m$^2$.[197,198] Thus,

by using this method, the appropriate solvent for exfoliating BN can be found, in which 1-Methyl-2-pyrrolidinone (NMP) is a good candidate.

### 2.3.3. Chemical Vapour Deposition of Graphene

#### 2.3.3.1. Introduction

As discussed in section 1.2.1, chapter 1, chemical vapour deposition (CVD) is a promising method to produce high quality graphene scalable in industry with relatively low cost. However, the polycrystalline nature of graphene produced by this method has affected mobility of the graphene film compared to the mechanical exfoliated graphene. In order to fabricate the large area single crystalline graphene by CVD for commercial applications, a novel method should be found. The discussion here is to review the mechanism study on Cu or Nickel catalyzed CVD graphene in the literature to lay out a foundation before answering the open question 3 and 4, which are proposed in section 1.3 in chapter 1.

#### 2.3.3.2. The Mechanism of CVD Graphene

The principle of CVD has been discussed in section 1.2.3., chapter 1, when the discussion of the synthesizing quantum dots using CVD has been made. It is similar principle for CVD graphene. The vaporized precursors are introduced into CVD furnace and absorbed molecules will either thermally or catalytically decompose and then react with other gases to form graphene. Three

stages could be considered during the CVD process. First, it is the mass transport of reactants to the growth surface via a boundary layer by diffusion. Second stage is chemical reactions on the growth surface. Thirdly, it is the removal of gas-phase reaction by-products from the growth surface. Although the synthesis of graphene by CVD has been done on various transition metals as the catalyst, such as copper,[97] nickel,[34, 98-99] on the (0001) face of ruthenium,[100-101, 200] and on the (111) face of iridium,[103] copper or nickel are the most promising candidates for large scale fabrication in industry for commercial application considering the cost. The discussion of the mechanism in this section shall be more focused on copper or nickel, especially on copper. Similar as the discussion on the mechanism of the synthesizing quantum dots and BN, the discussion on the mechanism of CVD graphene shall be focused on the thermodynamics, kinetics and the interplay between graphene and the substrate.

The procedure of CVD graphene on Cu or Ni is similar, in which normally methane is used as the carbon source mixed with hydrogen and argon. After annealing and reduction to treat the transitional metal, the vaporized precursor is decomposed at the target temperature over the catalyst, leading to the carbon deposition onto the catalytic surface. After the chemical reaction on the catalytic surface, the subsequent cooling is applied and then the graphene appears on the metal surface.

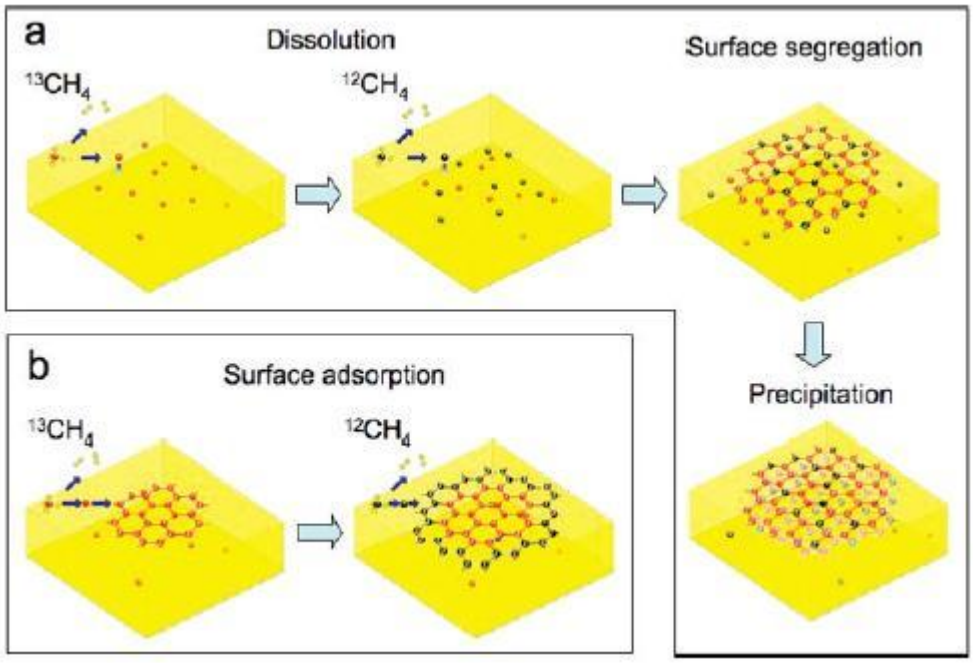


**Figure 2.27.** Growth mechanism of LPCVD graphene on Cu and Ni. The location of carbon isotopes after sequential gas flows of isotopes of methane on a grown graphene film informs which growth route was taken. (a) Ni catalyzed CVD: Isotopes mixed together suggest a surface segregation followed by precipitation pathway. (b) Cu catalyzed CVD: whilst distinct zones of isotopes would suggest surface adsorption. [[113]] (Reprinted with permission from ref 113. Copyright 2009 American Chemical Society)

From a thermodynamics point of view, a question is raised that how the reaction happens and to what extend the reaction occurs. In order to answer this question, investigation has been made by using mixed isotopes of carbon ($^{12}C$ and $^{13}C$) in the precursor methane gas to elucidate the different growth mechanism of Cu or Ni catalyzed graphene.[113] Figure 2.27 summarize the growth mechanism model from a thermodynamics point of view.[113] Equilibrium segregation refers to the thermodynamic equilibrium process by which lattice disorder or impurities diffuse out of the lattice and towards grain boundaries in order to minimize the overall free energy of the system.[201-202] The extend of equilibrium segregation effect decreases with increasing temperature as it is the

lowest energy state in the system. In contrast, the magnitude of non equilibrium segregation increases with increasing temperature and the alloy can be homogenized because its lowest energy state corresponds to a solute distribution. Either equilibrium or non-equilibrium segregation involves with non-phase separation. In comparison, precipitation involves in phase separation. Both precipitation and non-equilibrium segregation in CVD are due to the cooling effect on the surface composition. As described in figure 2.27, the Ni catalysed graphene growth (figure 2.27(a)) follows a surface segregation-precipitation route, while Cu catalyzed graphene(figure 2.27(b)) follows a surface absorption route, in which sequent carbon atoms attach to the previous carbon atoms on the Cu surface to form the honeycomb graphene network. These different routes on Cu and Ni are due to the solubility of carbon in Cu significantly lower than in Ni, perhaps caused by their electronic structure at Fermi level.[203] Thus, carbon is inhibited from diffusing far into the Cu face, and therefore copper effectively acts as the catalyst for decomposition of methane on the surface. In the low pressure CVD, Cu is claimed to have self-limiting effect on graphene.[97] During low pressure condition, when the graphene layer covers copper surface, the catalytic surface is prevented from interacting with methane, and thus inhibit the deposition of further layers, which is called self-limiting effect.[97] In comparison, more carbon can dissolve in Ni, and thus more carbon can precipitate out of the surface, increasing the thickness and decreasing the uniformity of the graphene.

In order for the graphene to nucleate, from a thermodynamics point of view, a minimum temperature, methane flow rate and methane partial pressure needs to be set. By varying these parameters, the graphene nucleation density could be controlled.[112] The hydrogen plays an important role in acting as the activator for the nucleation to happen and also as the etching reagent that controls the size and morphology of the graphene domains.[204] Based on the thermodynamics growth model shown in figure 2.27, the graphene nucleation on Cu proceeds as follows:[112] (1) Exposure of Cu to methane and hydrogen. (2) Catalytic decomposition of methane on Cu to form $C_xH_y$. (3) Depending upon the temperature, methane pressure, methane flow, and hydrogen partial pressure, the Cu surface is either undersaturated, saturated, or supersaturated with $C_xH_y$ species. (4) Formation of nuclei as a result of local supersaturation of $C_xH_y$ species. (5) Nuclei grow to form graphene islands (in the case of undersaturated surface, graphene nuclei do not form). (6) Full Cu surface coverage by graphene under certain temperature, methane flow rate and methane partial pressure.

Based on the thermodynamics model discussed above, the kinetic model similar as the polymerization is shown figure 2.28.[205] From a kinetics point of view to consider the reaction rate, the growth of graphene can be divided into four stages. In the initialization stage, methane is absorbed onto the Cu surface at elevated temperature, and hydrogen atoms are dissociated from the methane molecules to generate reactive carbon radicals on uniform crystal surface or irregularities,

such as stem edges or defects. Hydrogen radicals released by the hydrocarbon species will recombine and form hydrogen at any stages of the reaction. Carbon radicals on the Cu surface will diffuse to combine together to form polycyclic hydrocarbon rings. The edge atoms of the ring serve as growth seeds for other carbon radicals to join together, resulting graphene film. The possible reaction termination point is on the irregularities of the surface, such as grain boundaries and surface textures. The ratio between the reaction rate coefficient for chain propagation $k_p$ and termination $k_t$ can be used to express the size of the graphene domains.

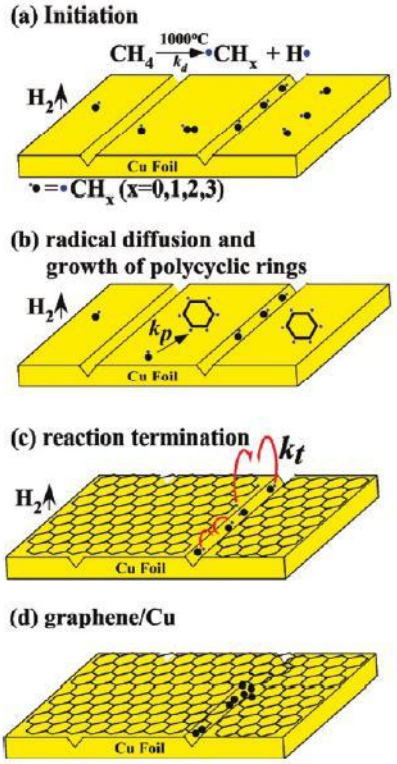


**Figure 2.28.** Proposed reaction pathways, analogous to free radical polymerization, for graphene growth on uneven Cu metal surface during CVD. (a) dissociation of hydrocarbon on heated Cu surface; (b) nucleation and growth of graphene; (c) reaction termination when two active centre react with each other; (d) final graphene with turbostatic structures and amorphorous carbon because of surface roughness. [205] (Reprinted with permission from ref 205. Copyright 2011 American Chemical Society)

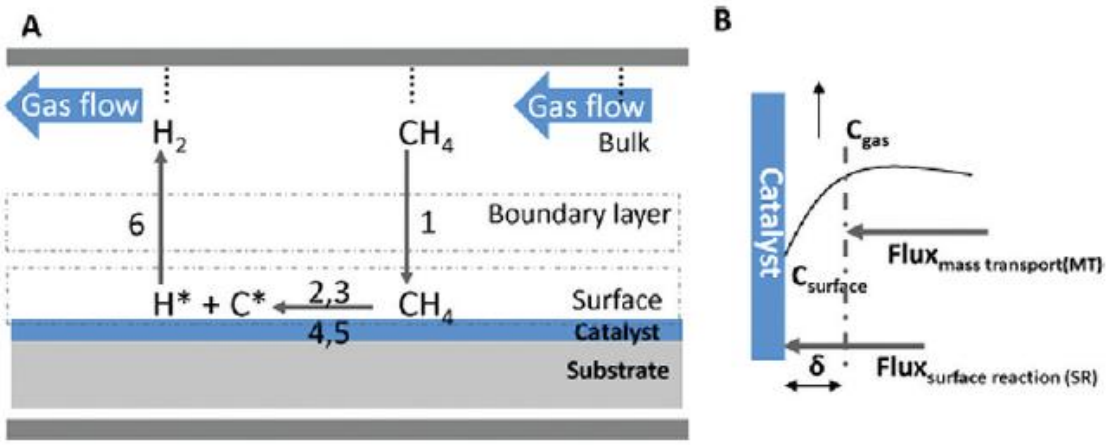


**Figure 2.29.** (a) Processes involved during graphene synthesis using low carbon solubility catalysts Cu in a CVD process (b) mass transport and surface reaction fluxes under steady state conditions. [206] (Reprinted with permission from ref 206. Copyright 2010 American Chemical Society)

Another kinetics model, shown in figure 2.29, based on the three stages of CVD process, namely as mass transport, surface reaction and gas release, is proposed.[206] This model shows the steady state kinetics of the reaction. The processes, shown in figure 2.29, can be described as the following six stages.[206] The carbon species first (1) diffuse through the boundary layer and reach the surface and then (2) absorbed on the surface (3) decompose to form active carbon species (4) diffuse on the surface of the catalyst or into the catalyst close to the surface and form the graphene lattice (5) inactive species (such as hydrogen) get desorbed from the surface to form molecular hydrogen and (6) diffuse away from the surface through the boundary layer and finally swept away by the bulk gas flow.[206] The flux for the mass transport and surface reaction period can be described in equation (2.49) and (2.50).

$$F_{mass\ transport}=k_g(C_g-C_s) \quad (2.49)$$

$$F_{surface\ reaction}=k_sC_s \quad (2.50)$$

where $F_{mass\ transport}$ is the mass transportation flux of the active species through the boundary layer, $F_{surface\ reaction}$ is the flux of the consumed active species at surface reaction (assuming first order kinetics). $C_g$ is the concentration of gas in the bulk. $C_s$ is the concentration of the active species at the surface. $K_g$ is the mass transport coefficient and $K_s$ is the surface reaction coefficient (assuming first-order rate kinetics). The slower process of these two flux is the rate limiting step during the CVD graphene synthesis. As the steady state, $F_{mass\ transport}= F_{surface\ reaction}=F_{total}$, which means no accumulation of active carbon species, the total flux can be written as equation (2.51) by combining equation (2.49) and (2.50) together.

$$F_{total}=\frac{k_sk_gc_g}{(k_s+k_g)} \quad (2.51)$$

When $k_g>>k_s$, it is surface reaction controlled kinetics regime. When $k_s>>k_g$, it is mass transport controlled kinetic regime. When $k_s\sim k_g$, it is the mixed kinetic regime. During the atmospheric pressure (AP) CVD, the mass transport though the boundary layer is the rate limiting step ($k_s>>k_g$), while under the low pressure (LP) CVD the surface reaction is the rate limiting step ($k_g>>k_s$).[206] This can be used to explain why the thickness of APCVD graphene is thicker than the LPCVD graphene and APCVD graphene lost its self-limiting properties.[206] As the mass transportation rate through the boundary layer is dependent on the pressure. The lower pressure leads to the increase in the diffusion rate through the boundary layer, and the surface reaction controlled limited graphene will be self limiting controlled monolayer. This is not the case at

atmospheric pressure when the mass transport of active carbon species is far beyond the surface reaction consumed. Thus, the thickness of APCVD graphene will increase unless to decrease the carbon species supply, which will decrease the flux of the mass transportation via the boundary layer.

Besides the discussion on the thermodynamics and kinetics of the CVD graphene, the interplay between the Cu and graphene needs to be explored as well. However, there is no comprehensive picture on this issue. Some study has shown that the morphology, orientation and defect on the Cu grains have influence on the graphene growth. Possible registry relationship exists between Cu and graphene lattice. A very flat surface morphology of Cu were shown to be the crucial factor leading to enhanced homogeneity and electronic properties of the resulting graphene material.[205] The number of nucleation seeds and graphene domain sizes have correlations with the impurity particles on the Cu surface, which is the origin of the multilayer graphene region.[207] The low pressure CVD graphene in each of the four lobes has a different crystallographic alignment with respect to the underlying Cu substrate.[208] These polycrystalline four lobe graphene islands arise from the heterogeneous nucleation events at surface imperfections, which is controlled by the angular dependent growth velocity.[208] The graphene domains with different orientation registry to the Cu lattice, stitch together to form larger sheets, in which numerous domain boundaries scatter electrons and decrease carrier mobilities through CVD graphene sheets.[209]

## 2.4. Summary

In order to answer the open questions proposed in section 1.3 of chapter 1, chapter 2 has laid out a foundation of methodology before answering these questions in the results chapters. Referring backing to open question 1, in order to synthesis Mn doped ZnSe with controlled shape and crystal structure, the mechanism of shape and crystal structure control in the colloidal synthesis has been discussed in this chapter. In order to examine the relationship between the crystal structure and optical properties, the physical principles of HRTEM and the optical spectroscopies, including PL, PLE, UV-vis-Absorption spectroscopy, have been reviewed, as HRTEM and SAED can provide the information about crystal structure and optical spectroscopies can provide information about the optical properties of the nanomaterials. Regarding the open question 2, in order to fabricate BN 2D atomic crystal, the mechanism of liquid phase exfoliation has been discussed. In order to study the atomic configuration of quantum dots on ultrathin BN sheets, the physical principles of HRTEM imaging and simulation have been discussed. In order to answer the open question 3 and 4, regarding the graphene growth mechanism investigation, the recent research progress on the mechanism of CVD graphene has been reviewed with the point of views from thermodynamics, kinetics and the interplay between the graphene and Cu. For the mechanism study to invent a novel method of fabricating large area single crystal 2D atomic crystals using CVD, a few

characterization methods have been reviewed and discussed, such as SEM for morphology and growth dynamics examination, EBSD for investigating interplay between graphene and Cu, Raman spectroscopy for examining the structural, thickness and defects, probe station for sheet resistance measurement. In summary, in order to answer the open questions, the necessary methodology, including characterization methods and synthetic methods, has been discussed in this chapter and laid out a solid foundation to solve these open questions in the following chapters.

# Chapter 3:

# Shape and Property Control of Mn doped ZnSe Quantum Dots: from Branched to Spherical

## 3.1. Motivation

Open questions have been proposed in chapter 1 and a foundation of methodology has been laid out in chapter 2. In this chapter, open question 1 will be answered. The questions are how Mn doped ZnSe quantum dots can be synthesized with controlled crystal structure and what is the relationship between crystal structure and optical properties of Mn doped ZnSe quantum dots.

The properties of quantum dots, also called semiconductor nanocrystals, can be tuned by the effects of quantum confinement imposed upon excitions.[210-211] Doping atoms in quantum dots give other discrete energy levels in the intrinsic dots, which enrich the energy dynamics of excitons.

This enhances optical, electronic, and magnetic properties of semiconductor nanocrystals,[212-213] which leads to broader applications, such as light emitting devices,[214-216] bioimaging,[217-219] solar cells,[220] and spintronics.[143-144] Although the cadmium chalcogenides, especially CdSe, and the related core/shell nanocrystals, are still the most widely used candidate in the applications of semiconductor nanocrystals, there are some attempts at using cadmium free quantum dots, such as Mn doped zinc chalcogenide quantum dots. Zn-based doped quantum dots have the advantages of lower toxicity, larger stocks shift and enhanced thermal and environmental stability.[196, 221-229] To synthesis Mn doped wurtzite nanocrystals is more difficult comparing than their zinc blende counterpart, due to the self purification mechanism and favourable impurity absorption on (001) facets of zinc blende structure.[212,225,230] Controlling the optical property of Mn doped ZnSe nanocrystals via the controlled synthesis of crystal phase and shape is still challenging. Understanding the correlation between atomic structure and optical properties of doped semiconductor nanocrystals is an important scientific issue for future designing and tailoring of their properties for applications.

Norris *et al*. studied photoluminescence and electron paramagnetic resonance properties of Mn doped ZnSe quantum dots to confirm that the Mn impurities were embedded inside the nanocrystals.[158] Suyver *et al.* found the increasing of $Mn^{2+}$ concentration in ZnSe nanocrystals would lead to the red shift of $Mn^{2+}$ related emission and decreasing the lifetime of $Mn^{2+}$ luminescence.[231] Erwin *et al.* claim the mechanism that controls doping is the initial adsorption of

impurities on the nanocrystal surface during the growth.[212] They claim this doping efficiency is determined by surface morphology, nanocrystal shape, and surfactants in the growth solution.[212] Peng *et al.* present a method to decouple the doping process from the nucleation and growth, which will allow to dope nearly all nanocrystals simultaneously.[221] They also showed the tuneable PL of Mn doped ZnSe quantum dots from 565 nm to 610 nm by nucleation doping strategy.[222] These dots can be made to be water soluble by coating and act as biomedical labels.[223] The shape of the dots can be controlled by varying the concentration ratio of ligands.[196] They also mention that the four elementary processes in doping nanocrystals are surface adsorption, lattice incorporation, lattice diffusion, and lattice ejection.[227] Cao *et al.* show the chemical kinetics of the doping process of the core/shell nanocrystals, which is dopant adsorption, replacement and shell growth.[226] Nag *et al.* show the reason why nanocrystals, especially wurtzite host, resist appreciable level of doping is because the local strain caused by the lattice mismatch between dopant and host.[225] The quantum efficiency decreases exponentially with the increase of the average number of $Mn^{2+}$ ions per nanocrystals.[225] Zeng *et al.* also shows the synthesis of spherical zinc blende Mn doped ZnSe quantum dots without pyrophoric reagents.[232] Panda et al. showed the generation of Mn and Cu co-doped ZnSe quantum dots.[233] Cao *et al.* found the photocatalytic activity and degradation rate of ZnSe microspheres is much higher and faster than the ZnSe commercial powder.[234] Dey *et al.* studied the electroluminescence property of ZnSe quantum dots and demonstrate a potential application of ZnSe quantum dots as colour tuning LED.[235]

Here, a simple method is demonstrated to control the crystal phase of Mn doped ZnSe quantum dots from zinc blende to wurtzite by changing the injection rates of zinc precursor. Also, the shape of Mn doped ZnSe from branched to spherical can be easily tuned by reducing the temperature during growth. It is found that Mn doped ZnSe quantum dots have a higher quantum yield when grown spherically with wurtzite crystal structure. In the synthesis used here, ligands that are in liquid form is used at room temperature instead of ones that are solid at room temperature.[223] At room temperature some ligands that are solid do not completely dissolve during the purification step and these results in them being centrifuged out along with the quantum dots. Thus, by using all liquid ligands instead the purification of the quantum dots is improved to obtain HRTEM images of them. Furthermore, by switching the Zn precursor from Zn Stearate, which is solid at room temperature, to the complex formed by mixing Oleic acid with $ZnCl_2$, a Zn precursor that is in liquid state at room temperature, the reaction temperature can be reduced due to the lower decomposition temperature. To get shape control of quantum dots, it needs to control the kinetics between crystal facets. Most of the previous work gets shape control of nanocrystals by varying the concentration ratio between ligands.[196,161,236] The ligands will selectively adhere to different facet of nanocrystals. The high energy facet will grow more quickly than the low energy facet in a kinetic regime.[161] However, the approach used here to get shape control is to switch between kinetic to thermodynamic growth mode by temperature. This is consistent with the previous work of shape control of intrinsic CdTe semiconductor nanocrystals by temperature.[237] This study will

provide general principles to tune the optical properties via controlled synthesis on the crystal phase and shape of Mn doped ZnSe quantum dots for photonic device, bioimaging and spintronics applications.

## 3.2. Experimental Details

### 3.2.1. Materials

Zinc chloride ($ZnCl_2$, 99.999%), Zinc Stearate ($ZnSt_2$, 12.5-14% ZnO), Oleylamine (technical grade, 70%). 1-Octadecene (ODE), Tributyl phosphine (TBP, 97%), Stearic acid (SA, 95%), Manganese chloride ($MnCl_2$, ~10 mesh, 99.999%), Rhodamine 101, were purchased from Sigma-Aldrich Ltd. Selenium powder (~200 mesh, 99.999%), tetramethylammonium hydroxide (TMAH), Methanol anhydrous (99.9%), were purchased from Alpha Aesar Ltd. Oleic acid and toluene were purchased from Fisher Scientific Ltd. All chemicals were used without further purification.

### 3.2.2. Synthesis of Manganese Stearate ($MnSt_2$)

Manganese stearate ($MnSt_2$) was first synthesized as a manganese precursor. In a typical synthesis, SA (20 mmol) was dissolved in 30 g of anhydrous methanol and heated to 50-60 °C until it became a clear solution and was allowed to cool down to room temperature to get SA solution.

The solution of TMAH was prepared by taking 20 mmol in 10 g anhydrous methanol and mixed with SA solution. The mixture was stirred for 15 minutes in a three neck flask with argon flow to ensure the reaction had gone completely. To this solution, $MnCl_2$ solution of 10 mmol in 10 g anhydrous methanol was added dropwise with vigorous stirring continuing with argon gas flow and a white precipitate of $MnSt_2$ slowly flocculated. The precipitates were filtered with vacuum filtration and washed repeatedly with methanol. Then the white precipitant was dried using under vacuum in a rotary evaporator at 70 °C for 3 hours. Then the white powder of $MnSt_2$ was properly stored in Argon atmosphere.


**Figure 3.1.** The schlenk line set up to synthesis Mn doped ZnSe quantum dots, located in 12/13 parks road, department of materials, University of Oxford.

### 3.2.3. Preparation of Stock Solutions

Tributylphorsphine (TBP) is used to dissolve selenium and form Tributylphorsphine selenium (TBPSe). TPBSe solution was prepared with a schlenk line, shown in figure 3.1, with argon gas flow by dissolving 1.9 g Se into 8 g Tributylphorsphine (TBP). Then TBPSe is diluted with oleylamine, to form a selenium precursor solution. The solution was stored in a bottle with rubber in the argon atmosphere.

Oleic acid acts as surface passivating agent to react with zinc stearate and non-coordinate solvent 1-octadecane (ODE) to form zinc precursor solution. Two types of zinc precursor solution were prepared according to the type of zinc salt used. For the case of $ZnSt_2$, $ZnSt_2$ (1.5 g, 0.002 mol), and 0.5 g Oleic acid were dissolved into 8 g ODE. For the case of $ZnCl_2$, $ZnCl_2$ (0.323g, 0.002 mol), 0.5 g Oleic acid, and 0.5 g Oleylamine were dissolved in 8.5 g ODE.

### 3.2.4 Synthesis of Branched Mn Doped ZnSe Quantum Dots

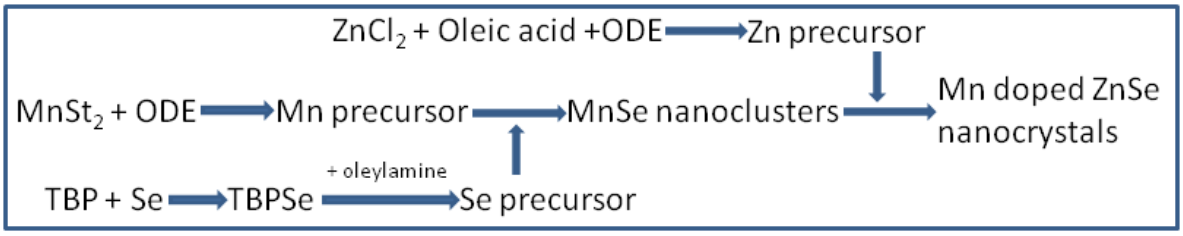


**Figure. 3.2.** Schematic illustration of synthetic procedure to get branched Mn doped ZnSe quantum dots.

The schematic illustration of synthetic procedure is shown in figure 3.2. The schematic setup of solution phase chemistry to synthesis Mn doped ZnSe quantum dots is shown in figure 3.3. Mixture of white Manganese stearate powder and ODE was heated up to get manganese stearate dissolved in non-coordinate solvent ODE at high temperature as the main reaction. In a typical reaction, 0.1 g of $MnSt_2$ and 25 g ODE were loaded in 100 ml three neck flask and degassed under argon bubbling for 15 minutes at 110 °C. Then the flow rate of argon gas was decreased to just keep an argon atmosphere with minimal over-pressure and the temperature of clear brownish manganese precursor solution was increased to 280 °C. At the same time, 1 ml TBPSe stock solution and 1 g oleylamine were mixed under argon gas flow and heat up to 70 °C acting as the selenium precursor. Once the temperature of the main reaction reached 280 °C, in which small nanoclusters of MnSe formed, the selenium precursor was quickly injected into the main reaction. The temperature of the main reaction dropped to 260 °C and was held there for 1 hour. At the same time, the stock solution of $ZnSt_2$ was heated up to 120 °C under the argon gas flow and became a clear solution to be used as the zinc precursor. After one hour annealing, the temperature of main reaction was then set to the temperature for the injection of zinc precursor, which were 290 °C or 260 °C described in the text. Once the target temperature for injection of the zinc precursor was reached, 3 ml of the zinc precursor was injected either in one fast application or slowly drop by drop into the MnSe yellowish solution. The temperature of the main reaction was decreased by 10 °C and kept constant. The same injection strategy was performed in another three

phases (3 ml each) with 15 minutes intervals for the reaction going completely and all the zinc precursor was injected into the main reaction. 15 minutes after the last injection of zinc precursor, the heating was turn off and the reaction mixture was allowed to cool down to room temperature with argon gas flow. Finally, the Mn doped ZnSe branched quantum dots were purified by first dissolving in toluene and precipitation out with acetone, centrifuging, and then re-dispersing in toluene. Branched Mn doped ZnSe quantum dots formed using these methods were reproducible. The nanocrystals were stable in toluene solution and showed no sign of aggregation over one month.

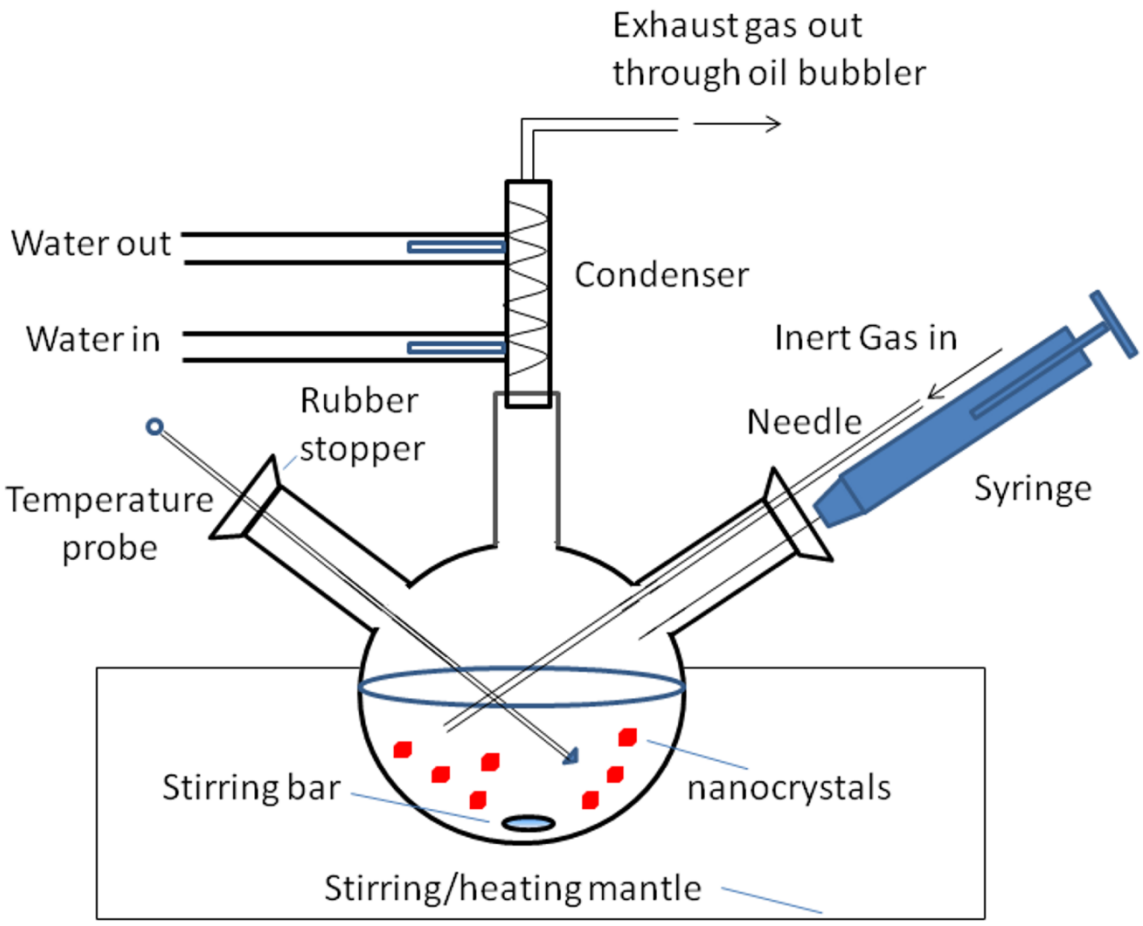


**Figure 3.3.** The schematic set up of solution phase chemistry to synthesize Mn doped ZnSe quantum dots.

### 3.2.5. Synthesis of Spherical Mn Doped ZnSe Quantum Dots

The $MnSt_2$ was dissolved in ODE at high temperature as the main reaction. In a typical reaction, 0.1 g $MnSt_2$ and 25 g ODE were loaded in 100 ml three neck flask and degassed under argon bubbling for 15 minutes at 110 °C. Then the flow rate of argon gas was decreased to just keep an argon atmosphere with minimal over-pressure and the temperature of clear brownish manganese precursor solution was increased to 280 °C. At the same time, 1 ml TBPSe stock solution and 1 g oleylamine were mixed in a separate flask under argon gas flow and heated up to 70 °C to form the selenium precursor. Once the temperature of the main reaction reached 280 °C, in which small nanoclusters of MnSe formed, the selenium precursor was quickly injected into the main reaction vessel. The temperature of the main reaction dropped to 260 °C and was held there for 1 hour. At the same time, the stock solution of $ZnCl_2$ was heated up to 120 °C under the argon gas flow until a clear solution was formed. After one hour annealing, the temperature of main reaction was then set to the temperature for the injection of zinc precursor, which was 220 °C described in the text. Once it reached the target temperature for injection of the zinc precursor, 3 ml of the zinc precursor was injected either in one swift application or slowly drop by drop. The temperature of the main reaction was decreased by 10 °C and kept constant. The same injection strategy was performed in another three phases (3 ml each) with 15 minutes intervals for the reaction going completely and all the zinc precursor was injected into the main reaction. 15 minutes after the last

injection of zinc precursor, the heating was turn off and the reaction mixture was allowed to cool down to room temperature with argon gas flow. Finally, nanocrystals were purified by first dissolving in toluene and precipitation out with acetone, centrifuging, and then re-dispersing in toluene. Spherical Mn doped ZnSe formed using these methods were reproducible. The nanocrystals were stable in toluene solution and showed no sign of aggregation over one month.

### 3.2.6. Transmission Electron Microscopy (TEM) and Selected Area Electron Diffraction (SAED) & Simulation

TEM was performed using a JEOL 4000EX HRTEM operating acceleration voltage at 400 kV with $LaB_6$ filament. Samples were prepared by dipping a Formvar-coated copper TEM grid into a solution of toluene containing purified nanocrystals. The TEM grid was dried in the air. Studies of the time-dependent growth dynamics were performed by removing aliquots at different stages of the reaction, then purifying and preparing TEM grids by dip coating and drying in the air. SAED was performed using a Philip CM20 TEM. TEM images processing was performed using Image J software and atomic models were constructed using *Accelys DS Viewer Pro.* Single crystal electron diffraction simulations were performed with *crystal diffract* software.

### 3.2.7. Optical Measurements

UV-Vis-Absorption spectra were recorded on a JASCO V-570 UV/VIS/NIR spectrophotometer. Photoluminescence (PL) and photoluminescence excitation (PLE) spectra were taken using

JASCO FP-6200 spectrofluorometer. The PL quantum yield measurements were performed using a comparative method of Williams *et al*. [238]

## 3.3. Branched Quantum Dots

### 3.3.1. The Structure of Branched Quantum Dots

Transmission electron microscopy was performed to understand the structure of quantum dots. Figures 3.4(a)-(d) show the TEM images with different magnifications of branched 15 nm Mn doped ZnSe quantum dots with an injection of zinc precursor and subsequence growth temperature at 290 °C. Figure 3.4(a) shows that Mn doped ZnSe quantum dots tend to form a honeycomb-like network due to the self-assembly mechanism. Figure 3.4(b) shows a higher magnification TEM image which indicates the dots are pods-like structure. A single pod-like Mn doped ZnSe quantum dot is shown in figure 3.4(c). These branched Mn doped ZnSe quantum dots have a relatively uniform size of 15 nm. The number of nanocrystals with tetropod shape [figure 3.4(a)-(c)] is about ninety percent, with some bipods shown in figure 3.4(d). The bipod Mn doped ZnSe quantum dot has a core of about 3.7 nm with arms about 7 nm shown in figure 3.4(d). The proposed atomic model, similar as branched CdTe model,[237] is shown in figure 3.4(e), which is zinc blende (111) plane of ZnSe core jointly with wurtzite $(000\bar{1})$ plane of ZnSe arms, while Mn atoms embedded in the core only. A time-dependent growth study of the reaction has been investigated to show the

branched Mn doped ZnSe quantum dots immediately form from MnSe nanoclusters after the first injection of zinc precursor which will be discussed later. Based on this study, the mechanism of shape control of Mn doped ZnSe quantum dot is proposed in figure 3.4(f).

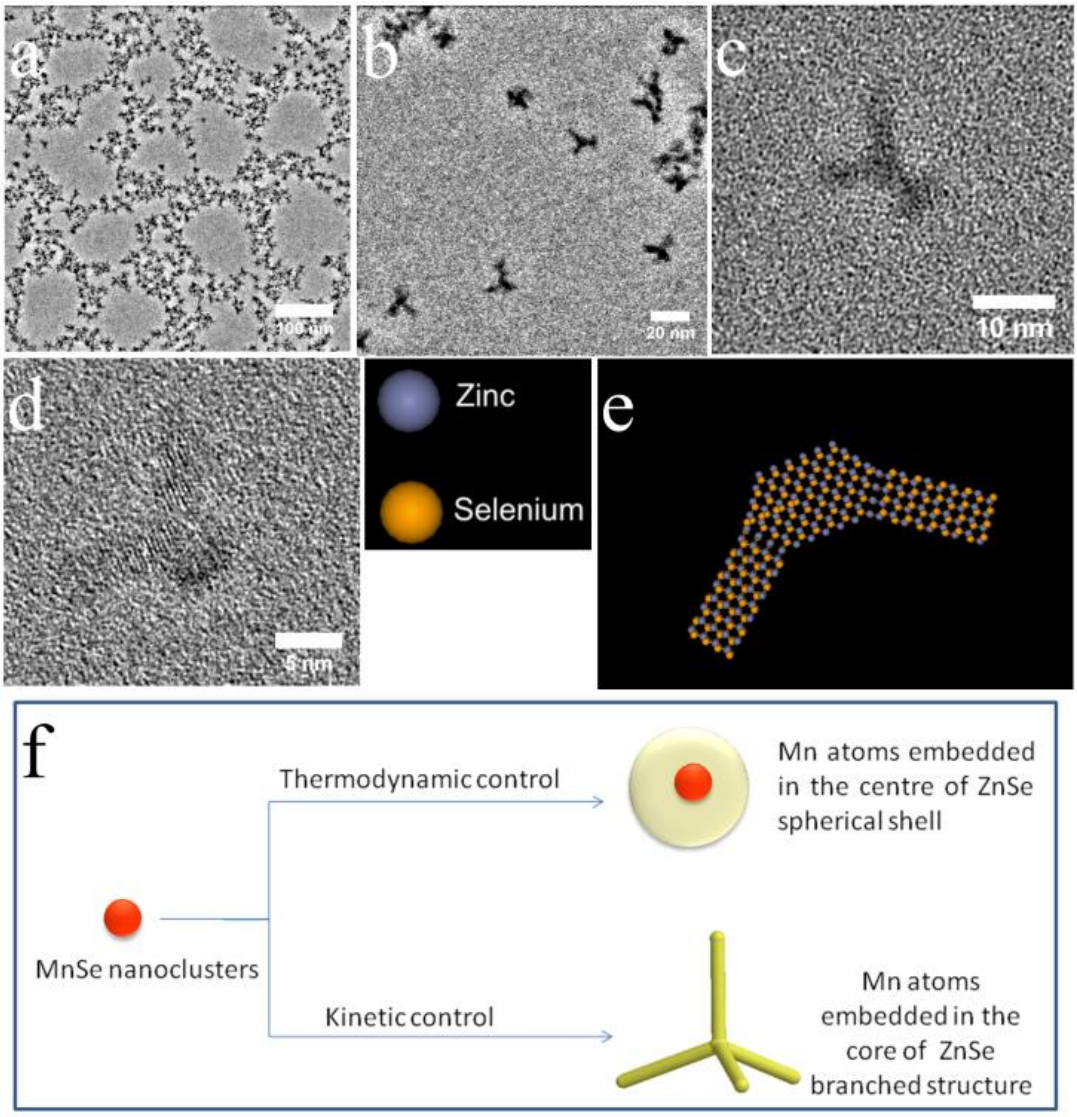


**Figure. 3.4** Different magnification of transmission electron microscopy (TEM) images of branched Mn doped ZnSe nanocrystals synthesized at injection and growth temperature at 290 °C using $ZnSt_2$ as Zinc precusor. (a) Low magnification TEM image shows self-assembled quantum dots on formvar carbon coated TEM grids. (b) Higher magnification of panel a shows high yield of branched Mn doped ZnSe quantum dots. (c) A TEM image shows tetrapods Mn doped ZnSe. (d) A HRTEM image shows bipod Mn doped ZnSe with lattice planes resolved. (e) An atomic model of branched Mn doped ZnSe quantum dots with the zinc blende (001) plane of the core jointly with wurtzite $(000\bar{1})$ plane of arms. (f) Schematic illustration of the mechanism of the shape control of Mn doped ZnSe quantum dots.

### 3.3.2. A TEM Study for Morphology Dynamics of Branched Quantum Dots

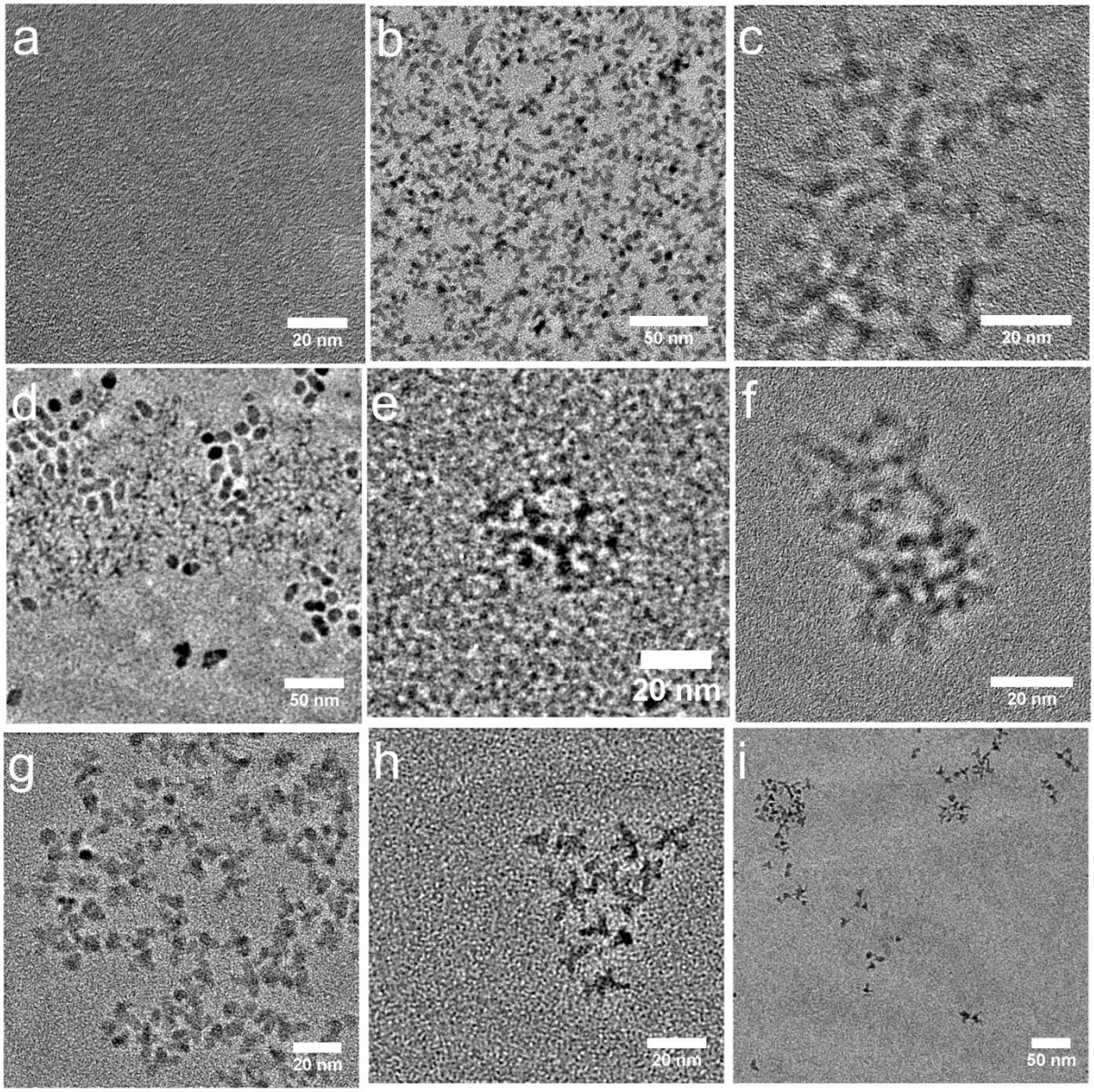


**Figure 3.5.** TEM images of morphology dynamics of branched Mn doped ZnSe quantum dots during and after reaction by swiftly quenching the reaction at different stages: (a) MnSe small nanoclusters annealed after one hour. (b) Immediately after the 1st injection of Zinc precursor at 290 °C. (c) Immediately after the 2nd injection of zinc precursor. (d) Immediately after the 3rd injection of zinc precursor. (e) Immediately after the 4th injection of zinc precursor. (f) 15 minutes after the $4^{th}$ injection of zinc precursor and then cooling down the reaction to 180 °C. (g) Cooling down to room temperature after the reaction. (h) One day after the reaction. (i) One months after the reaction.

In order to understand the growth mechanism and morphology dynamics of branched Mn doped ZnSe quantum dots during the reaction, a series in situ TEM study was performed by quenching the reaction at different reaction stages and taking the sample out for TEM study. Figure 3.5(a) shows the stage of MnSe small nanoclusters annealed after one hour, just before the first injection of zinc precursor. It is believed that MnSe nanoclusters formed,[222] although it is very hard to pick up this MnSe nanoclusters due to its relatively small size and invisible in the condition of TEM performance. Figure 3.5(b) shows the branched structure forms immediately after the first injection of zinc precursor. Morphology doesn't change very much after the first injection of zinc precursor. The morphology is quite stable without aggregation over one month.

### 3.3.3. The Shape Control Mechanism

In order to change the shape of Mn doped ZnSe quantum dots from branched to spherical, based on the proposed shape control mechanism, shown in figure 3.4(f), the temperature should be pushed down to the thermodynamics region if all the other parameters are kept the same. The anisotropic kinetics growth will lead to branched quantum dots, while isotropic thermodynamics growth will result in spherical dots. To get isotropic growth is to minimize the energy difference between the wurtzite and the zinc-blende structures, which determine the temperature range in which the two structures are not preferential during both nucleation and growth.[237] This means the

lower growth temperature within thermodynamics regime will favour the isotropic growth. If solid state $ZnSt_2$ is used, the required decomposition temperature is high which does not favour the isotropic growth and always leads to branched Mn doped ZnSe quantum dots. Thus, $ZnCl_2$ is used instead, which can decompose in relatively low temperature. This will help to reduce the temperature to get isotropic growth. All the other parameters were kept the same to study the temperature effects on the shape control of Mn doped ZnSe quantum dots. The reactions were performed with the injection of zinc precursor at certain temperature by both dropwise and fast injection. The fast injection of zinc precursor will lead to the sharp increase of the zinc concentration to the supersaturation point for the nucleation with higher internal reaction pressure, while the dropwise injection takes longer time to reach the supersaturation point for nucleation and with lower internal reaction pressure. This also changes the kinetics of the reaction. It may also affect the structure of the dots. When the reaction was performed at 260 °C for both dropwise and fast injection, they both produce branched Mn doped ZnSe quantum dots, similar as which is shown in figure 3.4. This indicates that 260 °C is still within kinetics regime, resulting in the anisotropic branched structure. Then, the injection temperature was reduced down further to 220 °C. At this temperature both slow and fast injection rates form non-branched structures, shown in figures 3.6 and 3.7 respectively. This means 220 °C is within thermodynamics growth regime, because there is no facet with preferential growth rate resulting in isotropic morphology. By simply controlling the temperature, the shape of Mn doped ZnSe quantum dots can be varied from

branched to spherical, and the key to achieving this is the use of $ZnCl_2$ instead of $ZnSt_2$ as a precursor.

## 3.4. Control the Crystal Phase of Spherical Quantum Dots

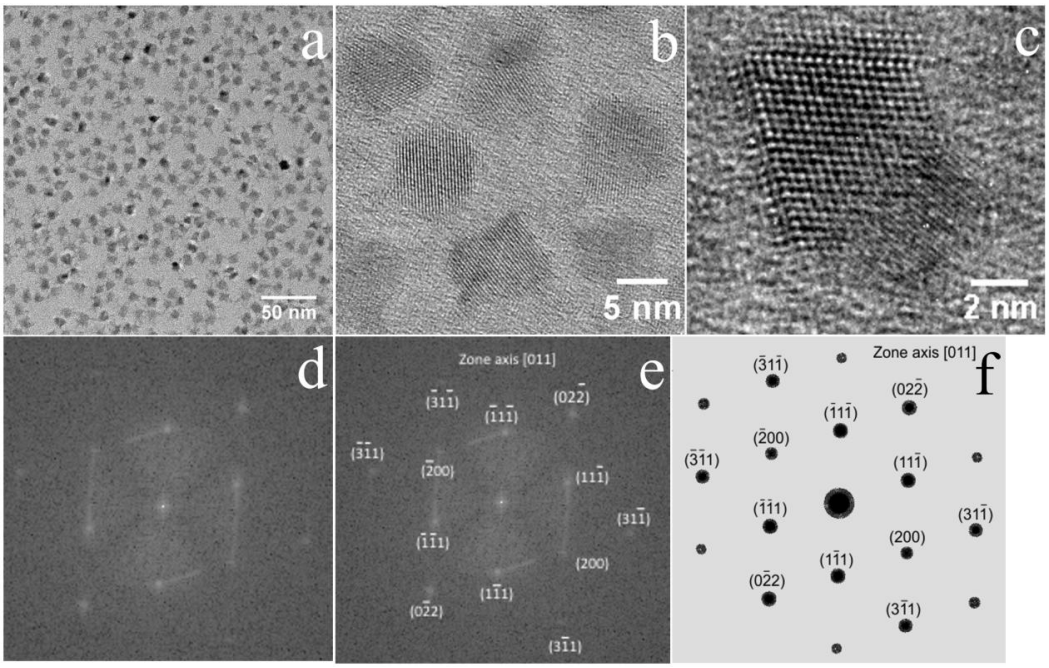


**Figure 3.6.** Formation of nearly spherical zinc blende Mn doped ZnSe quantum dots via the drop by drop injection of zinc precursor at 220 °C using $ZnCl_2$ instead of $ZnSt_2$: (a) Low magnification TEM image of nanocrystals. (b) Higher magnification TEM image of the nanocrystals. (c) HRTEM image of a single nanocrystal. (d) FFT of panel c. (e) Index of panel d, showing the nanocrystal is zinc blende Mn doped ZnSe quantum dots with [011] zone axis. (f) A simulated single crystal electron diffraction pattern of a zinc blende Mn doped ZnSe quantum dot with [011] zone axis.

Figures 3.6(a)-(c) show the dropwise injection of zinc precursor results in nearly spherical dots with twinning. The nanocrystals are relatively mono-disperse, shown in TEM image in figure 3.6(a) and (b) with different magnifications. HRTEM image of a single quantum dot is shown in figure 3.6(c), with corresponding 2D FFT shown in figure 3.6(d). The index of the 2D FFT pattern is

shown in figure 3.6(e) with [011] zone axis, matching the zinc blende crystal structure with $F\bar{4}3m$ space group. It is the only possibility indexing structure considering the angle between the principal plane normals and d spacing of spots. It rules out the possibility of wurtzite structure by comparing to the standard wurtzite structure electron diffraction patterns table. The simulated single crystal electron diffraction pattern of a zinc blende ZnSe quantum dot with [011] zone axis is shown in figure 3.6(f). The simulated single crystal electron diffraction pattern fits the experimental data figure 3.6(d) well, confirming the quantum dot is of zinc blende crystal phase.

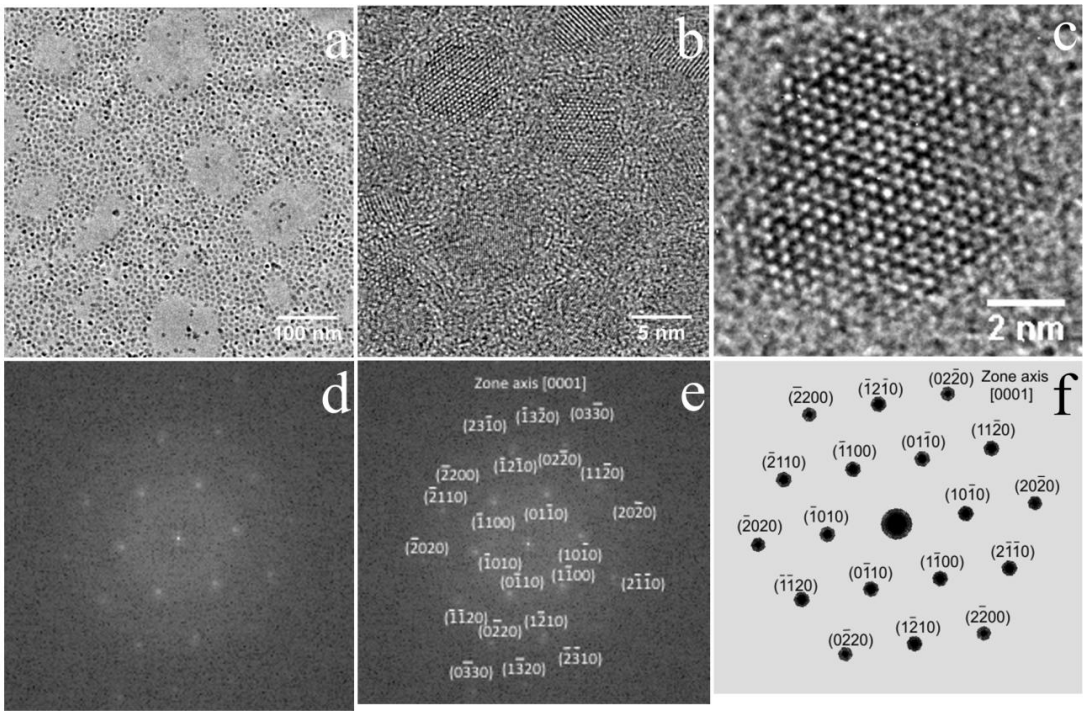


**Figure 3.7** Formation of spherical wurtzite Mn doped ZnSe quantum dots via the fast injection of zinc precursor at 220 °C using $ZnCl_2$ instead of $ZnSt_2$: (a) Low magnification TEM image of nanocrystals. (b) Higher magnification TEM image of the nanocrystals. (c) HRTEM image of a single nanocrystal. (d) FFT of panel c. (e) Index of panel d, showing the nanocrystal is wurtzite Mn doped ZnSe quantum dots with [0001] zone axis. (f) A simulated single crystal electron diffraction pattern of a wurtzite Mn doped ZnSe quantum dot with [0001] zone axis.

Figures 3.7(a)-(c) show that the fast injection of zinc precursor at the same temperature (220 °C) results in well defined spherical nanocrystals without twinning. The mono-dispersed Mn doped ZnSe nanocrystals are shown in figure 3.7(a) and (b) with different magnifications. HRTEM image of a single quantum dot is shown in figure 3.7(c) with lattice structure resolved. Figure 3.7(d) is the 2D FFT of panel c. The FFT pattern is indexed in figure 3.7(e), only matching a wurtzite crystal structure with P63mc space group with [0001] zone axis. Figure 3.7(f) shows the simulated electron diffraction pattern of a wurtzite ZnSe quantum dot with [0001] zone axis. This fits the experimental data figure 3.7(d) well. It can conclude the quantum dot is of wurtzite crystal structure.

The selective area electron diffraction (SAED) patterns of both slow and fast injection samples were also measured, indicating the crystal structure of slow injection quantum dots are zinc blende, whilst the crystal structure of the fast injection quantum dots are wurtzite crystal phase. Figure 3.8 and table 3.1 show the SAED patterns and analysis of both slow and fast injection Mn doped ZnSe quantum dots with injection temperature at 220 ℃, obtaining from a field of Mn doped ZnSe nanocrystals. By measuring the radial profiles, the positions of the rings are indentified. At least five separation diffraction rings are observed, and they are assigned in table 3.1. In Figure 3.8(d) ring 1 is unique to (100) plane of hexagonal (wurtize) structure. This confirms fast injection sample is wurtize structure while slow injection sample is zinc blende crystal phase. This is consistent with FFT analysis of HRTEM image of a few nanocrystals in

Figure 3.8(a) and (b). Both single crystal diffraction analysis and SAED studies show the injection rates have dramatic effects on controlling the crystal phase from zinc blende to wurtzite structure. Zero intensity for a group of diffracted beam is called systematic absence. For zinc blende structure, reflection must have either all even or odd number to be observed. This is consistent with our observation.

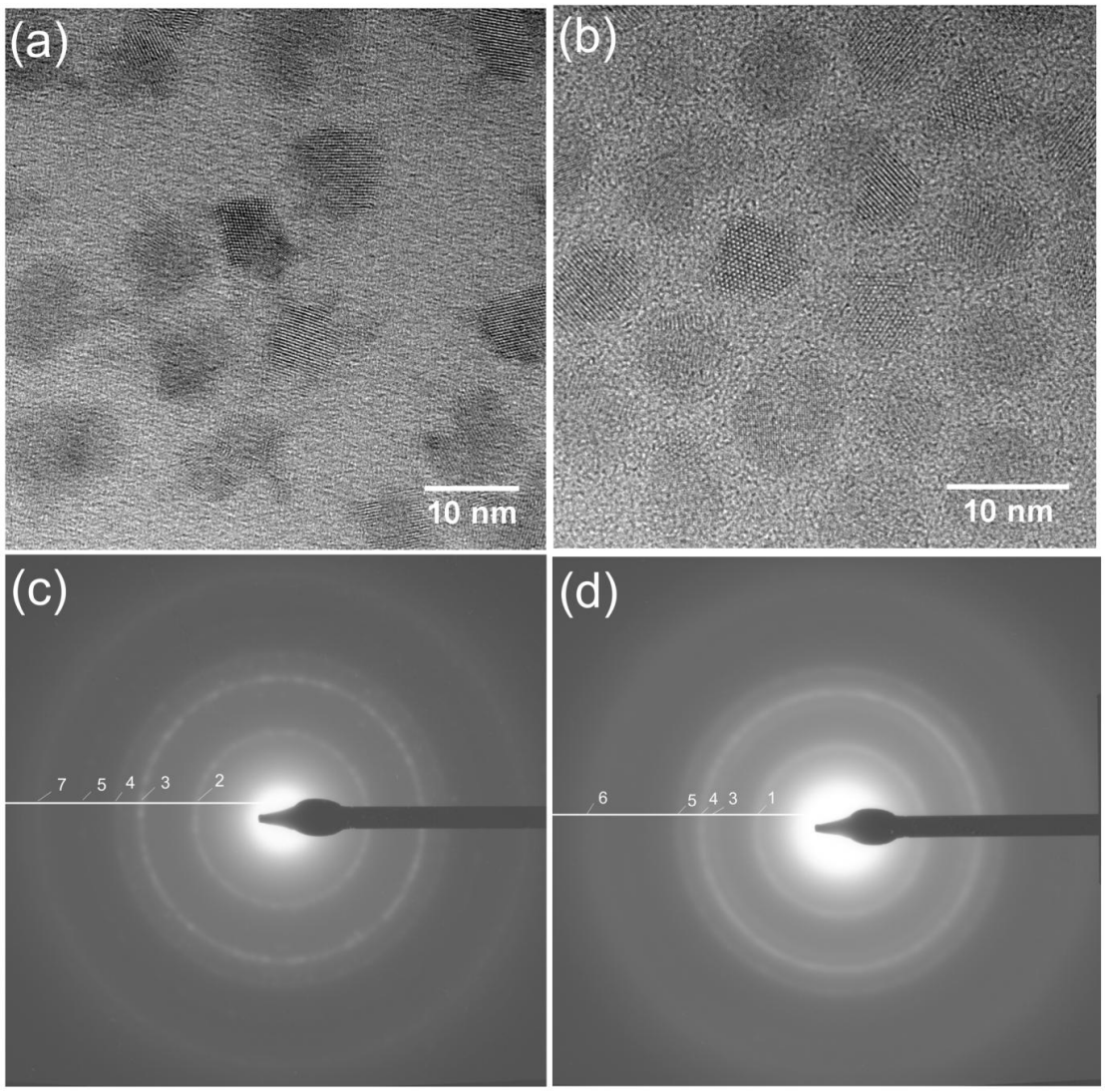


**Figure 3.8.** Selective area electron diffraction (SAED) measurements: (a) HETEM image of slow injection Mn doped ZnSe quantum dots with injection temperature at 220 °C. (b) HRTEM image of fast injection Mn doped ZnSe quantum dots with injection temperature at 220 °C. (c) SAED of slow injection Mn doped ZnSe quantum dots. (d) SAED of fast injection Mn doped ZnSe quantum dots.

| Ring | hkil (hexagonal) | hkl (cubic) | d [Å] |
|---|---|---|---|
| 1 | 100 | None | 3.519 |
| 2 | Not shown | 111 | 3.302 |
| 3 | 110 | 220 | 2.032 |
| 4 | 200 | 311 | 1.759 |
| 5 | 210 | 331 | 1.330 |
| 6 | 300 | Not shown | 1.173 |
| 7 | Not shown | 511 | 1.109 |

**Table 3.1**: Assignment of SAED rings to Mn doped ZnSe crystal structures; d: lattice spacing

For the formation of thermodynamically unstable wurtzite ZnSe nanostructure, the growth temperature, pressure and surface energy are the three important factors.[239-240] The transformation from zinc blende structure to wurtzite structure have possible to happen if the temperature is above the transition temperature $T_{tr}$.[240] This transition temperature is dependence of particle size.[240] This indicates 220 °C is already above the $T_{tr}$ for nanocrystals with about 7 nm in diameter. The dominant surface of $\{2\bar{1}\bar{1}0\}$, which have the lowest surface energy in wurtzite structure, will help to minimize the total surface energy of the nanostructure.[239-240] This is consistent with our case, as shown in figure 3.7(d)-(f), which has dominate surface of $\{2\bar{1}\bar{1}0\}$. The possible reason of the phase transition by injection rates may be the reaction internal pressure difference between two modes. The equilibrium pressure of wurtzite phase is always higher than the equilibrium pressure of the zinc blende phase.[239] In our case, the fast injection rates give higher internal reaction pressure than the dropwise injection rates. Thus, the wurtzite phase is produced by the fast injection rates method. In summary, the phase transition from zinc blende to wurtzite by injection

rates are due to the three reasons, the reaction temperature above $T_{tr}$, the lowest surface energy by the dominance surface of $\{2\bar{1}\bar{1}0\}$, and the reaction pressure difference between injection rates.

## 3.5. Quantum Yield Measurements

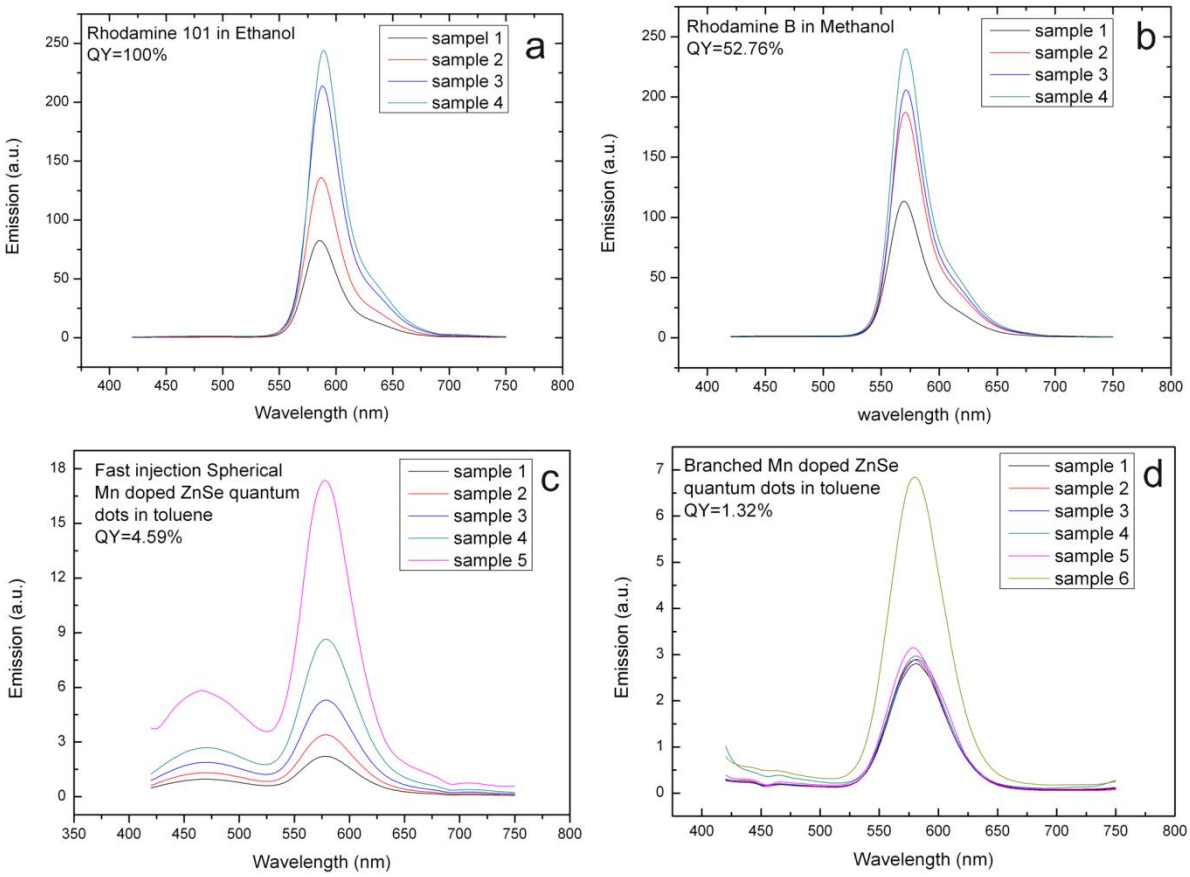


**Figure 3.9.** Determination of photoluminescence quantum yield: (a) Rhodamine 101 in ethanol, QY=100%. (b) Rhodamine B in ethanol, QY=52.76%. (c) Fast injection spherical Mn doped ZnSe quantum dots in toluene, QY=4.59%. (d) Branched Mn doped ZnSe quantum dots in toluene, QY=1.32%.

The PL quantum yield (QY) measurement of d-dots. The PL QY of the Mn doped ZnSe was determined by using Rhodamine 101 dye as reference and Rhodamine B dye for cross calibration. All the samples are excited at 400 nm wavelength and their emission varies from 420 nm to 750 nm, with dominate peaks at around 580 nm. In the first step, absorption of the sample spectrum was measured with subtraction of spectrum of solvent. The optical density of the samples was determined at 400 nm wavelength, which was used later as excitation wavelength for PL measurement. Then, emission spectrum were taken with only solvent and varies concentration of the samples by drop by drop techniques. The optical density of both dyes at 400 nm is less than 0.05 for avoiding detector saturation. The optical density of Mn doped ZnSe quantum dots at 400 nm is less than 0.1 for avoiding self quenching and no-linear effect. The PL spectrums of samples were corrected by subtracting emission spectrum of solvent from the emission spectrum of samples. The solvent-corrected PL spectrums were presented in figure 3.9(a)-(d). The graph of integrated fluorescence intensity verse absorbance at 400 nm excitation wavelength was plot and fitted linearly, shown in the figure 3.10(e)-(f). The gradients were determined by analysing the slope of the fitted line. The PL QY of both standard dyes and quantum dots samples were calculated with the following equation, which is suggested by IUPAC.[241]

$$\phi_{dot} = \phi_{REF}\left(\frac{Grad_{dot}}{Grad_{REF}}\right)\left(\frac{\eta_{dot}^2}{\eta_{REF}^2}\right)$$

Dot=nanocrystals, REF=Reference, η=refractive index of a solvent. The Quantum yield of Rhodamine 101 in ethanol is 100% [242] and Rhodamine B in methanol at 298k is 52% [243]. The measured value for standard dye fits the literature well, which gives cross calibration.

## 3.6. Structural-Optical Property Correlations

Figure 3.10(a) shows the UV-vis-Absorption, photoluminescence (PL) and photoluminescence excitation (PLE) spectra of the branched Mn doped ZnSe quantum dots. The red line shows the photoluminescence, with excitation wavelength of 400 nm, from the Mn dopant centre at emission wavelength of 580 nm (2.18 eV) due to the d-d transition, also called $^4T_1 \rightarrow {}^6A_1$ transition.[214] This 580 nm PL emission peak is characteristic of the $Mn^{2+}$ ion emission centres. This pure $^4T_1 \rightarrow {}^6A_1$ transition PL peak implies that $Mn^{2+}$ ion emission centres are located on the common lattice position and isolated from each other. Emission from this transition arises from delocalized electrons being trapped by the d-orbital of Mn dopants.[223] As the electron is more delocalized than the hole and encounter more repulsive force from the negative charged ligands, the electron is confined to the interior of the nanocrystal.[223] This increases the possibility of the electron being trapped by the d-orbital of Mn dopant and gives this d-d transition.[222,244] The Mn dopant emission centres should be as far away as possible from the potential surface trap states of the nanocrystals

to increase the possibility of the electrons being trapped into the d-orbital of Mn dopants and subsequently give this strong PL dopant emission at 580 nm wavelength from this transition.[222] Thus, from the strong PL emission at 580 nm, we confirm that the majority of Mn dopants are on the common lattice positions inside ZnSe quantum dots rather than at the surface of ZnSe quantum dots. If the Mn dopants are on the surface of ZnSe quantum dots, excitons on the surface will be easy to fall into the surface trap states rather than falling into the d-orbital of Mn atoms, resulting non-radiative events, because the process of trapping electrons into the defects will be more energetically favourable. Thus, if the Mn dopants are at the surface of ZnSe dots, it will not give a shape peak at 580 nm in photoluminescence spectrum. No PL peaks are shown are 650 nm, which is due to the Mn-Mn emission.[245] This Mn-Mn emission happens when Mn-Mn centres form with a Mn ion next to the Mn emission centre. This situation only occurs when Mn dopant concentration was very high in bulk materials.[245] It means the Mn dopants in branched quantum dots are isolated and its concentration is low. The small peak at 440 nm wavelength in the photoluminescence spectrum is due to the ZnSe band edge emission. The photoluminescence excitation and UV-vis-absorption both have the first transition peaks at 420 nm wavelength which is the band edge absorption of intrinsic zinc selenium nanocrystals indicated in figure 3.10(a). The PLE shows the optical excited states in the sample, in which the first transition peak of the spectrum gives the band edge width.[246] In figure 3.10(a), the band edge width matches the band edge absorption at 420 nm wavelength. This indicates the photon is first absorbed via the band

edge transition of ZnSe shell. The Stokes shift is shown by the wavelength difference between the band edge absorption peak of intrinsic ZnSe quantum dots at 420 nm in UV-vis-absorption spectrum to the Mn emission peak at 580 nm in PL spectrum. Combining these PL, PLE, UV-vis-absorption measurements, the energy dynamics of photoluminescence process can be understood, which is also illustrated in figure 3.10(b). When a photon first is absorbed by ZnSe shell, an exciton (an electron-hole pair) is generated in ZnSe energy levels. If the electron hole pair recombines directly from conduction band of ZnSe to valence band of ZnSe, it will give the band edge emission $I_{ZnSe}$ at 440 nm wavelength. Most of the electron-hole pairs on the surface will be trapped and eliminated by the surface defects. However, some of the delocalized electrons from excitons can penetrate into the ZnSe shell to approach to the Mn dopant atoms and fall into the d-orbital of Mn dopants. Then these electrons transfer to the Mn dopant energy levels and then decay to the ground state, it will give the Mn dopant emission $I_{Mn}$ due to the d-d transition.

The injection rates not only have dramatic effect on controlling the crystal phase but also have great influence on PL properties. The two samples, which were shown in the HRTEM images in figure 3.6 and 3.7 respectively, have the same concentration and optical density. Both samples have the same absorbance at the 400 nm in the UV-vis-Absorption spectrum, which is shown in figure 3.10(c). Photoluminescence spectra are taken with excitation wavelength at 400 nm. Figure 3.10(d) shows the fast injection rate sample (red line) has about ten times PL intensity than the slow injection sample with the same optical density. This means the crystal structure of the ZnSe

quantum dots has a dramatic effect on the PL properties. The PL intensity and energy drops during the phase transition from wurtzite to zinc blende induced by pressure, in $Zn_xCd_{1-x}Se$, $Zn_{1-x}Mn_xSe$ systems.[247,248] This is due to the band offsets change with different phase, resulting in the difference on quantum confinement energy for electrons and holes, and exciton binding (Rydberg energy).[248]

In order to correlate the PL properties with the structure of nanocrystals, a quantum yield measurement is performed in figure 3.9. The PL intensity from the fast injection branched structures shown in figure 3.4 with a quantum yield of 1%, which is smaller than the PL from fast injection spherical wurtzite dots shown in figure 3.7 with the quantum yield of 5%, which is shown in figure 3.10(e)-(f) with reference to standard dye Rhodamine 101 and Rhodamine B. Thus, the PL property of spherical dots is greater than both branched dots and nearly spherical dots. The PL quantum yield varies with different shape of quantum dots. It can be understood by the following reason. As the surface to volume ratio of our branched anisotropic quantum dots is greater than isotropic spherical quantum dots, it is likely that the number of surface trap states on the anisotropic quantum dots is greater than the isotropic spherical quantum dots. When the excitons are generated in the anisotropic dots have greater chance, than isotropic spherical dots, of being trapped by the surface defects along the pathway on the surface, which gives non-radiation or generate heat by Auger recombination. This leads to the exciton pathway varying with different shape of quantum dots, which decrease the PL quantum efficiency of anisotropic dots.

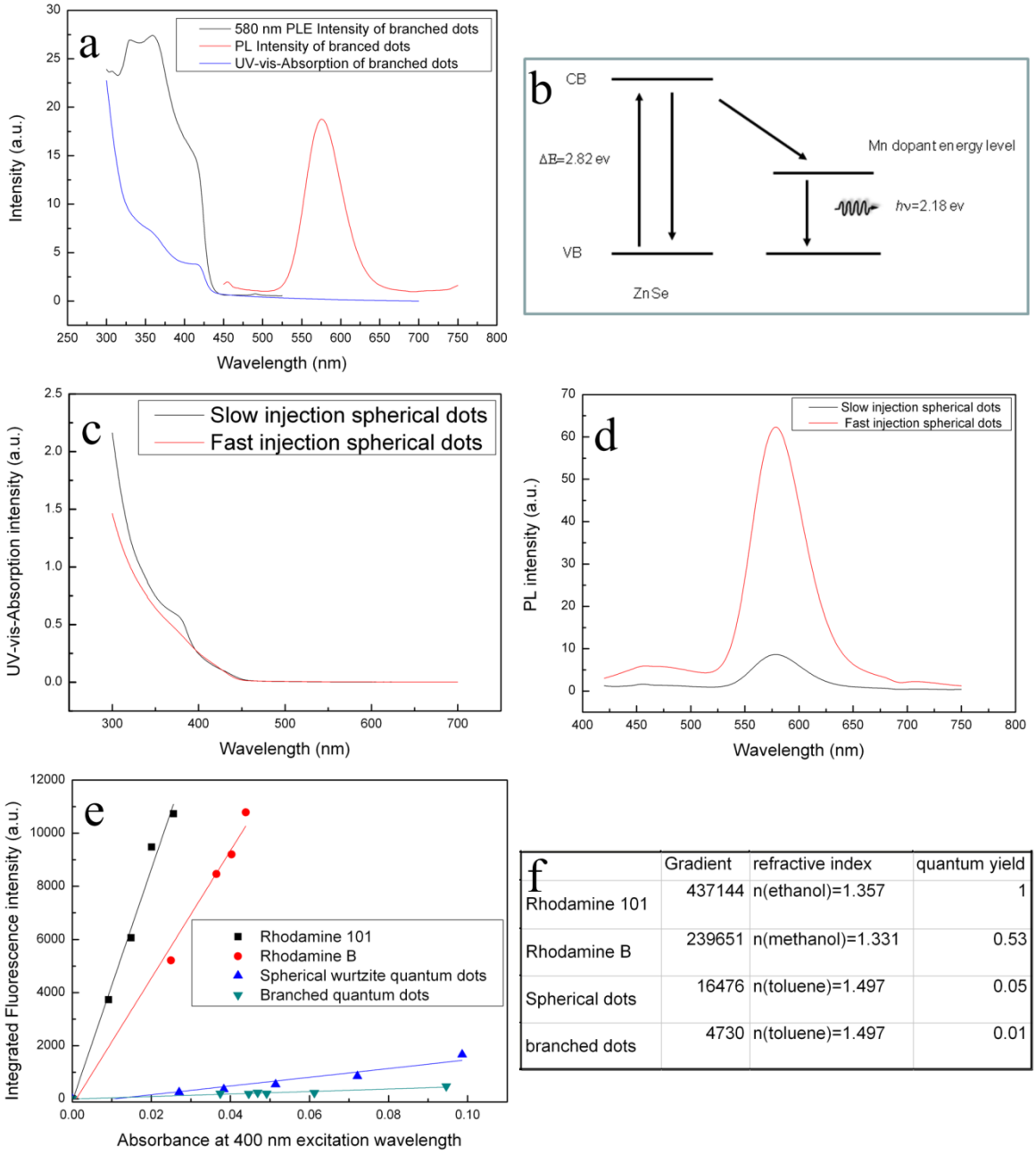


f

| | Gradient | refractive index | quantum yield |
|---|---|---|---|
| Rhodamine 101 | 437144 | n(ethanol)=1.357 | 1 |
| Rhodamine B | 239651 | n(methanol)=1.331 | 0.53 |
| Spherical dots | 16476 | n(toluene)=1.497 | 0.05 |
| branched dots | 4730 | n(toluene)=1.497 | 0.01 |

**Figure 3.10** (a) Optics measurements of branched Mn doped ZnSe quantum dots: Photoluminescence (red line), UV-vis-Absorption (blue line), and Photoluminescence excitation (black line). (b) Energy dynamics of photoluminescent Mn doped ZnSe quantum dots. (c) The UV-vis-Absorption of both the slow injection spherical dots and fast injection spherical dots with the same optical density at the wavelength of 400 nm. (d) The comparison of PL properties of the slow injection rate spherical (black line) and fast injection rate spherical dots (red line) with the same optical density with excitation wavelength at 400 nm. (e) Integrated fluorescence intensity verse absorbance at 400 nm excitation wavelength. (f) Quantum yield calculation for fast injection spherical quantum dots and branched quantum dots.

## 3.7. Conclusions

In summary, the synthesis of Mn doped ZnSe quantum dots with controlled crystal structure has been demonstrated. The correlation between crystal phase/shape and optical properties of Mn doped ZnSe quantum dots has been explored. Optics measurements and structural characterization prove that Mn doped ZnSe quantum dots are synthesized with Mn dopants inside ZnSe dots. A new in-situ morphology dynamics of branched Mn doped ZnSe quantum dots shows the MnSe forms small nanoclusters core. The branched structures immediately form immediately after the first injection of Zinc precursor and structure stability is quite well. A simple and easily purified way is reported to get shape control of Mn doped ZnSe quantum dots from branched to spherical with all liquid phase ligands by simply changing the injection temperature from kinetics region to thermodynamics region. Injection rates have been found to have dramatic effects on controlling the crystal phase from zinc blende to wurtzite. The crystal phase and shape of the nanocrystals have great influence on photoluminescence properties. The spherical wurtzite type Mn doped ZnSe quantum dots have the highest quantum yield comparing with other shape or crystal phase of the dots. This study is very important for understanding the correlation between structure and optical properties of doped quantum dots. This provides general principles to design the shape and crystal phase of doped quantum dots with tailored properties for the applications in photonic devices, bioimaging and spintronics.

# Chapter 4:

# Utilizing Boron Nitride Sheets as Thin Support for High Resolution Imaging of Nanocrystals

## 4.1. Introduction

In the previous chapter, shape and property control of Mn doped ZnSe quantum dots has been discussed and open question 1 has been answered. In this chapter, the discussion will be focused to answer open question 2, which will be whether it is possible to fabricate uniform single crystalline BN sheets as a carbon-free TEM ultrathin supporting film to study atomic configuration of other nanomaterials and whether liquid phase exfoliation method is good enough to fabricate large area single crystalline 2D atomic crystals.

Free standing atomic layer 2D sheet-like crystals have unique properties compared to their counterpart 3D bulk materials or rolled 1D single wall nanotubes.[3] Graphene is an example of a

2D atomic sheet that is attractive for fundamental materials physics and future nanoelectronic devices. [4,6] Compared with graphene, boron nitride (BN) is isoelectronic to $sp^2$ hexagonal carbon lattice, but it is an insulator independent of structure. Boron nitride has potential in nanotechnology because of its high thermal and chemical stability, deep ultraviolet photon emission, good mechanical strength, non-cytotoxicity and has been used as part of high temperature equipment or a solid state lubricant.[117, 125, 249-250] Though the research in BN is not as intense as graphene, the extension of the properties of boron nitride has attracted attention by integrating it with other nanomaterials to form unique hybrid materials.[251]

Since the 2D free standing atomic layer is ultrathin, it is ideal as a transmission electron microscopy (TEM) supporting film. In particular, using low voltage aberration corrected HRTEM enables the periodic atomic structure of the 2D crystal to be removed from the images via filtering of the 2D fast Fourier transform (FFT) and subsequent image reconstruction. To date, graphene[60-61, 252-253] and graphene oxide[254] have been utilized as an ultrathin TEM support for analysing both soft and hard materials. However both these materials are carbon based and seeking an alternative carbon-free 2D crystal may provide a framework for carbon-free spectroscopic measurements, such as electron energy loss spectroscopy (EELS). Recently, few layer BN sheets have been produced by chemical exfoliation using a variety of solvents such as dimethylformide (DMF), 1, 2-dichlorethane, octadecylamine (ODA), and N-methyl-2-pyrrolidone (NMP).[255-258] Mechanical exfoliation with iron etching[259] and electron beam irradiation[120, 260] have also been used.

Here, for the first time the utilization of few layer BN sheets as ultrathin TEM substrates for low-voltage aberration-corrected HRTEM is demonstrated. Mn doped ZnSe nanocrystals were deposited onto BN sheets and formed a uniform monolayer on the surface of the BN sheets. The phase contrast images are analyzed and also the resulting moiré interference patterns that arise from the electron beam propagating through the two crystalline nanomaterials are interpreted.

## 4.2. Experimental Methods

### 4.2.1. Preparing Free Standing BN Sheets and Mn Doped ZnSe Quantum Dots

Free standing few layer BN sheets are produced by sonicating hexagonal BN powder in the solvent N-methyl-2-pyrrolidone (NMP). Specifically, thin BN sheets were prepared by adding 5 ml N-methyl-2-pyrrolidone (NMP) to 0.1 mg *h*-BN powder (Sigma Aldrich) and using an ultrasonic bath for 3 hours. The solution was left to rest for 30 minutes to allow the large flakes to settle down to the bottom of the vial, leaving exfoliated *h*-BN in the upper solution. The synthesis of spherical Mn doped ZnSe quantum dots followed the method which has been discussed in chapter 3.

### 4.2.2. TEM Sample Preparation and Measurements

A lacey carbon coated TEM grid was decorated by BN sheets in NMP solution by drop coating. Residual NMP was washed off the grid by subsequent drop-casting of methanol. The strong adhesion between the BN sheets and the lacey carbon prevent the BN sheets from being washed off by the methanol. A drop of a toluene solution containing the Mn doped ZnSe nanocrystals was deposited onto the TEM grid with the BN sheets and left to dry. For low magnification TEM a JEOL 4000EX was used at 80 kV. Low-voltage aberration-corrected high resolution transmission electron microscopy was performed using Oxford's JEOL-2200MCO field emission HRTEM fitted with both probe and image aberration correctors and operated at an accelerating voltage of 80 kV.

### 4.2.3. Simulation and Analysis

HRTEM image processing was performed using *Image J* software. Atomic models and supercells were constructed using *crystal maker* and *Accelys DS Viewer Pro*. Multislice image simulations and Pendellösung plot calculation were performed using *JEMS* software, with acceleration voltage of 80kV, $C_S$=-0.005 nm, defocus spread = 4.3 nm, and defocus 2 nm. Matlab was used to solve the equations.

## 4.3. Shapes of BN 2D Atomic Crystals by Chemical Exfoliation

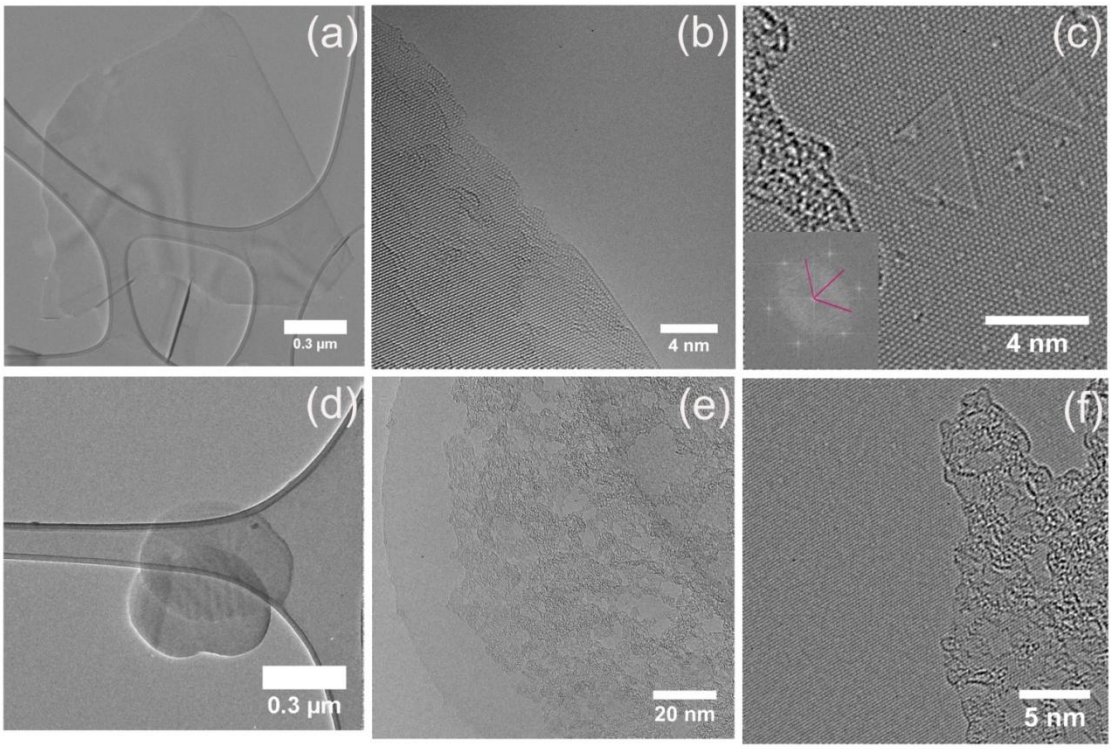


**Figure 4.1** (a) TEM image of a facet shaped BN sheet on a lacey carbon grid. (b) Higher magnification TEM image of the edge of faceted BN sheet. (c) HRTEM image of the surface of a BN sheet showing atomic lattice structure. Inset shows the 2D FFT with red lines indicating zigzag orientations**.** (d) TEM image of disc shaped BN sheets on a lacey carbon grid. (e) Higher magnification TEM image of the edge of a disc shaped BN sheet. (f) HRTEM image of the BN sheet with atomic lattice structure.

Free standing few layer BN sheets are produced by sonicating hexagonal BN (*h*-BN) powder in the solvent N-methyl-2-pyrrolidone (NMP). The solution was left to rest in order to allow large flakes to settle down to the bottom of the vial, leaving exfoliated *h*-BN in the upper solution. A lacey carbon coated TEM grid was decorated by BN sheets in NMP solution by drop coating. Residual NMP was washed off the grid by subsequent drop-casting of methanol. The strong adhesion between the BN sheets and the lacey carbon prevent the BN sheets from being washed off by the methanol. Mn doped ZnSe quantum dots were prepared separately according to

a method described in details in chapter 3. A drop of the toluene solution containing the Mn doped ZnSe was deposited onto the TEM grid decorated with BN sheets and left to dry.

It is found that two distinctly different types of BN sheets are produced, shown in figure 4.1(a) and figure 4.1(d). One type of BN sheet has faceted edges comprised of straight lines, whilst the other type has smooth round edges with a disc shape. Both types of sheets were hexagonal BN, as determined from atomic resolution images and selected area electron diffraction. The origin of the two different shapes may lie in the microcrystal they were exfoliated from. Figure 4.1(a) shows a typical facet-shaped few layer BN sheet with micron-sized dimensions on a lacey carbon film. The contrast of the BN sheets is lower than the lacey carbon film, indicating they are thinner than the traditional lacey carbon film. The observed wrinkles may come from the folding effect during the exfoliation in the sonication bath or during the deposition. Figure 4.1(b) shows a higher magnification TEM image of the edge of the faceted BN sheet. Small pieces of fragments partially cover the BN sheets, which come from the sonication process. Figure 4.1(c) shows a HRTEM image of the surface of a BN sheet with atomic structure apparent. Triangular nanopatterns are observed in the BN sheets due to electron beam irradiation and confirm the sheets are BN and not graphene or graphite impurities. In graphene or few layer graphene, electron beam irradiation leads to the appearance of circular holes, whereas in BN it leads to triangular nanopatterns.[256, 260, 261-262] A 2D FFT is shown in the bottom left inset of figure 4.1(c). The spots indicate the arm-chair direction, while red lines indicate zigzag direction.[263] Figure 4.1(d) shows two overlapping disc

shape BN sheets on a lacey carbon film. Figure 4.1(e) shows the edge of the disc shaped BN sheet with small fragments partially covering the surface and the corresponding HRTEM image with atomic structure is shown in figure 4.1(f).

## 4.4. Deposition of Quantum Dots onto BN Sheets

Figure 4.2 shows a faceted BN sheet suspended across two regions of the lacey carbon grid after depositing Mn doped ZnSe nanocrystals, with dark contrast from the nanocrystals. Figure 4.2(a)-(b) show that most of the nanocrystals prefer to stay away from the edge of the BN sheets. The edge of the sheets must be intrinsically less energetically favourable than the central area of the sheets. This may also be linked to the way in which the solvent dries and the self-assembly of the nanocrystals. The majority of the nanocrystals coat the BN sheet with a monolayer and the concentration increases as it gets closer to the left and right sides, near the lacey grid, leading to the formation of bilayers. A step edge is indicated with a red arrow in figure 4.2(b) and several nanocrystals are seen to be trapped at this boundary. This is shown in more detail in figures 4.2(c) and 4.2(d). The nanocrystals are aligned in a row at the step edge of BN sheets with different rotation angles with respect to the BN sheets. The diameters of the nanocrystals are approximately 5 nm and several are twinned and faceted.

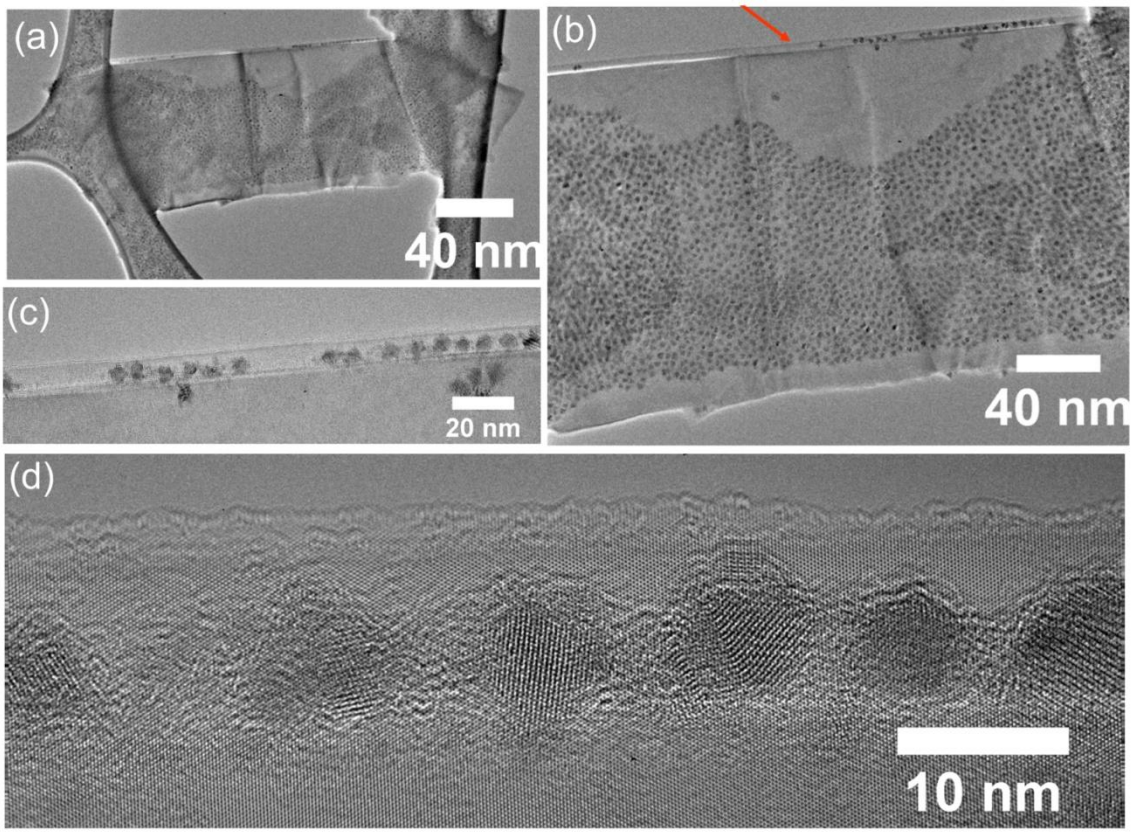


**Figure 4.2** (a) TEM image of a facet shape BN sheet decorated with Mn doped ZnSe nanocrystals. (b) Higher magnification of suspended facet shape BN sheet decorated with nanocrystals. (c) Higher magnification of nanocrystals aligned on the edge of BN sheet. (d) HRTEM of nanocrystals aligned on the edge of BN sheet.

Figure 4.3(a) shows a disc shaped BN sheet after deposition of Mn doped ZnSe nanocrystals. The nanocrystals again form a uniform monolayer and prefer to stay away from the edge of BN sheets, consistent with the behaviour of nanocrystals on facet shaped BN sheets. Figure 4.3(b) shows a higher magnification image of the surface of suspended BN sheets decorated with nanocrystals. Figure 4.3(c) shows the observation of atomic structure of both BN and Mn doped ZnSe nanocrystals. The surface capping ligands surrounding the quantum dots that prevent

them from aggregating are also seen as amorphous regions between the quantum dots in figure 4.3 (c).

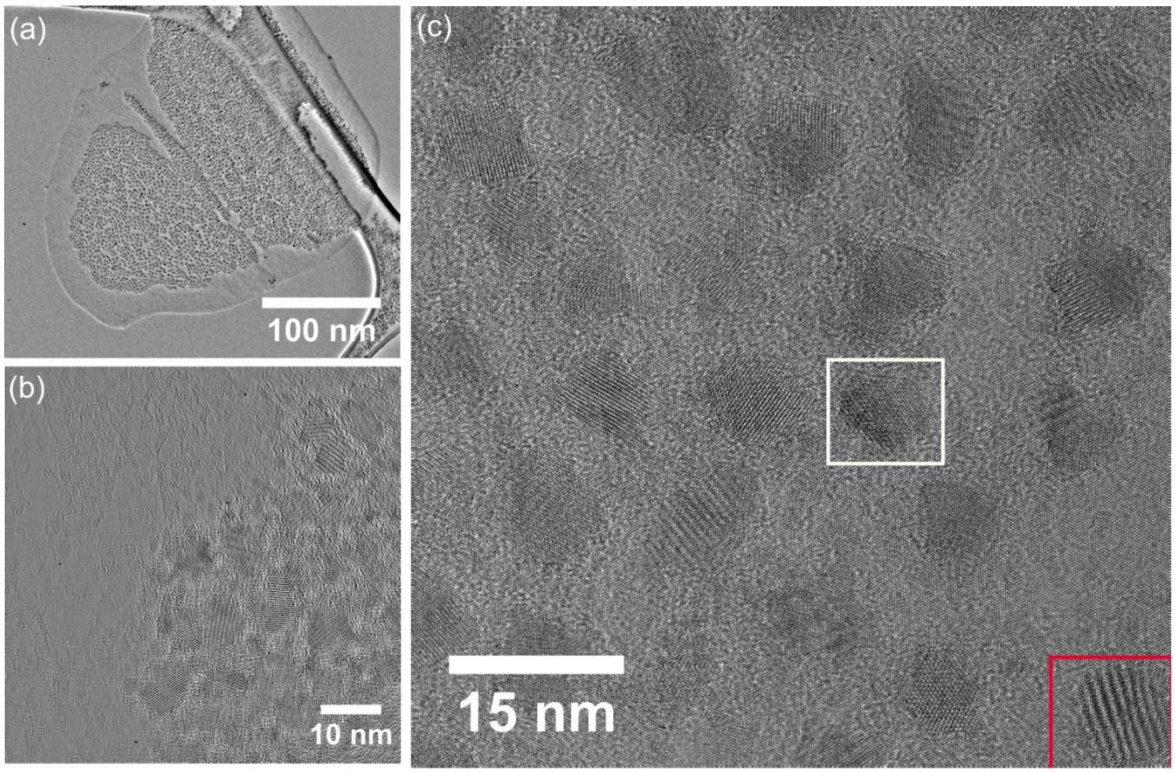


**Figure 4.3** (a) TEM image of a disc shape BN sheet decorated with Mn doped ZnSe nanocrystals. (b) Higher magnification of the surface of a suspended BN sheet decorated with nanocrystals. (c) HRTEM image showing several nanocrystals with crystalline lattice structure on the surface of disc shaped BN sheets.

## 4.5. Imaging and Analysis of Quantum Dots on BN 2D Atomic Crystals

### 4.5.1. Imaging and Simulation

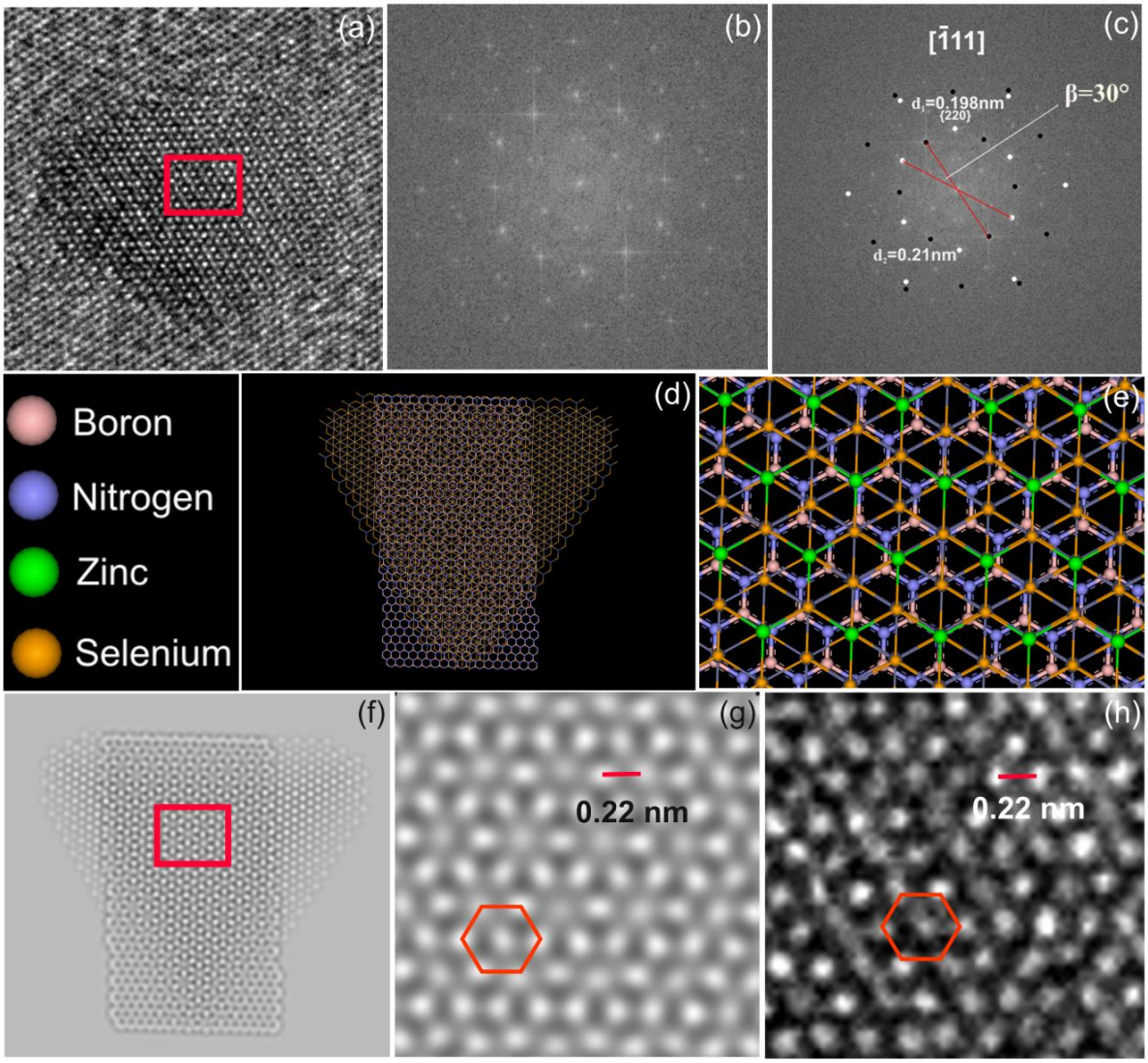


**Figure 4.4** (a) HRTEM image of a Mn doped ZnSe nanocrystal, indicated with a white box in figure 4.3(c). (b) FFT of panel a. (c) Index of BN and Mn doped ZnSe nanocrystals, black spots indicate BN, white spots indicate Mn doped ZnSe with [$\bar{1}$11] zone axis. The two crystals are rotated an angle of 30°, meaning the Mn doped ZnSe quantum dots are aligned with the zigzag direction of the BN sheet. (d) Projection view of low magnification atomic model of Mn doped ZnSe quantum dots on six layers BN sheets, along [$\bar{1}$11] zone axis. (e) High magnification atomic model, showing Mn doped ZnSe quantum dot aligned with zigzag direction of BN sheet, along [$\bar{1}$11] zone axis. (f) Simulated HRTEM image from the atomic model. (g) High magnification of simulated HRTEM image from the red box region in panel f. (h) High magnification of experimental HRTEM images from the red box region in panel a.

A HRTEM image of a single nanocrystal is shown in figure 4.4(a) from the region indicated with a white box in figure 4.3(c). In order to understand this phase contrast image, a 2D FFT of figure 4.4(a) is applied and shown in figure 4.4(b). To analyze this pattern, firstly reflection spots from each of the two nanomaterials are separated, namely, Mn doped ZnSe nanocrystals and the few layer BN sheets. Reflections from the BN sheets are indicated with black spots in figure 4.4 (c), with the largest d spacing of 0.21 nm. White spots indicate the reflection from the Mn doped ZnSe nanocrystals along the $[\bar{1}11]$ zone axis, giving reflections from the {220} and {422} sets of planes. The FFT pattern in figure 4.4(c) shows a rotation angle of 30° between white spots and black spots. This indicates the {220} set of planes in the ZnSe nanocrystal are aligned with the zigzag direction of the BN atomic layer, which is shown in the atomic model in figure 4.4(d) and (e). A simulated HRTEM image using this atomic model is shown in figure 4.4(f). The corresponding high magnification of the simulated HRTEM image from the red box region in figure 4.4(f) is shown in figure 4.4(g). This simulated image in figure 4.4(g) matches the experimental image figure 4.4(h) very well, which is a higher magnification from the red box region in figure 4.4(a). Both simulated image in figure 4.4(g) and experimental image in figure 4.4 (h) have hexagonal contrast, indicated by the colour boxes. The bright contrast to bright contrast distance in the simulated image is 0.22 nm, which matches the experimental data in figure 4.4(h). This distance is measured by taking the line profile of the calibrated images. From this analysis, we can confirm that the predominant pattern in the phase contrast image arises from the moiré

pattern due to the lattice structure of the nanocrystal and BN sheet. This interference between Mn doped ZnSe nanocrystals and BN sheets gives some new reflections in figure 4.4(c), which cannot be attributed to a single crystal. These new reflections arise from the electron beam being diffracted by both the Mn doped ZnSe nanocrystal and the BN sheets as it propagates through the composite in a process known as double diffraction.

The atomic model used for HRTEM image simulation is shown in figure 4.5 to elucidate the double diffraction process. Figure 4.5(a) shows the 3D atomic model in supercell with projection view, shown in figure 4.5(b) and side view, shown in figure 4.5(d). Figure 4.5(c) shows the illustration of double diffraction process. The primary beam $g^0$ transmits through both BN and QD. The beam $g^2$ is diffracted by both QD and BN. The phase difference between $g^0$ and $g^2$ will generate double diffraction spot.

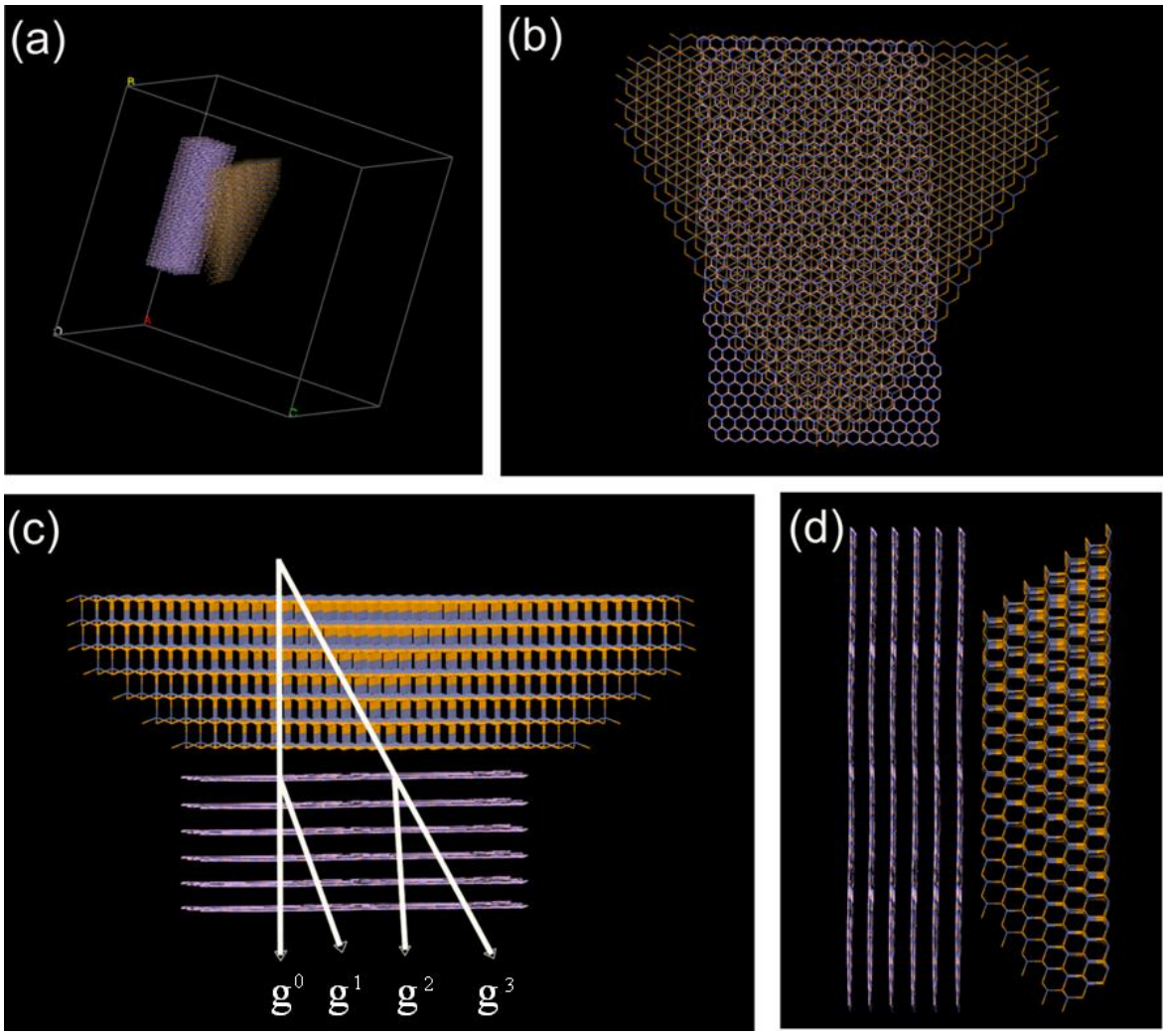


**Figure 4.5.** Atomic model shows the Mn doped ZnSe quantum dot aligns with the zigzag direction of BN, indicating the rotation angle of 30° between Mn doped ZnSe and BN; (a) 3D atomic model in super cell with coordinates O-ABC; (b) Projected view down $\overrightarrow{CO}$ direction with $[\bar{1}11]$ zone axis; (c) bottom up view along $\overrightarrow{OB}$ direction, an illustration of double diffraction process, $g^0$ is the primary beam transmitted through both the nanocrystal and BN sheets, $g^1$ is the beam transmitted through the nanocrystal but diffracted by the BN, $g^2$ is the beam diffracted by the nanocrystal and also by the BN (i.e double diffraction), $g^3$ is the beam diffracted by the nanocrystal and then transmitted through the BN. (d) side view down $\overrightarrow{OA}$ direction.

### 4.5.2. Quantitative Analysis and Vector Analysis

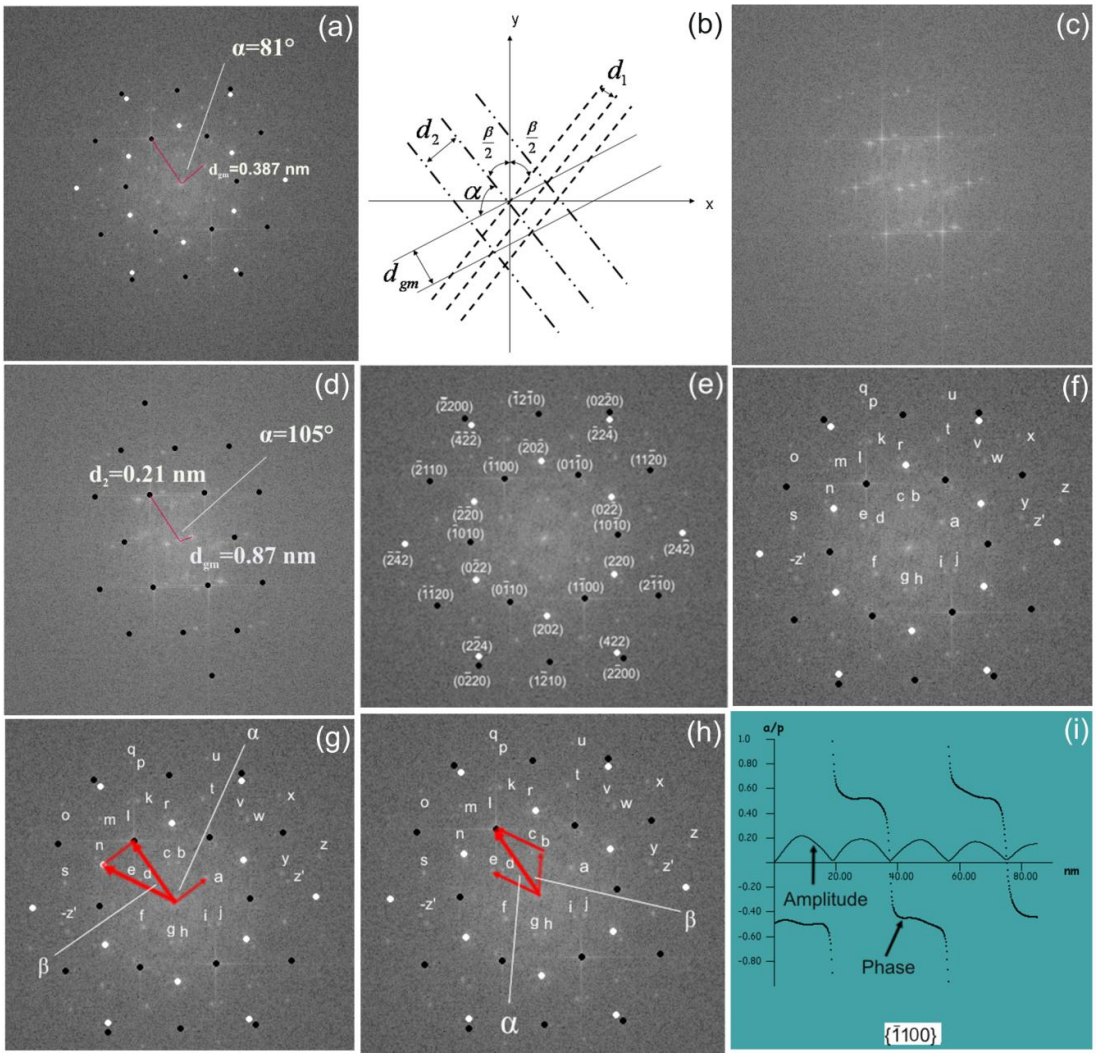


**Figure 4.6** (a) FFT analysis of the particle, indicated with the white box in figure 4.3(c): the angle α is the angle between moiré interference fringes with respect to BN lattice fringes; the spacing of moiré fringes $d_{gm}$. (b) An illustration of geometry relations of angle and d spacing definition in equation (4.1) and (4.2). (c) FFT of a different particle, indicated with a red box in figure 4.3(c). (d) FFT analysis of panel c: the angle α is the angle between moiré interference fringes with respect to BN lattice fringes; the spacing of moiré fringes $d_{gm}$. (e) Plane index of real reflections from BN and nanocrystal. The white spots indicate Mn doped ZnSe nanocrystal reflections with plane index (hkl), black spots indicate BN reflections with plane index (hkil). (f) Selected double diffraction spots are labelled with letters and higher order diffraction spots due to the diffracted beam from one crystal re-diffracted several times in another crystal. Only half of the patterns are labelled due to the symmetry of these reflection spots. (g) An example of vector analysis of double diffraction spot, $\bar{a} = (\bar{1}100)_{BN} - (\bar{2}\bar{2}0)_{ZnSe}$ with a rotation angle β between BN and nanocrystal, and the rotation angle α of the moiré fringes with respect to bottom crystal BN. (h) An example of vector analysis of triple diffraction spot, $\bar{e} = (\bar{1}100)_{BN} - \bar{b}$ with a rotation angle β between BN and Mn doped ZnSe nanocrystal, and the rotation angle α of the moiré fringes with respect to bottom crystal BN; (i) Pendellösung plot of BN sheets $\{\bar{1}100\}$ planes, with the thickness as x axis, amplitude and phase of the transmitted electron beam as y axis.

In order to analyze the real space images containing double-diffraction features quantitatively, a 2D FFT analysis is used in combination with the general formula[264] for the spacing of moiré fringes $d_{gm}$ given by equation (4.1).

$$d_{gm} = \frac{d_1 d_2}{\sqrt{(d_1 - d_2)^2 + d_1 d_2 \beta^2}} \tag{4.1}$$

The angle β is the rotation angle between the nanocrystal and the BN sheet. $d_1$ is the top crystal d spacing along this zone axis. $d_2$ is the bottom crystal d spacing along this zone axis. $d_{gm}$ is the spacing of the moiré fringes from the double-diffraction.

From figure 4.4(c), we obtain the following experimental data. $d_1=d_{Znse(220)}=0.198$ nm, $d_2=d_{(BN)}=0.21$ nm, and $\beta=30^o$. By putting these experimental data into equation (4.1), the value is obtained as $d_{gm}=0.39$ nm. Then, we apply the FFT of the particle, indicated in white box in figure 4.3(c) to measure $d_{gm}$ experimentally. The experimental value of $d_{gm}$ from the measurement in figure 4.6(a) is $d_{gm}=0.387$ nm. The theoretical calculated value matches the experimental value well. However, when other particles on the BN sheets are analyzed, it is sometimes difficult to measure the angle β, when the reflections from nanocrystals are extremely weak and no distinct spots are observed in the 2D FFT.

An equivalent approach uses the angle between the spots associated with double-diffraction and the spots from the BN sheets in the 2D FFT. To elucidate which lattice planes in

the two phase crystal composite contribute to the double-diffraction process, with the angle defined in figure 4.6(b), equation (4.2) is defined here.

$$\frac{d_1}{\sin(\alpha+\beta)} = \frac{d_2}{\sin\alpha} \tag{4.2}$$

The angle α is the rotation angle between the spots associated with the double-diffraction and the bottom crystal. An optical Moiré pattern can arise from simply overlapping two periodic structures.[265] However, a 2D FFT analysis would separate each periodic structure into their constituent frequencies and relative angular orientation and no new spots would be observed. In the case here, double diffraction leads to the production of new periodic patterns in the images that give rise to new spots in the 2D FFT analysis.[266]

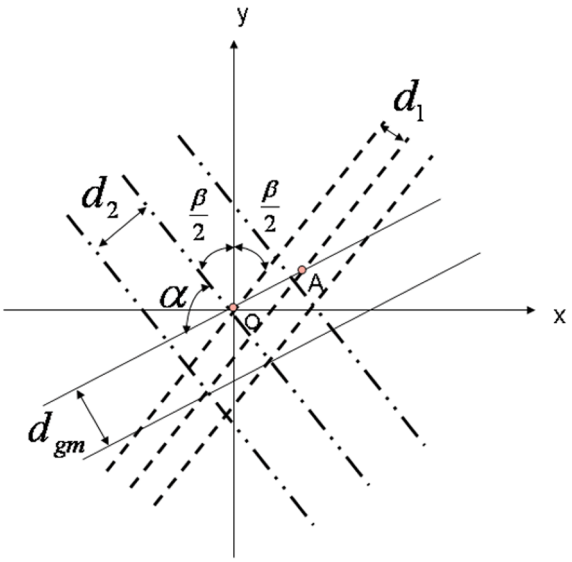


**Figure 4.7** Geometry relations between moiré fringes and d spacing of two crystals indicated in figure 4.6(b).

The derivation of equation (4.2) is shown in figure 4.7. Following the geometry relationship in figure 4.7, the distance OA can be written in terms of the two d spacing of the two crystals:

$$\overline{OA} = \frac{d_1}{\sin[\pi - (\alpha + \beta)]} = \frac{d_2}{\sin \alpha} \tag{4.3}$$

Thus, $$\frac{d_1}{\sin(\alpha + \beta)} = \frac{d_2}{\sin \alpha} \tag{4.4}$$

Another example is shown in figure 4.6(c), which is the FFT of the particle, indicated in the red box in figure 4.3(c). Figure 4.6(d) is the 2D FFT analysis of figure 4.6(c), with black spots indicating reflections from the BN sheets. The experimental data from measurement is $d_{gm}$=0.87 nm, $d_2$=0.21 nm and α = 105°, which are indicated in figure 4.6(d). This data of $d_{gm,}$ $d_2$, and α can be put into both equation (4.1) and (4.2) and solved to give $d_1$. The calculated value of $d_1$ and β for figure 4.6(d) is $d_1$=0.193 nm and β=12.3°. By referring the calculated value to the XRD data of ZnSe nanocrystals, it matches $ZnSe_{(220)}$ d spacing. This means the strong moiré interference pattern of the particle, indicated with red box in figure 4.3(c), originates from the double-diffraction of {220} planes in Mn doped ZnSe quantum dots and BN atomic layers with the lattice rotation angle of 12.31° with respect to each other.

| Table 4.1. Vector analysis of high order diffraction spots | | |
|---|---|---|
| **Double diffraction spots** | BN planes (hkil) | Mn doped ZnSe planes (hkl) |
| **a** | $(\bar{1}100)$ | $(\bar{2}\,\bar{2}\,0)$ |
| **b** | $(10\bar{1}0)$ | (220) |
| **c** | $(\bar{1}010)$ | $(0\bar{2}2)$ |
| **d** | $(01\bar{1}0)$ | $(02\bar{2})$ |
| **f** | $(1\bar{1}00)$ | (220) |
| **g** | $(\bar{1}010)$ | $(\bar{2}\,\bar{2}\,0)$ |
| **h** | $(10\bar{1}0)$ | $(02\bar{2})$ |
| **i** | $(0\bar{1}10)$ | $(0\bar{2}2)$ |
| **k** | $(01\bar{1}0)$ | (220) |
| **o** | $(\bar{1}100)$ | (220) |
| **q** | $(\bar{1}100)$ | (202) |
| **s** | $(\bar{1}100)$ | $(02\bar{2})$ |
| **t** | $(\bar{1}100)$ | $(0\bar{2}2)$ |
| **u** | $(01\bar{1}0)$ | (202) |
| **w** | $(10\bar{1}0)$ | (202) |
| **x** | $(01\bar{1}0)$ | $(0\bar{2}2)$ |
| **y** | $(01\bar{1}0)$ | $(\bar{2}\,\bar{2}\,0)$ |
| **z** | $(10\bar{1}0)$ | $(0\bar{2}2)$ |
| **Higher order diffraction spots** | BN planes (hkil) | Double diffraction spots |
| **e** | $(\bar{1}100)$ | b |
| **j** | $(10\bar{1}0)$ | a |
| **l** | $(\bar{1}100)$ | h |
| **m** | $(\bar{1}100)$ | i |
| **n** | $(01\bar{1}0)$ | z’ |
| **-p** | $(1\bar{1}00)$ | r |
| **r** | $(\bar{1}100)$ | f |
| **-v** | $(\bar{1}010)$ | r |
| **-z’** | $(\bar{1}100)$ | w |
| **General form for vector analysis, the n order diffraction vector $g_n=\{\bar{1}100\}_{BN}-g_{n-1}$** | | |

**Table 4.1** Vector analysis of high order diffraction spots labelled in figure 4.6(f), this indicates the interference planes to give these higher order diffraction spots, the general form for n order diffraction vector is $g_n=\{\bar{1}100\}_{BN}-g_{n-1}$.

In order to understand the origins of all the reflections in figure 4.6(a), a vector analysis is performed for all double diffraction spots in the 2D FFT. Planes from BN sheets with space group

$P6_3/mmc$ along the zone axis [0001] are carefully indexed with (hkil) system, which are shown in figure 4.6(e). Also, the plane index of Mn doped ZnSe nanocrystals with a space group $F\bar{4}3m$ along the $[\bar{1}11]$ zone axis is shown in figure 4.6(e). The double diffraction spots originating from the interference of the two crystals are labelled with different letters in figure 4.6(f). An example of the vector analysis of a double diffraction spot is shown in figure 4.6(g). The generation of double diffraction spot *a* can be assigned as $\bar{a} = (\bar{1}100)_{BN} - (\bar{2}\bar{2}0)_{ZnSe}$. This means the double diffraction spot *a* is generated by the interference between the $(\bar{1}100)$ plane in BN and the $(\bar{2}\ \bar{2}\ 0)$ plane in Mn doped ZnSe nanocrystals. The primary diffracted beam from the $(\bar{2}\ \bar{2}\ 0)$ plane in Mn doped ZnSe nanocrystals acts as an incident beam for BN and is diffracted for a second time by the $(\bar{1}100)$ plane of BN to give this double diffraction spot *a*. The rotation angle β =30°, is measured as the angle between the vectors $(\bar{1}100)$ and $(\bar{2}\ \bar{2}\ 0)$, shown in figure 4.6(g). The angle α=81°, the angle between moiré fringes and BN, is measured as the angle between vector *a* and $(\bar{1}$ 100), also shown in figure 4.6(g). For the higher order of diffraction, an example is shown in figure 4.6(h). The triple diffraction spot e can be assigned as $\bar{e} = (\bar{1}100)_{BN} - \bar{b}$. This indicates that the double diffracted beam from spot *b* is diffracted again by the $(\bar{1}100)$ in BN to give this triple diffraction spot *e*. The rotation angle β=39.50° is measured as the angle between vector $(\bar{1}100)$ and vector b. The angle α=30.30° is measured as the angle between the vector e and vector $(\bar{1}100)$. The $d_1$ is the d spacing of *b* vector, which is measured as $d_1$=0.39 nm. The $d_2$ is the d spacing of $\{\bar{1}$ 100} planes in BN, which is measured as $d_2$ =0.21 nm. Thus, the calculated value for spot *e*,

$d_{gm}$=0.32 nm, fits the experimental value $d_{gm}$=0.32 nm. The vector assignments of all the other double diffraction or higher order diffraction spots are shown in table 4.1. For the double diffraction spots, they can be assigned as $g_2$= $\{\bar{1}100\}_{BN}$-$\{220\}_{ZnSe}$, which indicates that they originate from the $\{\bar{1}100\}$ plane family in BN and the {220} plane family in ZnSe. For the triple diffraction spots, they can be assigned as $g_3$= $\{\bar{1}100\}_{BN}$-$g_2$, which means the triple diffraction spots are coming from the double diffracted beam to be re-diffracted again with $\{\bar{1}100\}$ set of planes in BN. Thus, the general form for the high order diffraction spots can be assigned as $g_n$= $\{\bar{1}100\}_{BN}$-$g_{n-1}$.

Higher order diffracted beams exhibits Pendellösung oscillations, which arise from a periodic exchange between wave fields inside the crystals. The characteristic distance from the resulting beating effects is known as the pendellösung length.[267] In the perfect crystals with parallel faces, the pendellösung effect depends on the thickness.[268] A Pendellösung plot shows the amplitude and phase of the transmitted electron beam as a function of thickness. The Pendellösung plot of the $\{\bar{1}100\}$ BN planes is calculated and presented in figure 4.6(i). The reflection amplitude of a transmitted beam should give contrast exceeding 10% in order for it to be observed on recorded images[269] and this occurs when the thickness is within the range of 5 nm to 15 nm. This is consistent with the thickness of BN sheets.

### 4.5.3. Reconstruction of Images

After careful analysis of both optical and double-diffraction moiré interference patterns, the equation method and vector method can be combined to understand the origins of all the reflections in the 2D FFT patterns quantitatively. Now it is time to reconstruct images using appropriate masks in the 2D FFT. Figure 4.8(a) is the crystal from the white box in figure 4.3(a) and its 2D FFT is shown in figure 4.8(b). Figure 4.8(d) presents the reconstructed image using the FFT mask in figure 4.8(c) to show only the atomic structure from the nanocrystal and the surrounding surface capping ligands. This enables us to image the nanocrystal as if it was suspended in free-space with minimal background effect.

Figure 4.8(f) shows the optical moiré pattern generated by the two sets of lattices from the BN and Mn doped ZnSe nanocrystals, with the 2D FFT mask used in figure 4.8(e). The double-diffraction spots are excluded using this mask. Figure 4.8(h) shows the moiré pattern produced by only considering the spots in the 2D FFT associated with double-diffraction, with the mask indicated in figure 4.8(g). Figure 4.8(h) shows subtle new features in moiré interference patterns due to double or higher order diffraction processes. This demonstrates that multiple diffraction events in composite nanomaterials give structure and contrast in the real space image, which is different from the optical moiré patterns arising from two overlapping period structures.

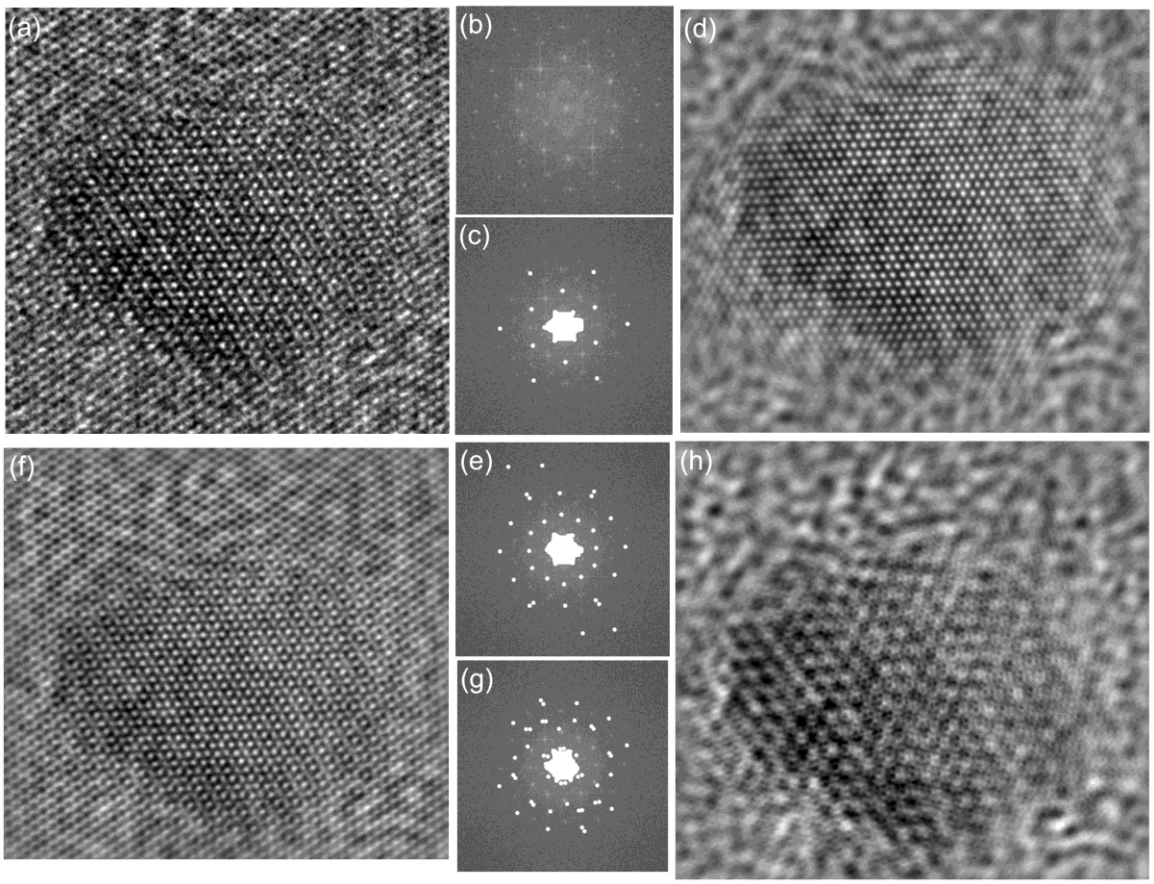


**Figure 4.8.** (a) Single crystal from the white box in figure 4.3(c). (b) 2D FFT of panel a; (c) Mask applied to 2D FFT to reconstruct nanocrystals with ligands and eliminating BN lattice and double diffraction and high order diffraction spots, white spots indicate region included. (d) Reconstructed HRTEM image generated from 2D FFT mask in panel c, with Mn doped ZnSe nanocrystal and ligands remained. (e) Mask applied to 2D FFT to reconstruct optical moiré fringes, which is only the overlap of two set of crystal lattice from BN and ZnSe, white spots indicate region including reflections from BN and ZnSe lattices. (f) Reconstructed optical moiré patterns, generated from 2D FFT mask in panel e, which indicates the optical overlapping of two lattices. (g) Mask applied to 2D FFT to reconstruct moiré patterns from double or higher order diffraction process, white spots indicate region included. (h) Reconstructed moiré interference pattern generated from 2D FFT mask in panel g.

## 4.6. Conclusions

In summary, a simple method is used to get BN sheets that were ultrathin and both faceted and round in their shape. These BN sheets are effective as a novel carbon-free thin TEM support for high resolution imaging of nanocrystals. Low voltage aberration-corrected HRTEM is used to investigate Mn doped ZnSe nanocrystals on the BN sheets. It was shown that the phase contrast images exhibit moiré patterns from both optical effects and double-diffraction effects. A method is developed to analyze the orientation of the nanocrystals with respect to the BN lattice. These results demonstrate the importance of using 2D FFT analysis to understand the details of the contrast and structure observed in phase contrast images obtained using low-voltage aberration-corrected HRTEM.

The study in this chapter demonstrates single crystalline BN sheets could be fabricated as a carbon free TEM ultrathin supporting film to study atomic configuration of other nanomaterials, for example Mn doped ZnSe quantum dots. Liquid phase exfoliation method is good enough is to produce uniform single crystalline 2D sheets. However, it only produces μm size film, thus not good enough to get large area single crystals 2D atomic crystals for industrial applications.

# Chapter 5:

# Growth Dynamics of Few Layer Graphene Domains on Copper by Atmospheric Pressure Chemical Vapour Deposition

## 5.1. Introduction

In the previous chapter, utilizing boron nitride sheets as thin support for high resolution imaging of nanocrystals has been discussed and the open question 2 was answered. Chapter 4 showed that chemical exfoliation is not good enough to get large area single crystal 2D atomic crystals for industrial applications. Another approach, which is chemical vapour deposition (CVD), is tried as an alternative method to achieve this goal. In order to achieve this target, the growth dynamics need to be explored first. Thus, in this chapter, the discussion will be focused to answer the open question 3, what is the growth mechanism of graphene using CVD and why polycrystalline graphene is normally produced using CVD.

Graphene is a 2D atomic crystal that exhibits remarkable optical and electronic properties with great potential in electronic device[4, 270] and many other applications.[6, 25] Metal catalyzed CVD is one of the most promising methods to fabricate large area graphene films for commercial applications, such as integration with current CMOS technology[4, 270-272] and transparent conducting electrodes[273-275]. Cu is one of the most promising catalysts for industrial scale fabrication of graphene film using CVD due to its low cost, large grain size, etchability, and their wide use and acceptance by semiconductor industry.[113] Growth of graphene at atmospheric pressure has the benefit of not needing vacuum conditions that are harder to implement on the large scale necessary for industrial development. Thus, to understand the growth mechanism of graphene by Cu catalyzed APCVD (atmospheric pressure chemical vapour deposition) is important. This is different from the graphene growth in Cu catalyzed LPCVD (low pressure chemical vapour deposition)[99, 112, 208, 276-279] by which excellent results have shown in producing monolayer[208, 276-277] and bilayer graphene.[278-279] The mechanism of graphene growth by LP-CVD has been studied by isotope labelling[113] and a two step CVD process.[112] However, to date, there are only a few studies of the growth dynamics of graphene and FLG on Cu foils using AP-CVD. These progresses of the synthesis of graphene using atmospheric pressure (AP) CVD[99, 205-206, 280] has shown the growth is not always self-limiting to monolayer graphene and indicates complex growth dynamics are at play. Bhaviripudi *et al.* have investigated how methane concentration influences the number of graphene layers using AP-CVD and found that reducing methane concentration led to a reduced

number of layers.[206] They studied the polycrystalline continuous network of merged graphene domains formed from long growth times (20-30 minutes).[206] Yao *et al.* investigated the effect of various ratios of carbon source to hydrogen gas in AP-CVD using a Cu catalyst on the final polycrystalline continuous graphene 2D film using optical imaging and Raman spectroscopy.[280] They found that reducing the amount of carbon source led to improved film quality.[280] They also studied the use of a variety of carbon precursors and found that liquid precursors, such as hexane, were effective in growing graphene on Cu catalysts.[280] Luo *et al.* also found that reducing the concentration of carbon precursor, in this case methane, led to improved graphene quality for AP-CVD using Cu catalyst.[205] They also demonstrated that improving the surface morphology of the Cu by removing the copper oxide surface layer and reducing roughness using electropolishing methods led to improved graphene film formation.[205] However, little information was obtained about the initial stage of nucleation process of individual domains before them emerging together as a continuous film, which is essential for building a deeper picture of the growth dynamics and understanding the polycrystalline nature of the 2D film that the domains grow to form.

Also, to date, there is very little knowledge regarding how the Cu lattice plays a role for the growth dynamics of graphene and few-layer graphene (FLG) on Cu foils using AP-CVD as well. Wofford *et al.* investigated the interplay of Cu foil and graphene under low pressure (LP) by in-situ low-energy electron microscopy.[208] They found that four lobe polycrystalline graphene domains grew on a pronounced Cu (100) textured surface with random orientation to the Cu

grain.[208] A growth mode dominated by edge kinetics with an angular dependent growth velocity is suggested as the growth mechanism for this type of four lobe polycrystalline graphene,[208] which is also observed by the work of the Ruoff group.[112-113] Rasool *et al.* studied the continuity of graphene on polycrystalline copper synthesized by LP-CVD.[281] They suggest the morphology and atomic arrangement of the underlying Cu foil do not affect the atomic arrangement of graphene.[281] The growth of graphene on single crystal Cu (111) in an ultrahigh vacuum chamber has been studied by scanning tunnelling microscopy.[209] They find the random shapes of graphene domains nucleate on Cu lattice with either 7º or 0º misorientation angle, which leads to numerous domain boundaries when domains emerge into continuous film.[209] This can dramatically reduce the carrier mobility of graphene grown by LP-CVD.[209] Zhao *et al* studied the graphene grown on Cu (111) and (100) under high vacuum by STM.[282] They found that graphene had a hexagonal superstructure on Cu (111) while a linear superstructure appeared on Cu (100).[282]

Here, individual FLG domains are examined before they merge together by limiting the growth time. This enables characterization of the nucleation density, domain shape and size, number of layers and crystal structure. In particular it is studied that the onset temperature of FLG nucleation, the large scale alignment of FLG domains, the hydrogen pre-treatment effect and cooling rate effect on the FLG nucleation. It is found the temperature has to be at least 960 °C in order to form micron sized hexagonal FLG domains. By increasing the quality of Cu foil catalyst and also controlling the growth temperature, hexagonal single crystal domains of few layer

graphene are produced that are highly aligned in their crystallographic orientation over a 5 mm distance scale. It is necessary to have hydrogen pre-treatment for the nucleation of FLG. The fast cooling rate will lead to more homogenous nucleation than the slow cooling rate. To understand this nucleation process, including onset temperature, nucleation sites, nucleation density, nucleation morphology and orientation of nucleation domains, is crucially important.

Also, it is investigated that the role Cu lattice has on the growth dynamics of FLG domains at atmospheric pressures in CVD. It is shown that reducing the growth temperature from 1000 $^{o}$C down to 980 $^{o}$C changes the growth dynamics of the system and enables the Cu lattice to start to play a role in the crystal growth. For the first time it is shown that the growth of aligned rectangular shaped FLG domains that form only on Cu (111) grains at 980 $^{o}$C. Hexagonal FLG domains are shown to grow on nearly all non-(111) Cu lattice planes. This reveals that the atomic structure of Cu does indeed play a role in the growth dynamics of graphene even at atmospheric pressure when the conditions such as temperature are appropriate. The study in this chapter will provide general principles to control the quality of large area graphene and be high beneficial for industrial production of graphene based applications.

## 5.2. Experimental Methods

### 5.2.1. Atmospheric Pressure (AP) CVD Growth of Few Layer Graphene

1 $cm^2$ copper foils of 99.999% purity and 0.1 mm thickness (Alfa Aesar) were loaded into a quartz tube and rested just outside the hot-zone in a horizontal split-tube furnace. After purging the whole system with argon gas, volume ratio 1:3 $H_2$:Ar gas mix at 600 sccm flow was introduced into the system and continued throughout the graphene synthesis and cooling. The temperature of the furnace was adjusted to the desired value for annealing and growth (*i.e.* 1000 °C, 990 °C, 980 °C). Once the furnace reached the desired temperature, the quartz tube was shifted so that the copper foil was moved to the hot-zone in the furnace, where it was annealed and reduced for 0.5 hour hydrogen pre-treatment time. Then, volume ratio 1:4 $CH_4$:Ar gas mix was introduced at a flow rate of 10 sccm for 3 minutes growth time. It means the volume ration is 1:75:229 $CH_4$:$H_2$:Ar during the reaction. The sample was then rapidly cooled to room temperature with an average cooling rate of 40 (°C/minute), which is shown in figure 5.1 describing the time dependence of experimental parameters, by removing them from the hot zone of the furnace under a hydrogen and argon atmosphere.

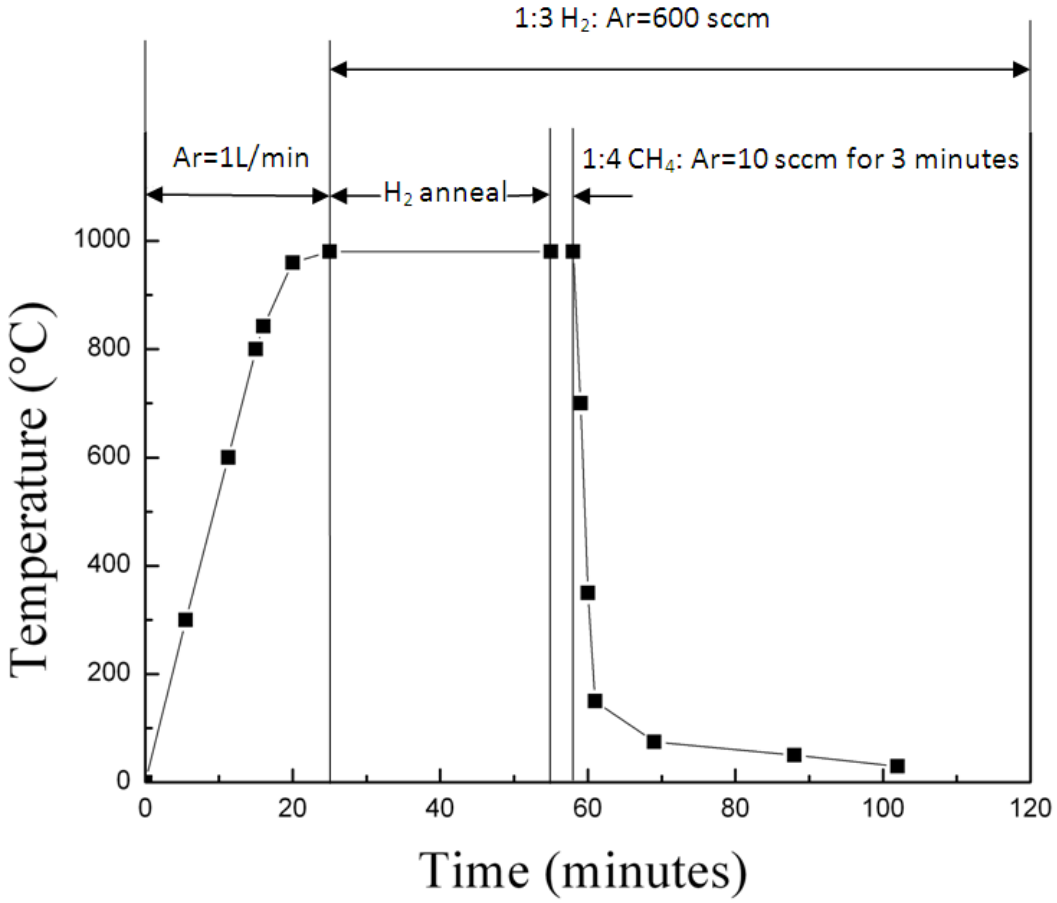


**Figure 5.1.** Time dependence of experimental parameters

### 5.2.2. Transfer Method of CVD Graphene

A PMMA supportive scaffold (8% wt. in anisole, 495k molecular weight) was spin cast onto the graphene surface on copper foil. A spin speed of 4700 rpm was used for 60 seconds, with the film then cured by heating at 180 °C for 90 seconds. Then underlying copper was etched away over night by an iron (III) chloride solution. The graphene/PMMA film was then rinsed in deionised (DI) water several times until the water was colourless. Then the graphene/PMMA film was

transferred to hydrochloric acid (30%) for 5 minutes to remove iron chloride residue and then transferred to a DI water bath to remove the residue of hydrochloric acid.

Then a perforated $Si_3N_4$ TEM grid (2 μm holes) was adhered to a glass slide with a gel film (Gel-Pak gel-film WF-40-X8-A) and the graphene/PMMA film was transferred onto it. A razor blade was used to cut out and lift off the TEM grid to another glass slide and then another drop of PMMA/anisole solution was applied to the TEM grid as a second layer of PMMA on graphene. This second layer of PMMA should help dissolve the previous layer of PMMA[275] and let the graphene relax onto the TEM grid overnight. The TEM grid on the glass slide was then put into a petri dish filled with acetone to remove most of the PMMA in two hours. Then the TEM grid was placed in the furnace in air at 350 °C for 4 hours.

### 5.2.3. Characterization

Scanning electron microscopy (SEM) was performed with a Zeiss NVison 40 FIB-SEM operating at 2 kV. Electron backscatter diffraction (EBSD) measurements were performed with JEOL 6500F at 20 kV. Raman spectra were taken using a JY Horiba Labram Aramis imaging confocal Raman microscope with a 532 nm frequency doubled Nd:YAG laser. Transmission electron microscopy and selective area electron diffraction were performed using a JEOL 4000EX TEM operating at an accelerating voltage of 80 kV.

## 5.3. The Nucleation of Few Layer Graphene Domains on Copper Surface

### 5.3.1. Temperature Threshold for the Nucleation of Graphene Domains

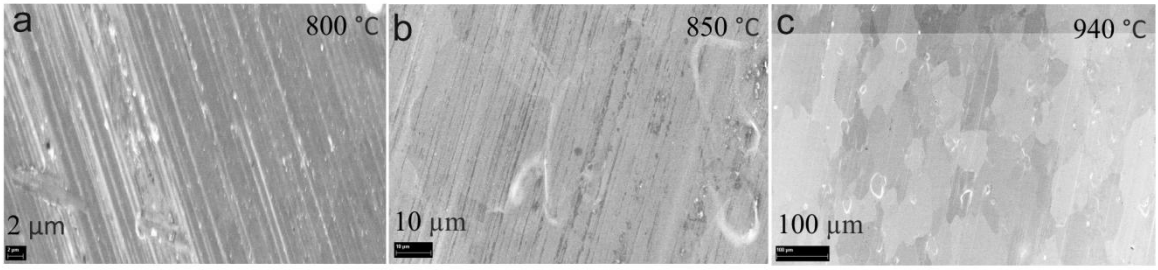


**Figure 5.2.** The SEM image of the reaction taken at (a) 800 °C, (b) 850 °C and (c) 940 °C, indicating no graphene is nucleated in this temperature range. The scale bar from (a)-(c) are 2 μm, 10 μm, 100 μm, respectively.

In previous work, Cu foils of 99.8% purity were used.[112-113, 276-277, 283] Here, higher quality Cu foils of 99.999% purity were used with increased thickness from 0.025 mm to 0.1 mm. The temperature dependence of the FLG growth was investigated by varying the reaction temperature within the range of 800 ºC to 1000 ºC, while keeping constant 30 minute hydrogen pre-treatment time and 3 minute growth time. For the temperature range of 800 ºC to 940 ºC no black contrast, typically associated with graphene or FLG, was observed on the Cu foil using a SEM operating at 2 kV using an in-lens detector which is shown in figure 5.2. It shows the SEM images of the samples of 800 °C, 850 °C, and 940 °C. No black contrast is shown in these images which indicate no FLG nucleates within this temperature region. From the temperature range of 950 ºC to 1000 ºC, black

contrast appeared on the bright white Cu background in the SEM images, shown in figure 5.3 for (a) 950 ºC, (b) 960 ºC, (c) 970 ºC, (d) 980 ºC, (e) 990 ºC, and (f) 1000 ºC. Well defined domains appear between 970 ºC to 1000 ºC.

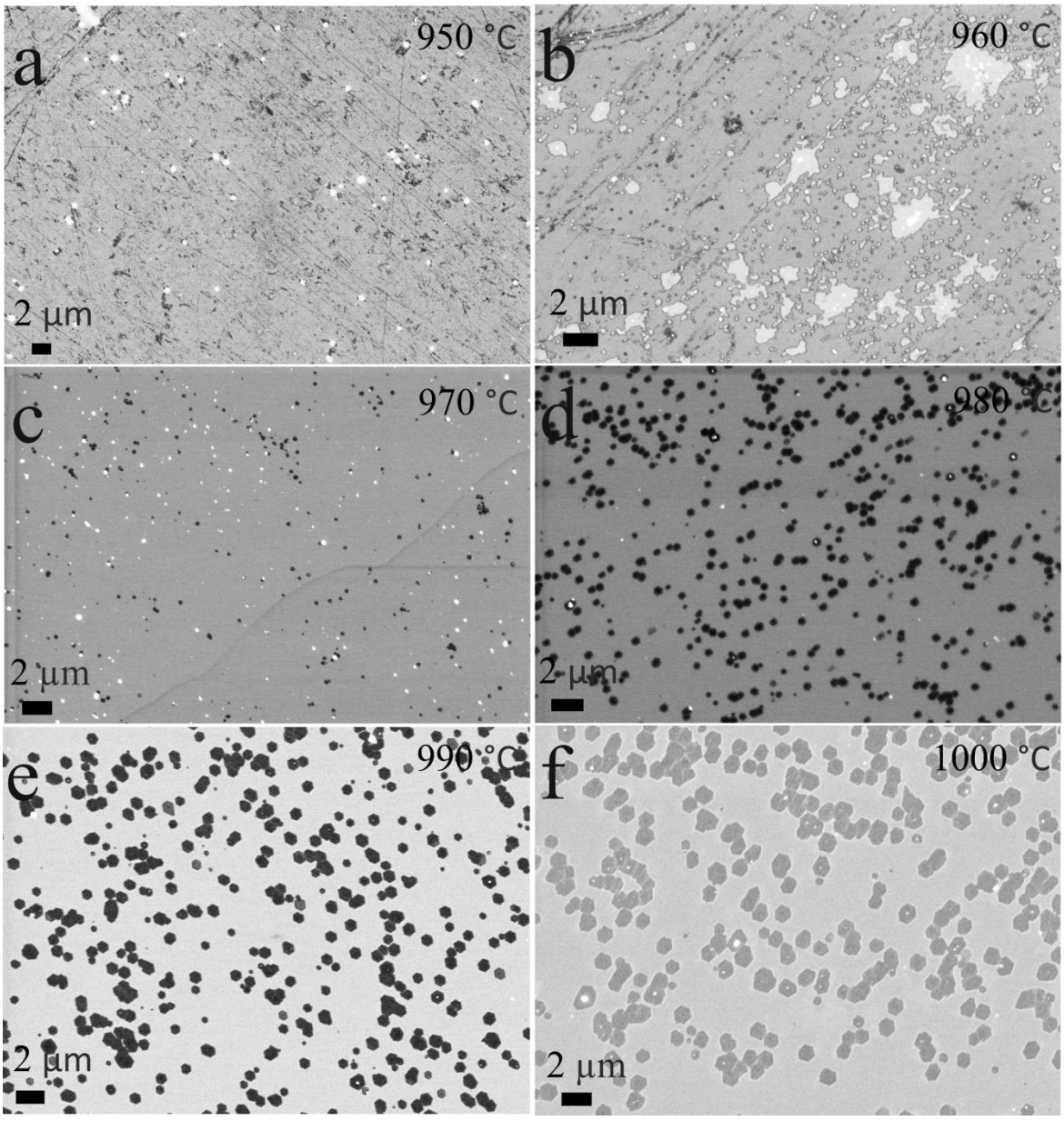


**Figure 5.3.** SEM images of the nucleation of graphene domains with different reaction temperatures: (a) 950 ºC (b) 960 ºC (c) 970 ºC (d) 980 ºC (e) 990 ºC (f) 1000 ºC. The scale bars in (a)-(f) are all 2 µm.

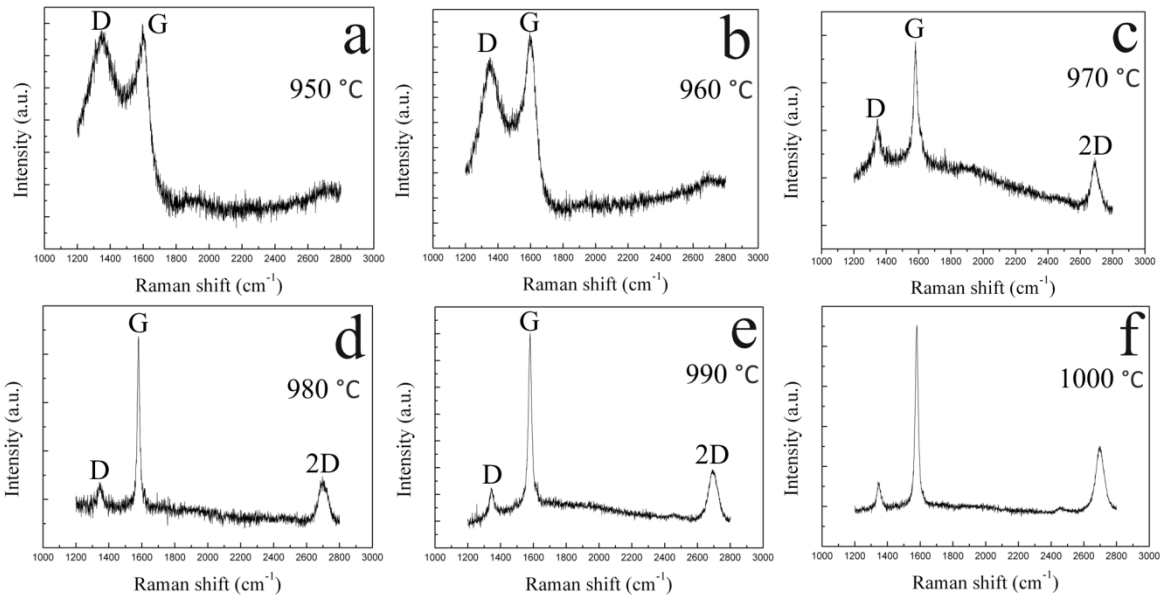


**Figure 5.4.** Raman spectra from the samples with corresponding reaction temperatures shown in figure 5.3: (a) 950 ºC (b) 960 ºC (c) 970 ºC (d) 980 ºC (e) 990 ºC (f) 1000 ºC.

In order to verify whether the dark contrast region is graphene or FLG, Raman spectroscopy was performed on the samples shown in figure 5.3. The Raman spectra for each respective temperature are shown in figure 5.4, with (a) 950 ºC, (b) 960 ºC, (c) 970 ºC, (d) 980 ºC, (e) 990 ºC, and (f) 1000 ºC. Figures 5.4(a)-(b) show a large D peak at 1345 $cm^{-1}$ and a G peak at 1600 $cm^{-1}$, which is about a 20 $cm^{-1}$ shift from the normal graphene G peak. The characteristic 2D peak of graphene/FLG at around 2700 $cm^{-1}$ is not observed in figures 5.4(a) and (b). In comparison, figures 5.4(c)–(f) show a distinct D peak at ~1345 $cm^{-1}$, G peak at ~1580 $cm^{-1}$ and 2D peak at ~2700 $cm^{-1}$, which are typical for few-layer graphene samples. The intensity peak ratio $I_D/I_G$ is 0.96 in figure 5.4(a), and decreases to 0.81 in figure 5.4(b) and then to 0.40 in figure 5.4(c), while the G peak position $\omega_G$ changes from 1600 $cm^{-1}$ to 1580 $cm^{-1}$. This decreasing of both $I_D/I_G$ and the

shift of $\omega_G$ to lower wave numbers is attributed to a transition from small nanocrystalline FLG domains to larger FLG domains.[284]

The reaction time was then further increased from 3 minutes to 20 minutes to evaluate the increase in size of the FLG domains with growth time.[283] Figure 5.5(a) shows a SEM image of a sample at 950 ºC reaction temperature for 20 minutes reaction time. Some regions of dark contrast are visible. The corresponding Raman spectrum of figure 5.5(a) is presented in figure 5.5(d), and shows a D peak at 1345 $cm^{-1}$ and a G peak at 1600 $cm^{-1}$ with no 2D peak observed. This is similar to the Raman spectrum taken after only 3 minutes growth, shown in figure 5.5(a), but with $I_D/I_G$ decreasing slightly to 0.79. This indicates that the domains formed at 950 ºC are still nanocrystalline graphite. Figure 5.5(b) shows a SEM image of a sample at 960 ºC reaction temperature after exposure to methane for 20 minutes. Hexagonal domains are seen in the image with a corresponding Raman spectrum shown in figure 5.5(e), indicative of few layer graphene with a D peak at ~1345 $cm^{-1}$, a G peak at ~1580 $cm^{-1}$ and 2D peak at ~2700 $cm^{-1}$. A continuous 2D FLG film was produced for a reaction temperature of 970 ºC with 20 minutes growth time, shown in the SEM image of figure 5.5(c) with corresponding Raman spectrum shown in figure 5.5(f). The Raman spectrum indicates it is few layer graphene with D peak at 1345 $cm^{-1}$, a G peak at 1580 $cm^{-1}$ and 2D peak at 2700 $cm^{-1}$. Comparing the samples grown at 950 ºC, 960 ºC and 970 ºC for 20 minutes, it could be concluded that micron sized FLG domains only start to form at a reaction temperature of 960 ºC, even with long growth times, and that the rate of growth of FLG material

increases with reaction temperature. The average nucleation density as a function of temperature has a maximum point at 980 ºC, which indicates the maximum activity of the catalyst under the conditions explored which is shown in section 5.3.6 for nucleation density analysis.

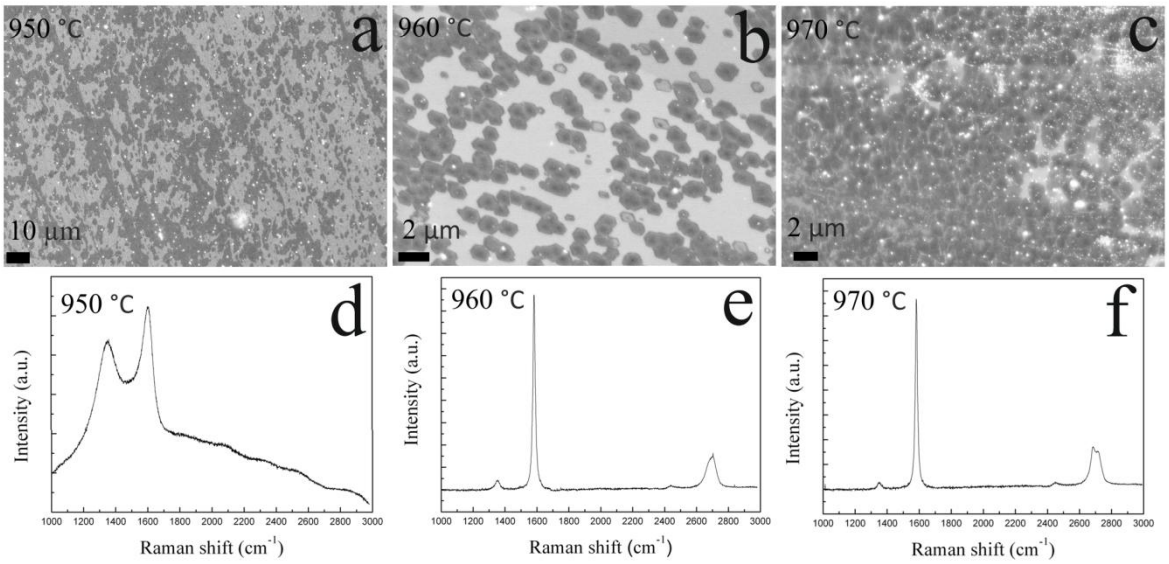


**Figure 5.5.** SEM images of samples after 20 minutes reaction time: (a) 950 ºC (b) 960 ºC (c) 970 ºC. Corresponding Raman spectra: (d) the sample shown in panel a. (e) the sample shown in panel b. (f) the sample shown in panel c. The scale bars in (a)-(c) are 10 µm, 2 µm, 2 µm, respectively.

### 5.3.2. Temperature Dependent Crystal Structure

In order to examine the thickness of the FLG domains, they were transferred to $Si_3N_4$ TEM grids using a PMMA film and high resolution transmission electron microscopy (HRTEM) was performed to examine the folded edges. It is important to evaluate how the FLG domains grown on the high purity 99.999% Cu foils compare to those reported that were grown on 99.8% purity Cu foils. Samples were examined with growth temperatures of 990 ºC, and 1000 ºC, and growth times of 3 minutes. The number of layers was determined by counting the lines of contrast of back-

folded edges. Figure 5.6(a)-(c) shows the HRTEM images of the edges of the graphene domains at a nucleation temperature of 1000 ºC, which varies from 2-4 layers, while the thickness of graphene domains grown at 990 ºC varies between 2-7 layers, as shown in figures 5.6(f)-4(h). These thickness values are comparable to those produced on the lower purity 99.8% foils.[283] A selected area electron diffraction (SAED) pattern of FLG domains at growth temperature of 1000 ºC is shown in figure 5.6(d) and at 990 ºC shown in figure 5.6(i). The SAED pattern shows the FLG domains are single crystal, with only six spots of reflection being observed in the inner hexagon of 0.21 nm lattice spacing. This indicates the crystal structure does not change when decreasing the nucleation temperature from 1000 ºC to 990 ºC or when using the higher purity Cu foils, *i.e.* they do not become turbostratic. The line profile along the green arrow indicated in figure 5.6(d) is shown in figure 5.6(e). The intensity ratio of outer peaks from equivalent planes $\{1\bar{2}10\}$ over inner peaks from $\{1\bar{1}00\}$ is approximately 4.8, which indicates it is not monolayer but AB stacked Bernal few layer graphene as the ratio of the outer peak to inner peak is larger than 1,[17, 278] most likely bilayer graphene for this particular domain chosen. The line profile along the blue arrow indicated in figure 5.6(i) is shown in figure 5.6(j). The intensity ratio of outer peaks from equivalent planes $\{1\bar{2}10\}$ over inner peaks from $\{1\bar{1}00\}$ is approximately 1.2, which indicate it is not monolayer or bilayer graphene, but AB Bernal stacked few layer graphene. Figure 5.6(k) shows a TEM image with the hexagonal shape of a FLG domain well resolved. The SAED pattern was taken on this single hexagon to elucidate not only the crystal structure but also the direction of

the lattice relative to the hexagon edges. Figure 5.6(l) presents the SAED and reveals they are single crystal structures with AB Bernal stacking. This was typical for all domains investigated. The direction of the spots in the SAED pattern indicates arm-chair lattice direction. Thus the SAED in figure 5.6(l) shows the edges of the hexagon are parallel to the zig-zag direction of the graphene lattice.

Selective area electron diffraction of temperature dependent sample is shown in figure 5.7(a)-(c). This indicates the crystal structure remains at AB Bernal stacking single crystal for 980 °C, 990 °C, and 1000 °C. The thickness of the samples is examined by high resolution electron microscopy, shown in figure 5.7(d)-(g).The thickness of the graphene domains is varying between 2-7 layers.

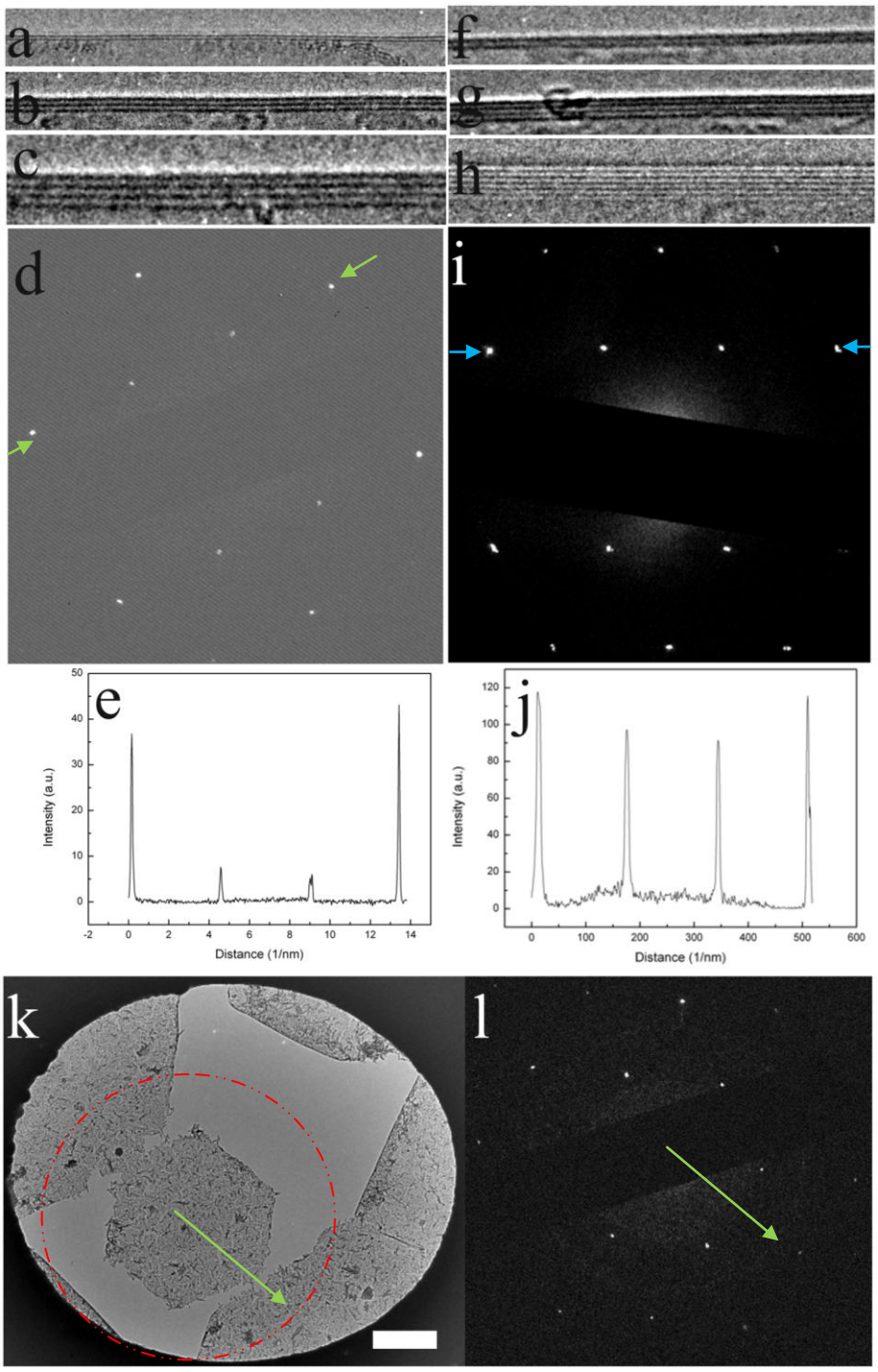


**Figure 5.6**. HRTEM images of the nucleation of graphene domains at 1000 ºC: (a) Bilayer. (b) Trilayers. (c)Four layers. (d) Selected area electron diffraction pattern taken from graphene domain. (e) Intensity profile along the green arrows in (d). HRTEM images of the nucleation of graphene domains at 990 ºC: (f) Bilayer. (g) Four layers. (h) Seven layers. (i) Selected area electron diffraction pattern taken from graphene domains. (j) Intensity profile along the blue arrows in (i). (k) Low-magnification TEM image showing a suspended FLG hexagon (indicated with red circle) on a holey $Si_3N_4$ membrane. (l) Selected area electron diffraction pattern taken from the single suspended hexagon in (k). Green arrows in (k) and (l) indicate the same zig-zag direction in both images. The scale bar in (k) is 0.5 µm.

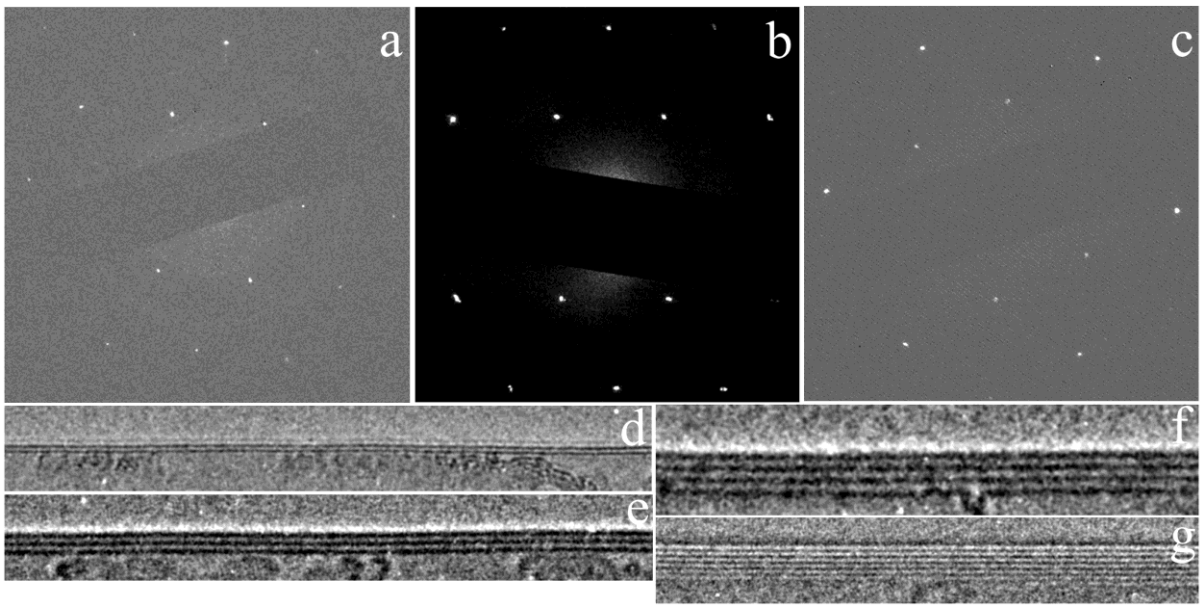


**Figure 5.7.** Selective area electron diffraction (SAED) of temperature dependent samples: (a) 980 °C (b) 990 °C (c) 1000 °C. High resolution electron microscopy (HRTEM) images of the edge of graphene domains: (d) Bilayers. (e) Trilayers. (f) Four layers. (g) Seven layers.

### 5.3.3. Alignment of Hexagonal Graphene Domains at Millimetre Scale

Figure 5.8(a) shows a SEM image of aligned domains of FLG grown at 990 ºC on the 99.999% Cu foil, with the red arrow indicating the alignment direction of the edges of the hexagons. From the analysis of the SAED patterns in figure 5.6(k)-(l), we know this direction corresponds to the zig-zag orientation of the graphene lattice. In order to confirm the long range alignment of the FLG domains we obtained SEM images at three different locations on the same Cu grain, figure 5.8(b) x, y = 41.8 mm, 64.9 mm, 5.8(c) x, y = 41.7 mm, 67.4 mm, and 5.8(d) x, y = 45.4 mm, 69.8 mm. All the coordinates are recorded with respect to the original point in SEM. These x y coordinates indicate the distance of sample movement. The distance between the SEM image in 5.8(b) and 5.8(d) corresponds to more than 5 mm which is shown in figure 5.9. Figure

5.9 shows a low magnification SEM image of the large Cu grain that exhibits alignment of the FLG hexagons over 5 mm range. Red arrows indicate regions examined by SEM at a higher magnification, resulting in a shadow effect from contamination during imaging. The regions for figure 5.8(b) and 5.8(d) lie beyond the field of view in figure 5.9. However, they are taken from within the same Cu grain as the two regions indicated with arrows in figure 5.9.

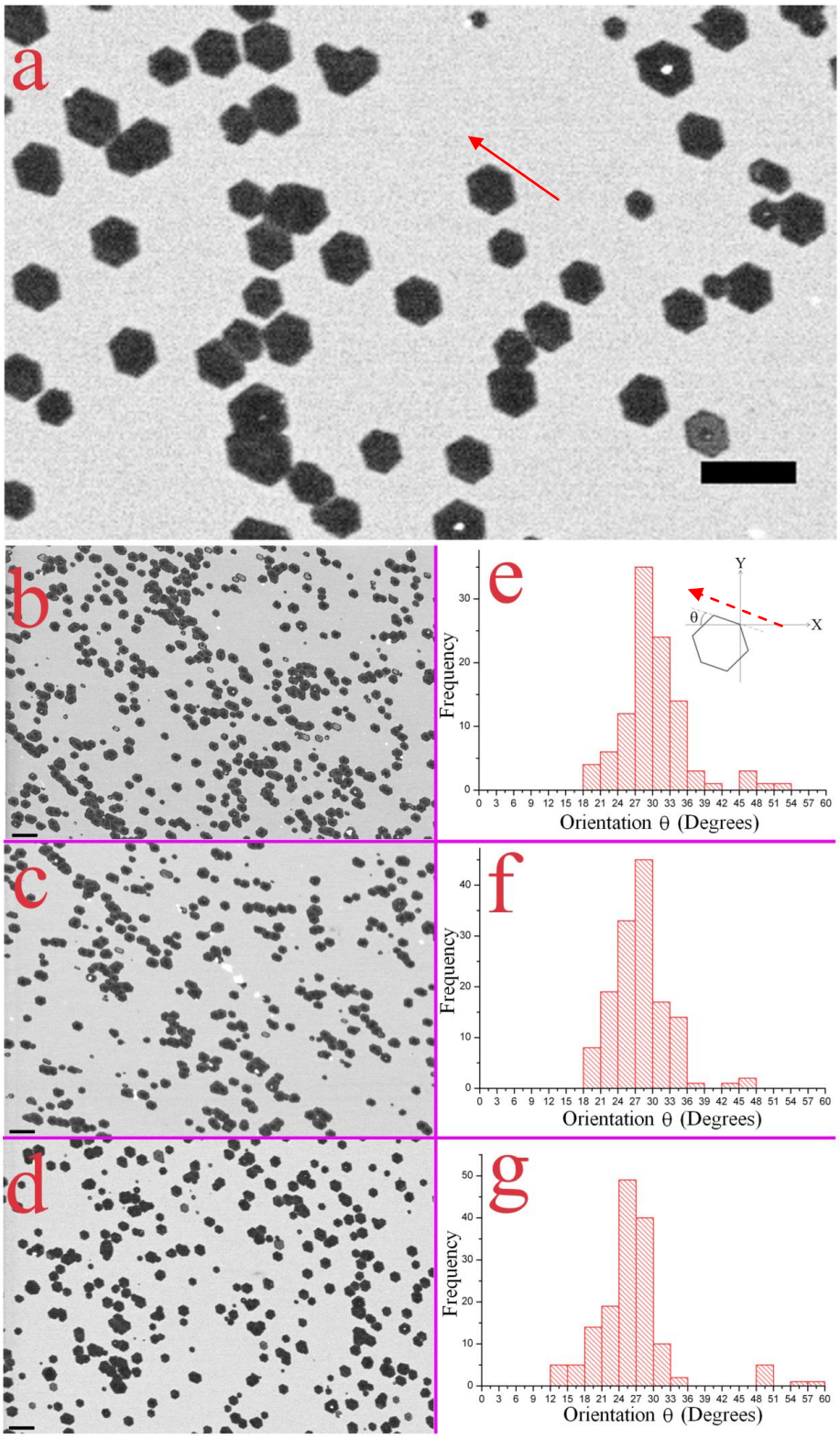


**Figure 5.8.** (a) SEM image (in-lens detector) showing alignment of the edges of few-layer graphene hexagons grown at 990 °C. (b) SEM image at position x, y = 41.8, 64.9 mm, (c) x, y = 41.7, 67.4 mm, and (d) x, y = 45.4, 69.8 mm. (e), (f) and (g) show the histograms of the orientation of the edge of the hexagons (θ) from the respective SEM images in (b), (c) and (d). Inset in (e) shows definition of (θ). Scale bar indicates 2 µm in all images.

Alignment of the edges of the hexagons is observed in all three cases. The FLG domains were tracked across the distance to ensure that the Cu domain was continuous and the alignment consistent and thus include the measurement taken in the middle, figure 5.8(c). The histograms presented next to each respective SEM image, figures 5.8(e), 5.8(f) and 5.8(g), plot the relative angle (θ) of the hexagons (defined in the inset of figure 5.8(e)), and shows the correlated orientations.

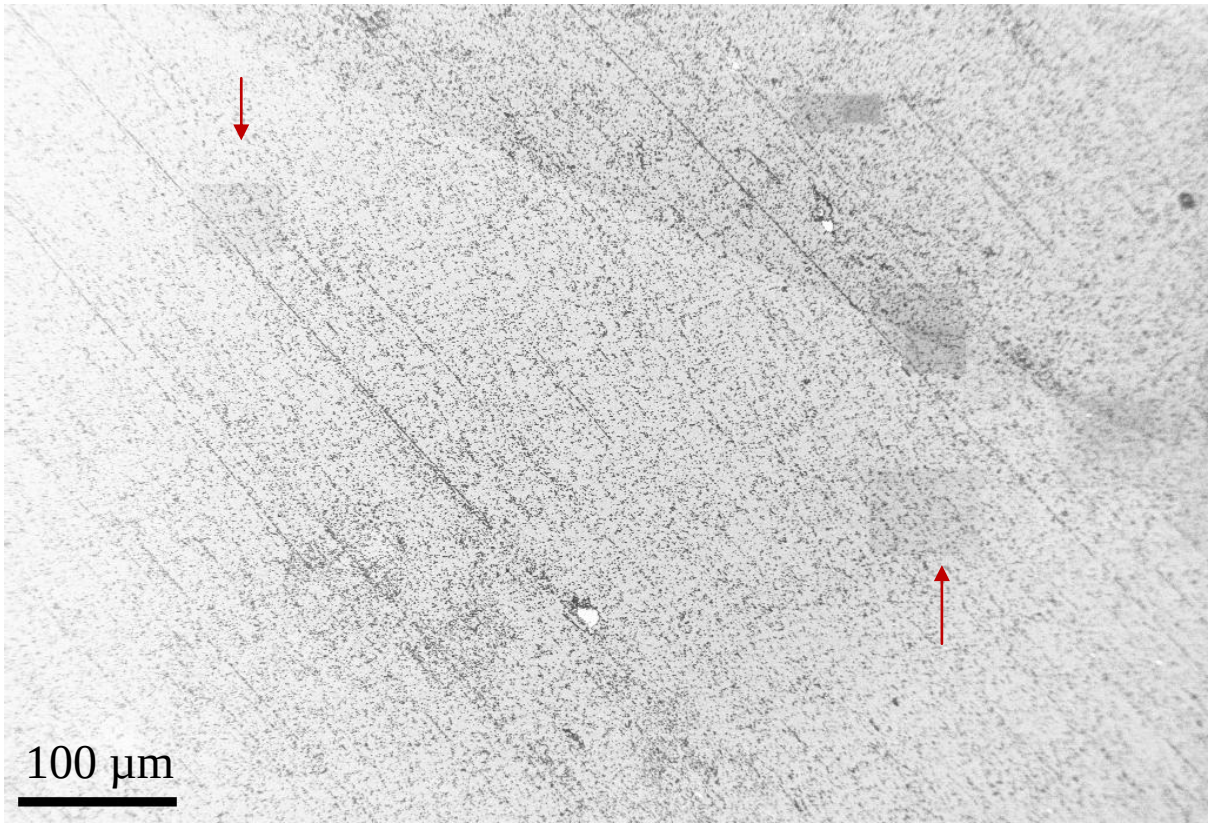


**Figure 5.9.** Millimetre scale alignment: SEM image of the large Cu grain with alignment of FLG hexagons over a 5 mm distance at 990 °C.

The ability to determine the alignment over such large distances is simplified by the hexagonal shape of the FLG domains, unlike previous reports of four-lobed graphene structures

grown at low-pressure.[112,208] Low magnification SEM is then used to scan over large distances and a straight-forward correlation between shape orientation and crystallographic orientation can be made due to the single crystalline nature of the FLG hexagonal domains. This avoids the necessity of having to measure diffraction from all domains to determine their crystallographic orientation. Furthermore, the single crystal nature of our FLG domains means that all crystallographic orientations are in the same direction, which would not be the case for domains that contain multiple grains.[208] Together with the TEM/SAED analysis, these data indicate that on the large scale the edges of the graphene domains are aligned along the zig-zag directions. This preferential alignment of the hexagons is only observed over small areas (i.e ~20 μm x 20 μm) for a growth temperature of 1000 ºC which is shown in figure 5.10, but increases substantially when the temperature is reduced to 990 ºC. Figure 5.10 shows a SEM image of a region of aligned FLG hexagons, indicated by the red arrow. Only some Cu grains exhibited aligned FLG domains, with the majority showing random orientations.

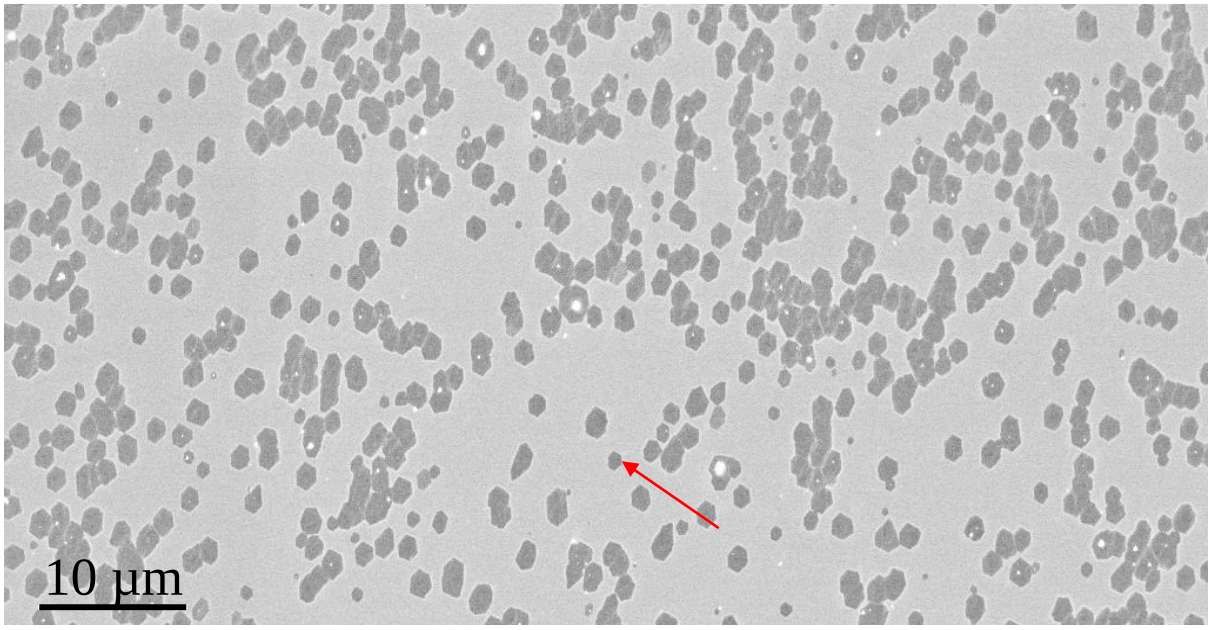


**Figure 5.10**. Small scale alignment: SEM image of aligned FLG domains grown at 1000 °C. Red arrow indicates edge alignment of hexagon.

### 5.3.4. Hydrogen Effect and Cooling Rates on Nucleation

The effect of the hydrogen pre-treatment process on the formation of FLG domains is investigated. The reaction temperature was kept constant at 1000 °C with 3 minutes of growth time whilst varying the hydrogen pre-treatment time for 0, 60 minutes and 120 minutes. Figure 5.11(a) shows the SEM images of 0 minutes hydrogen pre-treatment sample with corresponding Raman spectrum shown in figure 5.11(d). No distinct G peak and 2D peak are observed in figure 5.11(d), which indicates that graphene or FLG does not nucleate without some form of hydrogen pre-treatment in which the surface oxide on the Cu foil is removed. Figure 5.11(b) shows the SEM image for 60 minutes of hydrogen pre-treatment time with corresponding Raman spectrum shown in figure 5.11(e). A distinct G peak is seen at 1580 $cm^{-1}$ and a 2D peak at 2700 $cm^{-1}$ in figure

5.11(e), which indicates the FLG domains have nucleated. The nucleation density in figure 5.11(b) is about 0.25 ($\mu m^{-2}$). The SEM image of the sample with 120 minutes of hydrogen pre-treatment is shown in figure 5.11(c) with corresponding Raman spectrum in figure 6(f), showing a G peak and 2D peak. The nucleation density in figure 5.11(c) is about 0.19 ($\mu m^{-2}$), similar to the sample with 60 minutes of hydrogen pre-treatment. The variation of average nucleation density with respect to hydrogen pre-treatment time is shown in section 5.3.6. It shows the nucleation density is zero at none hydrogen pre-treatment time and has a maximum point at one hour hydrogen pre-treatment time.

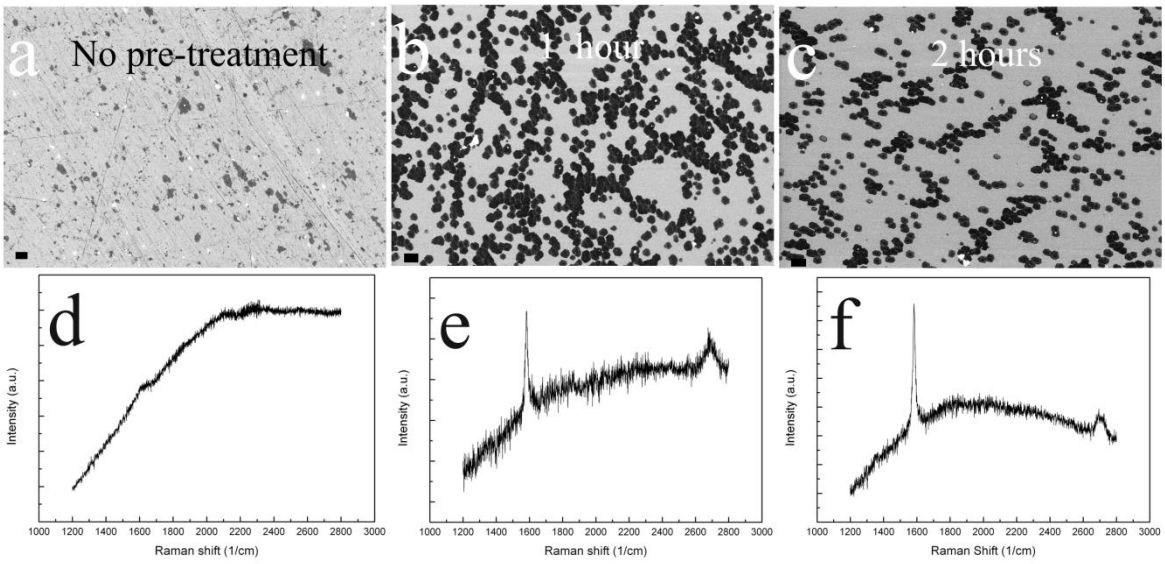


**Figure 5.11.** Hydrogen pre-treatment effect on nucleation of graphene domains: SEM image of (a) the sample with 0 minutes hydrogen pre-treatment. (b) The sample with 60 minutes hydrogen pre-treatment. (c) The sample with 120 minutes hydrogen pre-treatment. Raman spectrum: (d) the sample shown in panel a. (e) The sample shown in panel b. (f) the sample shown in panel c.

Figure 5.12 shows the cooling rate effect on the nucleation of graphene films. The fast cooling rate is done by removing the quartz tube from the hot zone of furnace under the argon and hydrogen atmosphere with heating control off until the temperature comes down to room temperature. The natural cooling is done by remaining the quartz tube inside furnace while turning off the heating control under the argon and hydrogen atmosphere until the temperature comes down to room temperature. Figure 5.12(a) shows a 3 minutes growth time with fast cooling rate which is more homogenous nucleation, comparing with the natural cooling rate sample with 3 minutes growth time, shown in figure 5.12(b). Figure 5.12(c) shows a 20 minutes growth time with fast cooling rate. The hexagonal FLG domains shown in figure 5.12(a) emerge into large area films with a few hexagonal FLG domains seen in the gap region. It is almost a homogenous film without much contrast variation in one Cu grain. Figure 5.12(d) shows a 20 minutes growth time with natural cooling rate, which has much larger variation in the contrast, which indicates the inhomogeneous thickness.

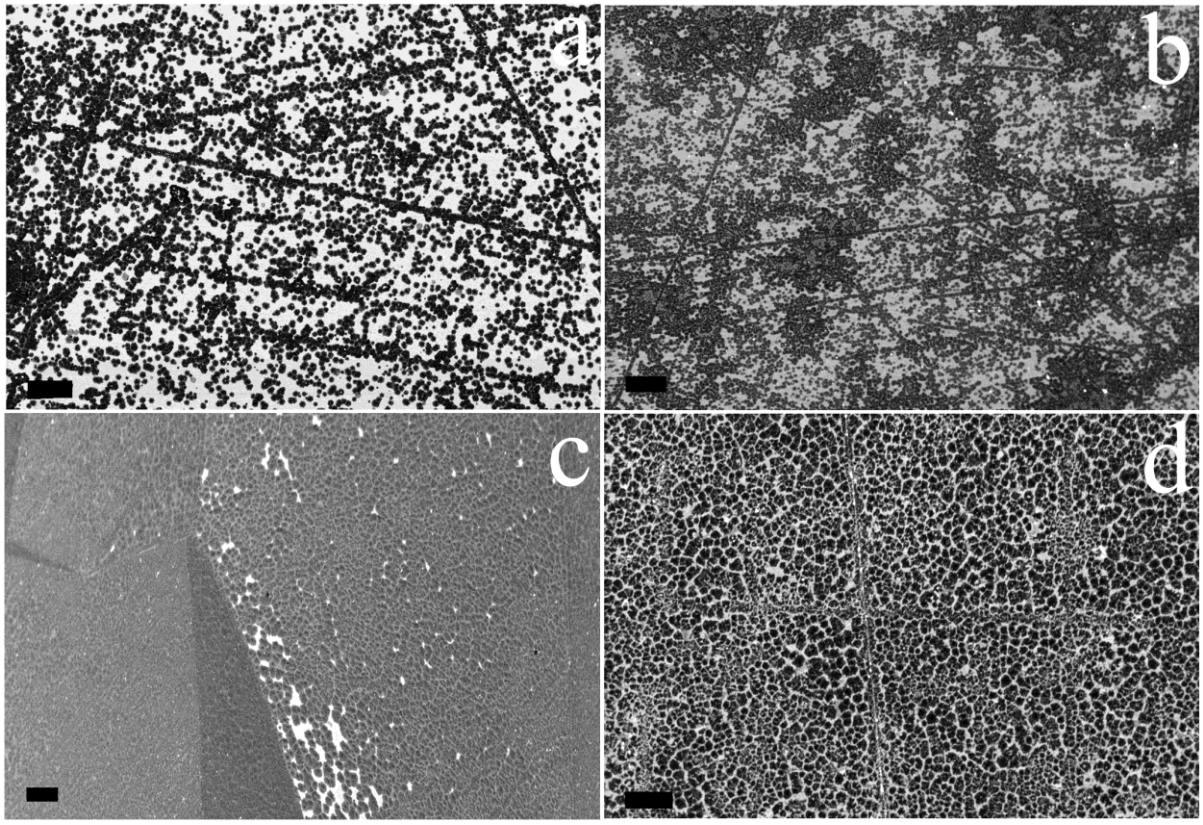


**Figure 5.12**. Cooling rate effect, SEM images of 1000 °C: (a) 3 minutes fast cooling rate (b) 3 minutes natural cooling rate (c) 20 minutes fast cooling rate (d) 20 minutes natural cooling rate. The scale bars from (a)-(d) are 10 μm, 10 μm, 20 μm, 10 μm, respectively.

HRTEM was performed to analyze the thickness and crystal structure of the large area graphene film shown in figure 5.12(c). Figure 5.13(a)-(c) shows the thickness of the 20 minutes fast cooling film is about 1-3 layers. Selective area electron diffraction (SAED) in figure 5.13(d) shows the graphene film remaining the AB Bernal stacking single crystal structure as the hexagonal FLG domains, which is shown in figure 5.6. This indicates the fast cooling rate could be preferable to fabricate the more homogenous thickness large area graphene film than natural cooling.

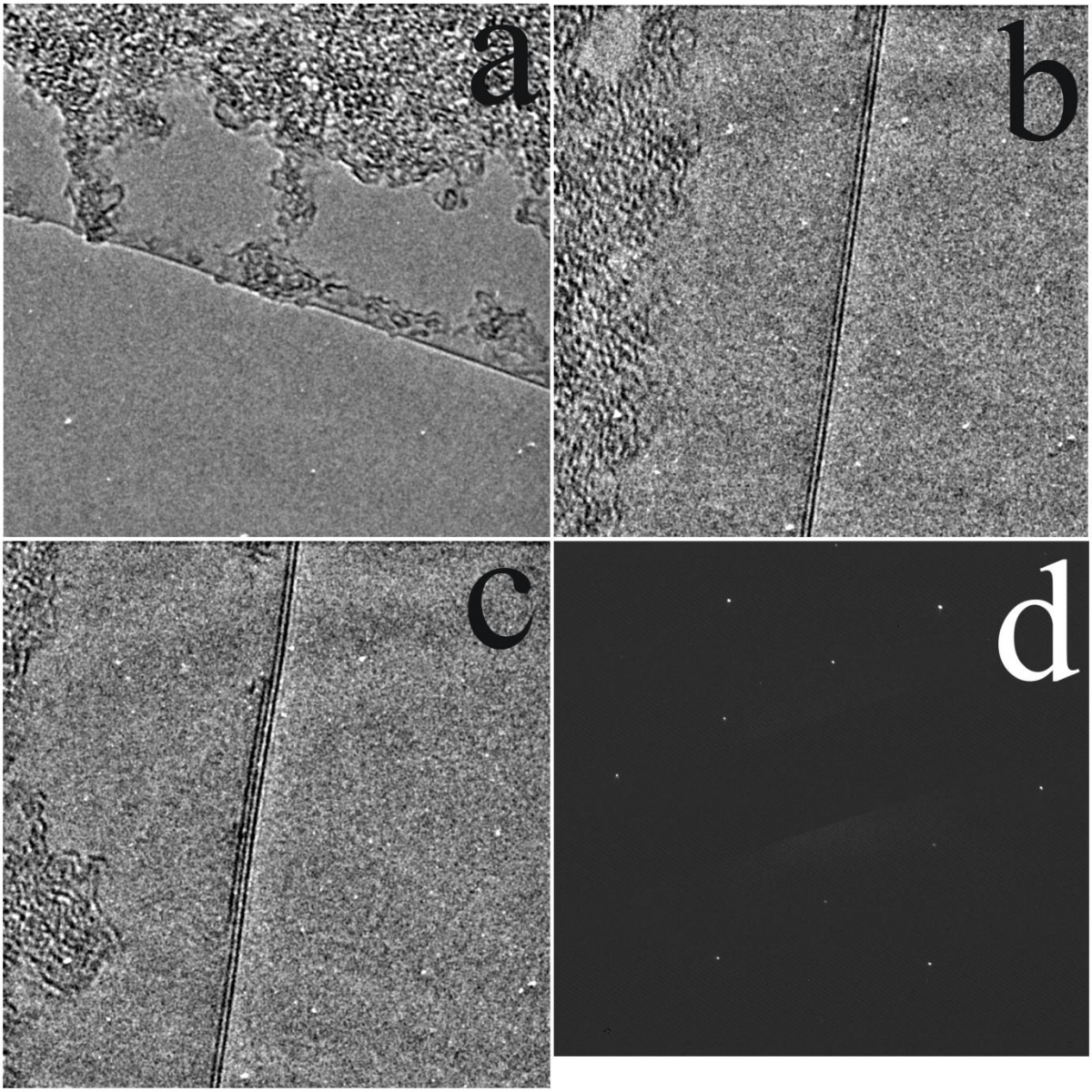


**Figure 5.13**. Thickness and crystal structure of large area graphene film grown at 1000 °C for 20 minutes with fast cooling rate: (a) monolayer (b) bilayers (c) Tri-layers (d) AB Bernal stacking single crystal.

### 5.3.5. Effect of Cu Foil Quality on Graphene Nucleation

From the study in section 5.3.1~5.3.4, the temperature effect, cooling rate effect, hydrogen effect on the nucleation of graphene has been studied. In this section, the Cu purity effect has been studied on graphene nucleation when 1000 °C and fast cooling are chosen as fixed parameters.

Figures 5.14(a) and 5.14(b) show low-magnification scanning electron microscope (SEM) images of Cu foils after 3 minutes exposure to methane at 1000 ºC for (a) 99.8% purity and (b) 99.999% purity. For the 99.8% Cu foil, macroscopic linear undulations are observed in the film, along with bumps in the surface texture. In comparison, the 99.999% Cu foil is free from deformations. Figure 5.14(a) shows several smaller Cu grains for the 99.8% Cu foil, whereas figure 5.14(b) shows the boundary of two large Cu grains. Figure 5.14(c) shows a low magnification SEM image (in-lens detector) of the FLG domains (seen as black contrast) grown on the 99.8% Cu foil after 3 minutes exposure to $CH_4$. A non-uniform distribution of the domains is observed and linear tracks of domains are produced along with clusters. The linear arrays of FLG domains correlate well with macroscopic deformations in the films surface likely induced by the rolling process. The higher magnification image in figure 5.14(d) shows the clustering of the FLG domains around regions containing impurities, shown by the bright white contrast. Figure 5.14(e) shows the same growth conditions but instead using the higher purity 99.999% Cu foil. A relatively homogenous distribution of FLG domains is achieved with minimal clustering. The higher magnification image in figure 5.14(f) shows reduced amounts of bright contrast spots associated with impurities and thus explains the decrease in the clustering of domains. The dark contrast in the centre of each graphene domains is the thicker region, forming the terraced structure.[283]

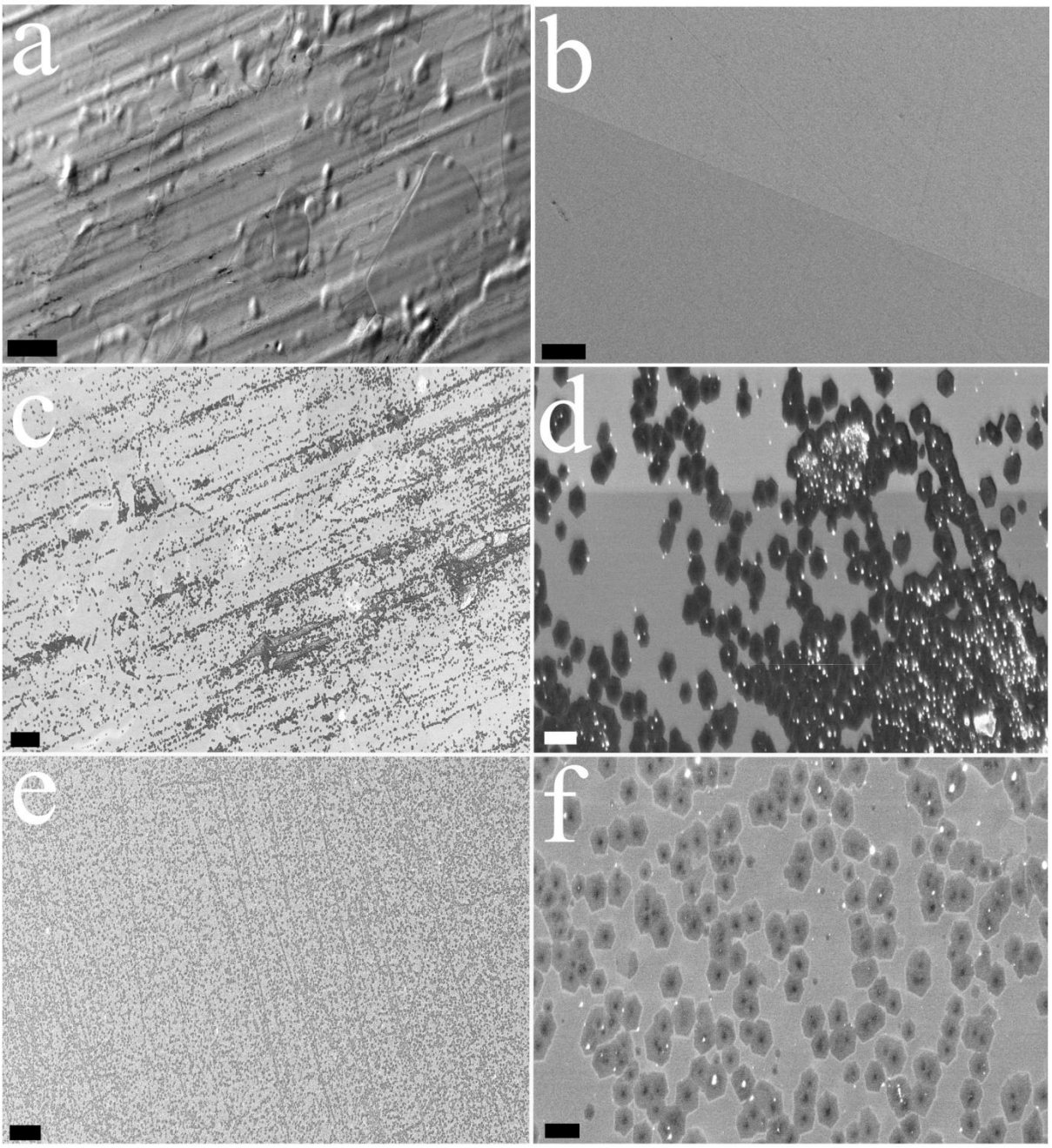


**Figure 5.14.** SEM images of (a) 99.8% purity 0.025 mm thick and (b) 99.999% purity 0.1 mm thick Cu foils. SEM images (in-lens detector) of few layer graphene with 3 minutes growth time on (c), (d) 99.8% purity 0.025 mm thick Cu foil, and (e), (f) 99.999% purity 0.1 mm thick Cu foil. The scale bars are 40 µm, 40 µm, 40 µm, 2 µm, 40 µm, 2 µm, from (a)-(f) respectively.

### 5.3.6. Nucleation Density Analysis

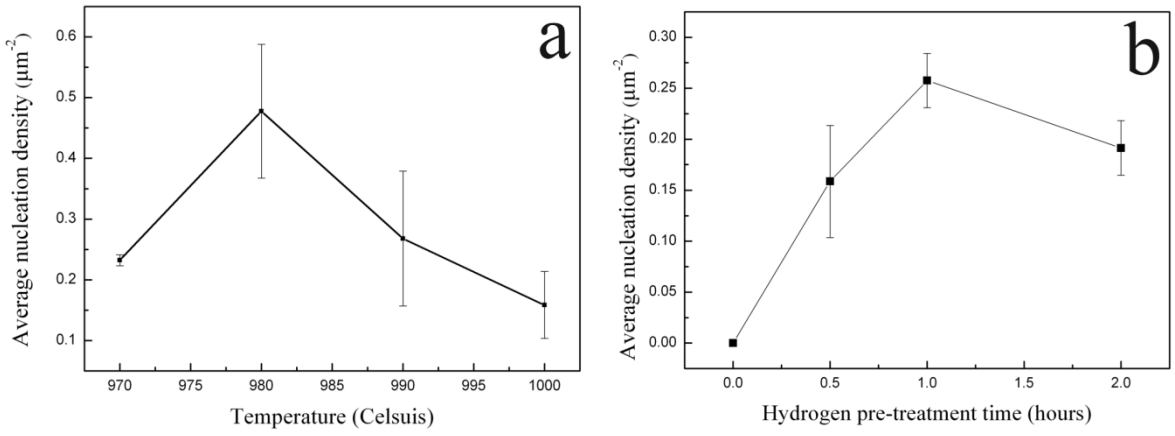


**Figure 5.15.** (a) The average nucleation density as a function of temperature at 0.5 hour hydrogen pre-treatment. (b) The average nucleation density as a function of hydrogen pre-treatment time at 1000 °C. The error bar is the standard deviation value for the statistics of each data point.

Method for calculating average nucleation density is as followed. The number of particles is counted for each SEM image. The area is calculated for each image as well. The nucleation density is calculated for each image by the definition that Nucleation density= number of particles/ area. The statistics are on the same temperature or the same hydrogen pre-treatment time to calculate the mean value and standard deviation for the average nucleation density with points indicating the mean value and error bar indicating the standard deviation value.

Figure 5.15(a) shows the average nucleation density as a function of temperature. The maximum average nucleation density appears at 980 ºC, which indicates the maximum activity of the catalyst is around 980 ºC under the condition explored. Figure 5.15(b) shows the average nucleation density as a function of hydrogen pre-treatment time. It shows the nucleation density is zero at

none hydrogen pre-treatment time and has a maximum point at one hour hydrogen pre-treatment time. The data extracted for calculating nucleation density are shown in figure 5.16-5.21.

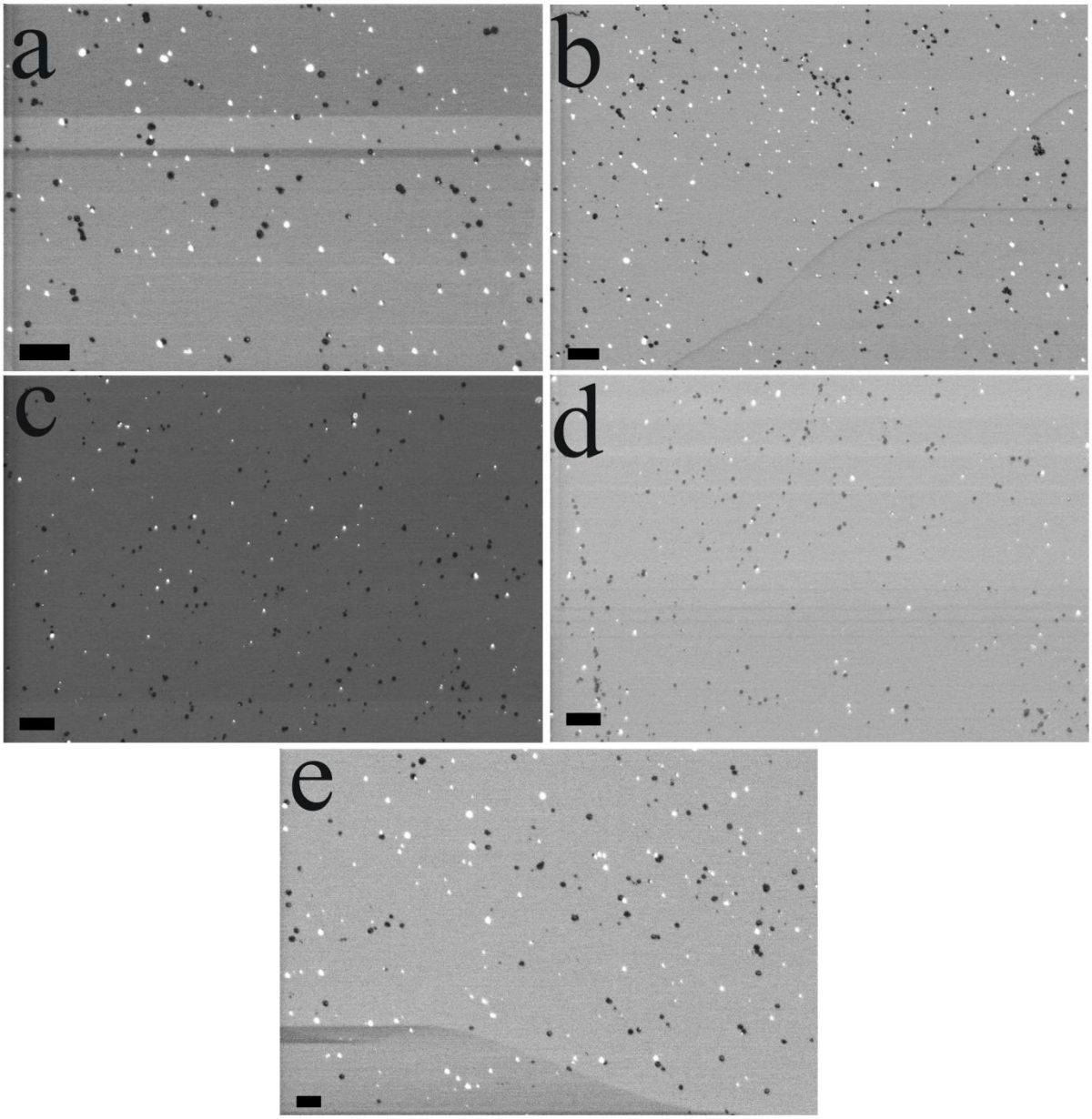


**Figure 5.16.** The SEM images as analyzed for determination of nucleation density as a function of temperature. Here temperature: 970 °C, 0.5 hour hydrogen pre-treatment. The scale bars from (a)-(e) are 2 µm, 2 µm, 2 µm, 2 µm, 1 µm, respectively.

Figure 5.16 shows the SEM images of the samples of 970 °C reaction temperature and 0.5 hours hydrogen pre-treatment time. These SEM images are used for building up statistics on the average nucleation density at 970 °C.

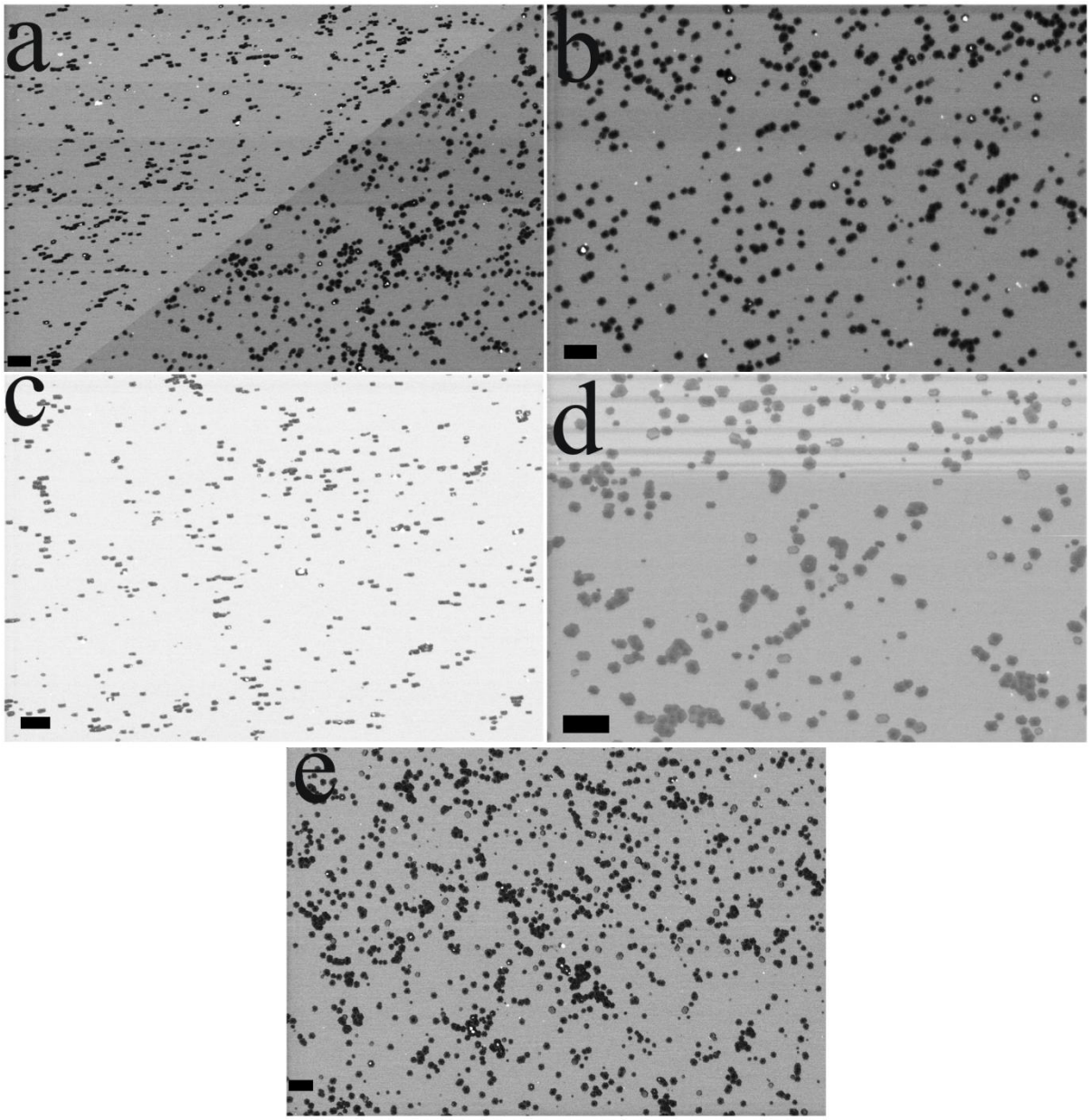


**Figure 5.17.** The SEM images as analyzed for determination of nucleation density as a function of temperature. Here temperature: 980 °C, 0.5 hour hydrogen pre-treatment. All the scale bars are 2 μm.

Figure 5.17 shows the SEM images of the samples of 980 °C reaction temperature and 0.5 hours hydrogen pre-treatment time. These SEM images are used for building up statistics on the average nucleation density at 980 °C.

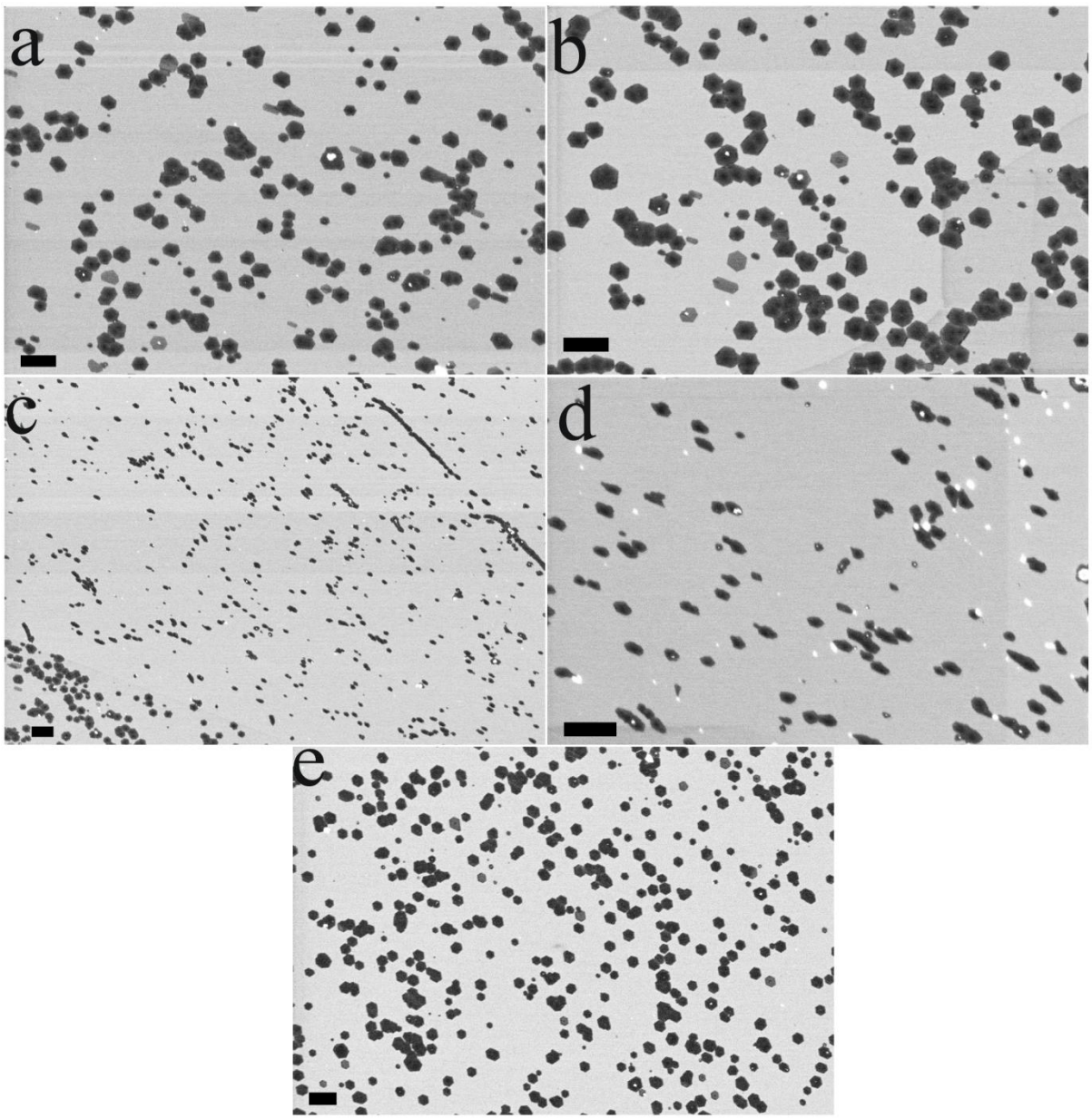


**Figure 5.18.** The SEM images as analyzed for determination of nucleation density as a function of temperature. Here temperature: 990 °C, 0.5 hour hydrogen pre-treatment. All the scale bars are 2 μm.

Figure 5.18 shows the SEM images of the samples of 990 °C reaction temperature and 0.5 hours hydrogen pre-treatment time. These SEM images are used for building up statistics on the average nucleation density at 990 °C.

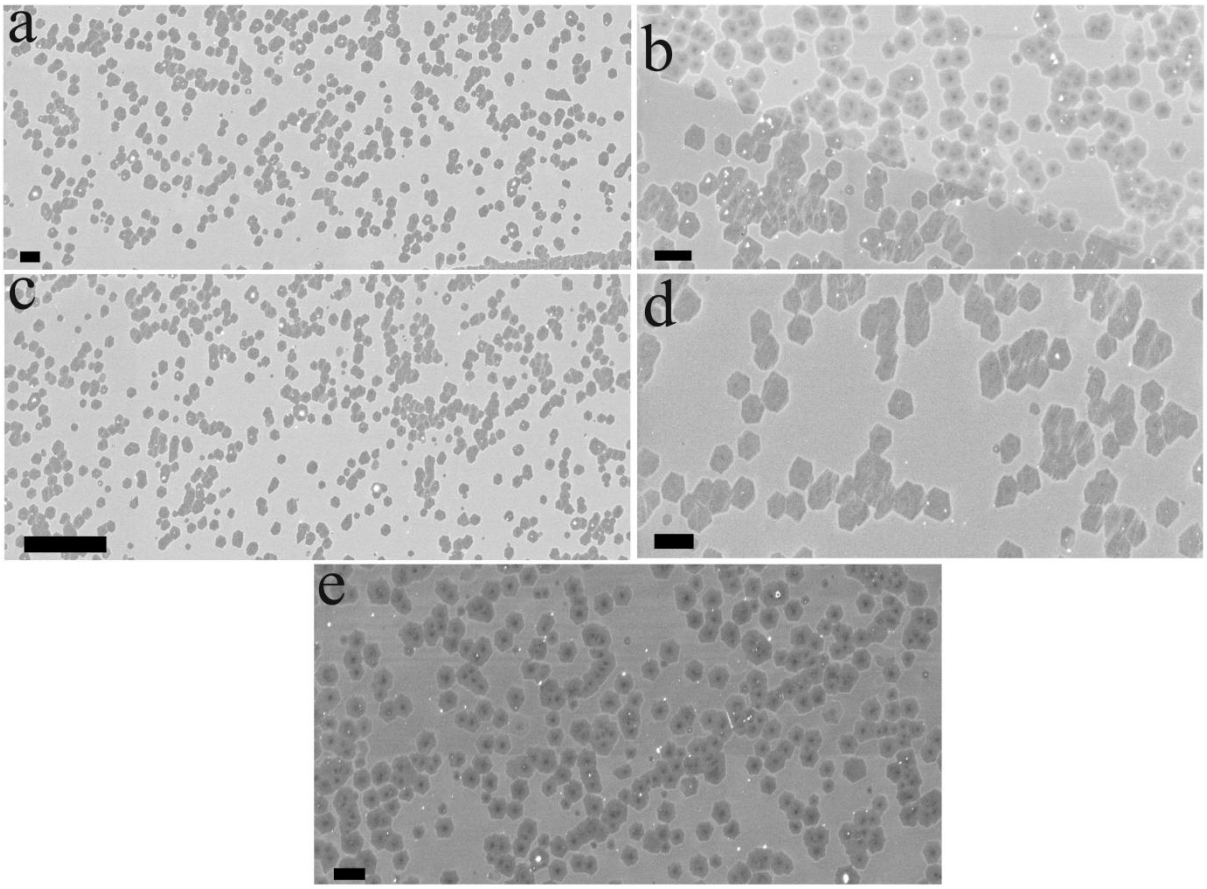


**Figure 5.19.** The SEM images as analyzed for determination of nucleation density as a function of temperature and hydrogen pre-treatment time. Here temperature: 1000 °C, 0.5 hour hydrogen pre-treatment. The scale bars from (a)-(e) are 2 μm, 2 μm, 10 μm, 2 μm, 2 μm, respectively.

Figure 5.19 shows the SEM images of the samples of 1000 °C reaction temperature and 0.5 hour hydrogen pre-treatment time. These SEM images are used for building up statistics on the average nucleation density at 1000 °C and for 0.5 hour hydrogen pre-treatment time.

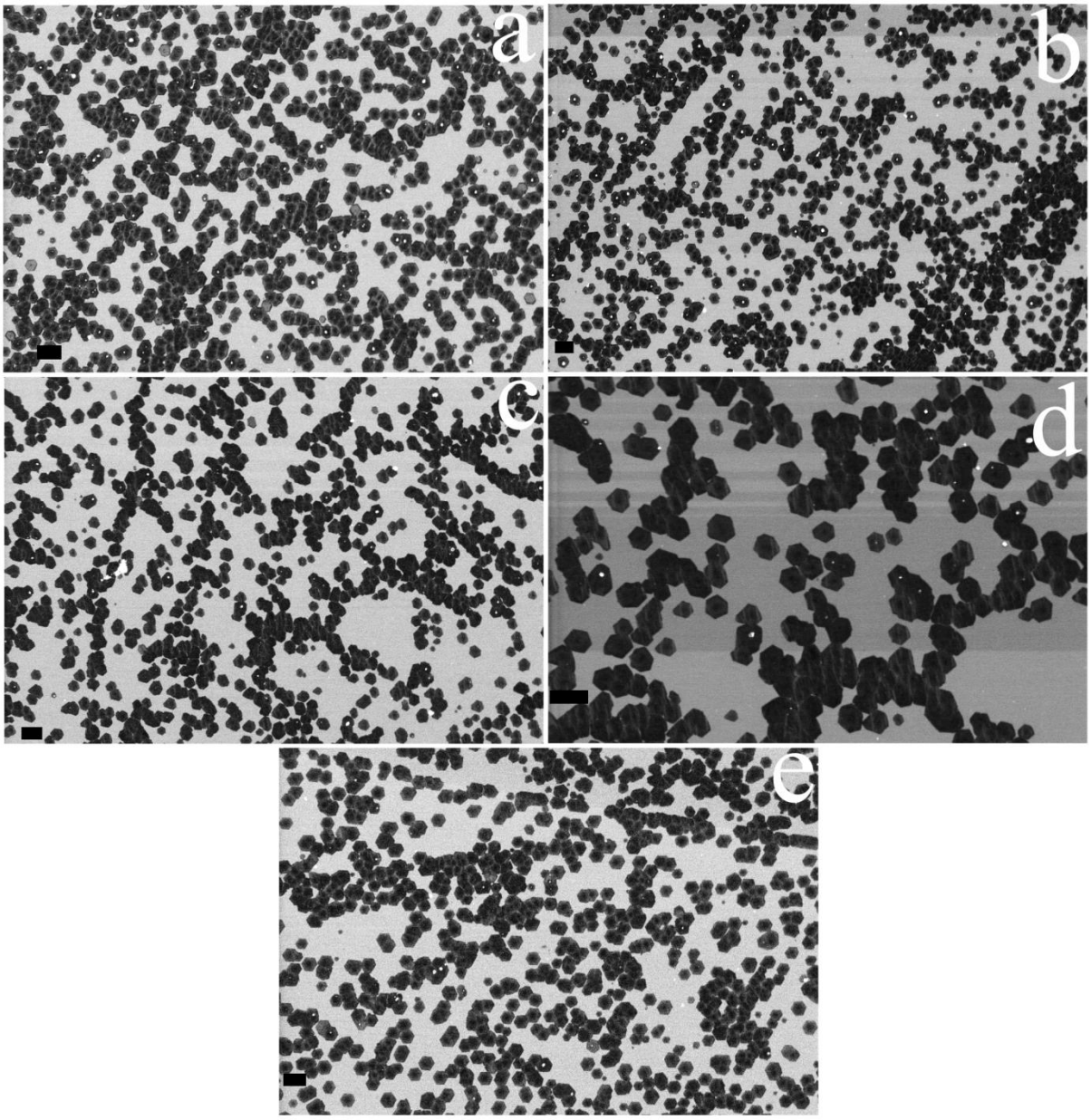


**Figure 5.20.** The SEM images as analyzed for determination of nucleation density as a function of hydrogen pre-treatment time. Here: 1 hour hydrogen pre-treatment, 1000 °C. All the scale bars are 2 μm.

Figure 5.20 shows the SEM images of the samples of 1000 °C reaction temperature and 1 hour hydrogen pre-treatment time. These SEM images are used for building up statistics on the average nucleation density for 1 hour hydrogen pre-treatment time.

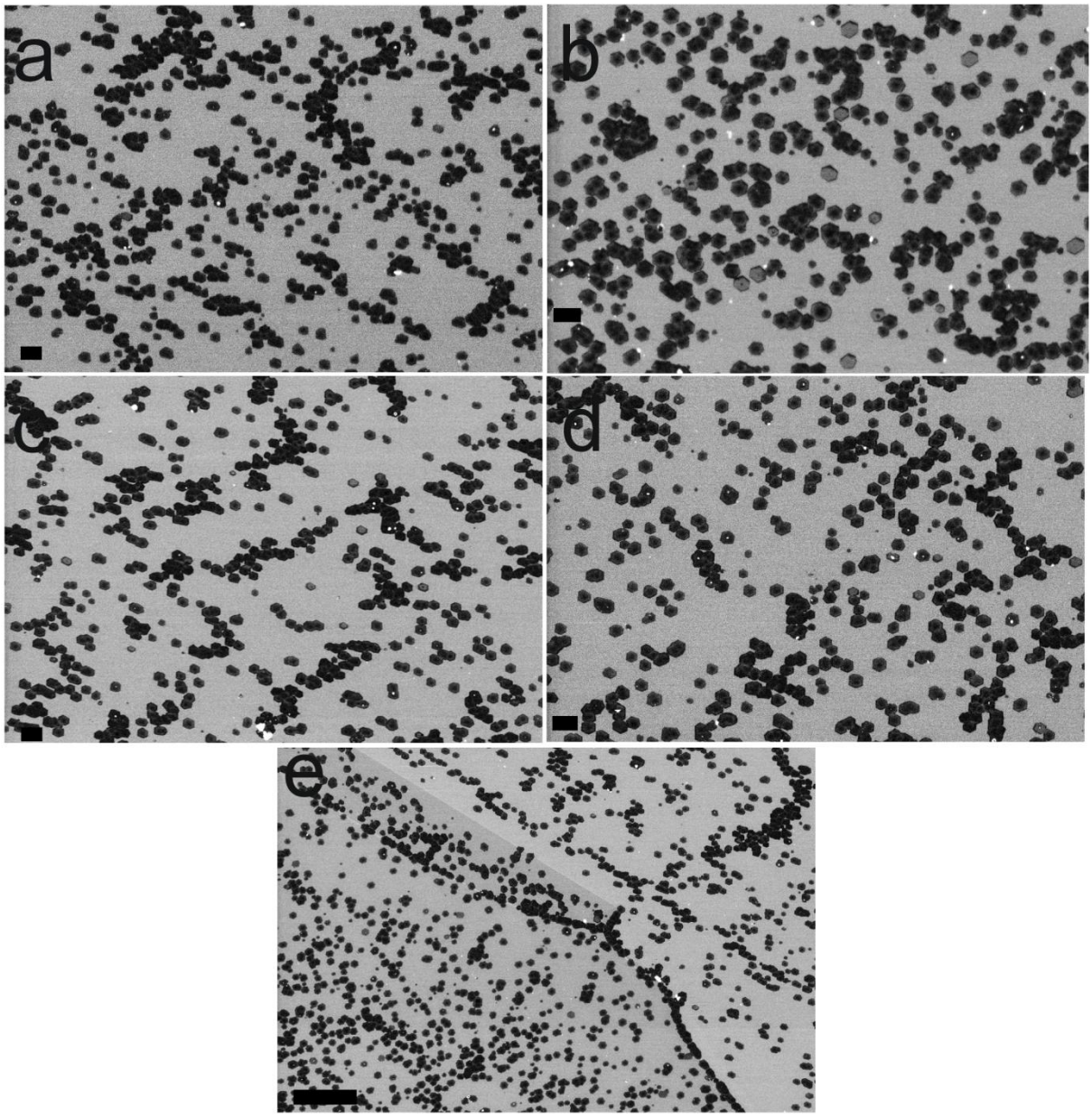


**Figure 5.21.** The SEM images as analyzed for determination of nucleation density as a function of hydrogen pre-treatment time. Here: 2 hours hydrogen pre-treatment, 1000 °C. The scale bars from (a)-(e) are 2 µm, 2 µm, 2 µm, 2 µm, 10 µm, respectively.

Figure 5.21 shows the SEM images of the samples of 1000 °C reaction temperature and 2 hours hydrogen pre-treatment time. These SEM images are used for building up statistics on the average nucleation density for 2 hours hydrogen pre-treatment time.

### 5.3.7. Discussions

From the study in section 5.3, the mechanism of graphene nucleation and growth under the conditions used in our APCVD is quite different from previous reports using LPCVD, regarding the onset temperature, the shape of graphene domains and alignment of graphene on Cu foil. The carbon source ($CH_4$) is decomposed by active Cu catalyst sites and forms $C_xH_y$ radicals. The Cu surface and possibly a small region in the sub-surface are locally supersaturated with these $C_xH_y$ radicals to form polycyclic rings.[113, 205] Then carbon radicals in other regions diffuse to attach to the polycyclic rings and make it grow larger into graphene.[113,205] This is called surface adsorption process and approved by the isotope labelling study.[113] In our case, no carbon radical could form below 940 °C. Thus, no graphene nucleates for the temperature below 940 °C. Within the temperature range between 950 °C and 960 °C, the diffusion velocity of the radicals is low due to the kinetics energy below or only a small amount above the diffusion barrier. This leads to the carbon radicals restricted in the localized region. Thus, only nanocrystalline graphite is produced within this temperature range rather than large area graphene domains. When the temperature is above 960 °C, the kinetics could be over the energy barrier for the efficient diffusion of carbon radicals to join the polycyclic ring for the growth of large graphene domains. The carbon radicals are no longer restricted within local region but diffuse over large areas. That's why large graphene domains nucleate instead of nanocrystalline graphene for the temperature above 960 °C.

From the first principal calculation, carbon-carbon interactions dominate the growth of graphene on Cu due to the relatively weaker surface diffusion barrier, comparing with other metals like Ir and Ru.[285] Under this carbon-carbon interaction dominating growth, rather than carbon-copper interaction, hexagonal shape of FLG forms due to its thermodynamically stable morphology. When reducing the pressure in CVD from atmospheric to relatively low, the kinetics of the system changes. This leads to the four lobe polycrystalline graphene domains instead of hexagonal shape. The activation energy is higher under atmospheric pressure than low pressure, thus the onset temperature of the graphene domains will be higher than the low pressure CVD, which is around 800 ºC.[286, 287] The maximum nucleation density is 980 ºC, reflecting the temperature of maximum activity of the active sites on the Cu surface.

The millimetre scale alignment of the single crystal hexagonal FLG along their zig-zag edge crystallographic orientation is observed. This is different from the random orientation between four lobe polycrystalline graphene and Cu lattice.[208] According to the first principles calculations, nucleation for Cu-catalyzed graphene is found on the crystal plane and the active sites are free-electron-like surface states in Cu.[18] Surface irregularities (*i.e.* metal step edges and other defects) do not serve as centres for carbon adsorption and growth nucleation.[285] This is different from low pressure CVD, in which graphene nucleates at Cu steps, pinning sites, and other imperfections.[208]

Hydrogen has an essential role to remove oxide, which is catalytic silent. This will help to the exposure of the catalytic site to the carbon source. Also, hydrogen plays a role to initial the reaction.[288] These are the reasons why no graphene domain nucleates without hydrogen pre-treatment. The total amount of carbon should be the same before cooling it down. However, from our cooling rate study, it can deduct that more carbon precipitates out during the low cooing rate than the fast cooling rate. Inhomogeneous clustering of the graphene domains happens under natural cooling rate. The extra carbon between fast cooling rate and natural cooling rate sample should come from the dissolved carbon in Cu, similar as Ni for the nucleation of graphene.[113] This indicates the carbon solubility in Cu is increased under the atmospheric pressure, comparing with low pressure. Thus, fast cooling rate is required for the homogenous nucleation of FLG, due to the insufficient time for the dissolved carbon to precipitate out.

## 5.4. Alignment Rectangular Few Layer Graphene Domains on Copper Surface

### 5.4.1. Alignment of Rectangular Few Layer Graphene Domains

Well-defined hexagonal single crystal FLG domains have been previously grown by AP-CVD using Cu foils of 99.8% purity at a growth temperature of 1000 $^{o}$C.[283,289] Cu foils of 99.8% purity were also used in many other reports of CVD growth by the Ruoff group.[112-113, 275-277] However, we found that when using these 99.8% Cu films, the graphene nucleation is dominated

by impurities on the surface and mechanical deformations which are shown in figure 5.14. Higher quality Cu foils of 99.999% purity were used with increased thickness from 0.025 mm to 0.1 mm as they enable the true interplay between the graphene domains and the Cu atomic structure to be revealed because the artificial nucleation points that are prevalent on 99.8% Cu foils are greatly reduced.

Figure 5.22(a) shows the grain boundary between two Cu grains for a growth temperature of 980 ºC. Figure 5.22(a) shows rectangular shaped FLG domains on the brighter contrast left sided Cu grain (red arrow), whilst hexagonal shaped FLG domains form on the darker contrast right sided region (blue arrow) with an inset showing an individual hexagonal domain. The nucleation density in these two Cu grains is similar but the size of the domains is different. The nucleation density in the light contrast grain is ~0.42 $\mu m^{-2}$ while the nucleation density in the dark contrast grain is ~0.47 $\mu m^{-2}$. The higher magnification SEM image of rectangular shaped FLG domains is presented in figure 5.22(b) with an inset showing an individual rectangular domain. Some shape variations of FLG domains were also observed at 990 ºC, shown in figure 5.22(c). However, this was only a minor deviation from the predominant hexagonal shapes. Hexagonal FLG domains are seen in the lower left region on one Cu grain (red arrow) with an inset showing single domain in figure 5.22(c), whilst elongated FLG domains that lack faceting are observed on the other larger Cu grain (blue arrow). The higher magnification image of the elongated non-faceted FLG domains is shown in figure 5.22(d) with an inset showing a single domain. In figures

5.22(a) and 5.22(c), the Cu grain boundary does not contain a larger proportion of FLG domains, indicating that it does not always act as a nucleation site for growth.[208] The Raman spectra corresponding to figure 5.22(a) and (c) is shown in figure 5.4(d) and (e). Transmission electron microscopy and selected area electron diffraction analysis of FLG domains transferred onto TEM grids indicated the domains were single crystals, shown in figure 5.7. At growth temperatures of 1000 $^{o}$C, all FLG domains were hexagonal, indicating that the Cu lattice no longer affected the shape of domains. Lowering the temperature further to 970 $^{o}$C led to reduced quality of FLG domains due to a decrease in the catalytic activity of the system. This indicates that a critical temperature of 980 $^{o}$C is required to get optimized Cu-FLG interactions. The rectangular shaped FLG domains were also aligned in their orientation. Figure 5.23 shows a SEM image of a large 44 μm x 30 μm area of aligned rectangular FLG domains with the red arrow indicating the direction of orientation of the domains.

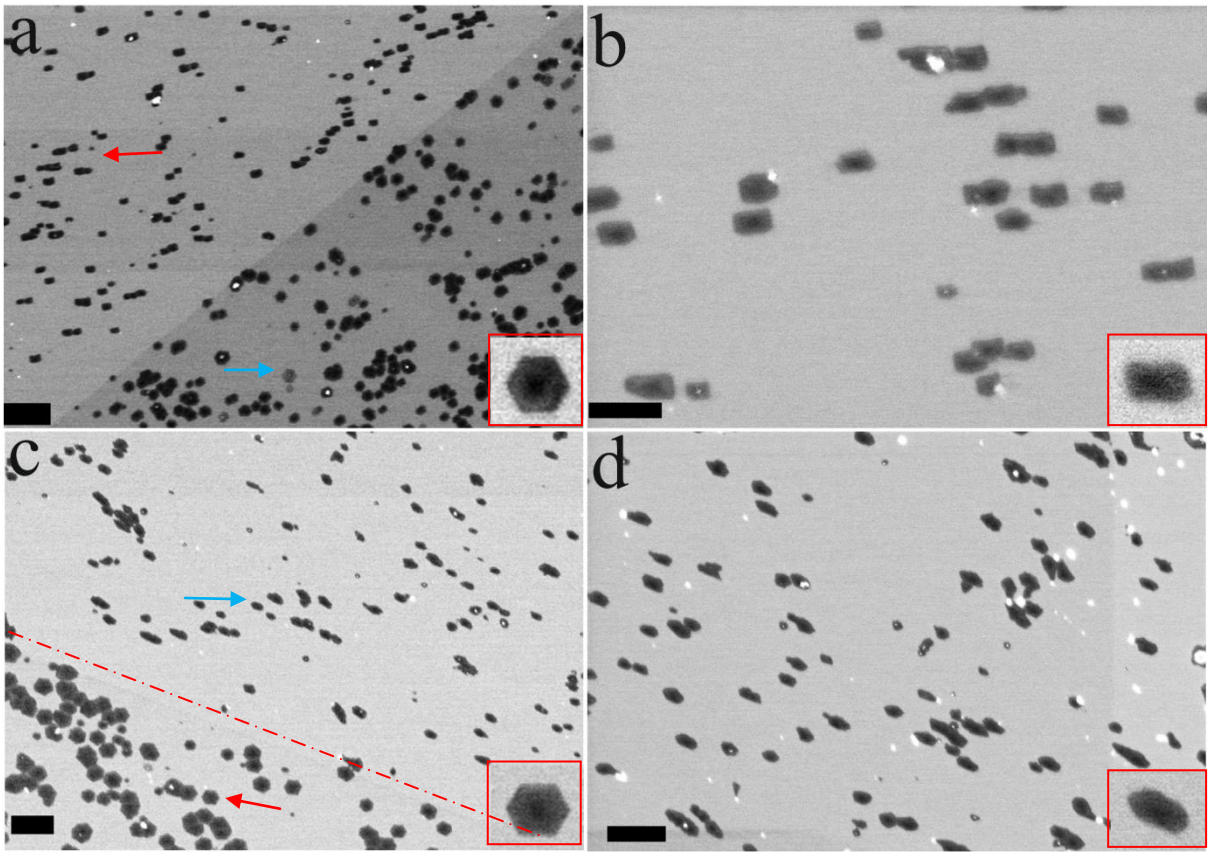


**Figure 5.22.** SEM images of Cu grain effect on shape control of the nucleation of graphene domains: (a) Rectangular shaped (red arrow) and hexagonal shaped (blue arrow) FLG domains nucleated on different Cu grains at 980 ºC. Inset in bottom right shows a single hexagon. (b) The higher magnification image of the rectangular shaped FLG domains at 980 ºC. (c) Hexagonal shaped (red arrow) and non-faceted elongated (blue arrow) FLG domains nucleated on different Cu grains at 990 ºC. Inset in bottom right shows a single hexagon. (d) The higher magnification image of elongated non-faceted FLG domains at 990 ºC. The scale bars in (a)-(d) are 2 µm, 1 µm, 2µm, 2µm, respectively. Insets show individual domain respectively.

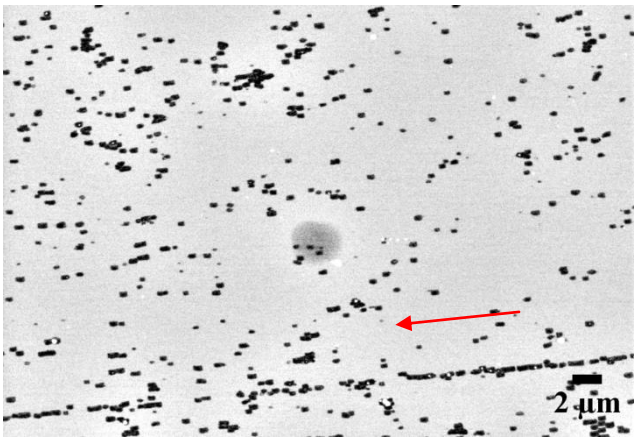


**Figure 5.23**. SEM image showing alignment of rectangular shaped few layer graphene domains over a region of 44 µm x 30 µm, indicated by red arrow.

### 5.4.2. Mechanism for Formation and Alignment of Graphene Domains in Solid State Copper

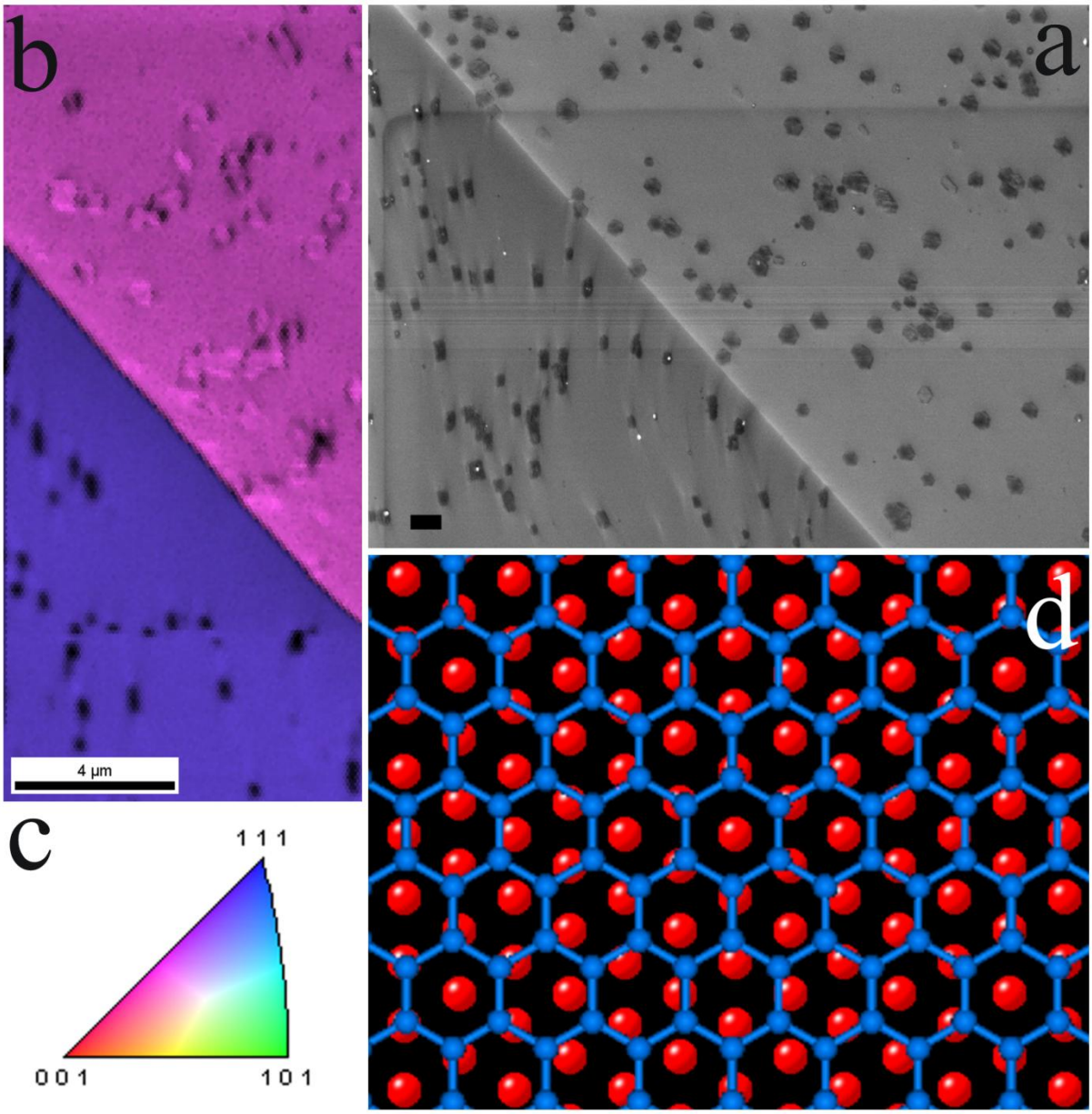


**Figure 5.24.** (a) SEM image shows two Cu grains associated with hexagonal or rectangular graphene domains, respectively. (b) EBSD mapping of the region shown in panel a. The scale bar is 1 µm. (c) Colour key used to index the EBSD mapping in figure 5.24 and 5.25. (d) Atomic model of graphene on Cu (111), corresponding to the blue region in panel b. The blue atoms are Carbon and red atoms are Cu.

In order to understand why the FLG domains changed shape from hexagonal to rectangular across different Cu grains, electron backscatter diffraction (EBSD) was used to measure the orientation of the Cu crystal structure in the regions of FLG shape change. EBSD was performed by Dr Susannah Speller from the Department of Materials, University of Oxford. When measuring the EBSD, the sample was tilted 70° from the horizontal plane, the graphene samples will have different contrast on different Cu crystal plane. Figure 5.24(a) shows the SEM image of the boundary region between two Cu grains, on which hexagonal (right) and rectangular (left) shaped FLG domains are grown. SEM contrast features were observed to surround the rectangular FLG domains but not the hexagonal FLG domains, and were attributed to deformation caused by the stress in the Cu crystal induced by the FLG domains. EBSD analysis has been carried out on a region surrounding the boundary in figure 5.24(a). The map in figure 5.24(b) shows the orientation of the Cu crystal lattice relative to the sample normal direction superimposed on the secondary electron image, colour according to the key in figure 5.24(c). The blue Cu grain in figure 5.24(b) is a Cu (111) plane, on which the rectangular FLG domains are produced. The pink Cu grain in figure 5.24(b) is associated with hexagonal FLG graphene domains and is a higher index plane between Cu (111) and (001). We found that the rectangular shaped FLG domains were only produced on the Cu (111) surfaces, whilst hexagonal shaped FLG domains were produced on all other Cu surfaces, which will be shown in figure 5.25.

Figure 5.24(d) shows an atomic model of graphene on the Cu (111) plane, which corresponds to the blue region in figure 5.24(a). A previous STM study shows the lattice of graphene is either strictly aligned with Cu (111) or with 7º misorientation angle with respect to the Cu lattice synthesized by LP-CVD.[209] However, in that report random shapes of graphene domains were produced on Cu (111) by LP-CVD.[209] The Cu (111) surface has 6 fold symmetry and a graphene lattice has 6-fold symmetry, but the resulting rectangular shaped FLG domains produced are 2 fold symmetric. The inter-atomic spacing of Cu atoms on a (111) surface is typically 0.148 nm, whilst the C-C separation in $sp^2$ bonded graphene is typically 0.142 nm leads to a small ~4% lattice mismatch between the graphene and copper surface and may lead to some strain in the system.[290] The elongated direction of the rectangle FLG domain has faster growth kinetics than the shorter direction and thus 2 fold symmetry is produced.

Figure 5.25(a) shows a normal direction EBSD map of another area that contained eight different Cu grains with labels 1-8. The orientation of the sample normal direction in each grain can be indentified using the colour key in figure 5.24(c). The results in figure 5.24(a) suggest that green Cu grains with labels 3-4 are Cu (101) plane, while the red grains with labels 5-6 are Cu (001) plane. The orange (label 1) and yellow (label 2) grains are high index planes between Cu (001) and (101). The pink grains labelled with 7-8 are higher index planes between Cu (001) and (111). SEM images corresponding to each individual Cu grain in figure 5.25(a) are shown in figure

5.25(b)-(i) with the same label number as the grains. It is interesting to note that only hexagonal FLG domains were grown on all these Cu grains, although they are different Cu lattice planes.

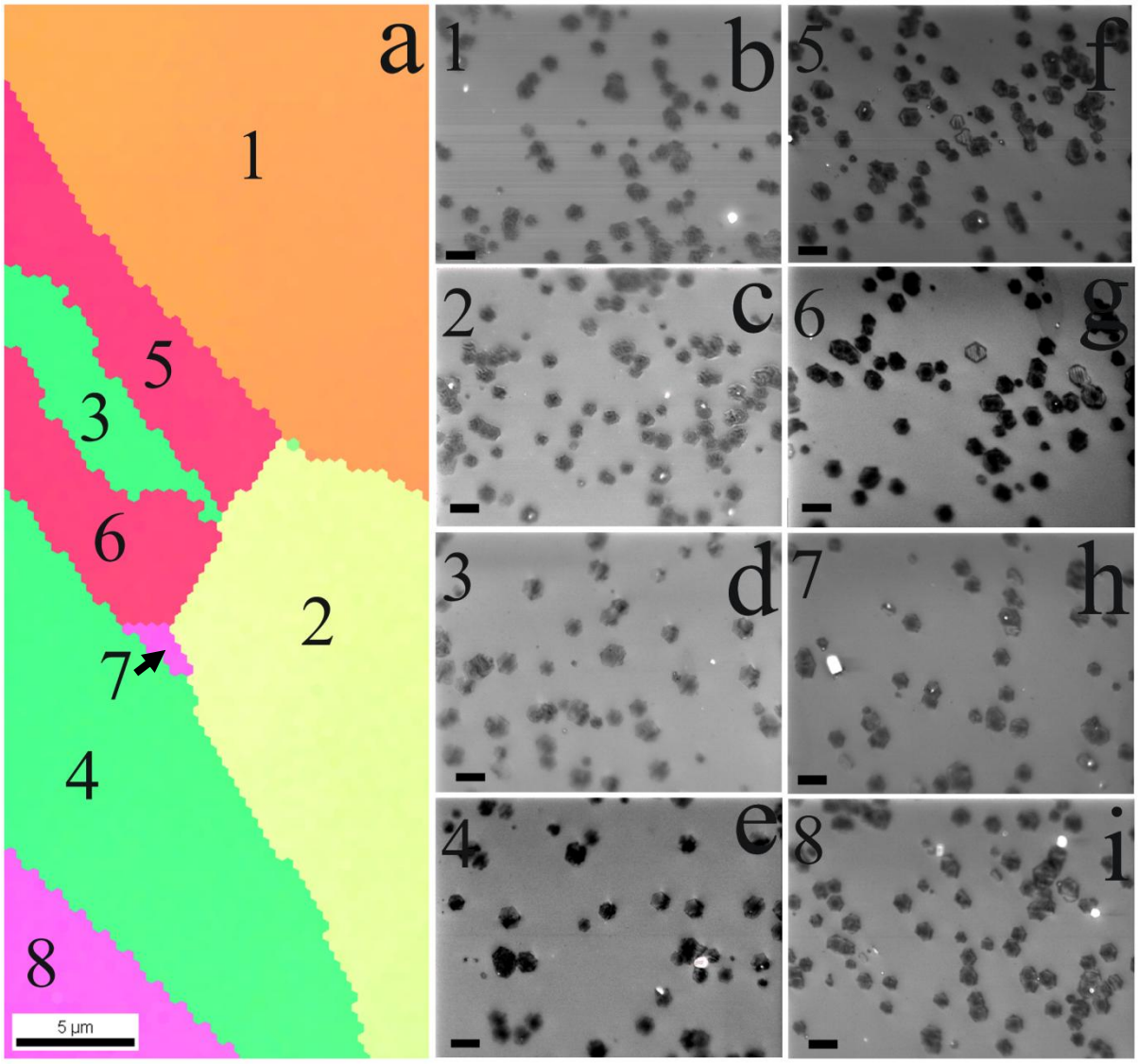


**Figure 5.25.** (a) EBSD mapping of another area containing eight Cu grains, which are labelled with numbers 1-8. (b)-(i) SEM images labelled with 1-8 are corresponding to the FLG grown on the Cu grains labelled with 1-8 in panel a, respectively. The scale bars of all SEM images are 1 µm.

Alignment due to the direction of gas flow can be ruled out as a cause. This is because within the one sheet of Cu, the direction of graphene domain alignment varies from Cu grain to

grain, due to the variation in the relative orientation of the different Cu grains. Within one Cu grain, graphene domains are aligned. This indicates that the mechanism for alignment is the relationship between the atomic structure of the Cu and the growing graphene, along with the role hydrogen plays in forming faceted structures. Since Cu (111) and the graphene hexagonal lattice are both 6 fold symmetric, it is surprising that this leads to a 2-fold symmetric rectangular graphene structure. The observation of strain in the Cu surrounding the rectangular domains suggests the situation is more complicated as the atomic structure of the underlying Cu (111) surface is distorted by the presence of graphene and this may lead to a growth direction that has lower energy and faster kinetics, or conversely a direction where hydrogen is more effective at etching away carbon atoms from the edge of the graphene domain, slowing growth in this direction. It is hard to predict the exact effect that atomic defects in the Cu lattice will have on the shape change and alignment, apart from being sites where nucleation of graphene domains may occur.

Thus, the different kinetics of this catalytic reaction on Cu (111) is the direct reason for the formation and alignment of the rectangular graphene domains. The different kinetics can be affected by the crystal structure of Cu (111), dislocations, or other reasons like hydrogen partial pressure. Vlassiouk *et al* studied the role of hydrogen partial pressure in controlling the size and morphology of graphene domains.[288] It is possible that hydrogen partial pressure play a role in

affecting the catalytic efficiency, and optimum temperature for the formation of various shapes of graphene domains.

From the study in section 5.4, it is clear that by reducing nucleation from impurities and improving the surface quality of the Cu foils it is possible to observe strong interactions between the atomic structure of Cu and the growth dynamics of graphene even at atmospheric pressures. The different growth kinetics on a Cu (111) plane in AP-CVD lead to aligned rectangular shaped single crystal FLG domains, rather than hexagonal domains. These results suggest that the Cu lattice is an important factor in the mechanism of graphene formation in AP-CVD and can be used to align polycrystalline domains in a 2D film and potentially reduce the effect of domain boundaries. By engineering Cu foil with a dominate (111) plane it could lead to large area formation of rectangular shape of graphene domains, which might exhibit interesting physics.

## 5.5. Conclusions

In summary, it is shown that a minimum temperature of 960 $^{o}$C is required for the nucleation of micron sized FLG domains on 99.999% purity Cu foil at atmospheric pressure CVD (APCVD) using methane. Using the high purity foil leads to single crystal FLG domains with layer numbers between 2-4 layers at 1000 $^{\circ}$C growth temperatures, similar to the results from lower purity 99.8% foils. Reducing the temperature of growth from 1000 °C to 990 °C leads to FLG domains

orientated over distances of up to 5 mm along the large scale zig-zag direction of graphene. It is necessary to have hydrogen pre-treatment for the nucleation of FLG domains. The fast cooling rate is required to fabricate the homogenous graphene films. These results show that slight variation in growth temperature can lead to significant variation in the FLG domains formed. By getting deeper understanding of the growth mechanism of graphene on Cu foil in APCVD, it could help to improve the quality of large area polycrystalline graphene film for commercialization of graphene based electronics with low cost.

Also, I have shown for the first time that a morphology transition of micron sized FLG domains from hexagonal to rectangular shape on 99.999% purity Cu foil at atmospheric pressure CVD (AP-CVD) using methane at 980 °C. The growth of hexagonal FLG domains is driven by the 6-fold symmetry of the graphene lattice thermodynamically, while the growth of rectangular FLG domains is heavily influenced by the different growth kinetics on Cu (111) plane. With the possibility of engineering Cu lattice planes on the foil to control the interplay between graphene and Cu, it may be possible to fabricate large area graphene films with improved carrier mobility due to its shape control and large scale alignment. This may pave the way for better quality graphene based electronics.

# Chapter 6:

# Large Area Single Crystals of Graphene on Melted Copper using Chemical Vapour Deposition

## 6.1. Introduction

In chapter 5, the growth dynamics of few layer graphene domains on Cu by APCVD has been studied. The nucleation and alignment of the graphene domains on solid state Cu were studied to answer the open question 3. It is found that the alignment of graphene domains on solid state Cu depends on specific Cu planes. Larger scale alignment of hexagonal or rectangular graphene domains is needed to overcome the polycrystalline nature of the CVD graphene. A more universal way is needed to get larger scale alignment which will lead to large area single crystals. Liquid Cu is considered as a better candidate to achieve this goal. In this chapter, a novel method is investigated to fabricate large area single crystal 2D atomic crystals with low cost using APCVD with open question 4 answered.

The key challenge for implementing graphene in applications is the ability to routinely fabricate large single crystal graphene domains within a continuous 2D film. Chemical vapour deposition (CVD) using copper as a metal catalyst is a promising route towards this goal.[276-277, 279, 283, 290-293] However, the quality for graphene grown by CVD is generally not as good as those exfoliated from graphite due to the small grain size and thus high amount of grain boundaries and defects.[4, 294-296] Improving the size of graphene domains is generally achieved by reducing the number of nucleation sites.[297] Recent work has shown that preparation of the copper surface is crucial to reducing nucleation sites.[297-298] The nucleation sites are often associated with surface roughness, impurities and copper grain boundaries.[208] Electro-polishing of the copper foils has been shown to improve the size of graphene domains.[298] Large sized graphene domains have been grown using low-pressure CVD by adopting the parcel approach, where a copper foil is folded into a small parcel to reduce the amount of methane entering and also provide a better environment for growth.[277] The large graphene domains grown by this method adopt a flower like shape. Ideally it would be beneficial to grow large domains with hexagonal geometry, rather than flower geometry, as these are known to be single crystal, and will have more uniform edge termination of the graphene lattice.[279, 283, 290-293] This is important when considering the interface of graphene domains, which will be more complicated when two flower shaped domains connect as compared to two hexagonal domains.[292]

An alternative method of obtaining graphene domains with increased size has been to use graphene seeds as preformed nucleation sites.[291-292] This was achieved by first growing graphene using conventional CVD methods on copper, then using lithography to pattern seeds at regular intervals. Whilst this is a powerful method of control, it requires substantially more effort and time to obtain larger domain graphene as compared to a one-step direct growth on copper foil approach.

Here a simple one-step method is presented to grow graphene on copper with single crystal sizes exceeding 200 μm. This is achieved by performing the growth at 1090 $^{o}$C, whereby the copper melts and forms a liquid state. Since the growth of graphene on copper is primarily a surface driven process, it does not require it to be in a solid form. It is shown that control of the supplied hydrogen during growth is essential for large graphene crystal sizes, indicating that it plays a major role in the catalytic process of graphene formation.[288] A wide range of parameters have been explored and here the key synthesis details that lead to desirable large domain graphene are reported.

## 6.2. Growth Dynamics and Transfer of Graphene on Melted Cu by CVD

### 6.2.1. Design of Novel Synthetic Method to Fabricate Graphene

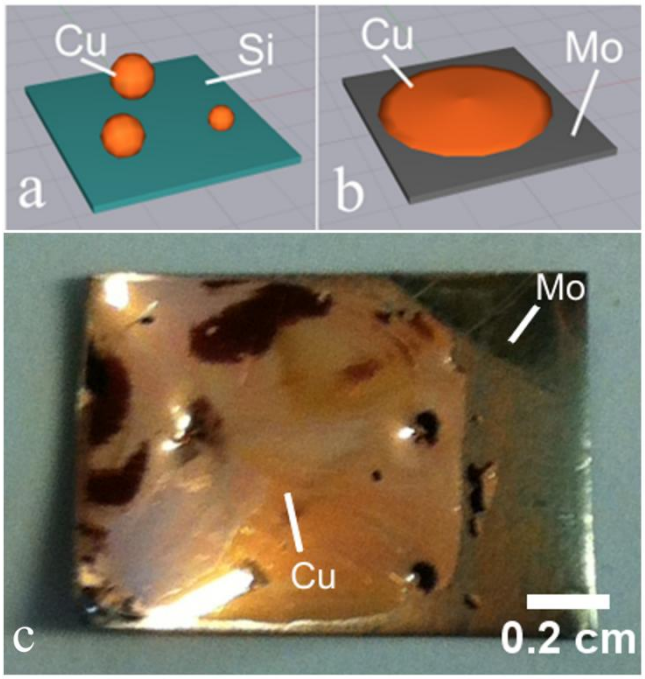


**Figure 6.1.** Schematic illustrations showing (a) balling of copper on silicon and (b) flat thin film of copper on molybdenum, after heating to melted phase (1090 $^{o}$C and cooling). (c) Photo of thin copper film on a molybdenum support after heating to melted phase and cooling.

In chapter 5, the growth mechanism of graphene on solid state Cu has been studied. The seamless merging of these aligned domains will have great possibility to produce large area single crystals. Thus, obtaining larger alignment of the hexagonal or rectangular graphene domains than on the solid state Cu is the key. In order to maintain the 2D flat nature of graphene on melted Cu, a flat copper surface is required. A molybdenum foil support was used to achieve this goal due to its wetting properties to Cu. This prevented balling of the copper that occurs if the reaction is performed on quartz, silicon, or other non-wetting supports, shown schematically in figure 6.1(a) and 6.1(b). Figure 6.1(c) shows a photo of the sample after such a procedure with the copper well spread across the Mo supporting film.

The experimental details are described as followed. The copper foil (99.999% purity, 0.1mm thick, Alfa Aesar) is placed on a Mo or W support (0.1mm thick) and positioned in a 1 inch quartz tube within a horizontal furnace. After purging the whole system with argon gas, it is then heated up to 1090 $^{o}$C under argon flow (200 sccm), which flow rate is remained as it is during the whole CVD process. Then the Cu is reduced in hydrogen (100 sccm) (1:3 $H_2$:Ar mix) at 1090 $^{o}$C for 30 minutes. The flow rate of hydrogen during growth was then adjusted among 10, 40, and 80 sccm and maintained as it is during growth and cooling stages. After this, $CH_4$ (10 sccm of 1:99 $CH_4$:Ar mix) was added for a desired period of growth time, which as adjusted among 15, 45, and 90 minutes. After reaction in $CH_4$, the samples were rapidly cooled by removing from the hot zone of the furnace and allowing cooling to room temperature under the argon and hydrogen atmosphere.

### 6.2.2. Variation in Graphene Growth by Increasing Hydrogen Flow Rate

In order to find the optimized condition for producing monolayer graphene, a systematic study has been pursued on the role of hydrogen for controlling the formation of graphene, since hydrogen both acts as an activator for graphene growth and as the etching agent to control the shape of graphene.[288] SEM images were used to examine the morphology of graphene domains using the in-lens detector on a Zeiss NVision SEM:FIB operating at 2 kV. Raman spectra were acquired to examine the thickness using a JY Horiba Labram Aramis imaging confocal Raman microscope

with a 532 nm frequency doubled Nd:YAG laser and subtracting the broad copper background signal.

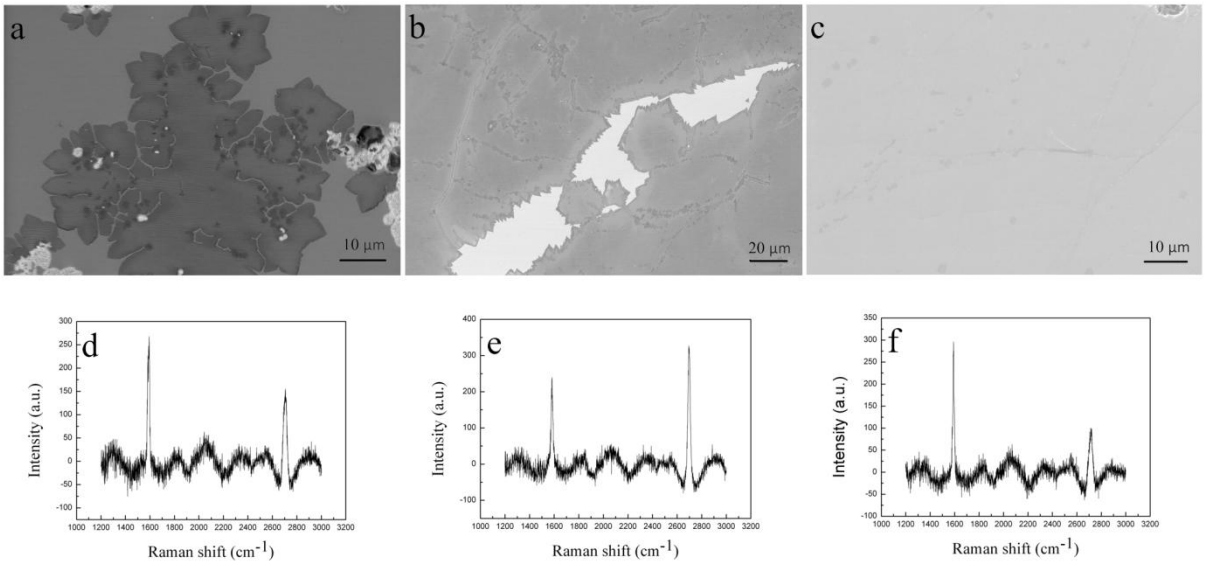


**Figure 6.2:** SEM images of graphene grown at 1090 ºC with a 10 sccm $H_2$ flow rate for times of (a) 15 minutes, (b) 45 minutes, (c) 90 minutes growth time, with corresponding Raman spectra, (d) 15 minutes, (e) 45 minutes, (f) 90 minutes.

The flow rate of hydrogen was first applied as 10 sccm. Figure 6.2(a)-(c) show the SEM images of graphene samples with different growth time ((a) 15 min, (b) 45 min and (c) 90 min) with 10 sccm $H_2$. The edges of the film in figure 6.2(b) were highly jagged, which was not the case for the samples with increasing hydrogen flow rate such as 40 sccm and 80 sccm flow rate shown later. Increasing the flow rate of hydrogen will lead to less jagged edges. The graphene domains merge into continuous film after 90 minutes growth time. The corresponding Raman spectra are shown in

figure 6.2(d)-(f). This indicates the 90 minutes sample with 10 sccm hydrogen is few layer graphene. It is thicker than the 90 minutes sample with 80 sccm hydrogen, which is monolayer, shown in section 6.3.

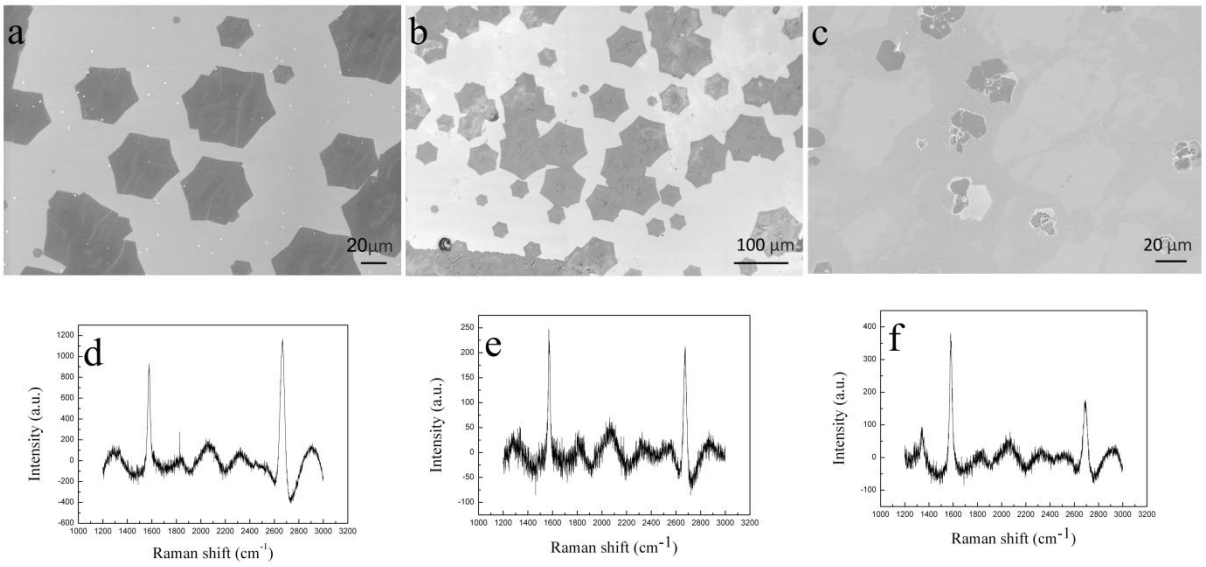


**Figure 6.3:** SEM images of graphene grown at 1090 ºC with a 40 sccm $H_2$ flow rate for times of (a) 15 minutes, (b) 45 minutes, (c) 90 minutes growth time, with corresponding Raman spectra, (d) 15 minutes, (e) 45 minutes, (f) 90 minutes.

Then the hydrogen flow rate was increased to 40 sccm. SEM images of graphene samples grown with only of 40 sccm $H_2$ are shown in figure 6.3 as compared to 80 sccm, which is the optimized condition shown in section 6.2.4 and section 6.3, with growth times of (a) 15 min, (b) 45 min and (c) 90 min. All other parameters were kept the same. The shape of the domains has changed slightly to a star shaped, compared to the highly hexagonal domains produced with 80 sccm $H_2$ flow rate. The domains eventually merge into a continuous film for 90 minutes growth. The corresponding Raman spectra are shown in figure 6.3 (d)-(f). The 2D:G ratio in the Raman spectra

for 45 min and 90 min growth times is less than 1, indicating they are likely to be few layer graphene. This is thicker than the 90 minutes sample with 80 sccm hydrogen, which is monolayer graphene.

### 6.2.3. Variation in Graphene Growth by Increasing Argon Gas Flow Rate

In order to explore how the growth dynamics were influenced by increasing the argon gas, the argon gas flow was increased from 200 sccm to 1 l/min to buffer the flow of both $H_2$ and $CH_4$ during the whole process. This effectively increases the overall flow rate of the reaction. The growth conditions were described as followed. The copper foil (99.8% purity 0.025mm thick) is placed on a Mo support (0.1mm thick) and positioned in a 1 inch quartz tube within a horizontal furnace. It is then heated up to 1000 $^{o}$C under argon flow (1 l/min) rather than 200 sccm Ar used in section 6.2.2 and then reduced in hydrogen (1:3 $H_2$:Ar mix) for 25 minutes. The temperature is then increased to 1090 $^{o}$C and $CH_4$ added (10 sccm of 1:99 $CH_4$:Ar mix) for the desired period of time. Reaction parameters explored were adjusting the flow rate of hydrogen (5, 20, 80 sccm) during growth and the length of growth time. After reaction in $CH_4$, the samples were rapidly cooled by removing from the hot zone of the furnace and allowing cooling to room temperature.

For a growth time of 3 minutes, no graphene was produced with only 5 sccm of volume ratio 1:3 $H_2$:Ar gas mix during growth. Figure 6.4 shows (a) – (c) SEM images and (d) Raman spectra for

samples with 3 minutes growth time and 20 sccm of 1:3 $H_2$:Ar gas mix. After only 3 minutes growth time hexagonal shaped domains were produced with domain size in excess of 20 μm. Figure 6.4(a) shows a larger number of domains that have merged together. Approximately 11 domains that have merged together are shown in figure 6.4(b) and an isolated individual domain is shown in figure 6.4(c). Raman spectra of the domains which are still on the copper is shown in figure 6.4(d) and with the $I_{2D}$:$I_G$ ratio of 1.32 and a Lorentzian FWHM of 30.4 $cm^{-1}$, indicating these domains are primarily monolayer. A central region of dark contrast is apparent in the SEM for some of the domains. It is likely that this region is a small area containing more layers of graphene and is the nucleation site for the domain. This central feature is generally present for samples with short growth times, but disappears for longer times. A possible explanation is that longer growth time results in hydrogen etching of the top graphene layers and the preferential growth of the bottom monolayer.

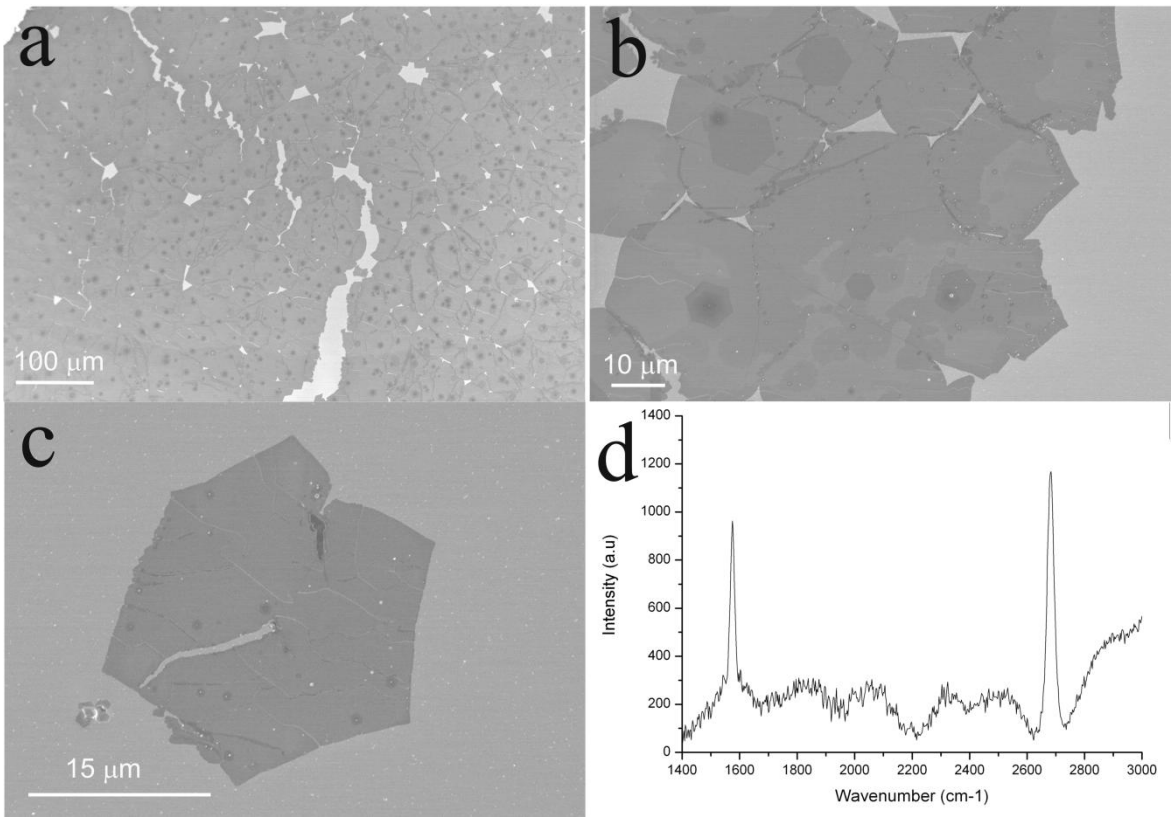


**Figure 6.4.** (a) – (c) SEM images of graphene grown with 20 sccm of hydrogen for 3 minutes. (d) Raman spectrum taken from a single graphene domain grown with 20 sccm of hydrogen for 3 minutes.

Figure 6.5 shows the effect of increasing the hydrogen flow from 20 sccm to 80 sccm, whilst retaining the 3 minute growth time. The SEM images in figures 6.5(a)-6.5(c) show better defined hexagonal domains than those in figure 6.4, indicating the extra hydrogen leads to sharper edges. Again a small dark contrast spot is observed in many of the central regions of the domains. Figure 6.5(c) shows a single isolated domain without the dark central spot and a point-to-point diameter of 41 μm. The Raman spectrum presented in figure 6.5(d) from these domains shows a 2D:G ratio of 1.44 and Lorentzian FWHM of 40.4 $cm^{-1}$, indicating it is primarily monolayer graphene.

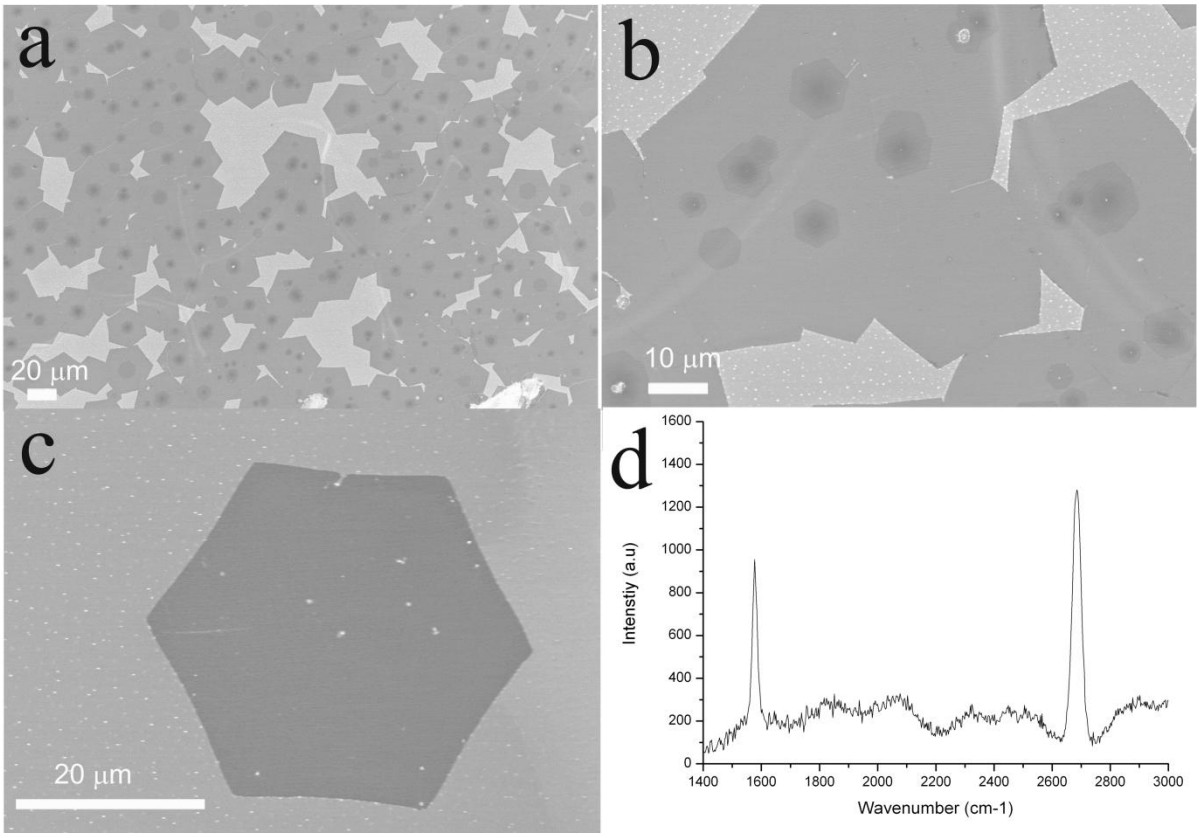


**Figure 6.5.** (a) – (c) SEM images of graphene grown with 80 sccm of hydrogen for 3 minutes. (d) Raman spectrum taken from a single graphene domain grown with 80 sccm of hydrogen for 3 minutes.

Next the growth time was increased to 30 minutes. The SEM images of large hexagonal graphene domains grown with 20 sccm of hydrogen flow are shown in figures 6.6(a)-(c). The Raman spectrum in figure 6.6(d) shows a $I_{2D}$:$I_G$ ratio of 2.03 and Lorentzian FWHM of 25.6 $cm^{-1}$, indicating the graphene domains are primarily monolayer. Figure 6.6(b) shows that a domain size of at least 100 μm is achievable. The edges of the hexagonal domains are not as well defined as those in figure 6.5, but are similar to those grown with 20 sccm of hydrogen for only 3 minutes in figure 6.4.

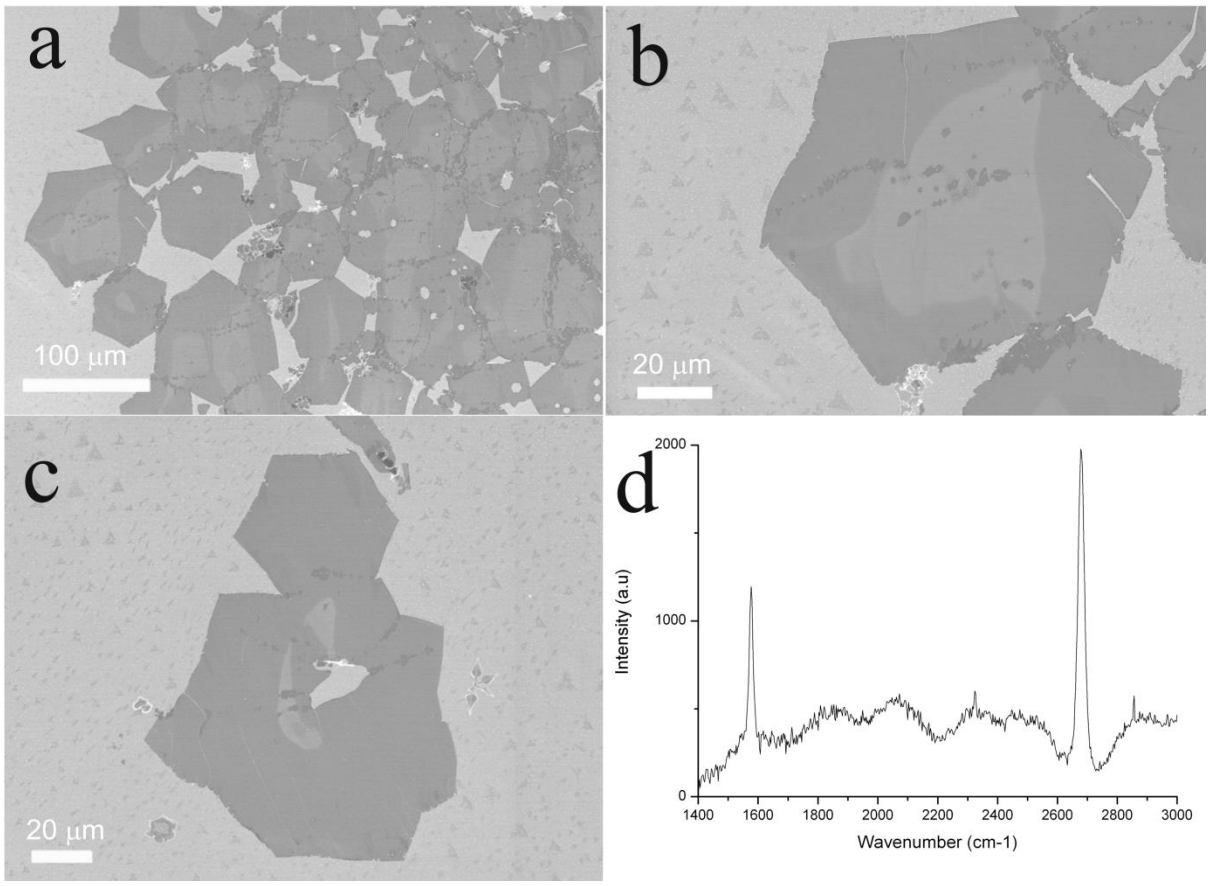


**Figure 6.6.** (a) – (c) SEM images of graphene grown with 20 sccm of hydrogen for 30 minutes. (d) Raman spectrum taken from a single graphene domain grown with 20 sccm of hydrogen for 30 minutes.

Figures 6.7(a)-(c) show the SEM images of large hexagonal graphene domains grown with 80 sccm of hydrogen flow for 30 minutes duration. Figure 6.7(b) shows a domain in the bottom left with point-to-point diameter of ~100 μm, with a total area of ~6550 $\mu m^2$. The Raman spectrum in figure 6.7(d) shows a $I_{2D}$:$I_G$ ratio of 1.2 and Lorentzian FWHM of 30.2 $cm^{-1}$, indicating that it is primarily monolayer. The hexagonal graphene domains grown with 80 sccm of hydrogen have sharper defined edges compared to those grown with 20 sccm of hydrogen, indicating that the hydrogen plays a role in defining the regularity of the edges. For growth with only 5 sccm of hydrogen, no graphene was produced even for 30 minutes duration.

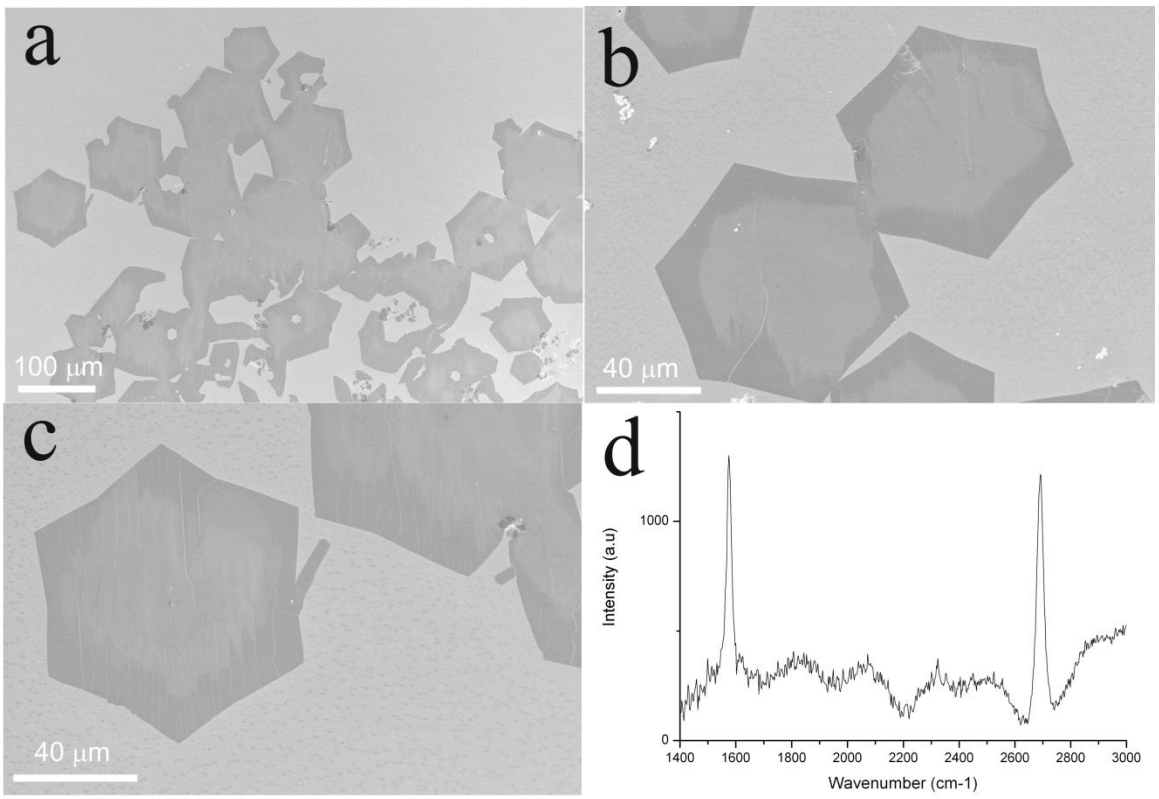


**Figure 6.7.** (a) – (c) SEM images of graphene grown with 80 sccm of hydrogen for 30 minutes. (d) Raman spectrum taken from a single graphene domain grown with 80 sccm of hydrogen for 30 minutes.

### 6.2.4. Optimization Growth for Producing Monolayer Graphene

After exploring a wide range of experimental parameters, it is found that using a flow rate of 80 sccm of hydrogen and 10 sccm of $CH_4$ with 200 sccm Ar led to the best results in terms of producing monolayer graphene of which the characterization result will be shown in section 6.3. Reducing the flow rate of hydrogen led to faster growth rates, but thicker films, which is shown in section 6.2.2. After 15 minutes of growth time with 80 sccm of hydrogen with 200 sccm Ar, the reaction was stopped, and this resulted in well-defined hexagonal graphene domains, shown in figures 6.8(a) and 6.8(b), plus the inset in 6.8(b). The nucleation density was low and this enabled

large domains to grow. Two different size ranges are observed, namely large domains greater than 100 μm and smaller domains between 20-40 μm. Surprisingly, the hexagonal domains were self aligned in their orientation which indicates in the red arrow. For 15 min growth a continuous film was not produced, only isolated domains. Figures 6.8(c) and 6.8(d) show SEM images of the graphene after 45 minutes of growth, and a continuous film was observed. Figures 6.8(e) and 6.8(f) show the SEM images for 90 minutes of growth, and a continuous film was also produced. The major difference between the 45 and 90 minute growth samples is that the 90 minutes growth showed less contrast variation in SEM, which may indicate more uniform layer coverage or reduced amounts of amorphous carbon on the surface. The SEM images in figures 6.8(c), 6.8(e) and 6.8(f) were intentionally taken in regions near the edge of the copper where the graphene films had ruptured or not fully covered to the edge, so that some contrast can be observed in the images. For 45 and 90 minutes of growth more than 90% of the copper is covered with a continuous film, with only the edges of the copper deviating. Samples can be easily trimmed around the edges to remove these broken bits to leave a fully continuous 2D film of graphene. Figure 6.8(g) shows a high magnification SEM image of the fully continuous region of the graphene film. Colour is used to highlight variation in contrast that arises due to changes in the number of graphene layers. Lines of contrast associated with wrinkles in graphene due to cooling are observed. Apart from the wrinkles, the overall contrast of the graphene is uniform.

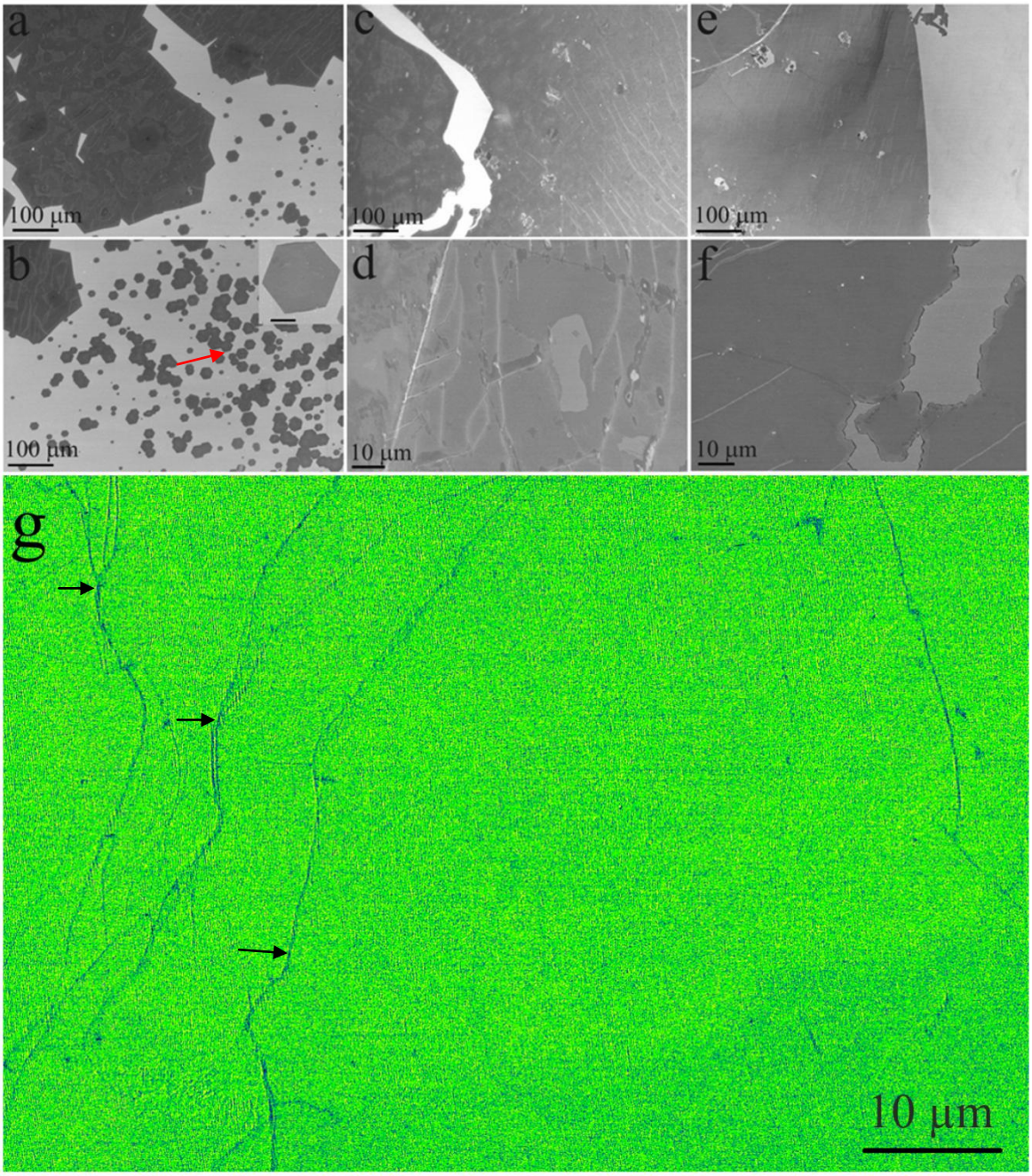


**Figure 6.8.** SEM images of graphene produced with 80 sccm hydrogen flow rate for growth times of (a)-(b) 15 minutes (inset shows hexagonal graphene domain with 20 µm scale bar), (c)-(d) 45 minutes, and (e)-(f) 90 minutes. (g) High magnification SEM image of graphene on copper produced with 90 minutes growth time. Colour is used to highlight contrast variation. Arrows indicate typical wrinkles in the graphene film.

### 6.2.5. Comparison of Molten Cu and Solid State Cu Catalyst

In order to show the advantages of melted Cu over solid state Cu, a comparison study was performed on solid state Cu. This synthetic experiment was done by Kuang He in Department of Materials, Oxford. In figure 6.8(e)-6.8(f), it has shown that 90 minutes of growth time at 1090 $^{o}$C under conditions of 10 sccm of methane, 80 sccm of hydrogen and 200 sccm Ar, led to continuous monolayer graphene films. Here, the same growth conditions are employed, but with the temperature at 1000 $^{o}$C, which is below the melting point (1060 $^{o}$C) of Cu, and thus the copper is not molten. A typical SEM image of such a graphene film produced at 1000 $^{o}$C for 90 minutes growth is shown in figure 6.9. It appears to contain more contrast variation than the one produced with the molten copper. The major difference is in the Raman spectra. Figure 6.10 shows 4 Raman spectra taken from random locations within the film. All Raman spectra showed 2D peak intensities lower than the G peak, indicative of few layer graphene. Comparison with figure 6.7(d) shows the difference in growth between the two temperatures.

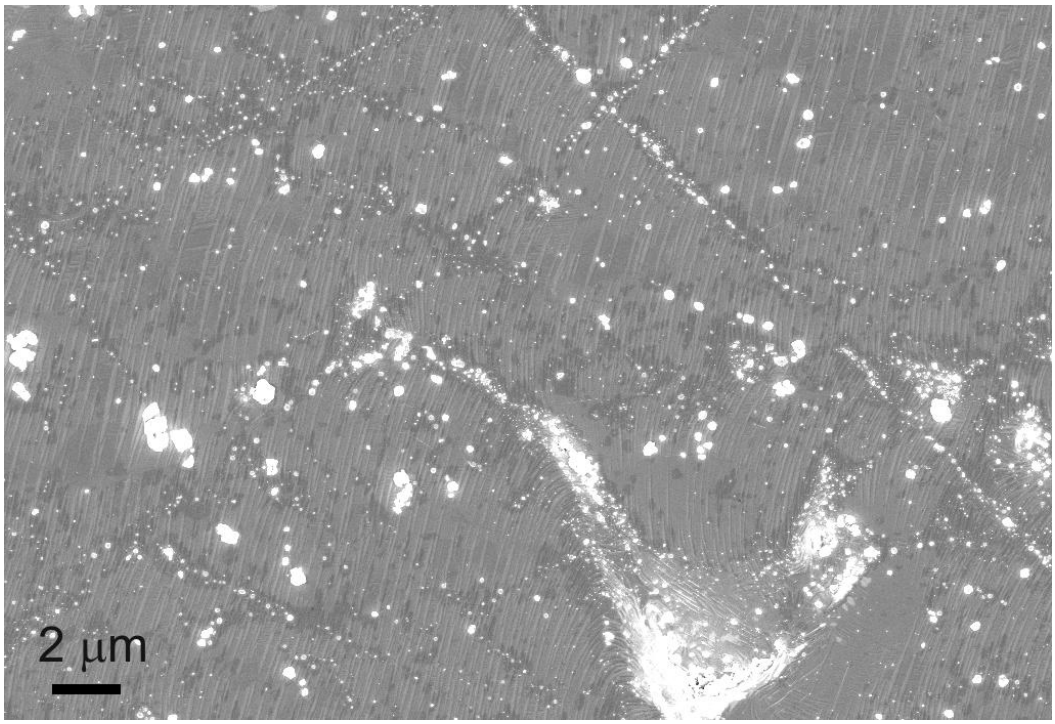


**Figure 6.9**. Typical SEM image of a region of a continuous graphene film produced with 90 minutes growth time at 1000 $^{o}$C, with 10 sccm of $CH_4$ and 80 sccm of $H_2$.

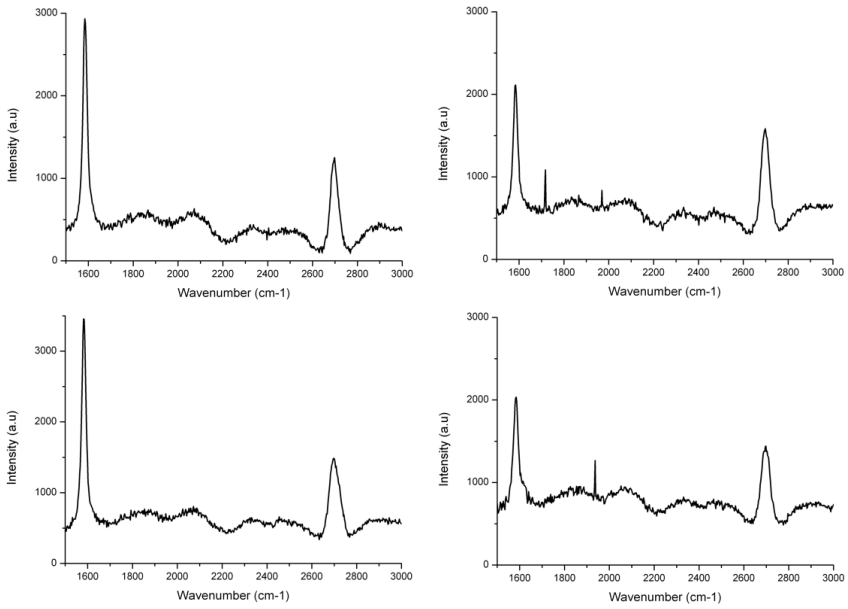


**Figure 6.10.** Raman spectra taken from random locations within the few layer graphene film shown above in figure 6.9.

## 6.2.6. Clean Transfer of Graphene

### 6.2.6.1. Method

A PMMA supportive scaffold (8% wt. in anisole, 495k molecular weight) was spin cast onto the graphene surface on the copper/molybdenum substrate after growth. A spin speed of 4700 rpm was used for 60 seconds, with the film then cured by heating at 180 °C for 90 seconds. Then the underlying copper/molybdenum film was etched away in 100ml of iron (III) chloride solution with 0.3 ml hydrochloric acid for 3 days. The graphene/PMMA film was then rinsed in deionised (DI) water several times until the water was colourless (i.e no more iron chloride is present). The graphene/PMMA film was transferred to a solution of hydrochloric acid (30%) for 5 minutes to remove any remaining iron chloride residue and then transferred to a DI water bath to remove the residue of hydrochloric acid. The graphene/PMMA film was then transferred onto $Si_3N_4$ TEM grids. The PMMA is finally removed using either acetone to dissolve it, or a combination of heating in air and in vacuum at temperatures below 400 $^{o}$C.

### 6.2.6.2 Optical Contrast of Graphene Transferred onto Si:$SiO_2$ Substrates

Optical microscopy was used to examine the graphene after transfer. Graphene grown for 90 minutes was transferred using a PMMA support onto a silicon substrate that has a 300 nm $SiO_2$ surface layer. The sample was heated at 150 $^{o}$C for an hour to adhere the graphene to the substrate and then immersed in acetone solution for 2 days to remove the PMMA, followed by annealing under vacuum at 300 $^{o}$C for 2 hours to remove any surface contaminants. Similar procedure was

performed for few layer graphene grown at 1000 $^{o}$C.[283] The optical images of graphene samples transferred onto silicon for graphene grown for 90 minutes at 1090 $^{o}$C are shown in figure 6.11(a)-(d). Figure 6.11(e) is the same image as in figure 6.11(a) but with the contrast and brightness adjusted with an arrow indicating the crack on graphene film, and figure 6.11(f) is graphene grown at 1000 $^{o}$C.[283] The optical images were taken in regions where holes in the film were present to demonstrate the contrast of graphene relative to the background. In figures 6.11(a) – (d), the area covered by graphene appears as blue. The contrast from the regions covered with graphene is uniform, apart from a long range variation due to the uneven illumination intensity of the light. No distinct steps in contrast are visible, (apart from the monolayer graphene relative to the uncovered area), that would be associated with increasing layer thickness from monolayer to bilayer graphene. However, the sample prepared at a temperature of 1000 $^{o}$C, which is known to have smaller domains and variation in the number of layers, shows significant variation in contrast across the image in figure 6.11(f).

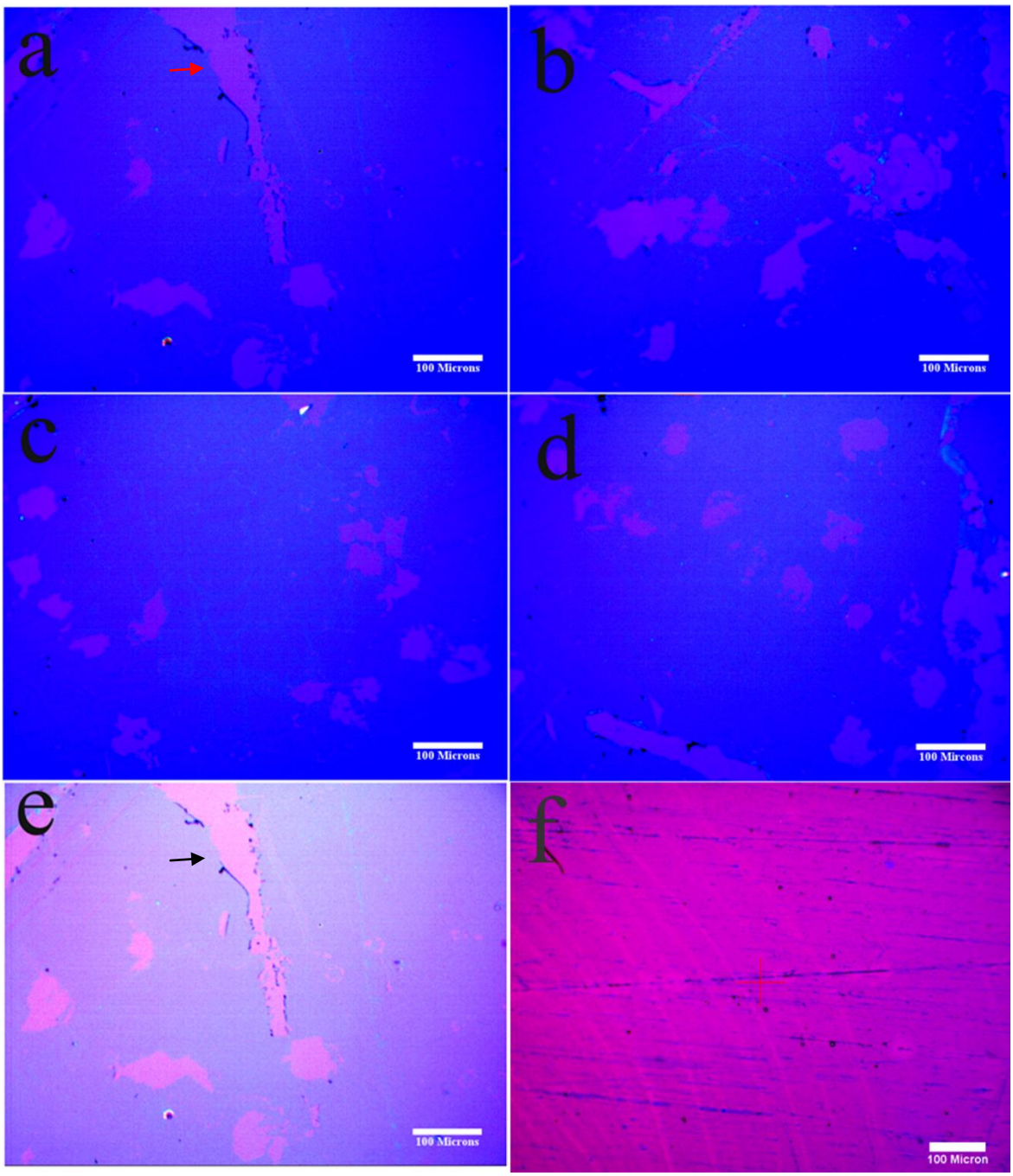


**Figure 6.11.** Optical images of graphene transferred onto a Si substrate with 300 nm oxide layer for (a)-(d) Graphene grown for 90 minutes at 1090 $^{o}$C. (e) Same image as in (a) but with adjusted contrast. (f) Graphene grown at 1000 $^{o}$C and transferred.

## 6.3. Characterization of Large Area Single Crystal Monolayer Graphene

### 6.3.1. Thickness Identification

#### 6.3.1.1. Raman Mapping

In order to examine the thickness of graphene produced with the optimized condition described in section 6.2.4, Raman spectroscopy was performed on these 3 graphene samples. Figures 6.12(a), 6.12(b), and 6.12(c) show the graphene samples with growth times of 15, 45 and 90 minutes respectively. In figure 6.12(a), Raman peak 2D:G ratio is less than 1 which indicates the hexagonal domains are likely to be more than one layer. In comparison, figures 6.12(b) and 6.12(c) show that the 2D:G ratio of Raman peaks is greater than 1, which indicates the graphene is between 1-2 layers. Further evidence will show that the 90 minute growth time (Figure 6.12(c)) is monolayer graphene and the attention is focussed on characterizing this sample in depth. 2D Raman spectroscopy mapping was performed with the sample grown for 90 minutes and extracted the intensity ratio of the 2D:G peaks and FWHM of the 2D peak as figures of merits for examining the thickness of graphene layers. The small area Raman mapping of graphene on Cu was performed first in a 20x20 μm with a step of 2 μm which are shown figure 6.12(d)-(e). Figure 6.12(d) shows the 2D map of the 2D:G intensity ratio, with values ranging from 2.5 – 6.5. The 2D map of the FWHM of 2D peak is extracted, which is shown in figure 6.12(e) with values ranging between 21 – 36 $cm^{-1}$. The important point to gather from figure 6.12(d) is that the 2D:G intensity peak ratios

are greater than 1, which indicates monolayer graphene.[181] Even considering the possible 2D peak broadening of graphene on Cu,[299] FWHM value range is less than 40 $cm^{-1}$ , which supports the notion that monolayer graphene is produced.[181] Thus, monolayer graphene is produced in this 20x20 μm region.

In order to examine the thickness over a larger area a 2D Raman map of graphene on the copper after 90 minutes growth at 1090 $^{o}$C taken over a 100x100 μm large area, in steps of 4 μm, was done, which is shown in figure 6.12(f)-(g). The 2D map of the 2D:G intensity ratio is shown in figure 6.12(f) with range from 2 to 10, while the FWHM of 2D peak is ranging from 3-32 $cm^{-1}$ in figure 6.12(g). The 2D:G intensity ratio is greater than 1 and the FWHM of 2D peak is less than 40 $cm^{-1}$, which both indicate monolayer graphene is produced in this 100x100 μm large region.[181] The reason why longer growth time (90 minutes) gives monolayer but short growth time gives multilayer graphene is because the hydrogen acting as an etchant can eat more top layers when grow longer.[204]

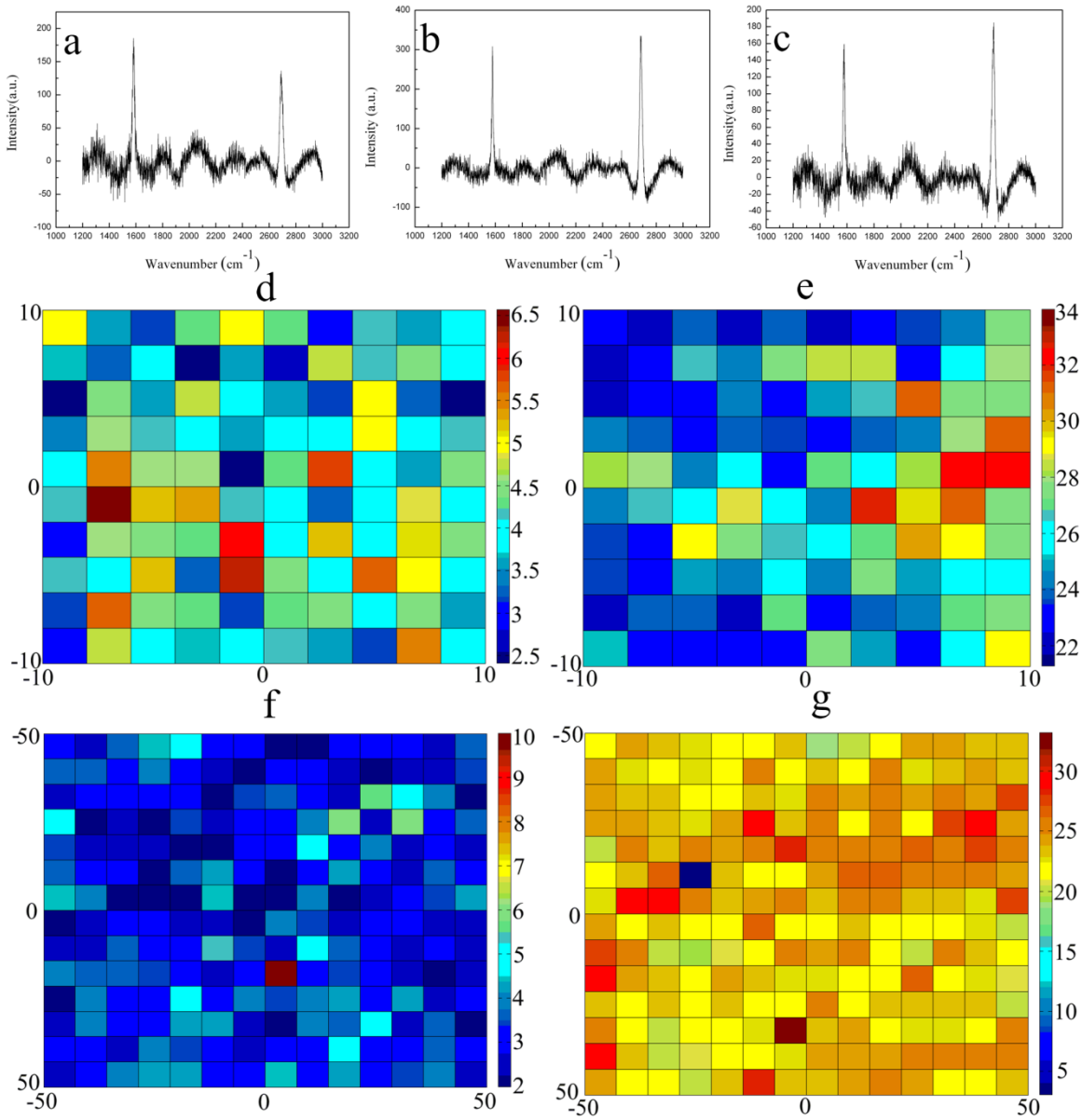


**Figure 6.12.** Raman spectra of points taken on copper after growth times of (a) 15 minutes, (b) 45 minutes, and (c) 90 minutes, (copper background subtracted for all spectra); Small area Raman mapping: (d) 2D map (20x20 µm, 2 µm step) of the 2D:G peak ratio of 2D peak of graphene grown for 90 minutes at 1090 °C on copper. (e) 2D map (20x20 µm, 2 µm step) of the FWHM of 2D peak of graphene grown for 90 minutes at 1090 °C on copper. Large area Raman mapping: (f) 2D map (100x100 µm, 4 µm step) of the 2D:G peak ratio of graphene grown for 90 minutes at 1090 °C on copper. (g) 2D map (100x100 µm, 4 µm step) of the FWHM of 2D peak of graphene grown for 90 minutes at 1090 °C on copper.

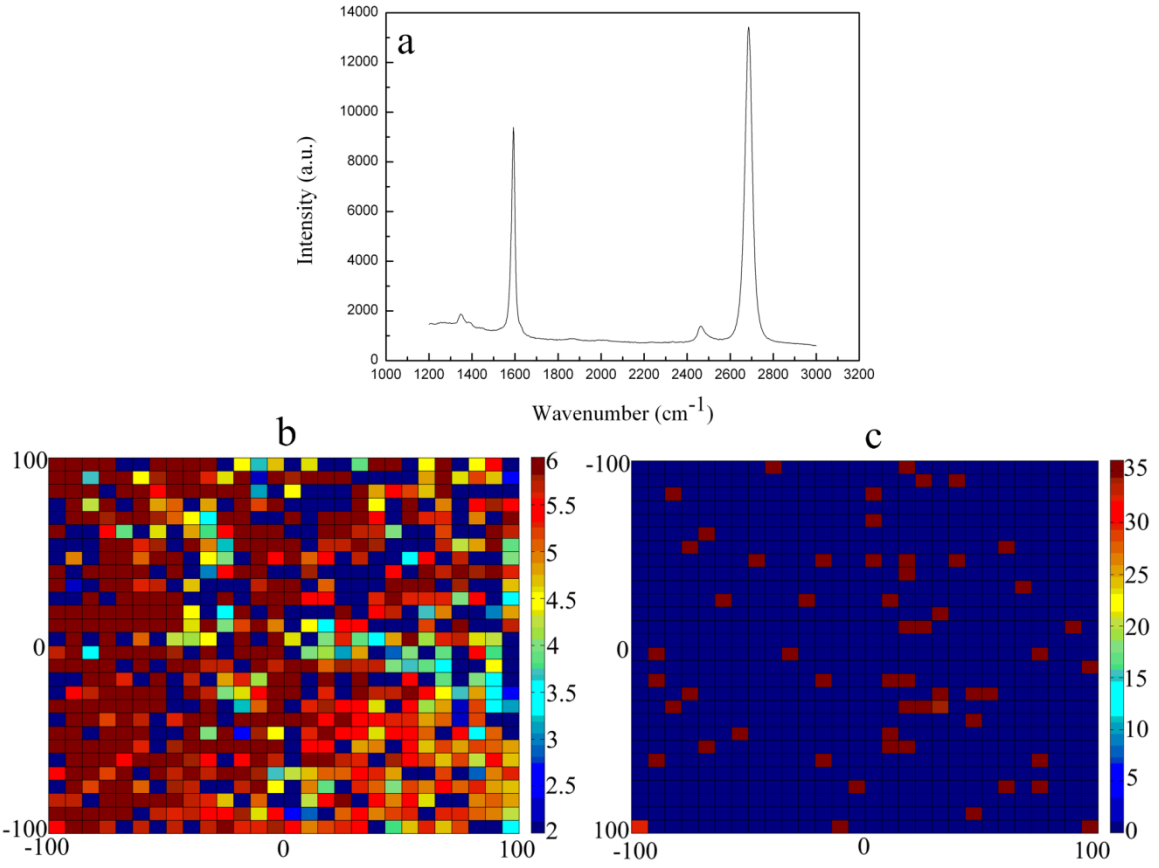


**Figure 6.13.** (a) Typical Raman spectrum of points taken from graphene grown for 90 minutes at 1090 °C and then transferred onto a $SiO_2$:Si substrate.(b) 2D map (200x200 µm, 8 µm step) of the 2D:G intensity ratio for graphene grown for 90 minutes at 1090 °C and then transferred onto a $SiO_2$:Si substrate. (c) 2D map (200x200 µm, 8 µm step) of the FWHM of 2D peak of graphene grown for 90 minutes at 1090 °C and then transferred onto a $SiO_2$:Si substrate.

In comparison, Raman spectroscopy was also performed with graphene transferred from Cu. A typical Raman spectrum of the graphene on the $SiO_2$:Si substrate is presented in figure 6.13(a). Figure 6.13(b) shows a 2D map of 2D:G ratio after transferring onto a $SiO_2$:Si substrate over a 200x200 µm area with 8 µm steps. The 2D Raman maps show that the 2D:G ratio, ranging from 2 to 6, is greater than 1 on the sample, indicating the sample is monolayer over this vast region after transferring from Cu to $SiO_2$:Si substrate.[181] The FWHM of 2D peak, ranging from 2 to 36 $cm^{-1}$ in

figure 6.13 (c), is less than 40 $cm^{-1}$, indicating the sample is monolayer over this vast region on $SiO_2$:Si substrate.[181]

The Raman background noise difference between Cu (figure 6.12(a)-(c)) and Si (figure 6.13(a)) is due to the different interactions between graphene and substrates.[299-302] The weak Van de Waals interaction between graphene and Si or $SiO_2$ substrate enhances the reflection of photons which will lead to better signal to noise ratio.[300-301] This is the reason why Raman spectroscopy of graphene is normally done after transferring to Si or $SiO_2$ substrate in the literature, which has similar spectrum as shown in figure 6.13 (a). However, the transfer of graphene will inevitably bring some defects or wrinkles, which is not the intrinsic nature of the graphene on Cu. Although the strong plasmonic effect exists between graphene and Cu,[302] which causes the lower signal to noise ratio and background noise, shown in figure 6.12(a) to (c), it preserves the intrinsic nature of pristine graphene directly grown on Cu. By doing Raman spectrum of graphene directly on Cu can even reveal the strains between graphene and Cu lattice.[299] Normally the 2D peak of graphene on Cu will be broadened compared with graphene transferred onto $SiO_2$.[299] Both Raman studies, shown in figure 6.12 and 6.13, give strong evidence that the graphene produced by this method is monolayer over a 200x200 μm area.

### 6.3.1.2. Electron Beam Sputtering and Direct Imaging

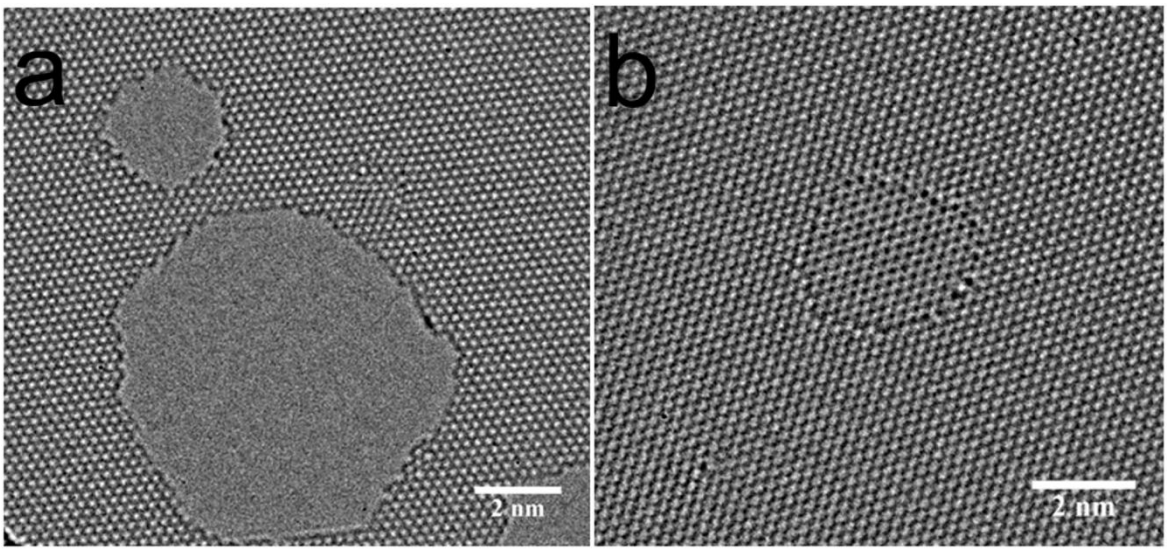


**Figure 6.14**. Electron beam irradiation of (a) monolayer graphene produced at 1090 ºC, for 90 minutes growth, and 80 sccm. (b) Few layer graphene produced at 1000 $^{o}$C with methods described in chapter 5.

In order to give further evidence that the graphene produced from 90 minutes growth was monolayer, Dr. Jamie H. Warner performed imaging of the atomic structure using the Oxford-JEOL-2200MCO FEG $C_s$ aberration-corrected HRTEM at an accelerating voltage of 80 kV. When examining graphene using aberration corrected HRTEM at an accelerating voltage of 80 kV, the number of graphene layers can be counted by a combination of sputtering and imaging.[303] Focusing the electron beam produces holes in the back graphene sheet for few layer graphene. Figure 6.14(a) shows holes sputtered into graphene grown for 90 minutes at 1090 $^{o}$C with 80 sccm of hydrogen gas flow described in section 6.2.4. The holes open up to vacuum, indicating it is monolayer graphene. Figure 6.14(b) shows the same procedure undertaken with multilayer graphene produced using copper in its solid state (i.e growth at 1000 $^{o}$C).[283] The hole in the back

monolayer does not open to vacuum, but instead to another graphene layer. Thus, this is not monolayer graphene.

### 6.3.1.3. Selective Area Electron Diffraction

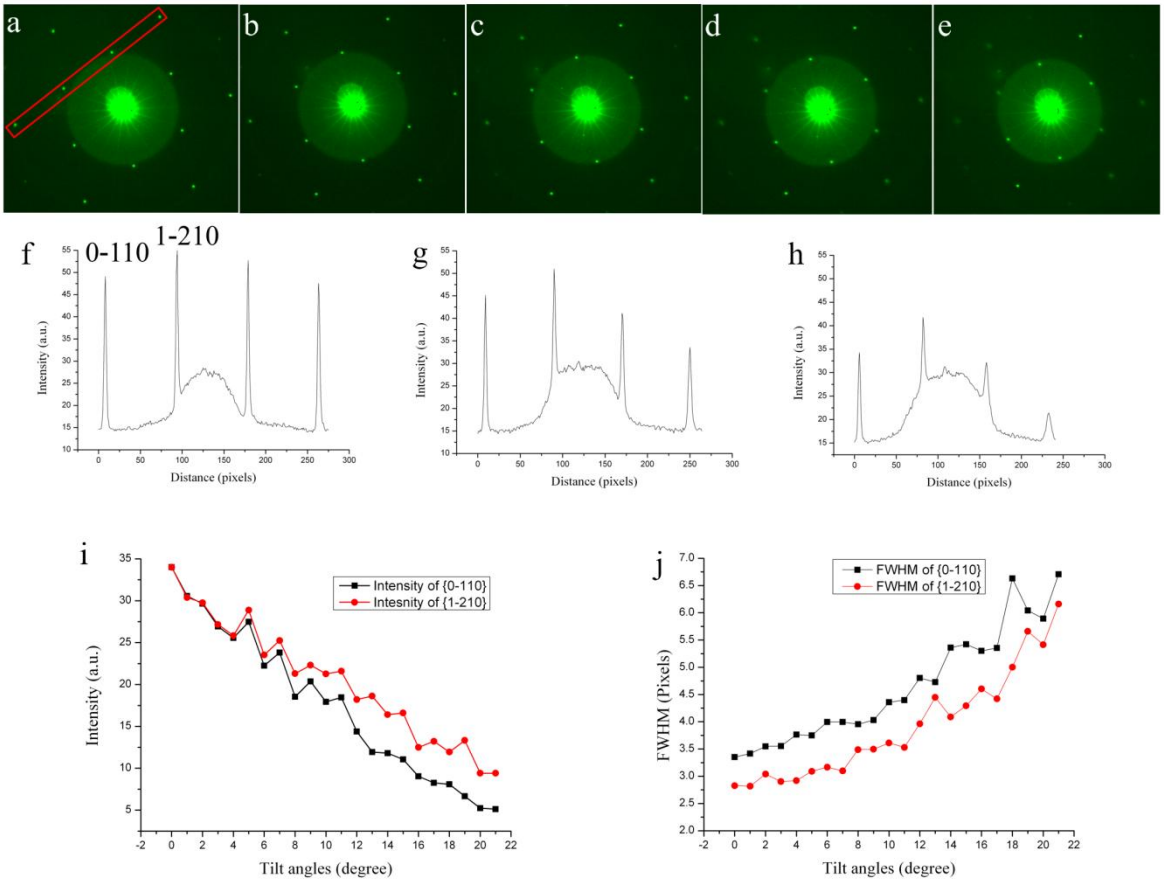


**Figure 6.15**. Selected area electron diffraction patterns from graphene with 90 minutes growth time at tilt angles of (a) 0 °, (b) 5 °, (c) 10 °, (d) 15 °, and (e) 20 °. (f) – (h) shows the line profiles for 0 °, 10 ° and 20 ° degree tilt angles respectively. (i) The intensity of the $\{1\bar{2}10\}$ and $\{0\bar{1}10\}$ peaks relative to the background for angles up to 21 °, in 1 ° intervals. (j) Full-width at half maxima as a function of tilt angle, obtained from Gaussian fits to the $\{0\bar{1}10\}$ and the $\{1\bar{2}10\}$ SAED peaks in the line profiles.

Further evidence on the thickness of graphene was provided by using selected area electron diffraction pattern as a function of tilt angle. The experiment was done by Dr. Jamie H. Warner at University of Oxford using the Oxford-JEOL-2200MCO FEG $C_s$ aberration-corrected HRTEM at an accelerating voltage of 80 kV. The intensity of the $\{1\bar{2}10\}$ and $\{0\bar{1}10\}$ spots in a selected area electron diffraction pattern from monolayer graphene as a function of tilt angles are different compared to bilayer and other few layer graphene samples. As monolayer graphene only has the zero order Laue zone, the intensity of diffraction peaks should monotonically decrease but without large fluctuation as the function of the tilting angles, in comparison of the large fluctuation with singularities for the case of bilayer graphene.[17] The peak widths should increase with tilting angles and proportionally to the peaks' position in reciprocal space for monolayer graphene.[17]

Figure 6.15 shows such a study with graphene produced with 90 minutes growth time. The SAED patterns taken from graphene at tilt angles of (a) $0^o$, (b) $5^o$, (c) $10^o$, (d) $15^o$, and (e) $20^o$ are shown in figures 6.15(a)-6.15(e) respectively. A colour 'green' LUT (lookup table) is used to enhance contrast by using Image J software. The red box in figure 6.15(a) shows the area used for a line profile analysis, i.e intensity Vs distance. Figures 6.15(f) – 6.15(h) show the line profiles for 0, 10 and 20 degree tilt angles respectively. The intensity of the $\{1\bar{2}10\}$ and $\{0\bar{1}10\}$ peaks relative to the background was determined and plotted in figure 6.15(i) for angles up to $21^o$, in $1^o$ intervals. The intensity of both peaks follows the expected trend for monolayer graphene with no large

swings in value, and just a smooth reduction in overall intensity. Figure 6.15(j) plots the full-width at half maxima (FWHM) as a function of tilt angle, obtained from Gaussian fits to the $\{0\bar{1}10\}$ and $\{1\,\bar{2}\,10\}$ SAED peaks in the line profiles. As expected for monolayer graphene, the FWHM increases with tilt angle.[17] Analysis of the intensity of the SAED spots as a function of tilt angle confirmed the graphene was monolayer and not bilayer.

### 6.3.2. Crystal Structure Examination

The clean transferred graphene on $Si_3N_4$ (denoted SiN) TEM grids that contained an array of 2.5 μm holes with 2.5 μm in diameter and a pitch of 4.5 μm, is shown in the optical image in figure 6.16(a). Figure 6.16(b) shows a low magnification TEM image of the holes with labeling of X, Y and Z axis to form a labeling system for identification of specific holes within the grid. Focused electron beam irradiation is known to open up holes in graphene layers, one by one, enabling the counting of layers. It is found that all the graphene examined using HRTEM was purely monolayer, with no signs of small extra bilayer that are often found in the CVD growth of graphene with solid copper catalysts. Figure 6.16(c) shows a HRTEM image of a typical region of graphene with two holes sputtered by electron beam irradiation. These holes directly open to vacuum and show that the graphene is monolayer. The small disorder in the graphene film is caused by the electron beam irradiation and not intrinsic to the film. During the extensive HRTEM investigation of more than 50 individual 2 μm windows in the TEM grid, no signs of noticeable

grain boundaries or any intrinsic large scale defects or disorder were found. In order to elucidate the typical crystallite size within the 2D film the selected area electron diffraction (SAED) pattern was measured from graphene along 45 consecutive windows of the TEM grid in the x-axis direction, starting from the 0 point in figure 6.16(b). Figure 6.16(d) shows the SAED patterns for several hole windows, numbered in the top left of each panel (i.e x1 corresponds to hole 1 along the x axis) The relative angle in degrees, θ, of the graphene lattice was measured from the SAED, as shown in the x0 plane in figure 6.16(d), and is marked in the bottom left of each panel. All SAED patterns were single crystal. Less than $2^{o}$ rotation of the graphene lattice direction is measured between x0 and x18, which corresponds to a distance of 81 μm. Between x18 and x22, a step increase of $3^{o}$ occurs, which correlated with a slight pinching of the film on the SiN grid. Overall a lattice rotation of less than $5^{o}$ occurs between x0 and x45, which corresponds to a distance of ~202 μm. Similar measurements were taken for windows in the y and z axes, both which showed similar orientations. The limitation of the measurements was that x45 was the last hole in the TEM grid. These results show a remarkable 200 μm single crystal of monolayer graphene has been produced.

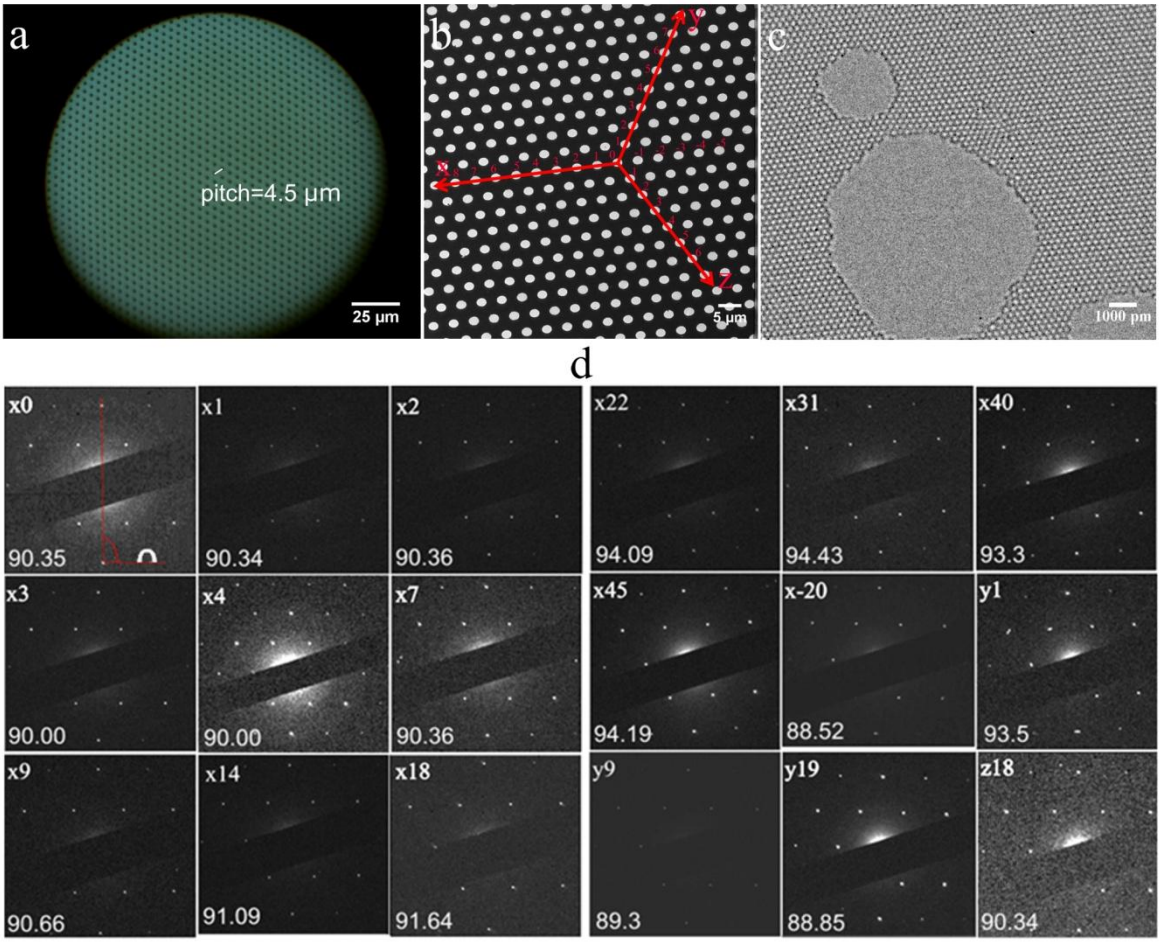


**Figure 6.16.** (a) Optical image of a SiN TEM grid with array of 2.5 µm window holes. (b) Low magnification TEM image of the SiN TEM grid with array of 2 µm window holes. (c) Aberration-corrected HRTEM image of graphene on SiN grid after prolonged electron beam irradiation to count the number of layers by hole opening. (d) Selected area electron diffraction patterns taken from different regions of the SiN TEM grid, labeled (top left in each panel) according to the X, Y, Z axis scheme indicated in (b). Measured angle (in degrees) of graphene lattice recorded in bottom left of each panel, according to the axis defined in first (x0) panel.

### 6.3.3. Band Structure Determination

Micro-spot angle-resolved photoemission spectroscopy (micro-ARPES) was used to examine the graphene on copper produced by the 90 minutes growth time, prior to transfer. The measurements have been performed at XPEEM/LEEM endstation, at National Synchrotron Light Source beamline U5UA by Dr. Jerzy T. Sadowsk in Brookhaven National Laboratory. Data were taken

with incident photon energy of 43 eV. Figure 6.17(a) shows detected intensity in the $k_x$-$k_y$ plane, at an energy 0.7 eV below the Fermi energy, $E_F$ and figure 6.17(b) the E(k) intensity close to the K point, along a line perpendicular to Γ−K, indicated in figure 6.17(a). The presence of multiple sets of features shown in micro-ARPES intensity map in figure 6.17(a) is attributed to terracing of the copper surface and subsequent deviation of the graphene lattice. Figure 6.17(b) shows a single, linear dispersion relationship close to $E_F$, indicating monolayer graphene and no sign of doping. This confirms the graphene is of high quality, and that despite the epitaxial nature of the growth, there is little electronic interaction with the substrate. Further from $E_F$ the structure is more difficult to ascertain due to contributions from both of the tilted domains.

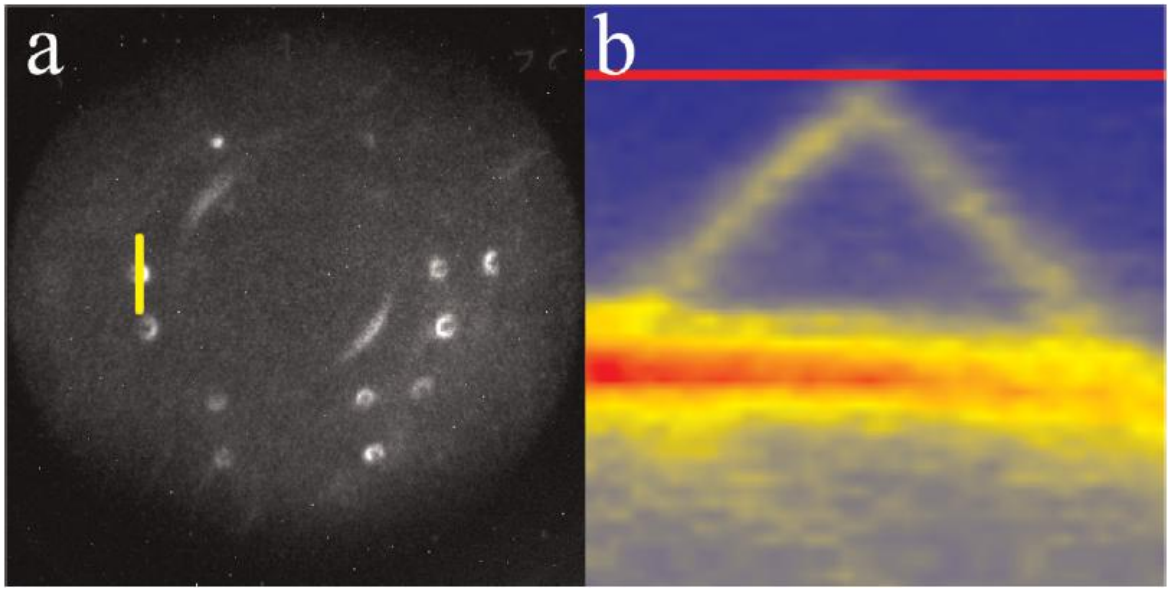


**Figure 6.17**. (a) Detected intensity in the $k_x$-$k_y$ plane, at an energy 0.7 eV below the Fermi energy, $E_F$. (b) E(k) intensity close to K point, along a line perpendicular to Γ-K (indicated by the yellow line in (a)), with the Fermi energy represented by the red line.

## 6.4. Growth Mechanism of Single Crystal Monolayer Graphene

### 6.4.1. Epitaxial Relationship between Cu Lattice and Hexagonal Graphene Domains

In order to understand the interplay between Cu and graphene in this novel synthetic method, the correlation between Cu lattice and graphene is examined. Electron back-scattered diffraction (EBSD) was used to examine the crystallographic nature of the copper beneath the graphene after growth. The EBSD experiment was performed by Dr. Susannah Speller at Department of Materials, University of Oxford. Electron Backscatter Diffraction analysis on the copper substrate was carried out using TSL software in a JEOL JSM 6500F FEGSEM. Figure 6.18(a) is a schematic showing the angle of the electron beam relative to the sample and the normal direction (ND) and in-plane direction (RD). In CVD reactions, the copper reaches some form of molten state and then rapid cooling leads to crystallization. Figure 6.18(b) shows a SEM image (tilted by $70^{o}$) of sample with 15 minutes growth time, as in figures 6.8(a) and 6.8(b), with aligned graphene hexagons. The inset in the top right shows the color codex used to display copper lattice directions in the EBSD maps. Figures 6.18(c) and 6.18(d) are 2D EBSD maps showing the crystallographic orientation of the copper lattice along the sample normal direction (ND) and an in-plane direction (RD), taken from the boxed region in figure 6.18(b). Figure 6.18(c) shows the copper has a {110} surface and figure 6.18(d) shows there are no in-plane rotations and the copper is a large single crystal. Similar measurements are presented in figures 6.18(e) and 6.18(f) (i.e ND and RD respectively), but over a

substantially larger area of copper for the 15 minute growth time. This reveals that upon cooling the melted copper forms a big single crystal structure with {110} surface. The pole figures of the EBSD map showing in figure 6.18(c) in conjunction with the SEM image in figure 6.18(b) enable the relative orientation of the copper lattice with respect to the hexagonal shaped graphene domain to be determined, which will be discussed in detail in section 6.4.2. The analysis result of the correlation between Cu lattice and graphene domains is shown schematically in figure 6.18(g). Figure 6.18(h) shows an EBSD image quality map which shows the hexagonal graphene domains (presumably because the graphene layer protects the Cu surface from environmental damage which reduces the quality of the EBSD patterns) with the red arrow indicating the $[\bar{1}10]$ copper lattice direction and the red cube showing the orientation of the underlying copper unit cell. It has been shown that the edges of hexagonal graphene domains correspond to the zig-zag direction in the graphene lattice.[292] This then provides correlation between the graphene lattice direction and the copper lattice direction. Finally the EBSD maps of graphene grown for 90 minutes were analyzed to see whether there is a change in the copper crystallography. Figures 6.18(i) and 6.18(j) show the ND and RD EBSD maps for the 90 minute growth time. This shows similar (110) copper surface and large single crystal is obtained. Some twinning of the copper lattice was observed and this also resulted in the rotation of the orientation of the graphene hexagons grown for 15 minutes. This indicates the alignment is driven purely by the epitaxial relationship with the copper lattice and not from other mechanisms such as gas flow. If the alignment is driven by the gas flow, it

would not see the rotation of the alignment direction on the twinning Cu planes of same sample. But it needs further investigation to elucidate whether the alignment happens during the Cu solidification stage or melted stage.

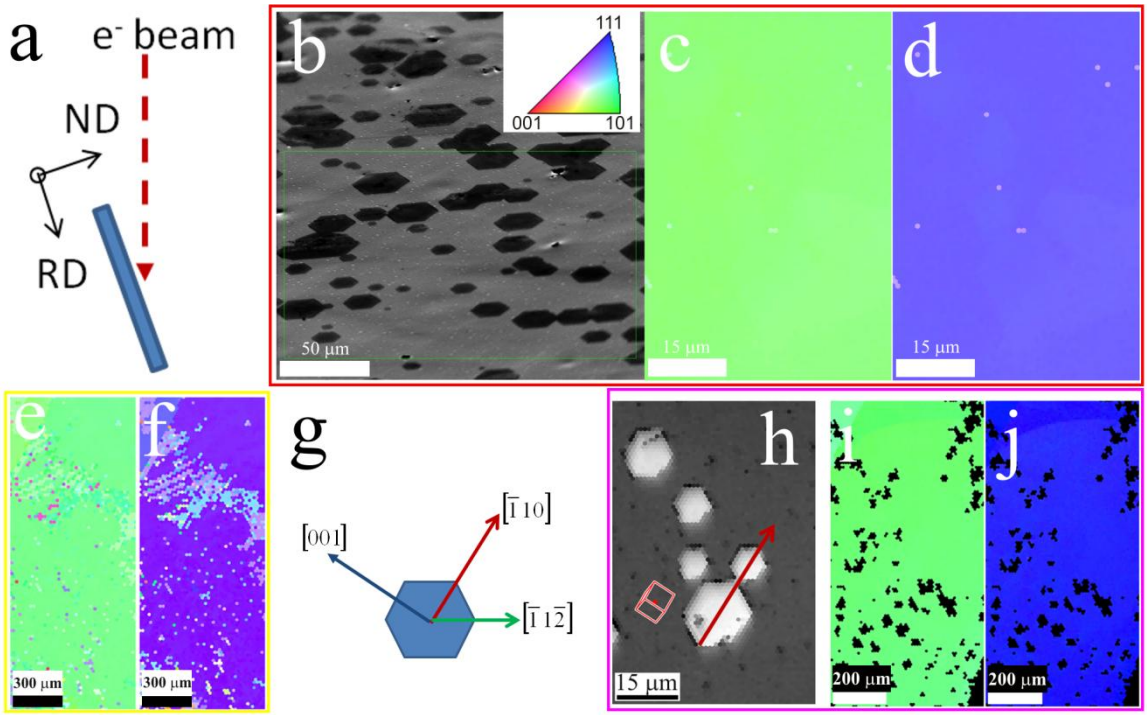


**Figure 6.18.** (a) Schematic showing the angle of the electron beam relative to the sample, with the normal direction (ND) and in-plane direction (RD). (b) SEM image of graphene on copper after 15 minutes growth. Inset shows color codex used for labeling copper lattice directions for Electron back-scattered diffraction (EBSD) maps. EBSD maps showing (c) ND of copper lattice, and (d) RD of copper lattice. Larger EBSD maps showing, (e) ND of copper lattice, and (f) RD of copper lattice. (g) Diagram showing orientation of copper lattice with respect to the hexagonal shaped graphene domain. (h) An EBSD image quality map showing hexagonal graphene domains with a red arrow indicating a copper <110> lattice direction. The red cube shows the orientation of the underlying copper unit cell. EBSD maps for graphene with 90 minutes growth time, showing (i) ND of copper lattice, and (j) RD of copper lattice.

### 6.4.2. Determination of Copper Lattice Orientation Relative to the Hexagonal Shaped Graphene Domains

In order to determine the crystallographic plane of the Cu over a large scale, a montage of low magnification EBSD maps is recorded by Dr. Susannah Speller at Department of Materials, University of Oxford. The copper surface is largely (110) aligned as shown in the figure 6.19 below. The green colour indicates regions where the surface is close to (110) alignment. As can clearly be seen, the grains are several millimetres in size. The bright pink areas are coherent twins ($60^{o}$ tilt about <111>). This indicates the dominance of the {110} plane after the melted Cu cooling down to room temperature. This may be due to the crystallography planes of the Mo substrate, which needs to be investigated further.

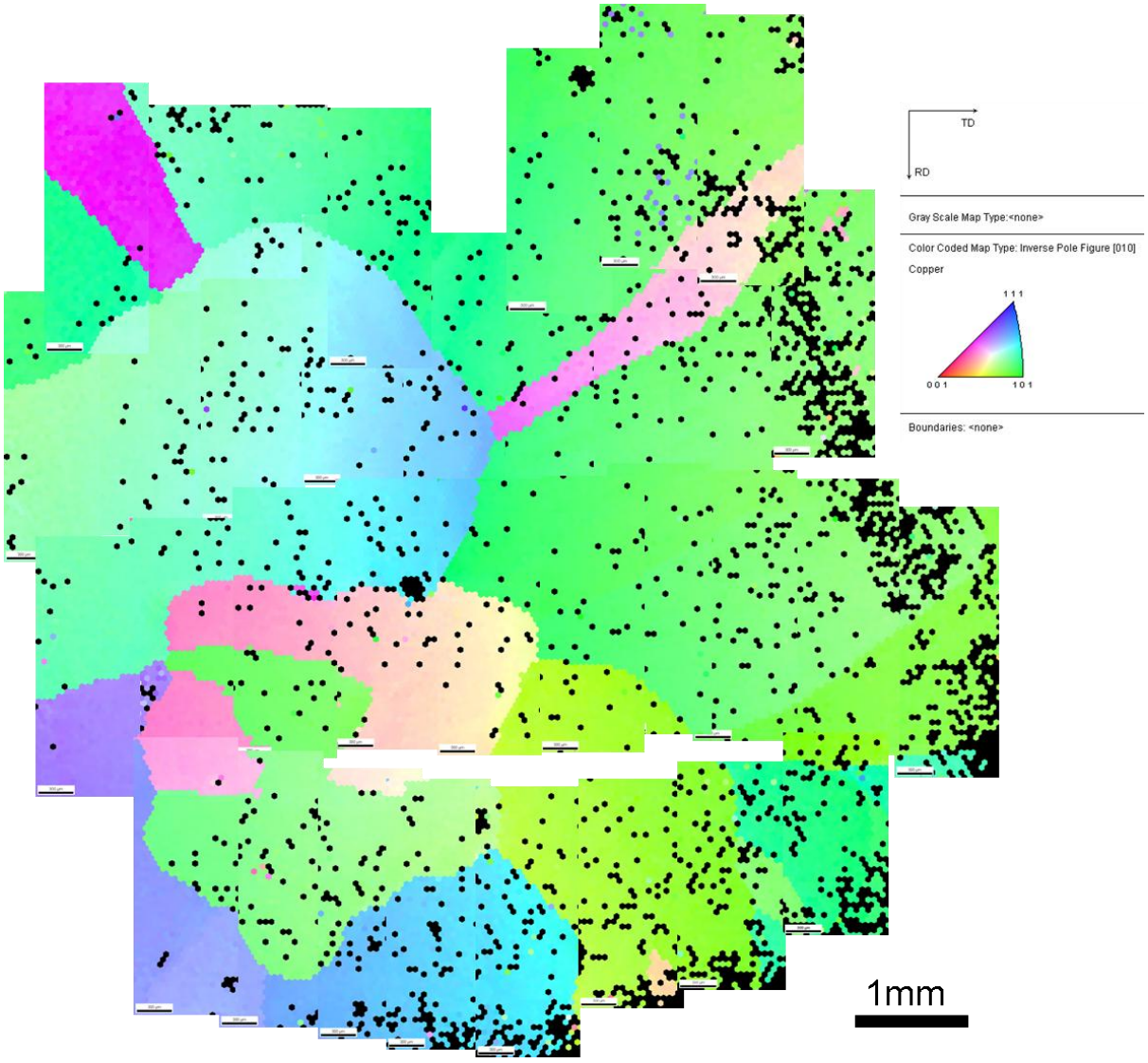


**Figure 6.19**. Montage of low magnification EBSD maps of graphene on copper after 90 minutes growth.

What is the correlation between Cu lattice and graphene domains? As indicated in figure 6.18(c) and figure 6.19, the plane of Cu surface is (110) dominance. The normal direction to the Cu surface is [110] direction. Because Cu is cubic structure, the crystal plane in figure 6.18(c) is (110) surface. Figures 6.20(a)-(b) show the pole figures of in-plane direction (Rotation direction) of EBSD measurement with [110] as normal direction. The red arrow shown in figure 6.20(b) is

parallel to the red arrow shown in figure 6.20(c), which is the schematic hexagonal graphene domain. The blue arrow in figure 6.20(a) is parallel to the blue arrow in figure 6.20(c). By comparing to the standard Cu crystallography pattern with [110] pole shown in figure 6.20(d), the direction of the green arrow could be determined to be $[11\bar{2}]$, which is about 55° rotation from $[\bar{1}10]$ direction. Also, the blue arrow is [001] direction which is 90° rotation from $[\bar{1}10]$ direction.

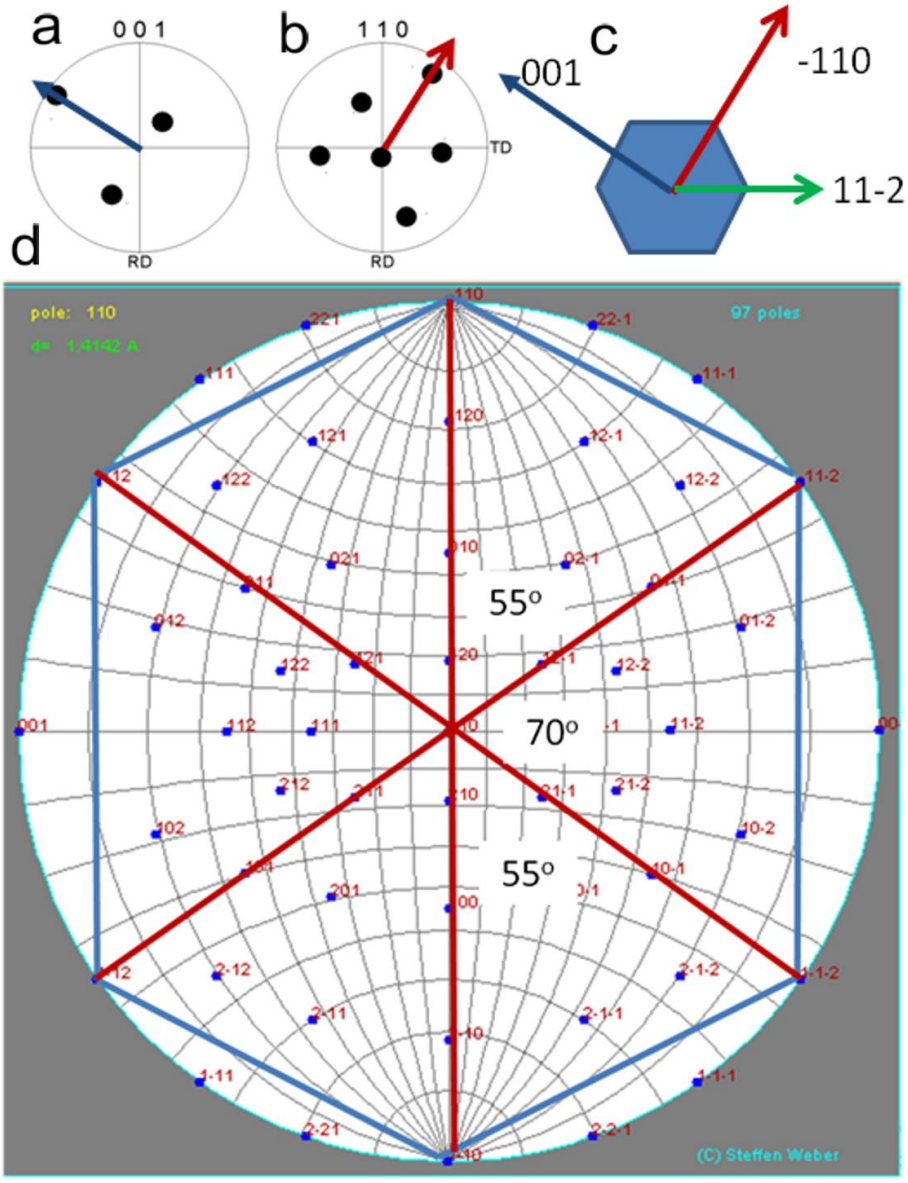


**Figure 6.20** EBSD measurements: (a)-(b) pole figures of 80 sccm $H_2$ to 10 sccm $CH_4$ sample with 15 minutes growth time. (c) The hexagonal graphene domains from the content figure 6 (f). (d) The crystallography pattern with [110] as normal direction.

The alignment of 8 different graphene islands relative to the in-plane [110] axis of the Cu has been measured which is shown in figure 6.21. The misorientation between the hexagon diagonal and Cu [110] is found to be 0.8 degrees on average. This is smaller than the accuracy of the measurement which is limited by the definition of the hexagonal islands. The clearest definition of these islands is obtained from the image quality EBSD map since the graphene layer protects the Cu surface from environmental damage, leading to higher quality diffraction patterns. The secondary electron images are less distinct due to the 70 degree tilt required for EBSD mapping.

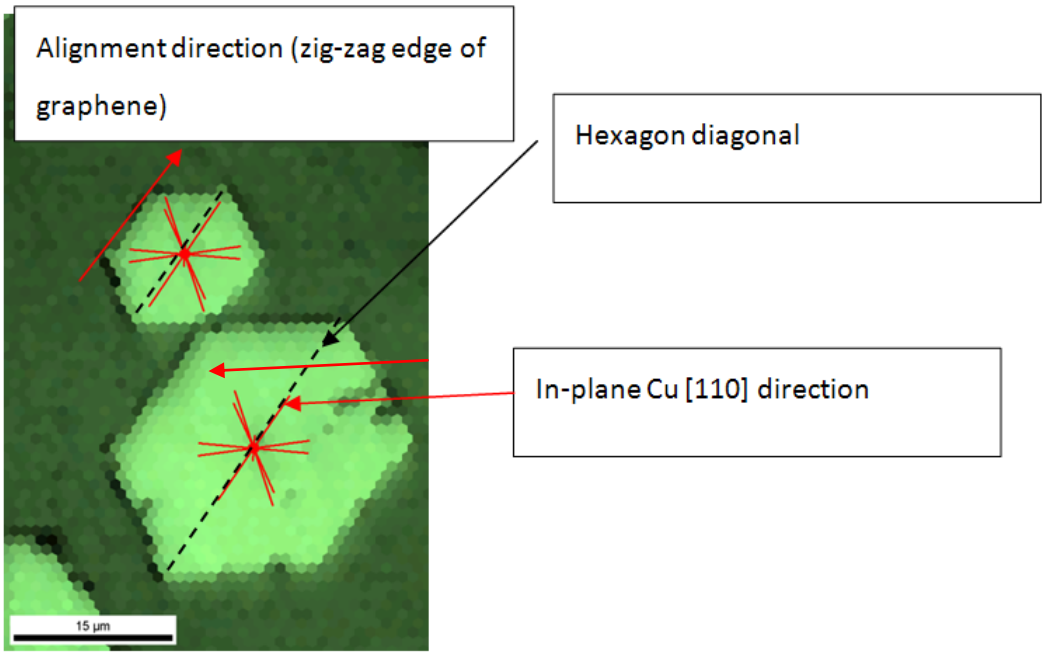


**Figure 6.21.** Alignment of hexagonal graphene domain with [110] Cu direction.

Thus, it is safe to conclude that the zig-zag edge of the hexagonal graphene domains is aligned in the [110] direction of Cu lattice. As graphene electronic properties have strong correlation with the

graphene edges,[304] this study will have impact to control the graphene electronic properties with tailoring Cu crystallography.

### 6.4.3. The Alignment of Graphene Domains on Copper Lattice

As discussed in section 6.2.1 and 6.4.2, the alignment is essential to get large area single crystal graphene. In order to examine how the graphene domains align on Cu using this novel method and make a comparison to the solid state Cu, a quantitative statistical analysis is performed. The hexagonal domains of graphene produced after 15 minutes of growth were aligned, which is shown in a SEM image of a region showing more than 50 domains over a region 750 μm x 500 μm in figure 6.22(a). The alignment direction is indicated with a red arrow. Figure 6.22(b) presents a histogram plotting the frequency count for measured orientation angles of more than 50 hexagonal domains. The inset in figure 6.22(b) illustrates the orientation angle, θ, relative to the horizontal used for the histogram. A Lorentzian distribution fits the data well, (black curve in figure 6.22(b)), giving a center point of 10.15 $^{o}$, and a width of 1.67 $^{o}$. Statistical analysis of the data set gives an average orientation angle of 10.15 $^{o}$ +/- 0.8 $^{o}$, which corresponds to a ~ 8 % standard deviation in the orientation angle of 60 hexagonal graphene domains. This confirms the tight alignment over distance scales exceeding 500 μm. This alignment scale is much larger than the solid state Cu, which is shown in section 5.3.3 in chapter 5.

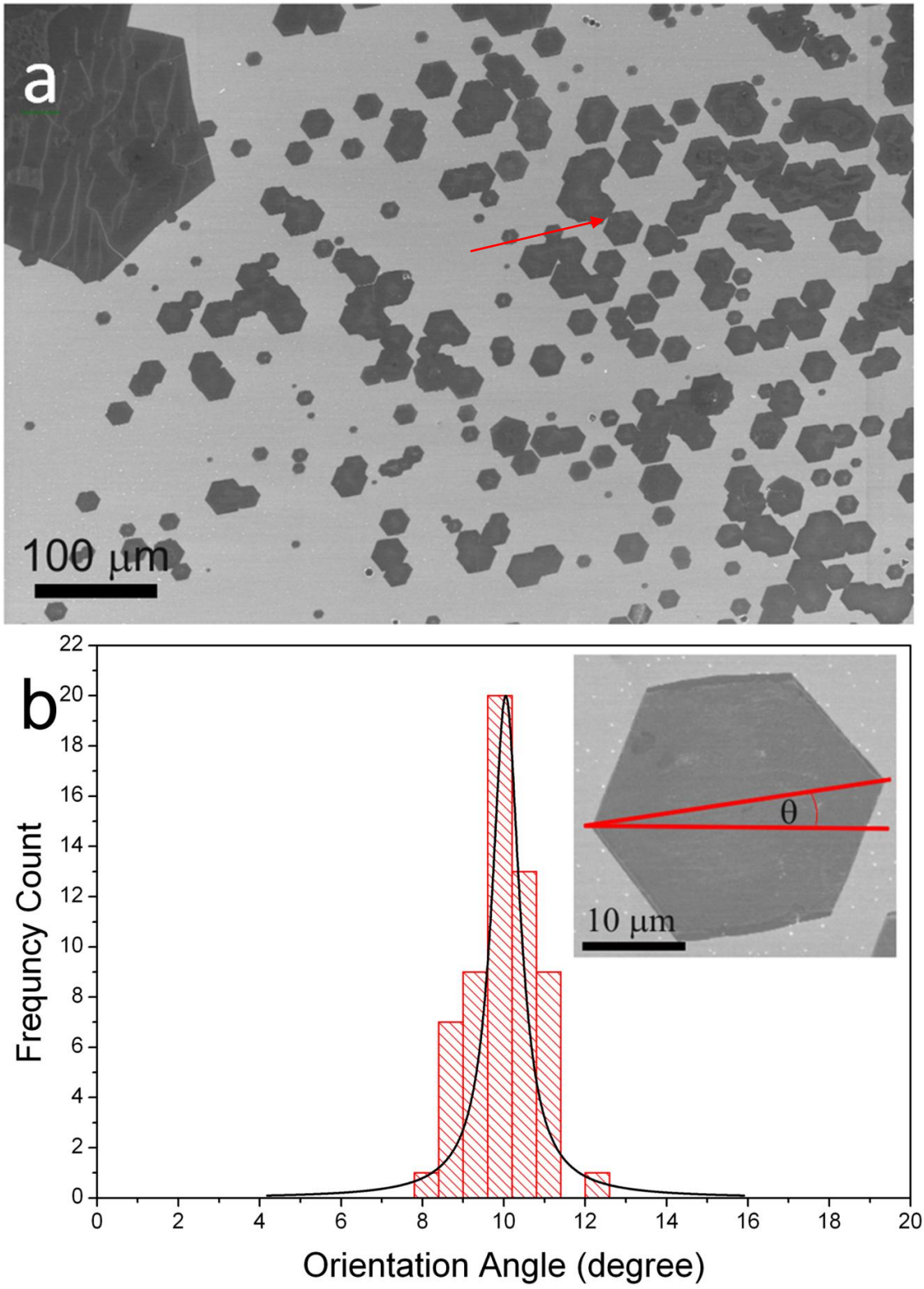


**Figure 6.22.** (a) SEM image of a region showing more than 50 domains over a region 750 µm x 500 µm. (b) A histogram plotting the frequency count for measured orientation angles of more than 50 hexagonal domains. A Lorentzian distribution fits the data well, black curve, giving a center point of 10.15 °, and a width of 1.67 °. The inset in figure 6.22(b) illustrates the orientation angle, θ, relative to the horizontal used for the histogram.

The alignment of the graphene domains means that the atomic lattice is orientated as well. This then prompts the discussion about the merger of multiple domains to form one larger graphene crystal. If two graphene domains are aligned in their lattice orientation and merge together during growth they will then become a single crystalline domain. The interface where the two domains merge together may contain defects and disorder if the alignment is not exact or the atomic stitching processes is flawed. But it is also possible that significant defects and disorder may not occur if the alignment between domains is excellent. During our extensive HRTEM search we could not find regions of significant disorder that might be associated with the interface where two aligned graphene domains merged together.

## 6.5. Electrical Properties of Single Crystal Monolayer Graphene

In order to test the electrical properties of graphene grown by this novel method, sheet resistance measurement was performed using a custom built four probe station, which was shown in section 2.2.4 in chapter 2. After transferring graphene onto the quartz substrate, van der Pauw method was applied to measure the sheet resistance. The principle of the van der Pauw measurement is shown in section 2.2.4. As shown in figure 6.23, $R_{13,24}$=130.61 ohms, $R_{24,13}$=130.74 ohms, $R_{12,34}$=1949.33 ohms, $R_{34,12}$=1949.59 ohms. According to equation (2.38), the sheet resistance $R_s$=4713.96 $\Omega \bullet sq^{-1}$. The resistance of the film is anisotropic, which means the resistance in one direction is larger than

the other perpendicular direction. The reason for these anisotropic properties in the film may be because the formation of the continuous film is the merger of the aligned hexagonal domains. The side to side seamless merger leads to the lower resistance due to the straightway electron tunneling channels. Meanwhile, the head to head merge leads to higher resistance resulting from narrow electron tunneling channels. However, this needs further investigation.

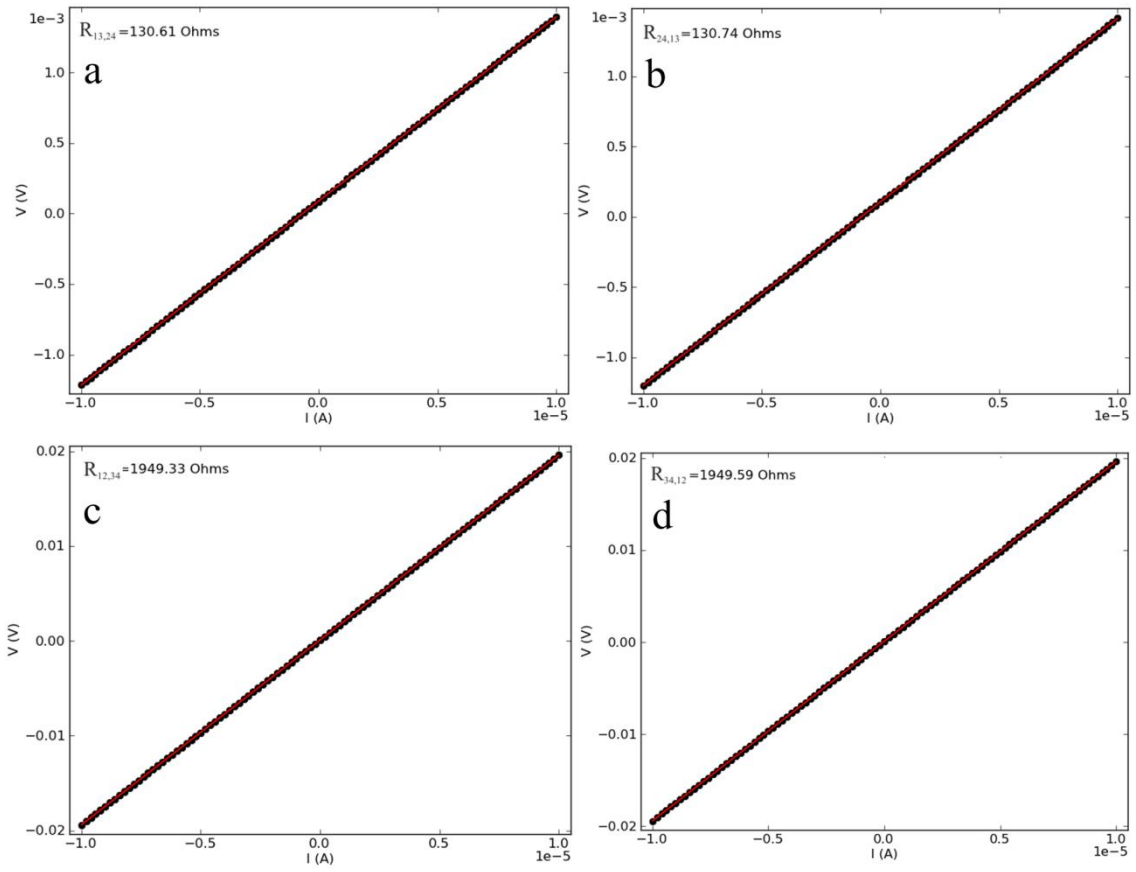


**Figure 6.23.** Four probe sheet resistance measurement using van der Pauw method: (a) $R_{12,34}$=130.61ohms. (b) $R_{24,13}$=130.74ohms. (c) $R_{12,34}$=1949.33ohms. (d) $R_{34,12}$=1949.59ohms.

## 6.6. Conclusions

In summary, the open question 4 has been answered, which is to invent a novel method to fabricate large area single crystal 2D atomic crystal with low cost for commercial applications. The results presented in this chapter show a simple method for obtaining large 200 μm single crystals of monolayer graphene within a continuous film. No fancy pretreatment of the copper is needed, nor do special seed sites need to be created. This approach can be easily applied widely to produce graphene on copper using CVD. It is surprising that hexagonal graphene domains produced after 15 minutes of growth were self aligned in their orientation. The EBSD indicated an epitaxial relationship between the copper surface and the graphene, but since the copper is in a liquid state during the addition of methane, this suggests a fairly complex growth model. The zig-zag edge of graphene domains is aligned along the [110] Cu direction. The epitaxial alignment of graphene domains provides a means for rapidly fabricating large single crystals from multiple domains and may be a key step towards wafer scale single crystals of monolayer graphene, which will have great impact on the commercialization of graphene products. The electrical measurement shows anisotropic properties of graphene grown by this method. By tailoring the Cu crystallography, it has great potential to get well aligned graphene domain edges, which is possible to exhibit interesting electrical properties.

# Chapter 7:

# Conclusions and Future Work

The thesis has been focused on the fundamental issue of the crystal structure of nanomaterials. The aim of the thesis, proposed in Chapter 1, has been to control the crystal structure of three types of nanomaterials, namely, Mn doped ZnSe quantum dots, BN and graphene 2D atomic crystals, with low cost for their applications in photonics, structural support and electronics respectively. This goal has been achieved by colloidal synthesis of Mn doped ZnSe quantum dots, liquid phase exfoliation of BN sheets, and the atmosphere pressure chemical vapour deposition of graphene. The crystallinity, crystal phase, morphology, growth dynamics and thickness of nanomaterials have been characterized with HRTEM either with imaging mode or diffraction mode. SEM has been used to investigate the growth dynamics, morphology of nanomaterials in large scale. EBSD has been used to examine the crystal structure of Cu substrate to investigate the correlation between Cu lattice and graphene lattice. Raman spectroscopy has been used to identify the thickness, defects, and structure of graphene. PL, PLE, and UV-vis-absorption have been used to characterize the optical properties of quantum dots. ARPES has been used to determine the band structure of graphene. Probe station has been used measure the sheet resistance of graphene. All

the principles of the experimental techniques and synthetic methods have been discussed in chapter 2.

Chapter 3 has been focused to answer the open question 1, which has been proposed in chapter 1. How can the Mn doped ZnSe quantum dots be synthesized with controlled crystal structure? The shape control of Mn doped ZnSe quantum dots from branched to spherical has been achieved by switching the injection temperature from kinetics region to thermodynamics region. The crystal phases of Mn doped ZnSe quantum dots have been controlled from zinc blende to wurtzite by controlling the injection rates of zinc precursors. What is the relationship between crystal structure and optical properties of Mn doped ZnSe quantum dots? The spherical wurtzite Mn doped ZnSe quantum dots have the highest quantum yield comparing with other shape or crystal phase of the dots. The study in chapter 3 has demonstrated the method to control the crystal structure and shape of Mn doped ZnSe quantum dots for low cost with potential applications in photonics.

Followed the study in chapter 3, Mn doped ZnSe quantum dots have been deposited onto the BN sheets for the first demonstration on utilizing BN sheets as a carbon-free TEM ultrathin supporting film to study atomic configuration of other nanomaterials in chapter 4. The study in chapter 4 has answered the open question 2, which was proposed in chapter 1, and demonstrated the method to

fabricate single crystalline BN sheets for the application as structural support. However, the study in chapter 4 has also shown that liquid phase exfoliation is not good enough to fabricate large area single crystals of 2D atomic crystals. That is why an alternative method should be found to achieve this goal.

Due to the limitation of liquid phase exfoliation, APCVD has been chosen as a promising method to fabricate large area single crystal 2D atomic crystals. Before achieving this goal, the growth mechanism of graphene using APCVD has been studied in chapter 5 to answer the open question 3. What is the growth mechanism of graphene using APCVD? The temperature threshold for the nucleation of graphene domains has shown to be 960 ºC. The crystal structure of the graphene domains has not varied with the increasing of temperature. The fast cooling rate is required for homogenous graphene films. The hydrogen pre-treatment is necessary for the nucleation of graphene domains. The Cu foil quality has effect on the nucleation of graphene domains. The alignment of graphene domains on this solid state Cu has been over the distance of up to 5 mm along the zig-zag edge of graphene hexagonal domains. The alignment of graphene domains in APCVD is important to overcome the polycrystalline nature of graphene, normally produced by LPCVD. The interplay between Cu lattices and graphene has shown to be an important role in controlling the graphene nucleation. The growth of hexagonal graphene domains is driven by the 6 fold symmetry of graphene lattice on the non-(111) Cu plane, while the growth of rectangular

graphene domains is heavily influenced by the Cu (111) plane. This has shown that the engineering of Cu crystal has the potential to control the crystal structure of graphene domains. It is possible to fabricate large area single crystal graphene films with the improvement of the alignment of graphene domains on the Cu surface on a larger scale.

Based on the understanding of the growth mechanism of graphene using APCVD, a novel method of using melted Cu on Mo substrate has been invented to fabricate large area single crystals of graphene using APCVD with open question 4 answered. An area of over 200 μm single crystals of monolayer pristine graphene within a continuous film has been achieved. The zig-zag edge of the hexagonal graphene domains is aligned in the [110] direction of Cu lattice over distance scales exceeding 500 μm, which is a great improvement compared to the alignment of hexagonal graphene domains on the solid state Cu. The sheet resistance measurement has shown some anisotropic effect on the resistance of graphene produced by this method. The studies in chapter 5 and 6 have achieved the goal of fabricating large area single crystals of graphene with low cost for potential application in electronics.

The results presented in this thesis have achieved the aim of the thesis. It provides general principles to control the crystal structure of nanomaterials, in order to tailor the properties for

applications. The synthetic methods used in this thesis are low cost and representative for semiconductors, insulators, and semimetals. They have great potential in the commercialization of nanomaterials in the area of photonics, structural support and electronics. This will be widely used and highly appreciated both by the scientific and industry community.

The future work could involve with the integration of these three types of nanomaterials into complex devices for broader applications. For example, the quantum dot/graphene solar cells will be an interesting system to combine the excellent optical properties of quantum dots with the extraordinary electron transport properties of graphene. This may greatly increase both the absorptivity rate of photons and charge separation rate of excitons, which may improve the efficiency of solar cells. Also, the graphene on BN 3D stacking system is a promising structure for future nanoelectronic devices as BN is an intrinsic insulator of 2D atomic crystals, which can provides better structural support for 2D graphene. This thesis has laid out a foundation to explore in these proposed areas, which may pave the way for broader applications of nanomaterials.

## References:


1. Roder, H.; Hahn, E.; Brune, H.; Bucher, J. P.; Kern, K., Building One-Dimensional and 2-Dimentional Nannostructures by Diffusion-Controlled Aggregation at Surfaces. *Nature* **1993,** *366* (6451), 141-143.
2. Pokropivny, V. V.; Skorokhod, V. V., Classification of nanostructures by dimensionality and concept of surface forms engineering in nanomaterial science. *Materials Science and Engineering: C* **2007,** *27* (5–8), 990-993.
3. Novoselov, K. S.; Jiang, D.; Schedin, F.; Booth, T. J.; Khotkevich, V. V.; Morozov, S. V.; Geim, A. K., Two-dimensional atomic crystals. *P Natl Acad Sci USA* **2005,** *102* (30), 10451-10453.
4. Novoselov, K. S.; Geim, A. K.; Morozov, S. V.; Jiang, D.; Zhang, Y.; Dubonos, S. V.; Grigorieva, I. V.; Firsov, A. A., Electric field effect in atomically thin carbon films. *Science* **2004,** *306* (5696), 666-669.
5. Graphene pioneers bag Nobel prize. *Institute of Physics, UK* **October 5, 2010**.
6. Geim, A. K.; Novoselov, K. S., The rise of graphene. *Nat Mater* **2007,** *6* (3), 183-191.
7. Boehm, H. P.; Clauss, A.; Fischer, G. O.; Hofmann, U., Das Adsorptionsverhalten sehr dünner Kohlenstoff-Folien. *Zeitschrift für anorganische und allgemeine Chemie* **1962,** *316* (3-4), 119-127.
8. Boehm, H. P.; Setton, R.; Stumpp, E., Nomenclature and Terminology of Graphite-Intercalation Compounds (Iupac Recommendations 1994). *Pure Appl Chem* **1994,** *66* (9), 1893-1901.
9. Peierls, R. E., Quelques proprietes typiques des corpses solides. *Ann. I. H. Poincare* **1935,** *5*, 177-222
10. Landau, L. D. L., E. M. , *Statistical Physics* Butterworth-Heinemann: 1980.
11. Mermin, N. D., Crystalline Order in Two Dimensions. *Physical Review* **1968,** *176* (1), 250-254.
12. Venables, J. A.; Spiller, G. D. T.; Hanbucken, M., Nucleation and growth of thin films. *Reports on Progress in Physics* **1984,** *47* (4), 399.
13. Evans, J. W.; Thiel, P. A.; Bartelt, M. C., Morphological evolution during epitaxial thin film growth: Formation of 2D islands and 3D mounds. *Surface Science Reports* **2006,** *61* (1-2), 1-128.
14. Shenderova, O. A., Zhirnov, V. V. & Brenner, D. W., Carbon nanostructures. *Crit Rev Solid State Mater Sci* **2002,** *27*, 227-356
15. Novoselov, K. S.; Geim, A. K.; Morozov, S. V.; Jiang, D.; Katsnelson, M. I.; Grigorieva, I. V.; Dubonos, S. V.; Firsov, A. A., Two-dimensional gas of massless Dirac fermions in graphene. *Nature* **2005,** *438* (7065), 197-200.

16. Zhang, Y. B.; Tan, Y. W.; Stormer, H. L.; Kim, P., Experimental observation of the quantum Hall effect and Berry's phase in graphene. *Nature* **2005,** *438* (7065), 201-204.
17. Meyer, J. C.; Geim, A. K.; Katsnelson, M. I.; Novoselov, K. S.; Booth, T. J.; Roth, S., The structure of suspended graphene sheets. *Nature* **2007,** *446* (7131), 60-63.
18. Fradkin, E., Critical-Behavior of Disordered Degenerate Semiconductors .2. Spectrum and Transport-Properties in Mean-Field Theory. *Physical Review B* **1986,** *33* (5), 3263-3268.
19. Lee, C.; Wei, X. D.; Kysar, J. W.; Hone, J., Measurement of the elastic properties and intrinsic strength of monolayer graphene. *Science* **2008,** *321* (5887), 385-388.
20. Nair, R. R.; Blake, P.; Grigorenko, A. N.; Novoselov, K. S.; Booth, T. J.; Stauber, T.; Peres, N. M. R.; Geim, A. K., Fine structure constant defines visual transparency of graphene. *Science* **2008,** *320* (5881), 1308-1308.
21. Kuzmenko, A. B.; van Heumen, E.; Carbone, F.; van der Marel, D., Universal Optical Conductance of Graphite. *Physical Review Letters* **2008,** *100* (11), 117401.
22. Castro Neto, A. H.; Guinea, F.; Peres, N. M. R.; Novoselov, K. S.; Geim, A. K., The electronic properties of graphene. *Reviews of Modern Physics* **2009,** *81* (1), 109-162.
23. Balandin, A. A.; Ghosh, S.; Bao, W. Z.; Calizo, I.; Teweldebrhan, D.; Miao, F.; Lau, C. N., Superior thermal conductivity of single-layer graphene. *Nano Lett* **2008,** *8* (3), 902-907.
24. Partoens, B.; Peeters, F. M., From graphene to graphite: Electronic structure around the K point. *Physical Review B* **2006,** *74* (7).
25. Geim, A. K., Graphene: Status and Prospects. *Science* **2009,** *324* (5934), 1530-1534.
26. Takagi, S.; Toriumi, A.; Iwase, M.; Tango, H., On the universality of inversion layer mobility in Si MOSFET's: Part I-effects of substrate impurity concentration. *Electron Devices, IEEE Transactions on* **1994,** *41* (12), 2357-2362.
27. Vonklitzing, K.; Dorda, G.; Pepper, M., New Method for High-Accuracy Determination of the Fine-Structure Constant Based on Quantized Hall Resistance. *Physical Review Letters* **1980,** *45* (6), 494-497.
28. Vonklitzing, K., The Quantized Hall-Effect. *Reviews of Modern Physics* **1986,** *58* (3), 519-531.
29. Levendorf, M. P.; Ruiz-Vargas, C. S.; Garg, S.; Park, J., Transfer-Free Batch Fabrication of Single Layer Graphene Transistors. *Nano Lett* **2009,** *9* (12), 4479-4483.
30. Zhou, S. Y.; Gweon, G. H.; Fedorov, A. V.; First, P. N.; de Heer, W. A.; Lee, D. H.; Guinea, F.; Castro Neto, A. H.; Lanzara, A., Substrate-induced bandgap opening in epitaxial graphene. *Nat Mater* **2007,** *6* (10), 770-775.
31. Han, M. Y.; Özyilmaz, B.; Zhang, Y.; Kim, P., Energy Band-Gap Engineering of Graphene Nanoribbons. *Physical Review Letters* **2007,** *98* (20), 206805.

32. Jiao, L.; Zhang, L.; Wang, X.; Diankov, G.; Dai, H., Narrow graphene nanoribbons from carbon nanotubes. *Nature* **2009,** *458* (7240), 877-880.
33. Kosynkin, D. V.; Higginbotham, A. L.; Sinitskii, A.; Lomeda, J. R.; Dimiev, A.; Price, B. K.; Tour, J. M., Longitudinal unzipping of carbon nanotubes to form graphene nanoribbons. *Nature* **2009,** *458* (7240), 872-876.
34. Kim, K. S.; Zhao, Y.; Jang, H.; Lee, S. Y.; Kim, J. M.; Kim, K. S.; Ahn, J. H.; Kim, P.; Choi, J. Y.; Hong, B. H., Large-scale pattern growth of graphene films for stretchable transparent electrodes. *Nature* **2009,** *457* (7230), 706-710.
35. Bae, S.; Kim, H.; Lee, Y.; Xu, X. F.; Park, J. S.; Zheng, Y.; Balakrishnan, J.; Lei, T.; Kim, H. R.; Song, Y. I.; Kim, Y. J.; Kim, K. S.; Ozyilmaz, B.; Ahn, J. H.; Hong, B. H.; Iijima, S., Roll-to-roll production of 30-inch graphene films for transparent electrodes. *Nat Nanotechnol* **2010,** *5* (8), 574-578.
36. Wang, X.; Zhi, L.; Mullen, K., Transparent, Conductive Graphene Electrodes for Dye-Sensitized Solar Cells. *Nano Lett* **2007,** *8* (1), 323-327.
37. Blake, P.; Brimicombe, P. D.; Nair, R. R.; Booth, T. J.; Jiang, D.; Schedin, F.; Ponomarenko, L. A.; Morozov, S. V.; Gleeson, H. F.; Hill, E. W.; Geim, A. K.; Novoselov, K. S., Graphene-Based Liquid Crystal Device. *Nano Lett* **2008,** *8* (6), 1704-1708.
38. Wu, J.; Agrawal, M.; Becerril, H. c. A.; Bao, Z.; Liu, Z.; Chen, Y.; Peumans, P., Organic Light-Emitting Diodes on Solution-Processed Graphene Transparent Electrodes. *ACS Nano* **2009,** *4* (1), 43-48.
39. Chen, J.-H.; Jang, C.; Xiao, S.; Ishigami, M.; Fuhrer, M. S., Intrinsic and extrinsic performance limits of graphene devices on $SiO_2$. *Nat Nano* **2008,** *3* (4), 206-209.
40. Schedin, F.; Geim, A. K.; Morozov, S. V.; Hill, E. W.; Blake, P.; Katsnelson, M. I.; Novoselov, K. S., Detection of individual gas molecules adsorbed on graphene. *Nat Mater* **2007,** *6* (9), 652-655.
41. Dan, Y.; Lu, Y.; Kybert, N. J.; Luo, Z.; Johnson, A. T. C., Intrinsic Response of Graphene Vapor Sensors. *Nano Lett* **2009,** *9* (4), 1472-1475.
42. Robinson, J. T.; Perkins, F. K.; Snow, E. S.; Wei, Z.; Sheehan, P. E., Reduced Graphene Oxide Molecular Sensors. *Nano Lett* **2008,** *8* (10), 3137-3140.
43. Tang, L.; Wang, Y.; Li, Y.; Feng, H.; Lu, J.; Li, J., Preparation, Structure, and Electrochemical Properties of Reduced Graphene Sheet Films. *Advanced Functional Materials* **2009,** *19* (17), 2782-2789.
44. Ohno, Y.; Maehashi, K.; Yamashiro, Y.; Matsumoto, K., Electrolyte-Gated Graphene Field-Effect Transistors for Detecting pH and Protein Adsorption. *Nano Lett* **2009,** *9* (9), 3318-3322.

45. Mohanty, N.; Berry, V., Graphene-Based Single-Bacterium Resolution Biodevice and DNA Transistor: Interfacing Graphene Derivatives with Nanoscale and Microscale Biocomponents. *Nano Lett* **2008,** *8* (12), 4469-4476.
46. Pan, D.; Wang, S.; Zhao, B.; Wu, M.; Zhang, H.; Wang, Y.; Jiao, Z., Li Storage Properties of Disordered Graphene Nanosheets. *Chemistry of Materials* **2009,** *21* (14), 3136-3142.
47. Simon, P.; Gogotsi, Y., Materials for electrochemical capacitors. *Nat Mater* **2008,** *7* (11), 845-854.
48. Lee, J. K.; Smith, K. B.; Hayner, C. M.; Kung, H. H., Silicon nanoparticles-graphene paper composites for Li ion battery anodes. *Chemical Communications* **2010,** *46* (12), 2025-2027.
49. Yao, J.; Shen, X.; Wang, B.; Liu, H.; Wang, G., In situ chemical synthesis of $SnO_2$–graphene nanocomposite as anode materials for lithium-ion batteries. *Electrochemistry Communications* **2009,** *11* (10), 1849-1852.
50. Paek, S.-M.; Yoo, E.; Honma, I., Enhanced Cyclic Performance and Lithium Storage Capacity of $SnO_2$/Graphene Nanoporous Electrodes with Three-Dimensionally Delaminated Flexible Structure. *Nano Lett* **2008,** *9* (1), 72-75.
51. Wang, G.; Wang, B.; Wang, X.; Park, J.; Dou, S.; Ahn, H.; Kim, K., Sn/graphene nanocomposite with 3D architecture for enhanced reversible lithium storage in lithium ion batteries. *Journal of Materials Chemistry* **2009,** *19* (44), 8378-8384.
52. Srinivas, G.; Zhu, Y. W.; Piner, R.; Skipper, N.; Ellerby, M.; Ruoff, R., Synthesis of graphene-like nanosheets and their hydrogen adsorption capacity. *Carbon* **2010,** *48* (3), 630-635.
53. Li, Y.; Tang, L.; Li, J., Preparation and electrochemical performance for methanol oxidation of pt/graphene nanocomposites. *Electrochemistry Communications* **2009,** *11* (4), 846-849.
54. Seger, B.; Kamat, P. V., Electrocatalytically Active Graphene-Platinum Nanocomposites. Role of 2-D Carbon Support in PEM Fuel Cells. *The Journal of Physical Chemistry C* **2009,** *113* (19), 7990-7995.
55. Xu, C.; Wang, X.; Zhu, J., Graphene−Metal Particle Nanocomposites. *The Journal of Physical Chemistry C* **2008,** *112* (50), 19841-19845.
56. Yoo, E.; Okata, T.; Akita, T.; Kohyama, M.; Nakamura, J.; Honma, I., Enhanced Electrocatalytic Activity of Pt Subnanoclusters on Graphene Nanosheet Surface. *Nano Lett* **2009,** *9* (6), 2255-2259.
57. Kou, R.; Shao, Y.; Wang, D.; Engelhard, M. H.; Kwak, J. H.; Wang, J.; Viswanathan, V. V.; Wang, C.; Lin, Y.; Wang, Y.; Aksay, I. A.; Liu, J., Enhanced activity and stability of Pt catalysts on functionalized graphene sheets for electrocatalytic oxygen reduction. *Electrochemistry Communications* **2009,** *11* (5), 954-957.

58. Eda, G.; Lin, Y. Y.; Miller, S.; Chen, C. W.; Su, W. F.; Chhowalla, M., Transparent and conducting electrodes for organic electronics from reduced graphene oxide. *Applied Physics Letters* **2008,** *92* (23).
59. Wu, J.; Becerril, H. A.; Bao, Z.; Liu, Z.; Chen, Y.; Peumans, P., Organic solar cells with solution-processed graphene transparent electrodes. *Applied Physics Letters* **2008,** *92* (26), 263302-3.
60. Booth, T. J.; Blake, P.; Nair, R. R.; Jiang, D.; Hill, E. W.; Bangert, U.; Bleloch, A.; Gass, M.; Novoselov, K. S.; Katsnelson, M. I.; Geim, A. K., Macroscopic Graphene Membranes and Their Extraordinary Stiffness. *Nano Lett* **2008,** *8* (8), 2442-2446.
61. Meyer, J. C.; Girit, C. O.; Crommie, M. F.; Zettl, A., Imaging and dynamics of light atoms and molecules on graphene. *Nature* **2008,** *454* (7202), 319-322.
62. Lee, Z.; Jeon, K.-J.; Dato, A.; Erni, R.; Richardson, T. J.; Frenklach, M.; Radmilovic, V., Direct Imaging of Soft−Hard Interfaces Enabled by Graphene. *Nano Lett* **2009,** *9* (9), 3365-3369.
63. Warner, J. H.; Rümmeli, M. H.; Bachmatiuk, A.; Wilson, M.; Büchner, B., Examining Co-Based Nanocrystals on Graphene Using Low-Voltage Aberration-Corrected Transmission Electron Microscopy. *ACS Nano* **2009,** *4* (1), 470-476.
64. Trauzettel, B.; Bulaev, D. V.; Loss, D.; Burkard, G., Spin qubits in graphene quantum dots. *Nat Phys* **2007,** *3* (3), 192-196.
65. Banerjee, S. K.; Register, L. F.; Tutuc, E.; Reddy, D.; MacDonald, A. H., Bilayer PseudoSpin Field-Effect Transistor (BiSFET): A Proposed New Logic Device. *Electron Device Letters, IEEE* **2009,** *30* (2), 158-160.
66. Hernandez, Y.; Nicolosi, V.; Lotya, M.; Blighe, F. M.; Sun, Z.; De, S.; McGovern, I. T.; Holland, B.; Byrne, M.; Gun'Ko, Y. K.; Boland, J. J.; Niraj, P.; Duesberg, G.; Krishnamurthy, S.; Goodhue, R.; Hutchison, J.; Scardaci, V.; Ferrari, A. C.; Coleman, J. N., High-yield production of graphene by liquid-phase exfoliation of graphite. *Nat Nano* **2008,** *3* (9), 563-568.
67. Buchsteiner, A.; Lerf, A.; Pieper, J., Water Dynamics in Graphite Oxide Investigated with Neutron Scattering. *The Journal of Physical Chemistry B* **2006,** *110* (45), 22328-22338.
68. Stankovich, S.; Piner, R. D.; Chen, X.; Wu, N.; Nguyen, S. T.; Ruoff, R. S., Stable aqueous dispersions of graphitic nanoplatelets via the reduction of exfoliated graphite oxide in the presence of poly(sodium 4-styrenesulfonate). *Journal of Materials Chemistry* **2006,** *16* (2), 155-158.
69. Jung, I.; Pelton, M.; Piner, R.; Dikin, D. A.; Stankovich, S.; Watcharotone, S.; Hausner, M.; Ruoff, R. S., Simple approach for high-contrast optical imaging and characterization of graphene-based sheets. *Nano Lett* **2007,** *7* (12), 3569-3575.

70. Lomeda, J. R.; Doyle, C. D.; Kosynkin, D. V.; Hwang, W. F.; Tour, J. M., Diazonium Functionalization of Surfactant-Wrapped Chemically Converted Graphene Sheets. *Journal of the American Chemical Society* **2008,** *130* (48), 16201-16206.
71. Tung, V. C.; Allen, M. J.; Yang, Y.; Kaner, R. B., High-throughput solution processing of large-scale graphene. *Nat Nanotechnol* **2009,** *4* (1), 25-29.
72. Wang, G. X.; Yang, J.; Park, J.; Gou, X. L.; Wang, B.; Liu, H.; Yao, J., Facile synthesis and characterization of graphene nanosheets. *J Phys Chem C* **2008,** *112* (22), 8192-8195.
73. Muszynski, R.; Seger, B.; Kamat, P. V., Decorating graphene sheets with gold nanoparticles. *J Phys Chem C* **2008,** *112* (14), 5263-5266.
74. Schniepp, H. C.; Li, J.-L.; McAllister, M. J.; Sai, H.; Herrera-Alonso, M.; Adamson, D. H.; Prud'homme, R. K.; Car, R.; Saville, D. A.; Aksay, I. A., Functionalized Single Graphene Sheets Derived from Splitting Graphite Oxide. *The Journal of Physical Chemistry B* **2006,** *110* (17), 8535-8539.
75. McAllister, M. J.; Li, J. L.; Adamson, D. H.; Schniepp, H. C.; Abdala, A. A.; Liu, J.; Herrera-Alonso, M.; Milius, D. L.; Car, R.; Prud'homme, R. K.; Aksay, I. A., Single sheet functionalized graphene by oxidation and thermal expansion of graphite. *Chemistry of Materials* **2007,** *19* (18), 4396-4404.
76. Williams, G.; Seger, B.; Kamat, P. V., TiO2-Graphene Nanocomposites. UV-Assisted Photocatalytic Reduction of Graphene Oxide. *ACS Nano* **2008,** *2* (7), 1487-1491.
77. Stankovich, S.; Dikin, D. A.; Piner, R. D.; Kohlhaas, K. A.; Kleinhammes, A.; Jia, Y.; Wu, Y.; Nguyen, S. T.; Ruoff, R. S., Synthesis of graphene-based nanosheets via chemical reduction of exfoliated graphite oxide. *Carbon* **2007,** *45* (7), 1558-1565.
78. Stankovich, S.; Dikin, D. A.; Dommett, G. H. B.; Kohlhaas, K. M.; Zimney, E. J.; Stach, E. A.; Piner, R. D.; Nguyen, S. T.; Ruoff, R. S., Graphene-based composite materials. *Nature* **2006,** *442* (7100), 282-286.
79. Viculis, L. M.; Mack, J. J.; Kaner, R. B., A chemical route to carbon nanoscrolls. *Science* **2003,** *299* (5611), 1361-1361.
80. Horiuchi, S.; Gotou, T.; Fujiwara, M.; Asaka, T.; Yokosawa, T.; Matsui, Y., Single graphene sheet detected in a carbon nanofilm. *Applied Physics Letters* **2004,** *84* (13), 2403-2405.
81. Dresselhaus, M. S.; Dresselhaus, G., Intercalation compounds of graphite. *Adv Phys* **2002,** *51* (1), 1-186.
82. Li, X.; Zhang, G.; Bai, X.; Sun, X.; Wang, X.; Wang, E.; Dai, H., Highly conducting graphene sheets and Langmuir-Blodgett films. *Nat Nano* **2008,** *3* (9), 538-542.
83. Park, S.; Ruoff, R. S., Chemical methods for the production of graphenes. *Nat Nanotechnol* **2009,** *4* (4), 217-224.

84. Dreyer, D. R.; Ruoff, R. S.; Bielawski, C. W., From Conception to Realization: An Historial Account of Graphene and Some Perspectives for Its Future. *Angewandte Chemie International Edition* **2010,** *49* (49), 9336-9344.
85. Lu, X.; Yu, M.; Huang, H.; Ruoff, R. S., Tailoring graphite with the goal of achieving single sheets. *Nanotechnology* **1999,** *10* (3), 269.
86. Lu, X.; Huang, H.; Nemchuk, N.; Ruoff, R. S., Patterning of highly oriented pyrolytic graphite by oxygen plasma etching. *Applied Physics Letters* **1999,** *75* (2), 193-195.
87. Wu, J.; Pisula, W.; Müllen, K., Graphenes as Potential Material for Electronics. *Chemical Reviews* **2007,** *107* (3), 718-747.
88. Cai, J.; Ruffieux, P.; Jaafar, R.; Bieri, M.; Braun, T.; Blankenburg, S.; Muoth, M.; Seitsonen, A. P.; Saleh, M.; Feng, X.; Mullen, K.; Fasel, R., Atomically precise bottom-up fabrication of graphene nanoribbons. *Nature* **2010,** *466* (7305), 470-473.
89. Van Bommel, A. J.; Crombeen, J. E.; Van Tooren, A., LEED and Auger electron observations of the SiC(0001) surface. *Surface Science* **1975,** *48* (2), 463-472.
90. Charrier, A.; Coati, A.; Argunova, T.; Thibaudau, F.; Garreau, Y.; Pinchaux, R.; Forbeaux, I.; Debever, J. M.; Sauvage-Simkin, M.; Themlin, J. M., Solid-state decomposition of silicon carbide for growing ultra-thin heteroepitaxial graphite films. *Journal of Applied Physics* **2002,** *92* (5), 2479-2484.
91. Berger, C.; Song, Z.; Li, T.; Li, X.; Ogbazghi, A. Y.; Feng, R.; Dai, Z.; Marchenkov, A. N.; Conrad, E. H.; First, P. N.; de Heer, W. A., Ultrathin Epitaxial Graphite: 2D Electron Gas Properties and a Route toward Graphene-based Nanoelectronics. *The Journal of Physical Chemistry B* **2004,** *108* (52), 19912-19916.
92. Berger, C.; Song, Z. M.; Li, X. B.; Wu, X. S.; Brown, N.; Naud, C.; Mayou, D.; Li, T. B.; Hass, J.; Marchenkov, A. N.; Conrad, E. H.; First, P. N.; de Heer, W. A., Electronic confinement and coherence in patterned epitaxial graphene. *Science* **2006,** *312* (5777), 1191-1196.
93. de Heer, W. A.; Berger, C.; Wu, X.; First, P. N.; Conrad, E. H.; Li, X.; Li, T.; Sprinkle, M.; Hass, J.; Sadowski, M. L.; Potemski, M.; Martinez, G., Epitaxial graphene. *Solid State Communications* **2007,** *143* (1–2), 92-100.
94. Emtsev, K. V.; Bostwick, A.; Horn, K.; Jobst, J.; Kellogg, G. L.; Ley, L.; McChesney, J. L.; Ohta, T.; Reshanov, S. A.; Rohrl, J.; Rotenberg, E.; Schmid, A. K.; Waldmann, D.; Weber, H. B.; Seyller, T., Towards wafer-size graphene layers by atmospheric pressure graphitization of silicon carbide. *Nat Mater* **2009,** *8* (3), 203-207.
95. Werner, M.; Locher, R., Growth and application of undoped and doped diamond films. *Reports on Progress in Physics* **1998,** *61* (12), 1665-1710.

96. Joseyacaman, M.; Mikiyoshida, M.; Rendon, L.; Santiesteban, J. G., Catalytic Growth of Carbon Microtubules with Fullerene Structure (Applied Physics Letter, Vol 62, Pg 202, 1993). *Applied Physics Letters* **1993,** *62* (6), 657-659.
97. Li, X.; Cai, W.; An, J.; Kim, S.; Nah, J.; Yang, D.; Piner, R.; Velamakanni, A.; Jung, I.; Tutuc, E.; Banerjee, S. K.; Colombo, L.; Ruoff, R. S., Large-Area Synthesis of High-Quality and Uniform Graphene Films on Copper Foils. *Science* **2009,** *324* (5932), 1312-1314.
98. Yu, Q. K.; Lian, J.; Siriponglert, S.; Li, H.; Chen, Y. P.; Pei, S. S., Graphene segregated on Ni surfaces and transferred to insulators. *Applied Physics Letters* **2008,** *93* (11).
99. Reina, A.; Jia, X. T.; Ho, J.; Nezich, D.; Son, H. B.; Bulovic, V.; Dresselhaus, M. S.; Kong, J., Large Area, Few-Layer Graphene Films on Arbitrary Substrates by Chemical Vapor Deposition. *Nano Lett* **2009,** *9* (1), 30-35.
100. Sutter, P. W.; Flege, J. I.; Sutter, E. A., Epitaxial graphene on ruthenium. *Nat Mater* **2008,** *7* (5), 406-411.
101. Marchini, S.; Gunther, S.; Wintterlin, J., Scanning tunneling microscopy of graphene on Ru(0001). *Physical Review B* **2007,** *76* (7).
102. Loginova, E.; Bartelt, N. C.; Feibelman, P. J.; McCarty, K. F., Evidence for graphene growth by C cluster attachment. *New Journal of Physics* **2008,** *10*.
103. Coraux, J.; N'Diaye, A. T.; Engler, M.; Busse, C.; Wall, D.; Buckanie, N.; Heringdorf, F. J. M. Z.; van Gastel, R.; Poelsema, B.; Michely, T., Growth of graphene on Ir(111). *New Journal of Physics* **2009,** *11*, 023006.
104. Coraux, J.; N'Diaye, A. T.; Busse, C.; Michely, T., Structural coherency of graphene on Ir(111). *Nano Lett* **2008,** *8* (2), 565-570.
105. Vaari, J.; Lahtinen, J.; Hautojarvi, P., The adsorption and decomposition of acetylene on clean and K-covered Co(0001). *Catal Lett* **1997,** *44* (1-2), 43-49.
106. Ueta, H.; Saida, M.; Nakai, C.; Yamada, Y.; Sasaki, M.; Yamamoto, S., Highly oriented monolayer graphite formation on Pt(111) by a supersonic methane beam. *Surface Science* **2004,** *560* (1-3), 183-190.
107. Wang, Y.; Chen, X. H.; Zhong, Y. L.; Zhu, F. R.; Loh, K. P., Large area, continuous, few-layered graphene as anodes in organic photovoltaic devices. *Applied Physics Letters* **2009,** *95* (6).
108. Verma, V. P.; Das, S.; Lahiri, I.; Choi, W., Large-area graphene on polymer film for flexible and transparent anode in field emission device. *Applied Physics Letters* **2010,** *96* (20).
109. Park, H. J.; Meyer, J.; Roth, S.; Skakalova, V., Growth and properties of few-layer graphene prepared by chemical vapor deposition. *Carbon* **2010,** *48* (4), 1088-1094.

110. Lee, Y.; Bae, S.; Jang, H.; Jang, S.; Zhu, S. E.; Sim, S. H.; Song, Y. I.; Hong, B. H.; Ahn, J. H., Wafer-Scale Synthesis and Transfer of Graphene Films. *Nano Lett* **2010,** *10* (2), 490-493.
111. Juang, Z. Y.; Wu, C. Y.; Lu, A. Y.; Su, C. Y.; Leou, K. C.; Chen, F. R.; Tsai, C. H., Graphene synthesis by chemical vapor deposition and transfer by a roll-to-roll process. *Carbon* **2010,** *48* (11), 3169-3174.
112. Li, X. S.; Magnuson, C. W.; Venugopal, A.; An, J. H.; Suk, J. W.; Han, B. Y.; Borysiak, M.; Cai, W. W.; Velamakanni, A.; Zhu, Y. W.; Fu, L. F.; Vogel, E. M.; Voelkl, E.; Colombo, L.; Ruoff, R. S., Graphene Films with Large Domain Size by a Two-Step Chemical Vapor Deposition Process. *Nano Lett* **2010,** *10* (11), 4328-4334.
113. Li, X. S.; Cai, W. W.; Colombo, L.; Ruoff, R. S., Evolution of Graphene Growth on Ni and Cu by Carbon Isotope Labeling. *Nano Lett* **2009,** *9* (12), 4268-4272.
114. Watanabe, K.; Taniguchi, T.; Kanda, H., Direct-bandgap properties and evidence for ultraviolet lasing of hexagonal boron nitride single crystal. *Nat Mater* **2004,** *3* (6), 404-409.
115. Taniguchi, T.; Watanabe, K.; Koizumi, S., Defect characterization of cBN single crystals grown under HP/HT. *physica status solidi (a)* **2004,** *201* (11), 2573-2577.
116. Gubanov, V. A.; Lu, Z. W.; Klein, B. M.; Fong, C. Y., Electronic structure of defects and impurities in III-V nitrides: Vacancies in cubic boron nitride. *Physical Review B* **1996,** *53* (8), 4377-4385.
117. Kubota, Y.; Watanabe, K.; Tsuda, O.; Taniguchi, T., Deep ultraviolet light-emitting hexagonal boron nitride synthesized at atmospheric pressure. *Science* **2007,** *317* (5840), 932-934.
118. Alem, N.; Erni, R.; Kisielowski, C.; Rossell, M. D.; Gannett, W.; Zettl, A., Atomically thin hexagonal boron nitride probed by ultrahigh-resolution transmission electron microscopy. *Physical Review B* **2009,** *80* (15), 155425.
119. Pacile, D.; Meyer, J. C.; Girit, C. O.; Zettl, A., The two-dimensional phase of boron nitride: Few-atomic-layer sheets and suspended membranes. *Applied Physics Letters* **2008,** *92* (13), 133107-3.
120. Meyer, J. C.; Chuvilin, A.; Algara-Siller, G.; Biskupek, J.; Kaiser, U., Selective sputtering and atomic resolution imaging of atomically thin boron nitride membranes. *Nano Lett* **2009,** *9* (7), 2683-2689.
121. Jin, C.; Lin, F.; Suenaga, K.; Iijima, S., Fabrication of a Freestanding Boron Nitride Single Layer and Its Defect Assignments. *Physical Review Letters* **2009,** *102* (19), 195505.
122. Engler, M., Lesniak,C., Damasch, R., Ruisinger,B., Elchler,J., Hexagonal Boron Nitride (hBN) : Applications from Metallurgy to Cosmetics. *Cfi/Ber.DKG* **2007,** *84* (12), E49-E53.

123. Pan, Z. C.; Sun, H.; Zhang, Y.; Chen, C. F., Harder than Diamond: Superior Indentation Strength of Wurtzite BN and Lonsdaleite. *Physical Review Letters* **2009,** *102* (5).
124. http://en.wikipedia.org/wiki/Boron_nitride
125. Chen, X.; Wu, P.; Rousseas, M.; Okawa, D.; Gartner, Z.; Zettl, A.; Bertozzi, C. R., Boron nitride nanotubes are noncytotoxic and can be functionalized for interaction with proteins and cells. *Journal of the American Chemical Society* **2009,** *131* (3), 890-891.
126. Tao, O. Y.; Chen, Y. P.; Xie, Y. E.; Yang, K. K.; Bao, Z. G.; Zhong, J. X., Thermal transport in hexagonal boron nitride nanoribbons. *Nanotechnology* **2010,** *21* (24).
127. Hu, J. N.; Ruan, X. L.; Chen, Y. P., Thermal Conductivity and Thermal Rectification in Graphene Nanoribbons: A Molecular Dynamics Study. *Nano Lett* **2009,** *9* (7), 2730-2735.
128. Lan, J. H.; Wang, J. S.; Gan, C. K.; Chin, S. K., Edge effects on quantum thermal transport in graphene nanoribbons: Tight-binding calculations. *Physical Review B* **2009,** *79* (11).
129. Davis, R. F., III-V nitrides for electronic and optoelectronic applications. *Proceedings of the IEEE* **1991,** *79* (5), 702-712.
130. Song, L.; Ci, L.; Lu, H.; Sorokin, P. B.; Jin, C.; Ni, J.; Kvashnin, A. G.; Kvashnin, D. G.; Lou, J.; Yakobson, B. I.; Ajayan, P. M., Large Scale Growth and Characterization of Atomic Hexagonal Boron Nitride Layers. *Nano Lett* **2010,** *10* (8), 3209-3215.
131. Liu, Z.; Song, L.; Zhao, S. Z.; Huang, J. Q.; Ma, L. L.; Zhang, J. N.; Lou, J.; Ajayan, P. M., Direct Growth of Graphene/Hexagonal Boron Nitride Stacked Layers. *Nano Lett* **2011,** *11* (5), 2032-2037.
132. Kim, K.; Choi, J. Y.; Kim, T.; Cho, S. H.; Chung, H. J., A role for graphene in silicon-based semiconductor devices. *Nature* **2011,** *479* (7373), 338-344.
133. Dean, C. R.; Young, A. F.; Meric, I.; Lee, C.; Wang, L.; Sorgenfrei, S.; Watanabe, K.; Taniguchi, T.; Kim, P.; Shepard, K. L.; Hone, J., Boron nitride substrates for high-quality graphene electronics. *Nat Nanotechnol* **2010,** *5* (10), 722-726.
134. Shi, Y. M.; Hamsen, C.; Jia, X. T.; Kim, K. K.; Reina, A.; Hofmann, M.; Hsu, A. L.; Zhang, K.; Li, H. N.; Juang, Z. Y.; Dresselhaus, M. S.; Li, L. J.; Kong, J., Synthesis of Few-Layer Hexagonal Boron Nitride Thin Film by Chemical Vapor Deposition. *Nano Lett* **2010,** *10* (10), 4134-4139.
135. Coleman, J. N.; Lotya, M.; O'Neill, A.; Bergin, S. D.; King, P. J.; Khan, U.; Young, K.; Gaucher, A.; De, S.; Smith, R. J.; Shvets, I. V.; Arora, S. K.; Stanton, G.; Kim, H. Y.; Lee, K.; Kim, G. T.; Duesberg, G. S.; Hallam, T.; Boland, J. J.; Wang, J. J.; Donegan, J. F.; Grunlan, J. C.; Moriarty, G.; Shmeliov, A.; Nicholls, R. J.; Perkins, J. M.; Grieveson, E. M.; Theuwissen, K.; McComb, D. W.; Nellist, P. D.; Nicolosi, V., Two-Dimensional

Nanosheets Produced by Liquid Exfoliation of Layered Materials. *Science* **2011,** *331* (6017), 568-571.

136. Zhi, C. Y.; Bando, Y.; Tang, C. C.; Kuwahara, H.; Golberg, D., Large-Scale Fabrication of Boron Nitride Nanosheets and Their Utilization in Polymeric Composites with Improved Thermal and Mechanical Properties. *Adv Mater* **2009,** *21* (28), 2889-2893.

137. Choi, C. L.; Alivisatos, A. P., From Artificial Atoms to Nanocrystal Molecules: Preparation and Properties of More Complex Nanostructures. *Annu Rev Phys Chem* **2010,** *61*, 369-389.

138. Steele, G. A.; GotzG; Kouwenhoven, L. P., Tunable few-electron double quantum dots and Klein tunnelling in ultraclean carbon nanotubes. *Nat Nano* **2009,** *4* (6), 363-367.

139. Leatherdale, C. A.; Woo, W. K.; Mikulec, F. V.; Bawendi, M. G., On the Absorption Cross Section of CdSe Nanocrystal Quantum Dots. *The Journal of Physical Chemistry B* **2002,** *106* (31), 7619-7622.

140. Michalet, X.; Pinaud, F. F.; Bentolila, L. A.; Tsay, J. M.; Doose, S.; Li, J. J.; Sundaresan, G.; Wu, A. M.; Gambhir, S. S.; Weiss, S., Quantum dots for live cells, in vivo imaging, and diagnostics. *Science* **2005,** *307* (5709), 538-544.

141. Smyder, J. A.; Krauss, T. D., Coming attractions for semiconductor quantum dots. *Mater Today* **2011,** *14* (9), 382-387.

142. Bimberg, D.; Pohl, U. W., Quantum dots: promises and accomplishments. *Mater Today* **2011,** *14* (9), 388-397.

143. Radovanovic, P. V.; Gamelin, D. R., High-temperature ferromagnetism in $Ni^{2+}$-doped ZnO aggregates prepared from colloidal diluted magnetic semiconductor quantum dots. *Physical Review Letters* **2003,** *91* (15).

144. Hanif, K. M.; Meulenberg, R. W.; Strouse, G. F., Magnetic ordering in doped $Cd_{1-x}Co_xSe$ diluted magnetic quantum dots. *Journal of the American Chemical Society* **2002,** *124* (38), 11495-11502.

145. Erwin, S. C.; Zu, L. J.; Haftel, M. I.; Efros, A. L.; Kennedy, T. A.; Norris, D. J., Doping semiconductor nanocrystals. *Nature* **2005,** *436* (7047), 91-94.

146. Talapin, D. V.; Murray, C. B., PbSe nanocrystal solids for n- and p-channel thin film field-effect transistors. *Science* **2005,** *310* (5745), 86-89.

147. Shim, M.; Guyot-Sionnest, P., N-type colloidal semiconductor nanocrystals. *Nature* **2000,** *407* (6807), 981-983.

148. Wang, C. J.; Shim, M.; Guyot-Sionnest, P., Electrochromic nanocrystal quantum dots. *Science* **2001,** *291* (5512), 2390-2392.

149. Yu, D.; Wang, C. J.; Guyot-Sionnest, P., n-type conducting CdSe nanocrystal solids. *Science* **2003,** *300* (5623), 1277-1280.

150. Pradhan, N.; Goorskey, D.; Thessing, J.; Peng, X. G., An alternative of CdSe nanocrystal emitters: Pure and tunable impurity emissions in ZnSe nanocrystals. *Journal of the American Chemical Society* **2005,** *127* (50), 17586-17587.
151. Bhargava, R. N.; Gallagher, D.; Hong, X.; Nurmikko, A., Optical-Properties of Manganese-Doped Nanocrystals of Zns. *Physical Review Letters* **1994,** *72* (3), 416-419.
152. Stowell, C. A.; Wiacek, R. J.; Saunders, A. E.; Korgel, B. A., Synthesis and characterization of dilute magnetic semiconductor manganese-doped indium arsenide nanocrystals. *Nano Lett* **2003,** *3* (10), 1441-1447.
153. Yang, Y. A.; Chen, O.; Angerhofer, A.; Cao, Y. C., Radial-position-controlled doping in CdS/ZnS core/shell nanocrystals. *Journal of the American Chemical Society* **2006,** *128* (38), 12428-12429.
154. Mocatta, D.; Cohen, G.; Schattner, J.; Millo, O.; Rabani, E.; Banin, U., Heavily Doped Semiconductor Nanocrystal Quantum Dots. *Science* **2011,** *332* (6025), 77-81.
155. Kagan, C. R.; Murray, C. B.; Nirmal, M.; Bawendi, M. G., Electronic energy transfer in CdSe quantum dot solids. *Physical Review Letters* **1996,** *76* (9), 1517-1520.
156. Achermann, M.; Petruska, M. A.; Crooker, S. A.; Klimov, V. I., Picosecond energy transfer in quantum dot Langmuir-Blodgett nanoassemblies. *J Phys Chem B* **2003,** *107* (50), 13782-13787.
157. Kim, J. H.; Holloway, P. H., Near-infrared-electroluminescent light-emitting planar optical sources based on gallium nitride doped with rare earths. *Adv Mater* **2005,** *17* (1), 91-+.
158. Norris, D. J.; Yao, N.; Charnock, F. T.; Kennedy, T. A., High-quality manganese-doped ZnSe nanocrystals. *Nano Lett* **2001,** *1* (1), 3-7.
159. McBain, J. W.; Salmon, C. S., Colloidal electrolytes. soap solutions and their constitution. *Journal of the American Chemical Society* **1920,** *42* (3), 426-460.
160. Burda, C.; Chen, X. B.; Narayanan, R.; El-Sayed, M. A., Chemistry and properties of nanocrystals of different shapes. *Chemical Reviews* **2005,** *105* (4), 1025-1102.
161. Yin, Y.; Alivisatos, A. P., Colloidal nanocrystal synthesis and the organic-inorganic interface. *Nature* **2005,** *437* (7059), 664-670.
162. Goodhew, P. J., Humphreys,F. J. , Beanland, R. , *Electron Microscopy and Analysis*. Taylor & Francis: 2001; p 66~76
163. Williams, D. B., and Carter, C. B. , *Transmission Electron Microscopy—A Text Book for Materials Science* Plenum Press New York, 1996.
164. Bragg, W. H. a. B., W. L. , The Reflection of X-rays by Crystals *Proc. R. Soc. Lond. A* **1913,** *88*, 428-438.
165. P.P., E., Zur Theorie der Interferenzen der Röntgentstrahlen in Kristallen. *Physik. Z.* **1913,** *14*, 465-472.

166. Cruickshank, D. W. J., Juretschke, H. J. , Kato, N. , *P. P. Ewald and his dynamical theory of X-ray diffraction*. Oxford University Press: Oxford, 1992; p 114~123
167. Williams, D. B., and Carter, C. B. , *Transmission Electron Microscopy—A Text Book for Materials Science*. Springer: New York 2009; p 389.
168. Scherzer, O., Über einige Fehler von Elektronenlinsen. *Zeitschrift für Physik* **1936,** *101*, 593-603
169. Shi, D., *Functional Thin Films and Functional Materials: New Concepts and Technologies*. Springer: 2003.
170. Scherzer, O., The Theoretical Resolution Limit of the Electron Microscope. *Journal of Applied Physics* **1949,** *20* (1), 20-29.
171. Williams, D. B., and Carter, C. B. , *Transmission Electron Microscopy—A Text Book for Materials Science* Springer: New York 2009; p 544.
172. http://en.wikipedia.org/wiki/Scanning_electron_microscope
173. Goldstein, J., Newbury, D. E., Echlin,P., Joy, D. C. , Romig Jr., A. D., Lyman,C. E., Fiori, C. and Lifshin, E., *Scanning Electron Microscopy and X-Ray Microanalysis: A Text for Biologists, Materials Scientists, and Geologists,* . 2nd ed.; Plenum Press New York, 1992.
174. http://en.wikipedia.org/wiki/Electron_backscatter_diffraction
175. Reed, S. J. B., *Electron Microprobe Analysis and Scanning Electron Microscopy in Geology*. 2nd ed.; Cambridge University Press: 2005; p 70.
176. Miller, F. A.; Kauffman, G. B., C. V. Raman and the discovery of the Raman effect. *Journal of Chemical Education* **1989,** *66* (10), 795.
177. Loudon, R., Theory of the First-Order Raman Effect in Crystals. *Proceedings of the Royal Society of London. Series A. Mathematical and Physical Sciences* **1963,** *275* (1361), 218-232.
178. http://en.wikipedia.org/wiki/Raman_spectroscopy
179. Ferraro, J. R., Nakamoto, K.,and Brown, C. W., *Introductory Raman Spectroscopy*. 2nd ed.; Academic Press, Elsevier Science: 2003.
180. Dresselhaus, M. S.; Jorio, A.; Hofmann, M.; Dresselhaus, G.; Saito, R., Perspectives on Carbon Nanotubes and Graphene Raman Spectroscopy. *Nano Lett* **2010,** *10* (3), 751-758.
181. Ferrari, A. C.; Meyer, J. C.; Scardaci, V.; Casiraghi, C.; Lazzeri, M.; Mauri, F.; Piscanec, S.; Jiang, D.; Novoselov, K. S.; Roth, S.; Geim, A. K., Raman Spectrum of Graphene and Graphene Layers. *Physical Review Letters* **2006,** *97* (18), 187401.
182. http://en.wikipedia.org/wiki/Intersystem_crossing
183. Griffiths, D. j., *Introduction to Quantum Mechanics*. Prentice Hall: 1995; p 165.
184. http://teaching.shu.ac.uk/hwb/chemistry/tutorials/molspec/lumin1.htm
185. http://teaching.shu.ac.uk/hwb/chemistry/tutorials/molspec/uvvisab1.htm

186. Scholes, G. D., Long-Range Resonace Energy Transfer in Molecular Systems. *Annual Review of Physical Chemistry* **2003,** *54* (1), 57-87.
187. Doering, R., and Nishi, Y., *Handbook of semiconductor manufacturing technology*. 2nd ed.; CRC press Taylors and Francis group: 2008; p 1360.
188. http://en.wikipedia.org/wiki/Van_der_Pauw_method
189. Weller, R. A., An algorithm for computing linear four-point probe thickness correction factors. *Review of Scientific Instruments* **2001,** *72* (9), 3580-3586.
190. Van der Pauw, L. J., A Method of Measuring the Resistivity and Hall Coefficient on Lamellae of Arbitrary Shape. *Philips Tech. Rev.* **1958,** *20*, 220–224.
191. Peng, X.; Manna, L.; Yang, W.; Wickham, J.; Scher, E.; Kadavanich, A.; Alivisatos, A. P., Shape control of CdSe nanocrystals. *Nature* **2000,** *404* (6773), 59-61.
192. Manna, L.; Scher, E. C.; Alivisatos, A. P., Synthesis of soluble and processable rod-, arrow-, teardrop-, and tetrapod-shaped CdSe nanocrystals. *Journal of the American Chemical Society* **2000,** *122* (51), 12700-12706.
193. Peng, Z. A.; Peng, X. G., Mechanisms of the shape evolution of CdSe nanocrystals. *Journal of the American Chemical Society* **2001,** *123* (7), 1389-1395.
194. Puntes, V. F.; Krishnan, K. M.; Alivisatos, A. P., Colloidal Nanocrystal Shape and Size Control: The Case of Cobalt. *Science* **2001,** *291* (5511), 2115-2117.
195. Scher, E. C.; Manna, L.; Alivisatos, A. P., Shape control and applications of nanocrystals. *Philosophical Transactions of the Royal Society of London. Series A: Mathematical, Physical and Engineering Sciences* **2003,** *361* (1803), 241-257.
196. Viswanatha, R.; Battaglia, D.; Curtis, M.; Mishima, T.; Johnson, M.; Peng, X., Shape control of doped semiconductor nanocrystals (d-dots). *Nano Research* **2008,** *1* (2), 138-144.
197. Coleman, J. N.; Lotya, M.; O'Neill, A.; Bergin, S. D.; King, P. J.; Khan, U.; Young, K.; Gaucher, A.; De, S.; Smith, R. J.; Shvets, I. V.; Arora, S. K.; Stanton, G.; Kim, H.-Y.; Lee, K.; Kim, G. T.; Duesberg, G. S.; Hallam, T.; Boland, J. J.; Wang, J. J.; Donegan, J. F.; Grunlan, J. C.; Moriarty, G.; Shmeliov, A.; Nicholls, R. J.; Perkins, J. M.; Grieveson, E. M.; Theuwissen, K.; McComb, D. W.; Nellist, P. D.; Nicolosi, V., Two-Dimensional Nanosheets Produced by Liquid Exfoliation of Layered Materials. *Science* **2011,** *331* (6017), 568-571.
198. Rathod, N.; Hatzikiriakos, S. G., The effect of surface energy of boron nitride on polymer processability. *Polymer Engineering & Science* **2004,** *44* (8), 1543-1550.
199. Batchelor, G. K., *An Introduction To Fluid Dynamics*. Cambridge University Press: 1962.
200. Loginova, E.; Bartelt, N. C.; Feibelman, P. J.; McCarty, K. F., Evidence for graphene growth by C cluster attachment. *New Journal of Physics* **2008,** *10*, 093026.
201. McLean, D., *Grain boundaries in metals*. Clarendon Press: 1957.

202. Shelton, J. C.; Patil, H. R.; Blakely, J. M., Equilibrium Segregation of Carbon to a Nickel (111) Surface - Surface Phase-Transition. *Surface Science* **1974,** *43* (2), 493-520.
203. Zhang, Q. G., X., Wells, J..C., Carbon Absorption on Copper and Nickel Surface: A Comparative First Principle Study. In *American Physical Society March Meeting*, **2005**; p abstract #W20.007.
204. Vlassiouk, I.; Regmi, M.; Fulvio, P. F.; Dai, S.; Datskos, P.; Eres, G.; Smirnov, S., Role of Hydrogen in Chemical Vapor Deposition Growth of Large Single-Crystal Graphene. *ACS Nano* **2011,** *5* (7), 6069-6076.
205. Luo, Z. T.; Lu, Y.; Singer, D. W.; Berck, M. E.; Somers, L. A.; Goldsmith, B. R.; Johnson, A. T. C., Effect of Substrate Roughness and Feedstock Concentration on Growth of Wafer-Scale Graphene at Atmospheric Pressure. *Chemistry of Materials* **2011,** *23* (6), 1441-1447.
206. Bhaviripudi, S.; Jia, X. T.; Dresselhaus, M. S.; Kong, J., Role of Kinetic Factors in Chemical Vapor Deposition Synthesis of Uniform Large Area Graphene Using Copper Catalyst. *Nano Lett* **2010,** *10* (10), 4128-4133.
207. Han, G. H.; Gunes, F.; Bae, J. J.; Kim, E. S.; Chae, S. J.; Shin, H. J.; Choi, J. Y.; Pribat, D.; Lee, Y. H., Influence of Copper Morphology in Forming Nucleation Seeds for Graphene Growth. *Nano Lett* **2011,** *11* (10), 4144-4148.
208. Wofford, J. M.; Nie, S.; McCarty, K. F.; Bartelt, N. C.; Dubon, O. D., Graphene Islands on Cu Foils: The Interplay between Shape, Orientation, and Defects. *Nano Lett* **2010,** *10* (12), 4890-4896.
209. Gao, L.; Guest, J. R.; Guisinger, N. P., Epitaxial graphene on Cu(111). *Nano Lett* **2010,** *10* (9), 3512-3516.
210. Murray, C. B.; Norris, D. J.; Bawendi, M. G., Synthesis and characterization of nearly monodisperse CdE (E = S, Se, Te) semiconductor nanocrystallites. *Journal of the American Chemical Society* **1993,** *115* (19), 8706-8715.
211. Warner, J. H.; Tilley, R. D., Synthesis and self-assembly of triangular and hexagonal CdS nanocrystals. *Adv Mater* **2005,** *17* (24), 2997-3001.
212. Erwin, S. C.; Zu, L.; Haftel, M. I.; Efros, A. L.; Kennedy, T. A.; Norris, D. J., Doping semiconductor nanocrystals. *Nature* **2005,** *436* (7047), 91-94.
213. Norris, D. J.; Efros, A. L.; Erwin, S. C., Doped nanocrystals. *Science* **2008,** *319* (5871), 1776-1779.
214. Bhargava, R. N.; Gallagher, D.; Hong, X.; Nurmikko, A., Optical properties of manganese-doped nanocrystals of ZnS. *Physical Review Letters* **1994,** *72* (3), 416-419.
215. Colvin, V. L.; Schlamp, M. C.; Alivisatos, A. P., Light-emitting diodes made from cadmium selenide nanocrystals and a semiconducting polymer. *Nature* **1994,** *370* (6488), 354-357.

216. Klimov, V. I.; Ivanov, S. A.; Nanda, J.; Achermann, M.; Bezel, I.; McGuire, J. A.; Piryatinski, A., Single-exciton optical gain in semiconductor nanocrystals. *Nature* **2007,** *447* (7143), 441-446.
217. Chan, W. C. W.; Nie, S., Quantum dot bioconjugates for ultrasensitive nonisotopic detection. *Science* **1998,** *281* (5385), 2016-2018.
218. Bruchez Jr, M.; Moronne, M.; Gin, P.; Weiss, S.; Alivisatos, A. P., Semiconductor nanocrystals as fluorescent biological labels. *Science* **1998,** *281* (5385), 2013-2016.
219. Zimmer, J. P.; Kim, S. W.; Ohnishi, S.; Tanaka, E.; Frangioni, J. V.; Bawendi, M. G., Size series of small indium arsenide-zinc selenide core-shell nanocrystals and their application to in vivo imaging. *Journal of the American Chemical Society* **2006,** *128* (8), 2526-2527.
220. Greenham, N. C.; Peng, X.; Alivisatos, A. P., Charge separation and transport in conjugated-polymer/semiconductor-nanocrystal composites studied by photoluminescence quenching and photoconductivity. *Physical Review B - Condensed Matter and Materials Physics* **1996,** *54* (24), 17628-17637.
221. Pradhan, N.; Goorskey, D.; Thessing, J.; Peng, X., An alternative of CdSe nanocrystal emitters: Pure and tunable impurity emissions in ZnSe nanocrystals. *Journal of the American Chemical Society* **2005,** *127* (50), 17586-17587.
222. Pradhan, N.; Peng, X., Efficient and color-tunable Mn-doped ZnSe nanocrystal emitters: Control of optical performance via greener synthetic chemistry. *Journal of the American Chemical Society* **2007,** *129* (11), 3339-3347.
223. Pradhan, N.; Battaglia, D. M.; Liu, Y.; Peng, X., Efficient, stable, small, and water-soluble doped ZnSe nanocrystal emitters as non-cadmium biomedical labels. *Nano Lett* **2007,** *7* (2), 312-317.
224. Thakar, R.; Chen, Y.; Snee, P. T., Efficient emission from core/(Doped) shell nanoparticles: Applications for chemical sensing. *Nano Lett* **2007,** *7* (11), 3429-3432.
225. Nag, A.; Chakraborty, S.; Sarma, D. D., To dope $Mn^{2+}$ in a semiconducting nanocrystal. *Journal of the American Chemical Society* **2008,** *130* (32), 10605-10611.
226. Yang, Y.; Chen, O.; Angerhofer, A.; Cao, Y. C., On doping CdS/ZnS core/shell nanocrystals with Mn. *Journal of the American Chemical Society* **2008,** *130* (46), 15649-15661.
227. Chen, D.; Viswanatha, R.; Ong, G. L.; Xie, R.; Balasubramaninan, M.; Peng, X., Temperature dependence of "elementary processes" in doping semiconductor nanocrystals. *Journal of the American Chemical Society* **2009,** *131* (26), 9333-9339.
228. Srivastava, B. B.; Jana, S.; Karan, N. S.; Paria, S.; Jana, N. R.; Sarma, D. D.; Pradhan, N., Highly luminescent Mn-doped ZnS nanocrystals: Gram-scale synthesis. *Journal of Physical Chemistry Letters* **2010,** *1* (9), 1454-1458.

229. Deng, Z.; Tong, L.; Flores, M.; Lin, S.; Cheng, J. X.; Yan, H.; Liu, Y., High-quality manganese-doped zinc sulfide quantum rods with tunable dual-color and multiphoton emissions. *Journal of the American Chemical Society* **2011,** *133* (14), 5389-5396.

230. Dalpian, G. M.; Chelikowsky, J. R., Self-purification in semiconductor nanocrystals. *Physical Review Letters* **2006,** *96* (22).

231. Suyver, J. F.; Wuister, S. F.; Kelly, J. J.; Meijerink, A., Luminescence of nanocrystalline ZnSe:$Mn^{2+}$. *Physical Chemistry Chemical Physics* **2000,** *2* (23), 5445-5448.

232. Zeng, R.; Rutherford, M.; Xie, R.; Zou, B.; Peng, X., Synthesis of highly emissive Mn-Doped ZnSe nanocrystals without pyrophoric reagents. *Chemistry of Materials* **2010,** *22* (6), 2107-2113.

233. Panda, S. K.; Hickey, S. G.; Demir, H. V.; Eychmüller, A., Bright white-light emitting manganese and copper co-doped ZnSe quantum dots. *Angewandte Chemie - International Edition* **2011,** *50* (19), 4432-4436.

234. Cao, H.; Xiao, Y.; Zhang, S., The synthesis and photocatalytic activity of ZnSe microspheres. *Nanotechnology* **2011,** *22* (1).

235. Dey, S. C.; Nath, S. S., Electroluminescence of colloidal ZnSe quantum dots. *Journal of Luminescence* **2011,** *131* (12), 2707-2710.

236. Watt, J.; Young, N.; Haigh, S.; Kirkland, A.; Tilley, R. D., Synthesis and structural characterization of branched palladium nanostructures. *Adv Mater* **2009,** *21* (22), 2288-2293.

237. Manna, L.; Milliron, D. J.; Meisel, A.; Scher, E. C.; Alivisatos, A. P., Controlled growth of tetrapod-branched inorganic nanocrystals. *Nat Mater* **2003,** *2* (6), 382-385.

238. Rhys Williams, A. T.; Winfield, S. A.; Miller, J. N., Relative fluorescence quantum yields using a Computer-controlled luminescence spectrometer. *The Analyst* **1983,** *108* (1290), 1067-1071.

239. Jin, L.; Choy, W. C. H.; Leung, Y. P.; Yuk, T. I.; Ong, H. C.; Wang, J. B., Synthesis and analysis of abnormal wurtzite ZnSe nanowheels. *Journal of Applied Physics* **2007,** *102* (4).

240. Liu, S. Y.; Choy, W. C. H.; Jin, L.; Leung, Y. P.; Zheng, G. P.; Wang, J.; Soh, A. K., Triple-crystal zinc selenide nanobelts. *J Phys Chem C* **2007,** *111* (26), 9055-9059.

241. Eaton, D. F., Reference Materials for Fluorescence Measurement. *Pure Appl Chem* **1988,** *60* (7), 1107-1114.

242. Karstens, T.; Kobs, K., Rhodamine-B and Rhodamine-101 as Reference Substances for Fluorescence Quantum Yield Measurements. *J Phys Chem-Us* **1980,** *84* (14), 1871-1872.

243. Chang, T. L.; Cheung, H. C., Solvent effects on the photoisomerization rates of the zwitterionic and the cationic forms of rhodamine B in protic solvents. *The Journal of Physical Chemistry* **1992,** *96* (12), 4874-4878.
244. Brus, L. E., A simple model for the ionization potential, electron affinity, and aqueous redox potentials of small semiconductor crystallites. *The Journal of Chemical Physics* **1983,** *79* (11), 5566-5571.
245. Chen, W.; Sammynaiken, R.; Huang, Y.; Malm, J. O.; Wallenberg, R.; Bovin, J. O.; Zwiller, V.; Kotov, N. A., Crystal field, phonon coupling and emission shift of $Mn^{2+}$ in ZnS:Mn nanoparticles. *Journal of Applied Physics* **2001,** *89* (2), 1120-1129.
246. Hebert, D. N.; Soares, J. A. N. T.; Rockett, A. A., Photoluminescence and Photoluminescence Excitation Spectroscopy of Cu(In,Ga)$Se_2$ Thin Films. *MRS Proceedings* **2009,** *1165,* 1165-M03-05 doi:10.1557/PROC-1165-M03-05.
247. Ni, Z. H.; Fan, H. M.; Kasim, J.; You, Y. M.; Feng, Y. P.; Han, M. Y.; Shen, Z. X., High pressure photoluminescence and Raman studies of $Zn_xCd_{1-x}Se$ quantum dots. *Journal of Physics: Condensed Matter* **2008,** *20* (32), 325214.
248. Tuchman, J. A.; Sui, Z.; Kim, S.; Herman, I. P., Photoluminescence of ZnSe/ZnMnSe superlattices under hydrostatic pressure. *Journal of Applied Physics* **1993,** *73* (11), 7730-7738.
249. Han, W. Q.; Mickelson, W.; Cumings, J.; Zettl, A., Transformation of $B_xC_yN_z$ nanotubes to pure BN nanotubes. *Applied Physics Letters* **2002,** *81* (6), 1110-1112.
250. Golberg, D.; Costa, P. M. F. J.; Lourie, O.; Mitome, M.; Bai, X.; Kurashima, K.; Zhi, C.; Tang, C.; Bando, Y., Direct force measurements and kinking under elastic deformation of individual multiwalled boron nitride nanotubes. *Nano Lett* **2007,** *7* (7), 2146-2151.
251. Ci, L.; Song, L.; Jin, C.; Jariwala, D.; Wu, D.; Li, Y.; Srivastava, A.; Wang, Z. F.; Storr, K.; Balicas, L.; Liu, F.; Ajayan, P. M., Atomic layers of hybridized boron nitride and graphene domains. *Nat Mater* **2010,** *9* (5), 430-435.
252. Lee, Z.; Jeon, K. J.; Dato, A.; Erni, R.; Richardson, T. J.; Frenklach, M.; Radmilovic, V., Direct imaging of soft-hard interfaces enabled by graphene. *Nano Lett* **2009,** *9* (9), 3365-3369.
253. Warner, J. H.; Rümmeli, M. H.; Bachmatiuk, A.; Wilson, M.; Büchner, B., Examining co-based nanocrystals on graphene using low-voltage aberration- corrected transmission electron microscopy. *ACS Nano* **2010,** *4* (1), 470-476.
254. Wilson, N. R.; Pandey, P. A.; Beanland, R.; Young, R. J.; Kinloch, I. A.; Gong, L.; Liu, Z.; Suenaga, K.; Rourke, J. P.; York, S. J.; Sloan, J., Graphene Oxide: Structural Analysis and Application as a Highly Transparent Support for Electron Microscopy. *ACS Nano* **2009,** *3* (9), 2547-2556.

255. Zhi, C.; Bando, Y.; Tang, C.; Kuwahara, H.; Golberg, D., Large-scale fabrication of boron nitride nanosheets and their utilization in polymeric composites with improved thermal and mechanical properties. *Adv Mater* **2009,** *21* (28), 2889-2893.
256. Warner, J. H.; Rümmeli, M. H.; Bachmatiuk, A.; Büchner, B., Atomic resolution imaging and topography of boron nitride sheets produced by chemical exfoliation. *ACS Nano* **2010,** *4* (3), 1299-1304.
257. Lin, Y.; Williams, T. V.; Connell, J. W., Soluble, exfoliated hexagonal boron nitride nanosheets. *Journal of Physical Chemistry Letters* **2010,** *1* (1), 277-283.
258. Krivanek, O. L.; Chisholm, M. F.; Nicolosi, V.; Pennycook, T. J.; Corbin, G. J.; Dellby, N.; Murfitt, M. F.; Own, C. S.; Szilagyi, Z. S.; Oxley, M. P.; Pantelides, S. T.; Pennycook, S. J., Atom-by-atom structural and chemical analysis by annular dark-field electron microscopy. *Nature* **2010,** *464* (7288), 571-574.
259. Alem, N.; Erni, R.; Kisielowski, C.; Rossell, M. D.; Gannett, W.; Zettl, A., Atomically thin hexagonal boron nitride probed by ultrahigh-resolution transmission electron microscopy. *Physical Review B - Condensed Matter and Materials Physics* **2009,** *80* (15).
260. Jin, C.; Lin, F.; Suenaga, K.; Iijima, S., Fabrication of a freestanding boron nitride single layer and Its defect assignments. *Physical Review Letters* **2009,** *102* (19).
261. Xu, L.; Zhan, J.; Hu, J.; Bando, Y.; Yuan, X.; Sekiguchi, T.; Mitome, M.; Golberg, D., High-yield synthesis of rhombohedral boron nitride triangular nanoplates. *Adv Mater* **2007,** *19* (16), 2141-2144.
262. Auwärter, W.; Suter, H. U.; Sachdev, H.; Greber, T., Synthesis of One Monolayer of Hexagonal Boron Nitride on Ni(111) from B-Trichloroborazine (ClBNH) 3. *Chemistry of Materials* **2004,** *16* (2), 343-345.
263. Warner, J. H.; Schäffel, F.; Rümmeli, M. H.; Büchner, B., Examining the edges of multi-layer graphene sheets. *Chemistry of Materials* **2009,** *21* (12), 2418-2421.
264. Williams, D. B., Carter, C.B., *Transmission Electron Microscopy-A Text Book for Materials Science*. Springer: New York, 2009; p 393.
265. Warner, J. H.; Rümmeli, M. H.; Gemming, T.; Büchner, B.; Briggs, G. A. D., Direct imaging of rotational stacking faults in few layer graphene. *Nano Lett* **2009,** *9* (1), 102-106.
266. Tietz, L. A.; Carter, C. B.; McKernan, S., Top-bottom effects in double diffraction. *Ultramicroscopy* **1995,** *60* (2), 241-246.
267. Reis, D. A.; DeCamp, M. F.; Bucksbaum, P. H.; Clarke, R.; Dufresne, E. M.; Merlin, R.; Wahlstrand, J.; Adams, B.; Wark, J. S., Time-resolved pendellösung oscillations from impulsively strained crystals. In *Conf. on Quantum Electronics and Laser Science (QELS)—Technical Digest Series*, **2002**; Vol. 74, p 122.

268. Stacy, W. T.; Janssen, M. M., X-ray Pendellösung in garnet epitaxial layers. *J Cryst Growth* **1974,** *27* (C), 282-286.
269. Williams, D. B., Carter, C.B., *Transmission Electron Microscopy-A Text Book for Materials Science*. Springer: New York, **2009**; p 371.
270. Schwierz, F., Graphene transistors. *Nat Nanotechnol* **2010,** *5* (7), 487-496.
271. Lemme, M. C.; Echtermeyer, T. J.; Baus, M.; Kurz, H., A graphene field-effect device. *IEEE Electron Device Letters* **2007,** *28* (4), 282-284.
272. Meric, I., Baklitskaya, N., Kim, P., Shepard, K.L. In *IEDM Tecnical Digest*, 2008 Electron Devices Meeting, San Francisco, CA, Dec 15-17; IEEE: Piscataway, NJ, : San Francisco, CA, 2008; p paper 21.2.
273. Kim, K. S.; Zhao, Y.; Jang, H.; Lee, S. Y.; Kim, J. M.; Ahn, J. H.; Kim, P.; Choi, J. Y.; Hong, B. H., Large-scale pattern growth of graphene films for stretchable transparent electrodes. *Nature* **2009,** *457* (7230), 706-710.
274. Bae, S.; Kim, H.; Lee, Y.; Xu, X.; Park, J. S.; Zheng, Y.; Balakrishnan, J.; Lei, T.; Ri Kim, H.; Song, Y. I.; Kim, Y. J.; Kim, K. S.; Özyilmaz, B.; Ahn, J. H.; Hong, B. H.; Iijima, S., Roll-to-roll production of 30-inch graphene films for transparent electrodes. *Nat Nanotechnol* **2010,** *5* (8), 574-578.
275. Li, X.; Zhu, Y.; Cai, W.; Borysiak, M.; Han, B.; Chen, D.; Piner, R. D.; Colomba, L.; Ruoff, R. S., Transfer of large-area graphene films for high-performance transparent conductive electrodes. *Nano Lett* **2009,** *9* (12), 4359-4363.
276. Li, X. S.; Cai, W. W.; An, J. H.; Kim, S.; Nah, J.; Yang, D. X.; Piner, R.; Velamakanni, A.; Jung, I.; Tutuc, E.; Banerjee, S. K.; Colombo, L.; Ruoff, R. S., Large-Area Synthesis of High-Quality and Uniform Graphene Films on Copper Foils. *Science* **2009,** *324* (5932), 1312-1314.
277. Li, X. S.; Magnuson, C. W.; Venugopal, A.; Tromp, R. M.; Hannon, J. B.; Vogel, E. M.; Colombo, L.; Ruoff, R. S., Large-Area Graphene Single Crystals Grown by Low-Pressure Chemical Vapor Deposition of Methane on Copper. *Journal of the American Chemical Society* **2011,** *133* (9), 2816-2819.
278. Lee, S.; Lee, K.; Zhong, Z. H., Wafer Scale Homogeneous Bilayer Graphene Films by Chemical Vapor Deposition. *Nano Lett* **2010,** *10* (11), 4702-4707.
279. Yan, K.; Peng, H. L.; Zhou, Y.; Li, H.; Liu, Z. F., Formation of Bilayer Bernal Graphene: Layer-by-Layer Epitaxy via Chemical Vapor Deposition. *Nano Lett* **2011,** *11* (3), 1106-1110.
280. Yao, Y. G.; Li, Z.; Lin, Z. Y.; Moon, K. S.; Agar, J.; Wong, C. P., Controlled Growth of Multilayer, Few-Layer, and Single-Layer Graphene on Metal Substrates. *J Phys Chem C* **2011,** *115* (13), 5232-5238.

281. Rasool, H. I.; Song, E. B.; Allen, M. J.; Wassei, J. K.; Kaner, R. B.; Wang, K. L.; Weiller, B. H.; Gimzewski, J. K., Continuity of graphene on polycrystalline copper. *Nano Lett* **2011,** *11* (1), 251-256.
282. Zhao, L.; Rim, K. T.; Zhou, H.; He, R.; Heinz, T. F.; Pinczuk, A.; Flynn, G. W.; Pasupathy, A. N., Influence of copper crystal surface on the CVD growth of large area monolayer graphene. *Solid State Communications* **2011,** *151* (7), 509-513.
283. Robertson, A. W.; Warner, J. H., Hexagonal Single Crystal Domains of Few-Layer Graphene on Copper Foils. *Nano Lett* **2011,** *11* (3), 1182-1189.
284. Ferrari, A. C.; Robertson, J., Raman spectroscopy of amorphous, nanostructured, diamond-like carbon, and nanodiamond. *Philos T R Soc A* **2004,** *362* (1824), 2477-2512.
285. Chen, H.; Zhu, W.; Zhang, Z., Contrasting Behavior of Carbon Nucleation in the Initial Stages of Graphene Epitaxial Growth on Stepped Metal Surfaces. *Physical Review Letters* **2010,** *104* (18), 186101.
286. Sun, Z. Z.; Yan, Z.; Yao, J.; Beitler, E.; Zhu, Y.; Tour, J. M., Growth of graphene from solid carbon sources. *Nature* **2010,** *468* (7323), 549-552.
287. Zangwill, A.; Vvedensky, D. D., Novel Growth Mechanism of Epitaxial Graphene on Metals. *Nano Lett* **2011,** *11* (5), 2092-2095.
288. Vlassiouk, I.; Regmi, M.; Fulvio, P.; Dai, S.; Datskos, P.; Eres, G.; Smirnov, S., Role of hydrogen in chemical vapor deposition growth of large single-crystal graphene. *ACS Nano* **2011,** *5* (7), 6069-6076.
289. Bi, H.; Huang, F.; Liang, J.; Xie, X.; Jiang, M., Transparent conductive graphene films synthesized by ambient pressure chemical vapor deposition used as the front electrode of CdTe solar cells. *Adv Mater* **2011,** *23* (28), 3202-3206.
290. Wu, B.; Geng, D. C.; Guo, Y. L.; Huang, L. P.; Xue, Y. Z.; Zheng, J.; Chen, J. Y.; Yu, G.; Liu, Y. Q.; Jiang, L.; Hu, W. P., Equiangular Hexagon-Shape-Controlled Synthesis of Graphene on Copper Surface. *Adv Mater* **2011,** *23* (31), 3522-3525.
291. Wu, W.; Jauregui, L. A.; Su, Z. H.; Liu, Z. H.; Bao, J. M.; Chen, Y. P.; Yu, Q. K., Growth of Single Crystal Graphene Arrays by Locally Controlling Nucleation on Polycrystalline Cu Using Chemical Vapor Deposition. *Adv Mater* **2011,** *23* (42), 4898-4903.
292. Yu, Q. K.; Jauregui, L. A.; Wu, W.; Colby, R.; Tian, J. F.; Su, Z. H.; Cao, H. L.; Liu, Z. H.; Pandey, D.; Wei, D. G.; Chung, T. F.; Peng, P.; Guisinger, N. P.; Stach, E. A.; Bao, J. M.; Pei, S. S.; Chen, Y. P., Control and characterization of individual grains and grain boundaries in graphene grown by chemical vapour deposition. *Nat Mater* **2011,** *10* (6), 443-449.
293. Wu, Y. A.; Robertson, A. W.; Schaffel, F.; Speller, S. C.; Warner, J. H., Aligned Rectangular Few-Layer Graphene Domains on Copper Surfaces. *Chemistry of Materials* **2011,** *23* (20), 4543-4547.

294. Huang, P. Y.; Ruiz-Vargas, C. S.; van der Zande, A. M.; Whitney, W. S.; Levendorf, M. P.; Kevek, J. W.; Garg, S.; Alden, J. S.; Hustedt, C. J.; Zhu, Y.; Park, J.; McEuen, P. L.; Muller, D. A., Grains and grain boundaries in single-layer graphene atomic patchwork quilts. *Nature* **2011,** *469* (7330), 389-392.
295. Robertson, A. W.; Bachmatiuk, A.; Wu, Y. A.; Schäffel, F.; Rellinghaus, B.; Büchner, B.; Rümmeli, M. H.; Warner, J. H., Atomic Structure of Interconnected Few-Layer Graphene Domains. *ACS Nano* **2011,** *5* (8), 6610-6618.
296. Robertson, A. W.; Bachmatiuk, A.; Wu, Y. A.; Schäffel, F.; Büchner, B.; Rümmeli, M. H.; Warner, J. H., Structural Distortions in Few-Layer Graphene Creases. *ACS Nano* **2011,** *5* (12), 9984-9991.
297. Han, G. H.; Güneş, F.; Bae, J. J.; Kim, E. S.; Chae, S. J.; Shin, H. J.; Choi, J. Y.; Pribat, D.; Lee, Y. H., Influence of copper morphology in forming nucleation seeds for graphene growth. *Nano Lett* **2011,** *11* (10), 4144-4148.
298. Luo, Z.; Lu, Y.; Singer, D. W.; Berck, M. E.; Somers, L. A.; Goldsmith, B. R.; Johnson, A. T. C., Effect of substrate roughness and feedstock concentration on growth of wafer-scale graphene at atmospheric pressure. *Chemistry of Materials* **2011,** *23* (6), 1441-1447.
299. He, R.; Zhao, L.; Petrone, N.; Kim, K. S.; Roth, M.; Hone, J.; Kim, P.; Pasupathy, A.; Pinczuk, A., Large Physisorption Strain in Chemical Vapor Deposition of Graphene on Copper Substrates. *Nano Lett* **2012,** *12* (5), 2408-2413.
300. Wang, Y. Y.; Ni, Z. H.; Yu, T.; Shen, Z. X.; Wang, H. M.; Wu, Y. H.; Chen, W.; Wee, A. T. S., Raman studies of monolayer graphene: The substrate effect. *J Phys Chem C* **2008,** *112* (29), 10637-10640.
301. Ni, Z. H.; Wang, Y. Y.; Yu, T.; Shen, Z. X., Raman Spectroscopy and Imaging of Graphene. *Nano Research* **2008,** *1* (4), 273-291.
302. Salihoglu, O., Balci, S., Kocabas, C., Plasmon-polaritons on graphene-metal surface and their use in biosensors *Appl. Phys. Lett.* **2012,** *100*, 213110.
303. Warner, J. H.; Rummeli, M. H.; Ge, L.; Gemming, T.; Montanari, B.; Harrison, N. M.; Buchner, B.; Briggs, G. A. D., Structural transformations in graphene studied with high spatial and temporal resolution. *Nat Nanotechnol* **2009,** *4* (8), 500-504.
304. Casiraghi, C.; Hartschuh, A.; Qian, H.; Piscanec, S.; Georgi, C.; Fasoli, A.; Novoselov, K. S.; Basko, D. M.; Ferrari, A. C., Raman Spectroscopy of Graphene Edges. *Nano Lett* **2009,** *9* (4), 1433-1441.